Quantum-transport analysis of transistors based on nanoribbons of novel 2D materials

Matić, Mislav

Doctoral thesis / Disertacija

2024

University of Zagreb

FACULTY OF ELECTRICAL ENGINEERING AND COMPUTING

Mislav Matić

QUANTUM-TRANSPORT ANALYSIS OF TRANSISTORS BASED ON NANORIBBONS OF NOVEL 2D MATERIALS

DOCTORAL THESIS

Zagreb, 2024

University of Zagreb

FACULTY OF ELECTRICAL ENGINEERING AND COMPUTING

Mislav Matić

QUANTUM-TRANSPORT ANALYSIS OF TRANSISTORS BASED ON NANORIBBONS OF NOVEL 2D MATERIALS

DOCTORAL THESIS

Supervisor: Associate Professor Mirko Poljak, PhD

Zagreb, 2024

Sveučilište u Zagrebu

FAKULTET ELEKTROTEHNIKE I RAČUNARSTVA

Mislav Matić

KVANTNOTRANSPORTNA ANALIZA TRANZISTORA TEMELJENIH NA NANOVRPCAMA NOVIH 2D MATERIJALA

DOKTORSKI RAD

Mentor: izv. prof. dr. sc. Mirko Poljak

Zagreb, 2024.

The doctoral thesis was completed at the University of Zagreb Faculty of Electrical Engineering and Computing, Department of Electronics, Microelectronics, Computers and Intelligent Systems, Zagreb, Croatia.

Supervisor: Associate Professor Mirko Poljak, PhD

The thesis has: 119 Pages

Thesis number:______

About the Supervisor

Mirko Poljak is an Associate Professor at the Faculty of Electrical Engineering and Computing, University of Zagreb (UNIZG-FER). At this institution, he received the PhD degree in the field of nanoelectronics in May 2013 under the supervision of Prof. Tomislav Suligoj, PhD (UNIZG-FER) and Prof. Kang L. Wang, PhD (University of California Los Angeles, UCLA). In summer 2009 he attended the European School on Nanosciences and Nanotechnologies in Grenoble (France). In the academic year 2011/2012 he was a Visiting Researcher - Fulbright Fellow - in the Device Research Lab, Department of Electrical Engineering, UCLA (USA). In December 2014 and June 2015 he did research visits at the Atomistic Simulation Centre, Queen's University Belfast, Belfast (UK).

Prof. Poljak's research is focused on theoretical understanding and developing models and numerical simulators for the design, analysis and optimization of electron devices at the nanoscale. During his doctoral studies, he worked on carrier transport in low-dimensional nanoelectronic devices such as UTB SOI, FinFET and UTB InGaAs-OI. During his stay at UCLA, he investigated electronic and transport properties of graphene and graphene nanoribbons, both experimentally and theoretically. His current research interests include the development of an atomistic quantum-transport numerical tool (TCAD) for the analysis of nanodevices based on 2D/1D materials for applications in nanoelectronics. Prof. Poljak has authored more than 30 papers in international journals and more than 50 conference papers.

He serves as reviewer for Nature Electronics, IEEE Electron Device Letters, IEEE Transactions on Electron Devices, Applied Physics Letters, 2D Materials, Nanoscale, Journal of Applied Physics, Solid-State Electronics, etc. Prof. Poljak is a Senior Member of IEEE since 2019, and member of IEEE Electron Devices Society and Croatian Society MIPRO since 2007. In the period 2018-2021 he was Chair, in 2022-2023 Vice-Chair, and from 2024 again Chair of the Joint ED/SSC Chapter, IEEE Croatia Section. He is member of the Program Committee for MIPRO-MEET from 2021. Prof. Poljak was awarded the National Science Award (2017), Annual Science Award by the Association of University Professors in Zagreb (2017), FER's Science Award for World-Class Research Achievement (2016), Vera Johanides Award by the

Croatian Academy of Engineering (2014), FER's Silver Medal and "Josip Lončar" Award for Outstanding PhD Thesis (2013), FER's Science Award for Outstanding Research Achievements (2013) and the prestigious Fulbright Fellowship by the US Government (2011). He is the author of the university textbook "Quantum Transport on the Nanoscale" (Element, Zagreb, 2023).

- https://orcid.org/0000-0001-7075-6688
- https://scholar.google.hr/citations?user=vTvsOCIAAAAJ&hl
- https://www.researchgate.net/profile/Mirko_Poljak
- https://www.scopus.com/authid/detail.uri?authorId=24344736100
- https://publons.com/researcher/2532146/mirko-poljak/

O mentoru

Mirko Poljak je izvanredni profesor na Fakultetu elektrotehnike i računarstva Sveučilišta u Zagrebu (UNIZG-FER). Na ovoj instituciji je doktorirao u svibnju 2013. u području nanoelektronike pod mentorstvom prof. dr. sc. Tomislava Suligoja (UNIZG-FER) i prof. dr. sc. Kanga L. Wanga (University of California Los Angeles, UCLA). U ljeto 2009. usavršavao se na European School on Nanosciences and Nanotechnologies u Grenobleu (Francuska). U akad. god. 2011./2012. bio je gostujući istraživač - Fulbright Fellow - u grupi Device Research Lab, Department of Electrical Engineering, UCLA (SAD). U prosincu 2014. i lipnju 2015. je bio na dva jednotjedna usavršavanja u Atomistic Simulation Centre, Queen's University Belfast, Belfast (UK).

Znanstveni rad profesora Poljaka fokusiran je na teorijsko razumijevanje te razvoj modela i numeričkih simulatora za projektiranje, analizu i optimizaciju elektroničkih komponenti na nanoskali. Za vrijeme doktorskog studija, bio je fokusiran na transport nosilaca u niskodimenzionalnim nanoelektroničkim strukturama poput UTB SOI, FinFET i UTB InGaAs-OI. Za vrijeme boravka na UCLA-u, istraživao je transportna i elektronska svojstva grafena i grafenskih nanovrpci, eksperimentalno i teorijski. Trenutni fokus je na razvoju atomističkog kvantnotransportnog simulatora za nanoelektroničke komponente s 2D/1D materijalima za primjene u elektronici na nanoskali. Prof. Poljak je autor preko 30 radova u međunarodnim časopisima i preko 50 znanstvenih radova na međunarodnim konferencijama.

Recenzent je časopisa Nature Electronics, IEEE Electron Device Letters, IEEE Transactions on Electron Devices, 2D Materials, Nanoscale, Applied Physics Letters, Journal of Applied Physics, Solid-State Electronics itd. Prof. Poljak je IEEE Senior Member od 2019., te član IEEE Electron Devices Society i Hrvatske udruge MIPRO od 2007. godine. U periodu 2018.-2021. bio je predsjednik, u periodu 2022.-2023. dopredsjednik te od 2024. godine ponovno predsjednik Zajedničkog odjela ED/SSC Hrvatske sekcije IEEE. Od 2021. godine član je programskog odbora međunarodne konferencije MIPRO-MEET. Prof. Poljak je dobitnik Državne nagrade za znanost (2017.), Godišnje nagrade Društva sveučilišnih nastavnika i znanstvenika u Zagrebu (2017.), Nagrade za znanost FER-a za svjetski priznati istraživački rezultat (2016.), Nagrade Vera Johanides za mlade znanstvenike Akademije tehničkih znanosti Hrvatske (2014.), Srebrne plakete "Josip Lončar" za naročito uspješnu doktorsku disertaciju (2013.), Nagrade za znanost FER-a za iznimno postignuće u istraživačkom radu (2013.) te prestižne Fulbrightove stipendije Vlade SAD-a (2011.). Autor je sveučilišnog udžbenika "Kvantni transport na nanoskali" (Element, Zagreb, 2023.).

- https://orcid.org/0000-0001-7075-6688
- https://scholar.google.hr/citations?user=vTvsOCIAAAAJ&hl
- https://www.researchgate.net/profile/Mirko_Poljak
- https://www.scopus.com/authid/detail.uri?authorId=24344736100
- https://publons.com/researcher/2532146/mirko-poljak/

Acknowledgments

First of all, I would like to thank my supervisor, Assoc. Prof. Mirko Poljak, for his invaluable guidance, support and patience during my doctoral journey. His insights and expertise were fundamental to the successful completion of this research, and I am incredibly fortunate to have had the opportunity to learn under his mentorship in the CONAN2D project (Computational design of nanotransistors based on novel 2D materials, Grant. No. UIP-2019-04-3493, sponsored by the Croatian Science Foundation).

Furthermore, I would like to thank two people who guided me long before I started my doctoral studies and significantly influenced my academic path: Prof. Petar Pervan and my primary school teacher for mathematics and physics Tanja Djaković.

I am deeply grateful to my colleagues and friends in the Department of Electronics, Microelectronics, Computer and Intelligent Systems (ZEMRIS), especially in room D352, where Lovro, Filip, Ivan, Borna, Azra and Dario have been a constant source of support and inspiration. I would also like to thank my students with whom I worked during my doctoral studies: Tin, Karolina, Ivan, Josip and Tomo.

I owe special thanks to my friends who have stood by me through every challenge and celebrated every small victory.

From the bottom of my heart, I owe the biggest thanks to my family whose unwavering support and belief in me has motivated me along the way. To my parents, Tomislav and Nedjeljka, my sister Marija, her husband Frane and my nieces Lucija and Karla. Also, to my godparents, godchildren, grandparents, aunts, uncles and cousins. Thank you all for your love and encouragement.

Finally, I thank God for giving me the strength to overcome all the challenges. Thank you, God, for this path you have led me on and for all the wonderful people you have placed in my life.

Abstract

The continuous miniaturization of transistors has been driving the semiconductor industry for more than six decades. However, current silicon-based semiconductor technology is reaching its limits due to the strong quantum confinement and short-channel effects present in downscaled silicon devices. One of the potential solutions is to use new channel materials that could replace silicon, such as two-dimensional (2D) materials that have an atomic thickness and a dangling-bond-free surface and, therefore, have the potential for excellent device performance. The characteristics of 2D materials can be further engineered and optimized by patterning them into quasi-one-dimensional (1D) nanostructures called nanoribbons, which could potentially be employed as channel material in future state-of-the-art gate-all-around (GAA) field-effect transistors (FETs) that currently utilize ultrathin semiconductor nanosheets. However, the fabrication of 2D materials and nanoribbons is complex and an experimental demonstration is currently limited to only a few materials. Fabrication efforts are still in an early experimental stage, however, thousands of 2D materials have been theoretically predicted to exist with characteristics promising for applications in ultra-scaled FETs. Due to the large number of 2D materials and complex physics governing carrier transport at the nanoscale, potential candidates for future logic devices need to be investigated numerically using advanced theoretical formalisms and atomistic simulations.

This thesis presents an *ab initio* quantum transport study of nanoribbons of novel 2D materials using the density functional theory (DFT) to obtain the electronic band structure and maximally localized Wannier functions (MLWFs) to transform the DFT Hamiltonians into a spatially localized basis suitable for quantum transport simulation. The MLWF Hamiltonians are coupled with the non-equilibrium Green's function (NEGF) formalism-based quantum transport solver called QUDEN (from Quantum-Transport Device Engineering in Nanoelectronics), which was developed in-house in MATLAB. QUDEN is used to obtain the electronic and transport parameters of the analyzed nanostructures, while the top-of-the-barrier (TOB) ballistic FET model and under-the-barrier (UTB) tunneling leakage current model are employed to calculate and analyze the device performance of nanoribbon-based FETs (NR FETs). The nanoribbons of novel 2D materials investigated in this thesis include: (i) armchair (AC) and zigzag (ZZ) nanoribbons of MX_2-enes (MX_2NRs) with M = {Hf, Zr} and X = {S, Se}; (ii) AC and ZZ nanoribbons of monolayer germanium-sulfide (GeSNRs); (iii) nanoribbons of monolayer molybdenum-disulfide (MoS_2NRs). For all the examined devices, nanoribbon widths (W) range from ~7 nm down to only ~0.8 nm.

A detailed analysis is performed concerning quantum mechanical and scaling effects on the electronic and transport properties as well as on the performance of nanoribbon-based FETs using *ab initio* quantum transport calculations. The results presented in this thesis demonstrate a strong influence of the nanoribbon material, nanoribbon width, crystal phase and edge configuration on the characteristics of the investigated materials and, consequently, on the performance of nanoribbon-based devices. Although scaling down the nanoribbon width decreases the ON-state performance of most NR FETs, there are some surprising exceptions where the device performance is boosted by width downscaling. Such devices are AC-MX_2NR PFETs, ZZ-MX_2NR NFETs, and ZZ-GeSNR PFETs, where the maximum ON-state current is reported in devices with ~ 2 nm-wide nanoribbon channels. This is surprising because usually the widest NR FETs exhibit the best figures-of-merit. All studied devices are compared against the requirements set by the IEEE International Roadmap for Devices and Systems (IRDS) for future semiconductor logic technology nodes. This work reports that all Hf-based ZZ-MX_2NRs, ZZ-ZrS_2NRs with $W < 3$ nm, ZZ-$ZrSe_2$NRs with $W < 6$ nm, and AC-GeSNRs with $W > 1.1$ nm fulfill the IEEE IRDS requirements on the ON-state performance for both N- and P-type FETs. In contrast, it is shown that MoS_2NR FETs do not meet the goals defined in IEEE IRDS. While future work must address the impact of carrier scattering, this thesis clearly demonstrates that nanostructured Hf- and Zr-based MX_2-enes and GeS are promising channel materials for future ultra-scaled GAA FETs.

Keywords: two-dimensional (2D) materials, one-dimensional (1D), quasi-1D, nanoribbon, density functional theory (DFT), maximally localized Wannier functions (MLWFs), quantum transport, non-equilibrium Green's function (NEGF) formalism, ballistic transport, top-of-the-barrier (TOB) model

Kvantnotransportna analiza tranzistora temeljenih na nanovrpcama novih 2D materijala

Kontinuirana minijaturizacija tranzistora već više od šest desetljeća pokreće industriju poluvodičke elektronike. Međutim, trenutna poluvodička tehnologija temeljena na siliciju doseže svoje granice zbog snažnih efekata kvantnog ograničenja i efekata kratkog kanala prisutnih u ultra-skaliranim silicijskim elektroničkim elementima. Jedno od mogućih rješenja je korištenje novih materijala za kanal tranzistora koji bi mogli zamijeniti silicij, kao što su dvodimenzionalni (2D) materijali s atomskom debljinom i površinom bez nezasićenih kemijskih veza, stoga elementi temeljeni na 2D materijalima imaju potencijalno balističke performanse. Karakteristike 2D materijala mogu se dodatno projektirati i optimizirati oblikovanjem 2D materijala u kvazi-jednodimenzionalne (1D) nanostrukture zvane nanovrpcama (engl. *nanoribbon*, NR) koje bi se potencijalno mogle koristiti kao materijal kanala tranzistora u budućim tranzistorima s efektom polja (engl. *field effect transistor*, FET) s *gate all around* (GAA) strukturom koji koriste ultra-tanke poluvodičke nanolistove. Međutim, procesiranje 2D materijala i nanovrpci složeno je, a demonstracija je trenutno ograničena na nekoliko materijala te je još uvijek u ranoj eksperimentalnoj fazi, dok su tisuće potencijalnih 2D materijala teoretski predviđene, ali još nisu eksperimentalno potvrđene. Zbog velikog broja 2D materijala i kompleksne fizike transporta nosilaca na nanoskali, potencijalni kandidati za buduće logičke elemente moraju se numerički analizirati korištenjem naprednih teorijskih formalizama i atomističkih simulacija.

Cilj ove doktorske disertacije je razviti metodu temeljenu na *ab initio* kvantnotransportnom izračunu za analizu elektronskih i transportnih svojstava nanovrpci temeljenih na novim 2D materijalima te istražiti performanse FET-ova temeljenih na nanovrpcama 2D materijala. *Ab initio* istraživanje kvantnog transporta nanovrpci novih 2D materijala temelji se na teoriji funkcionala gustoće (engl. *density functional theory*, DFT) za dobivanje elektronske strukture i maksimalno lokaliziranih Wannierovih funkcija (engl. *maximally localized Wannier functions*, MLWF) za transformaciju DFT hamiltonijana u prostorno lokaliziranu bazu prikladnu za simulaciju kvantnog transporta. MLWF hamiltonijani povezani su s našim internim *solverom* za kvantni transport temeljenim na formalizmu Greenove funkcije izvan ravnoteže (engl. *non-equillibrium Green's function*, NEGF) zvanim QUDEN (od engl. *Quantum-Transport Device Engineering in Nanoelectronics*) za dobivanje elektronskih i transportnih svojstava ovih nanostruktura, dok se balistički FET model vrha barijere (engl. *top-of-the-barrier*, TOB) i model ispod barijere (engl. *under-the-barrier*, UTB) koriste za izračun i analizu performansi FET-ova temeljenih na nanovrpcama.

Doktorska disertacija strukturirana je na sljedeći način: prvo poglavlju daje uvod u temu disertacije s naglaskom na motivaciju te ciljeve koji se žele postići; u drugom poglavlju dan je pregled novih 2D materijala otkrivenih nakon grafena i nanovrpci te njihov potencijal za primjene u budućim FET-ovima na nanoskali; u trećem poglavlju opisan je pregled teorije koja stoji iza *ab initio* simulacija kvantnog transporta korištenih u ovoj disertaciji za proučavanje FET-ova temeljenih na nanovrpcama; četvrto poglavlje razrađuje glavne doprinose rada i povezuje ih s publikacijama uvezenim u disertaciju; peto poglavlje sadrži sve publikacije u časopisima i konferencijama predane kao dio disertacije i daje sažetak autorova doprinosa publikacijama; a posljednje, šesto poglavlje daje sažetak rada te ga zaključuje najvažnijim nalazima.

Znanstveni doprinos ovog rada može se podijeliti u tri glavna dijela. Prvi dio bavi se *ab initio* metodom kvantnog transporta razvijenom za proučavanje FET-ova temeljenih na nanovrpcama, od atomističke definicije materijala do potpuno kvantnomehaničkih simulacija transporta. Drugi dio bavi se primjenom razvijene metode za proučavanje utjecaja kvantnomehaničkih efekata i skaliranja dimenzija na elektronska i transportna svojstva te na performanse FET-ova temeljenih na nanovrpcama novih 2D materijala. Posljednji dio daje optimalne konfiguracije novih FET-ova temeljenih na nanovrpcama i procjenjuje njihov potencijal za buduće logičke tranzistore. Sljedeći pododjeljci ukratko opisuju tri komponente znanstvenog doprinosa ove disertacije.

1. Samokonzistentna metoda za simulacije kvantnog transporta u nanoelektroničkim elementima temeljenim na nanovrpcama novih 2D materijala

Kako bi se pravilno analizirali nanoelektronički elementi, proces simulacije mora uključiti svu relevantnu fiziku. Stoga je razvijena metoda koja koristi više naprednih teorijskih i računskih tehnika koje se mogu podijeliti u dva dijela. Prvi dio su atomistička konstrukcija proučavanih nanovrpci novih 2D materijala te dobivanje elektronske strukture i hamiltonijana materijala. Drugi dio predstavlja simulaciju kvantnog transporta tranzistora koja kao ulaz koristi spomenuti hamiltonijan. Prvi dio postupka počinje definiranjem inicijalne strukture gdje se jedinična ćelija 2D materijala koristi za konstruiranje nanovrpci različitih širina i konfiguracija rubova. Potom se rubovi nanovrpci pasiviziraju, čime je nanovrpca konstruirana. Inicijalna struktura predstavlja ulaz u DFT izračune koji se koriste za dobivanje hamiltonijana i pripadajuće elektronske strukture, odnosno strukture energijskih vrpci. Nadalje, dobiveni DFT hamiltonijan transformira se u prostorno lokaliziranu bazu pomoću MLWF-a, što je jedan od glavnih ulaza u simulacije kvantnog transporta. Simulacije kvantnog transporta koriste NEGF u kombinaciji s TOB modelom za samokonzistentno izračunavanje strujno-naponskih karakteristika tranzistora. Oba modula, NEGF i TOB, prilagođena su i optimizirana za kvazi-1D materijale s DFT-MLWF hamiltonijanima kao ulazima. NEGF se koristi u ravnoteži za dobivanje transmisije i gustoće stanja, a te dvije veličine pak služe kao ulaz u TOB modul. TOB se koristi za modeliranje FET-a s jednom upravljačkom elektrodom s trima točkama potencijala ili energije, odnosno Fermijevom razinom uvoda i odvoda te TOB potencijalom koji predstavlja visinu potencijalne barijere između uvoda i odvoda u kanalu tranzistora. Iako je ovaj model jednostavan, za tranzistore s kanalima duljim od 15 nanometara pokazao je slične rezultate u usporedbi s naprednijom metodom koja rješava i višedimenzionalnu Poissonovu jednadžbu za elektrostatiku, kako je navedeno u [Pub 5]. Jedna od najvećih prednosti razvijenog i implementiranog DFT-MLWF-NEGF-TOB pristupa je kratko vrijeme izračuna, koje je nekoliko redova veličine kraće u usporedbi s punom 3D simulacijom u komercijalnom softveru. Kao rezultat, implementirana metoda može se koristiti za brzo pretraživanje različitih novih 2D materijala oblikovanih u nanovrpce s fizičkom ispravnošću transporta na nanoskali i visokom točnošću u usporedbi s naprednijim simulatorima.

2. Analiza kvantnomehaničkih efekata i efekata skaliranja na elektronska i transportna svojstva te na performanse tranzistora temeljenih na nanovrpcama novih 2D materijala korištenjem *ab initio* proračuna strukture energijskih vrpci

Zbog svoje veličine, na karakteristike proučavanih nanovrpci snažno djeluje kvantno ograničenje koje mijenja svojstva materijala, što posljedično utječe na performanse tranzistora temeljenih na takvim nanostrukturama. Provedena je analiza kvantnomehaničkih efekata i efekata skaliranja na elektronska i transportna svojstva te na performanse tranzistora temeljenih na nanovrpcama tranzistora. Neke od fizičkih varijabli i opservabli proučenih u ovom radu uključuju strukturu energijskih vrpci, efektivnu masu elektrona i šupljina za paraboličku aproksimaciju strukture energijskih vrpci, širinu zabranjenog pojasa, gustoću stanja, transmisiju, injekcijsku brzinu elektrona i šupljina, ukupnu gustoću naboja u kanalu, efektivnu transportnu masu elektrona i šupljina te energijsku gustoću struje. Sve te veličine zasebno se analiziraju za određeni materijal nanovrpce, širinu i tip nosioca, dok zajedno pružaju jasnu sliku o fizici utjecaja kvantnomehaničkih efekata i efekata skaliranja. U ovom radu proučavaju se nanovrpce novih 2D materijala, posebno *armchair* i *zig-zag* MX_2NR nanovrpce gdje je M = {Hf, Zr} i X = {S, Se} u [Pub 1], [Pub 2] i [Pub 5]; *armchair* i *zig-zag* GeSNR nanovrpce u [Pub 2] i [Pub 3]; i MoS_2NR nanovrpce u [Pub 6] i [Pub 7]. Nanovrpce su atomski tanke, sa širinama u rasponu od oko 0,8 do 7 nanometara. Analiza struje aktivnog stanja (I_{ON}) pokazuje da se za većinu elemenata I_{ON} pogoršava sa smanjenjem širine nanovrpce, i to za 50 do 95 posto u odnosu na najšire promatrane nanovrpce. Međutim, neki od analiziranih FET-ova pokazuju neočekivano povećanje I_{ON} sa smanjenjem širine nanovrpce, s povećanjem do 70 posto za *zig-zag* MX_2NR NFET-ove, do 20 posto za *armchair* MX_2NR PFET-ove i do 6 puta za *zig-zag* GeSNR PFET-ove. Zanimljivo je da I_{ON} svih tranzistora čije se performanse povećavaju sa smanjenjem širine nanovrpce doseže maksimum kada se širina nanovrpce smanji na približno 2 nanometra.

3. Optimalne konfiguracije tranzistora temeljenih na nanovrpcama novih 2D materijala za buduće ekstremno skalirane poluvodičke elektroničke tehnologije

Optimalne konfiguracije tranzistora temeljenih na nanovrpcama novih 2D materijala pronalaze se usporedbom sa zahtjevima koji su definirani u IEEE IRDS-u (engl. *International Roadmap for Devices and Systems*) za buduće tehnološke čvorove ili generacije. Glavni zahtjevi iz IRDS-a relevantni za ovu disertaciju su balistički I_{ON} i injekcijska brzina nosilaca (v_{inj}) koji uključuju sve fizikalne karakteristike materijala i geometriju tranzistora. Sastav materijala, kristalna faza i konfiguracija ruba unaprijed određuju svojstva materijala, stoga se optimizacija performansi NR FET-ova može postići podešavanjem širine nanovrpce, dopiranjem uvoda i odvoda te odabirom materijala i debljine oksida upravljačke elektrode. Međutim, sva podesiva svojstva u simulacijskom okruženju moraju ostati unutar ostvarivih granica mogućih konfiguracija u budućim tranzistorima. Usporedba performansi analiziranih NR FET-ova sa zahtjevom IRDS-a za I_{ON} od ~2 mA/µm za buduće tehnološke čvorove pokazuje da većina *zig-zag* MX_2NR-a zadovoljava zahtjev za NFET i PFET tranzistore. Od *zig-zag* MX_2NR-ova u [Pub 1], ZZ-HfS_2NR i ZZ-$HfSe_2NR$ ispunjavaju zahtjeve IRDS-a za sve širine nanovrpci, dok je za *zig-zag* MX_2NR-ove temeljene na cirkoniju kriterij zadovoljen samo za ZZ-ZrS_2NR sa širinom manjom od 3 nanometra i ZZ-$ZrSe_2NR$ sa širinom manjom od 6 nanometara. Nasuprot tome, samo performanse PFET-ova s kanalom *armchair* MX_2NR-a dovoljno su visoke da zadovolje zahtjev IRDS-a. Nadalje, AC-GeSNR sa širinom većom od

1,86 nanometara u [Pub 3] zadovoljavaju I_{ON} kriterij za oba NFET i PFET elemenata, dok MoS_2NR ne zadovoljava zahtjev IRDS-a za I_{ON} za bilo koju konfiguraciju, kao što je detaljno analizirano u [Pub 6]. Iako budući rad mora analizirati utjecaj raspršenja nosioca, ova disertacija jasno pokazuje da su nanostrukture GeS-a i MX_2-ena temeljenih na hafniju i cirkoniju materijali s potencijalom za kanale budućih ultra-skaliranih GAA FET-ova.

Ključne riječi: dvodimenzionalni (2D) materijali, jednodimenzionalno (1D), kvazi-1D, nanovrpca, teorija funkcionala gustoće (DFT), maksimalno lokalizirane Wannierove funkcije (MLWF), kvantni transport, formalizam Greenovih funkcija izvan ravnoteže (NEGF), balistički transport, model vrha barijere (TOB)

Contents

Chapter 1

Introduction

1.1. Background and Motivation

The growth of the high-tech industry over the last 60 years has been driven by continued miniaturization of transistors. In addition to miniaturization, the performance of transistors has also been enhanced by the introduction of metal gates, high-*k* gate dielectrics and strain of the crystal lattice within the channel. Current state-of-the-art devices in production are gate-all-around (GAA) field effect transistors (FETs) with bulk-silicon nanosheets or nanowires whose active region is no more than a few 10s of nanometers in all directions [1], [2], [3]. At such a scale, manufacturing is complex, and quantum mechanical effects are strong, with tunnelling deteriorating the digital switching performance [4]. Although GAA FETs provide high control over device electrostatics, maintaining good electrostatic properties and suppressing short channel effects has become hard at ultra-short gate lengths, i.e. for $L_g \leq 20$ nm [5]. Two paths are being considered to extend the development in the semiconductor industry [6], [7]: “More Moore”, which focuses on the miniaturization of transistor size while suppressing short channel effects; and “More than Moore”, which focuses on functional diversification of electronic systems. One of the research areas on the “More Moore” path includes FETs based on 2D materials (2DMs). 2DMs consist of one or a few atomically thin layers in which in-layer atoms are connected by covalent bonds while adjacent layers are connected by the Van der Waals force. Due to their atomically thin thickness and dangling-bond-free surface, 2D materials offer exceptional electrostatic properties, i.e. nearly perfect control by the gate electrode[8], [9]. On the other hand, 2D materials have high source and drain (S/D) contact resistances in the range of ~ kΩ·µm which limits the performance of such devices [10], [11], [12]. Besides contact resistance, structural defects [13], surface optical phonon scattering [14], and interactions with charged impurities [15] are further limiting factors for the use of 2D materials in electronics, but it is expected that these defects will become negligible with the improvement of the production methods. 2DMs have already been included in plans for future GAA technology nodes by leading semiconductor companies with first samples already been showcased in [16], as shown in Figure 1.1, and projected consumer products as early as the late 2020s in the form of the multi-bridge channel (MBC) FETs [17] and Ribbon FETs [16], [18], [19] which provides further motivation for studying these devices.

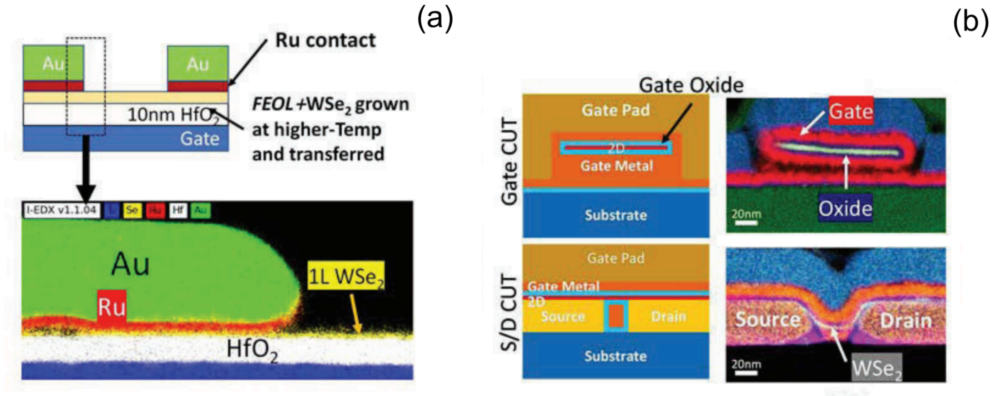

Figure 1.1 Schematic and TEM image with elemental mapping of (a) single gate FET and (b) GAA FET with WSe_2 channel [16].

More than 1800 2D materials have been shown to be theoretically stable [20], and several dozen of them are currently considered possible candidates for future FETs, with a focus on transition metal dichalcogenides (TMDs), e.g. MoS_2, $MoTe_2$, $MoSe_2$, WS_2, WSe_2, SnS_2, etc. [21], [22], [23], group-IV monolayers (graphene, silicene, germanene, stanene) [24], [25], [26], group-V monolayers (phosphorene, arsenene, antimonene, bismuthene) [27], [28], [29], and many others. These 2D materials can be configured into various nanostructures such as nanoribbons [30], [31], [32], nanosheets [1], and nanowires [33], with each of them providing excellent electrostatic control over the channel and thus reducing the short-channel effects. These nanostructures could be integrated in current GAA FETs, as shown in Figure 1.2a, where channel material are nanoribbons [34] with top view and side view shown in Figure 1.2b and Figure 1.2c, respectively. Moreover, the patterning of 2D materials into nanostructures provides an additional way of tuning the electronic, transport and device properties that include e.g.

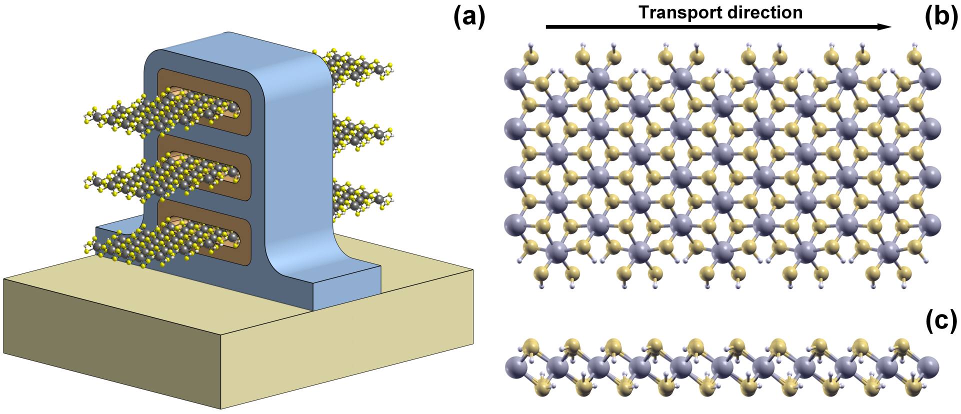

Figure 1.2 (a) Model of a MBC FET with nanoribbon channel. (b) Top view, and (c) side view of nanoribbon. [34]

bandgap, effective mass, injection velocity, etc., due to strong quantum mechanical effects in such extremely scaled material systems. Therefore, due to the trade-off between improved electrostatic control over the channel and altered electronic and transport properties, we need systematic physics-based modeling and simulation within an advanced physical framework for accurate design, analysis and optimization of nanoscale devices.

1.2. Objective of the Thesis

Although many 2D materials have been considered and studied both theoretically and numerically [1], most of them have not yet been produced experimentally. With such a large number of options available for future FETs, advanced modeling and simulation are crucial for the development of future transistors based on 2D materials [35]. Advanced physical and numerical models must incorporate the underlying electronic transport physics. The most advanced method to study low-dimensional materials is by obtaining the electronic structure using *ab initio* calculations performed using density functional theory (DFT) [36], where the accuracy depends on the exchange-correlation (XC) functional. The DFT calculations come with a downside of the high computational cost that consequently limits the calculations to structures consisting of at most dozens of atoms. In addition, the electronic structure is described with a Hamiltonian that, in the case of the DFT output, is a large and dense matrix that is not suitable for quantum transport simulations. To enable simulations of devices of realistic size, which can contain up to thousands of atoms [37], [38], while preserving the accuracy of DFT simulations, maximally localized Wannier functions (MLWFs) [39] are used to transform DFT Hamiltonians into a localized basis, resulting in tight-biding (TB) like sparse matrices that are more suitable for quantum transport simulations in terms of memory consumption and simulation time.

Quantum transport simulations used in this work are based on the non-equilibrium Green's function (NEGF) formalism [40], [41], [42], [43]. The NEGF formalism is used to directly solve Schrödinger's equation with open boundary conditions (OBCs). The FET device can be simulated by employing a self-consistent NEGF-Poisson solver, or in the case of a ballistic device, a simplified top-of-the-barrier (TOB) model [37] can be used in combination with NEGF. In the TOB model, a FET is defined by three potential or energy points, i.e. S/D quasi-Fermi levels and the self-consistently calculated barrier height in the channel, which is called the TOB potential. The main inputs for TOB are the density of states (DOS) and transmission calculated in equilibrium using NEGF, the gate oxide material and thickness, and the S/D Fermi levels due to doping. The NEGF-based quantum transport simulations are well-established and widely used in the device research community, both in academia and industry. Many 2D materials have already been considered and related devices simulated [5], however, there is a limited number of studies dealing with devices based on nanoribbons of novel 2D materials discovered after graphene. Therefore, this research aims to fill the knowledge gap by investigating the electronic, transport and device characteristics of various 2D material nanostructures by employing the advanced *ab initio* quantum transport technique.

In summary, novel materials and device architectures are required for the further development and optimization of future electronic technologies. The 2D materials exhibit promising electronic and transport properties and patterning them into quasi-1D nanostructures called nanoribbons facilitates their potential usage in GAA FETs and, additionally, allows the tuning of material properties by quantum confinement, which can also enable the optimization of nanotransistor performance. The aim of this dissertation is to provide evidence about the suitability of quasi-1D materials such as armchair (AC) and zigzag (ZZ) nanoribbons of MX_2-enes (MX_2NRs) with M = {Hf, Zr} and X = {S, Se}, AC and ZZ nanoribbons of monolayer germanium-sulfide (GeSNRs), as well as nanoribbons of monolayer molybdenum-disulfide (MoS_2NRs) for future GAA FETs using the quantum transport method in conjunction with *ab initio* calculations of the electronic bandstructure of such nanostructures.

The scientific contribution of this thesis is as follows:

1. Self-consistent method for simulations of quantum transport in nanoelectronic devices based on nanoribbons of novel 2D materials

2. Analysis of quantum-mechanical and scaling effects on the electronic and transport properties and on the performance of transistors based on nanoribbons of novel 2D materials using *ab initio* bandstructure calculations
3. Optimum configurations of transistors based on nanoribbons of novel 2D materials for future extremely scaled semiconductor electronic technologies

1.3. Structure of the Thesis

The thesis is structured as follows:

- Chapter 2 provides a review of novel 2D materials and nanoribbons and their potential for future nano-scale FETs
- Chapter 3 reviews the theory behind the *ab initio* quantum transport simulations used in this thesis to study nanoribbon-based FETs for future logic devices
- Chapter 4 elaborates on the main contributions of the paper and links them to the publications
- Chapter 5 provides all journal and conference publications submitted as part of the thesis and summarizes the author's contribution to the publications
- Chapter 6 summarizes the work and concludes the thesis with the most important findings

Chapter 2

2D Materials for Future Nanoelectronics

2.1. Overview of 2D Materials

The first theoretical concepts for 2D materials emerged as early as the 1940s [44], but scientists believed that 2DMs could not exist in nature due to their environmental instability. However, this opinion changed with the experimental discovery of graphene in 2004 [45], [46] by A. K. Geim and K. S. Novoselov, which led to the emergence of a new research field for 2D materials and attracted widespread research interest in the scientific community. 2DMs benefit from atomically thin thickness and dangling-bond-free surfaces [47], and consequently, some 2DMs can provide high carrier mobilities or near-ballistic transport properties that can be utilized for high-performance electron devices. However, the high contact resistance in devices with 2DM channels is one of the major problems and technology limiters.

Patterning into quasi-one-dimensional nanoribbons [30], [48], which could be used in GAA FETs [17], provides an additional way of tuning electronic, transport and device properties, such as bandgap, effective mass, injection velocity, etc. [49], [50], [51], [52]. Experimental work on NRs is limited to a few materials due to the high complexity of fabrication with the main challenge being the reliable control of crystal phase, edge structure, and dimensionality [53]. Nevertheless, the continuous progress in this field affirms fabrication potential and makes nanoribbons interesting structures for future nanodevices [54], [55], [56]. The search for potential 2DM candidates for future logic devices is a challenging task, as recently more than 1800 2DMs have been theoretically investigated using DFT [20] and of these materials about one hundred showed a bandgap suitable for future logic devices, i.e. $E_g > 1$ eV. Given the large number of materials and the high experimental costs, it is necessary to evaluate which materials are worth considering as experimental candidates for future logic devices. A recent theoretical study [5] compared all hundred 2D material candidates with appropriate bandgaps for future logic devices and found 13 best-performing FETs with 2DM channel that meet the International Roadmap for Devices and Systems (IRDS) [57] requirements for future technology nodes. Thirteen 2D materials whose FETs showed highest performance of all studied devices include monolayers of group-IV monoelemental materials (α phase phosphorene or black phosphorus, α and β arsenene, and α phase antimonene), TMDs (HfS_2 and ZrS_2), monolayer Group-IV monochalcogenides (GeS and GeSe), and other non-grouped 2DMs (O_6Sb_4, Si_2H_2, $Ti_2Br_2N_2$, and $Ti_2N_2Cl_2$). In this work, the focus is on nanoribbons that are made by patterning 2DMs along one of the lattice directions, where the nanoribbons in each direction have a different structure and consequently different material properties. An example of patterning 2D materials into various structures is shown in Figure 2.1a for graphene, which can be patterned in the zigzag direction (as shown in Figure 2.1b) and armchair direction (as shown in Figure 2.1c), with the name of each nanoribbon based on the edge type. As result of patterning 2DMs into nanoribbons along various crystal directions, an even larger number of combinations are possible that need to be investigated and consequently finding the best candidates for future logic devices is a challenging task. Nevertheless, one can start by patterning 2DMs which showed potential such as the previously mentioned thirteen 2DMs whose FETs showed the highest performance of all 2DMs [5]. Most of these materials have not yet been patterned into nanoribbons and have not been studied theoretically or experimentally. These 13 materials include GeS, HfS_2 and ZrS_2,

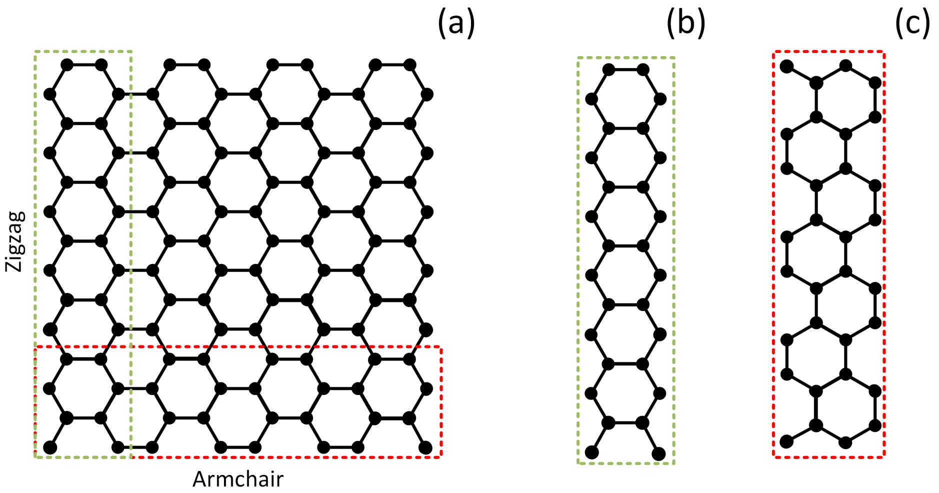

Figure 2.1 (a) Graphene monolayer cut into (b) armchair and (c) zigzag directions.

which are patterned into nanoribbons of various widths and edge types and analyzed in this thesis. In the following sections, we will examine the properties of the most promising 2DMs obtained from both theoretical and experimental studies.

2.2. Monoelemental 2D Materials

Research on monoelemental 2D materials (Xenes) is mostly focused on group-IV (graphene, silicene, and germanene) and group-V (phosphorene, arsenene, antimonene, and bismuthene) monolayer materials. Group-IV monolayer materials are represented with graphene which is the first synthesized and most studied 2D material, both theoretically and experimentally. Graphene has been studied in various configurations and integration levels from sample FET devices in [58], as shown in Figure 2.2 to wafer lever integration compatible with complementary-metal-oxide-semiconductor (CMOS) technology in [59]. Graphene, silicene, and germanene have a hexagonal structure and zero bandgap due to the existence of Dirac-like dispersion at the *K*-point and as a direct consequence, effective mass tends to zero while group-IV mobility exceeds a few 10,000s $\text{cm}^2\text{V}^{-1}\text{s}^{-1}$ [60]. Although group-IV materials exhibit high mobility, zero bandgap is a significant problem for usage as channel materials in digital logic devices as these devices would have poor switching capabilities, and consequently high-power consumption in the supposedly OFF-state [61]. Nevertheless, high-mobility materials are suitable for high-speed electronics where power consumption is not a problem. Finally,

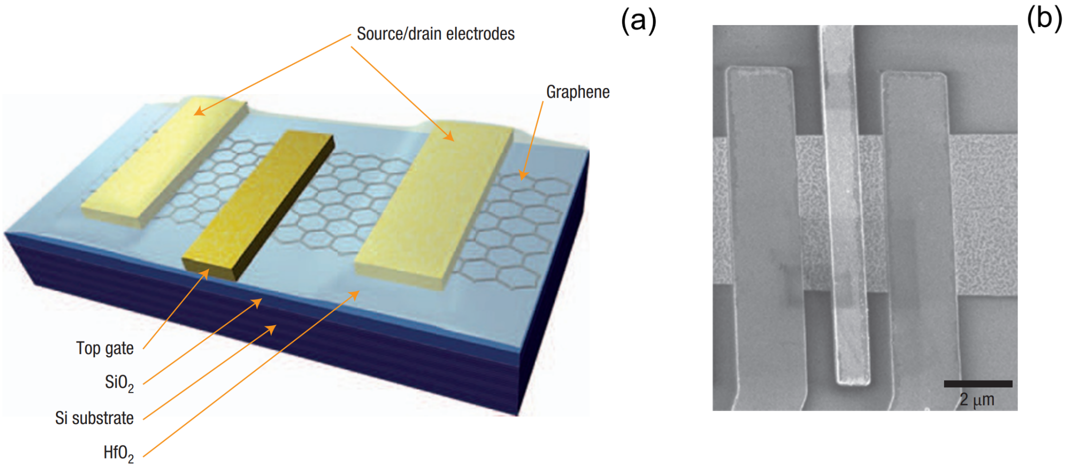

Figure 2.2 a) Shematic of top-gated graphene FET design and (b) SEM image of top-gated graphene FET. [58]

group-IV materials can be patterned into ultra-narrow nanoribbons with reported bandgap opening which potentially makes them suitable for logic devices [62].

Group-V monolayer semiconductors are fundamentally *p*-type semiconductors and found in two stable phases: α phase group-V 2D materials form puckered monolayer formations which exhibit orthorhombic structure and β phase group-V 2D materials form wavy monolayer formations which exhibit rhombohedral structure. Group-V 2D materials have been studied theoretically [63] and experimentally [64], [65]. Theoretical DFT study [66] using HSE06 XC functional predicted electron and hole mobilities of black phosphorus to be ~1100 $cm^2V^{-1}s^{-1}$ and ~700 $cm^2V^{-1}s^{-1}$ along the armchair direction and zigzag direction ~80 $cm^2V^{-1}s^{-1}$ and ~10,000 $cm^2V^{-1}s^{-1}$. Arsenene is a semiconductor with a wide and direct bandgap of ∼1.7 eV for α-phase and ∼2.5 eV for β-phase. Electron and hole mobilities of β-phase arsenene are ~635 $cm^2V^{-1}s^{-1}$ and ~1700 $cm^2V^{-1}s^{-1}$ [67]. Antimonene is an indirect semiconductor with a bandgap of ∼1.2 eV for α-phase and ∼2.3 eV for β-phase. The β-phase antimonene electron and hole mobilities are ~630 $cm^2V^{-1}s^{-1}$ and ~1737 $cm^2V^{-1}s^{-1}$ [68]. Bismuthene is an indirect semiconductor with a bandgap of ∼0.36 eV for α-phase and ∼0.99 eV for β-phase. The β-phase bismuthene exhibits electron mobility up to a few 100s $cm^2V^{-1}s^{-1}$ [69]. High electron mobility and suitable bandgaps in the 1 eV to 2.5 eV range of most group-V materials make them potential materials for future logic devices.

The α phase phosphorene or black phosphorus, α and β arsenene, and β phase antimonene are all one of the 13 best-performing 2D materials based on the ON-state current (I_{ON}) benchmark from the recent theoretical study [5] where black phosphorus showed the highest performance of all 2D materials when both N- and P-FET I_{ON} performance is considered. On the topic of experimental work on group-IV FETs, single and few-layer *p*-type black phosphorus FET was reported in [64]. Black phosphorus was characterized only for the few-layer case, with I_{ON}/I_{OFF} ratio >10^4, I_{ON} ∼0.2 mA/μm (~20× lower than the theorized ON-state current), and mobility up to 286 $cm^2V^{-1}s^{-1}$.

2.3. Transition Metal Dichalcogenides (MX_2-enes)

TMDs are a family of 2D materials with a general formula being MX_2, where M is a transition metal element (e.g., Mo, Hf, Zr, W, Ti, Sn) and X is a chalcogen element (e.g., S, Se, Te). Alongside monoelemental 2DMs represent one of the most studied materials. TMDs show promising electronic and transport properties such as low effective mass, high electron velocity, and a wide range of bandgaps for future FETs. TMDs have a trigonal prismatic (2H) or octahedral (1T) structure [70], as shown in Figure 2.3, with mobility up to a few 100s $cm^2V^{-1}s^{-1}$ [21], [35]. Although the mobility is significantly lower compared to group-IV and group-V Xenes, the ON/OFF switching ratio of transistors based on TMDs exceeds 10^6 which is acceptable for next-generation FETs [5].

In this work, we focus on transition metal dichalcogenides MX_2 (M = {Zr, Hf}, X = {S, Se}) as some of the most promising 2DMs [5], [71], [72]. Theoretical study on electronic properties of MX_2-enes in [72] reported bandgaps with HSE06 XC-functional as follows: 2.17 eV for ZrS_2, 1.07 eV for $ZrSe_2$, 2.4 eV for HfS_2, and 1.32 eV for $HfSe_2$, confirming all materials have appropriate bandgaps for logic devices. Furthermore, an *ab initio* study in [73] reported phonon limited mobility of mentioned MX_2-enes in range of a few thousand $cm^2V^{-1}s^{-1}$ with: 1247 $cm^2V^{-1}s^{-1}$ for ZrS_2, 2316 $cm^2V^{-1}s^{-1}$ for $ZrSe_2$, 1833 $cm^2V^{-1}s^{-1}$ for HfS_2, and 3579 $cm^2V^{-1}s^{-1}$ for $HfSe_2$ which is 4-12 times higher compared to MoS_2, one of the most studied 2D materials, for which 340 $cm^2V^{-1}s^{-1}$ mobility was reported. The potential of 2D MX_2 TMDs has been studied in depth [5], [73], [74] by advanced theoretical calculations and experimental work was reported in [75], [76]. Experimental work showed high compatibility of Hf and Zr-based TMDs to industry standard high-*k* oxides (HfO_2, ZrO_2)[77], [78], with FETs reported in [78] with schematic and scanning electron microscope (SEM) image shown in Figure 2.4. Although TMDs and TMD FETs are still experimental, research affirms production possibility. The MX_2 nanoribbon (MX_2NR) research is quite limited with electronic properties studied for ZrS_2NRs [79], and $HfSe_2NRs$ [80]. As for MX_2NR FETs, only a single $ZrSe_2NR$ FET was studied in [81] with the detailed study reported in our group and this thesis in [34], [82], which showed the potential of these devices for the future logic devices.

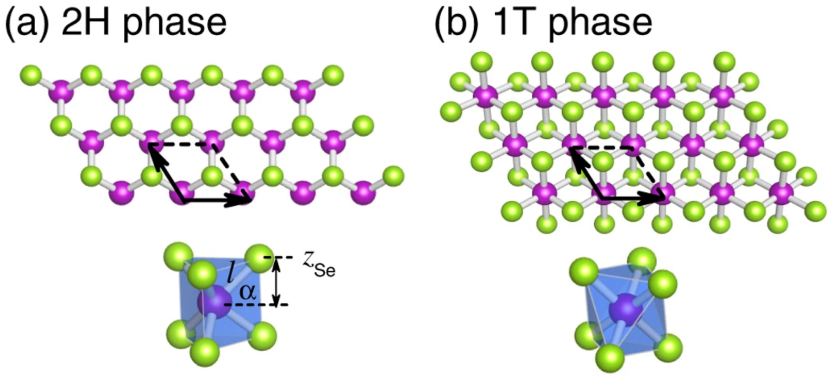

Figure 2.3. Illustration of the crystal structure of (a) 2H and (b) 1T phase of TMD 2D materials. [70]

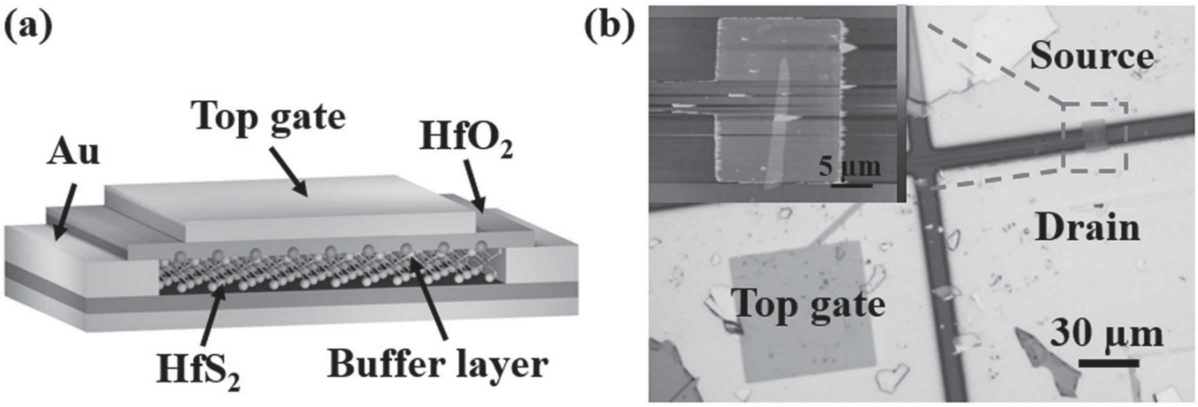

Figure 2.4. a) Schematic and (b) SEM image of top-gated HfS_2 FET. [78]

2.4. Monolayer Group-IV Monochalcogenides

Monolayer Group-IV monochalcogenides or MX-enes where ($M \in \{Ge, Si, Sn\}$ and $X \in \{S, Se\}$) are one of the most researched 2D materials. A recent theoretical study in [5] showed 2D GeS and GeSe as one of the best performing 2D materials based on ON-state current I_{ON} benchmark for logic devices with reported higher performance GeS compared to GeSe which served as initial motivation to study GeS.

The 2D germanium monosulfide (GeS) is a member of MX-enes with a phosphorene-like buckled orthorhombic lattice which indicates anisotropic transport. Theoretical study in [83] showed that 2D GeS exhibits an indirect bandgap of 2.34 eV, electron mobility higher than 3000 $cm^2V^{-1}s^{-1}$ and a relatively low hole mobility of 160 $cm^2V^{-1}s^{-1}$. A recent quantum transport study of sub-10 nm monolayer GeS FETs [84] showed the great potential of GeS as a material for future short-channel transistors. Experimental work on GeS is limited to a few studies which affirm production potential [85], [86]. Before our group's study, reported in [87], [88], very little was known about quasi-1D GeS nanoribbon (GeSNR) devices, with the information being limited to electronic bandstructure [89]. Electronic properties of armchair and zigzag GeSNRs with bare and H-terminated edges were studied in [89]. This study demonstrated a high dependence of electronic properties on edge termination as ZZ GeSNRs with bare edges show metallic properties while all bare-edge AC-GeSNRs exhibit semiconducting behavior. On the other hand, termination by H atoms is presented as a good option to stabilize the AC- and ZZ-GeSNRs that exhibit semiconducting behavior.

Chapter 3

Computational Design of Nanotransistors using *Ab Initio* Quantum Transport Simulations

3.1. Overview of the Simulation Approach

Simulation of transistors and inclusion of all relevant physics is a demanding task, especially when working with materials that exhibit one or more dimensions at the nanometer scale such as 2D materials and nanoribbons where quantum confinement greatly affects the material properties. Employing the classical drift-diffusion (DD) model [90] of electron flow is insufficient to study these devices as it does not account for the quantum mechanical nature of materials and electron kinetics. There are semiclassical models based on the Boltzmann transport equation that incorporate some of the quantum mechanical effects that are good for micron-sized devices but do not fully capture the discrete nature of electron states and their wave functions. Therefore, the problem needs to be assessed at the quantum mechanical level, i.e. solving the Schrödinger equation of the studied system.

Solving the Schrödinger equation directly even for a simple system of N particles is a complex task as we have a $3N$ dimensional problem that is impossible to solve even for a few particles. The problem is reduced from a many-particle problem to many single-particle problems, and each electron is treated as a point charge in the field of other electrons. Now we have a 3-dimensional problem that can be solved in real computational time. Schrödinger's equation describes a closed system and to include electron injection and extraction through the device one can employ non-equilibrium Green's function (NEGF) formalism to solve the Schrödinger equation for open-boundary conditions.

The main input of NEGF formalism is the Hamiltonian of the device. For macroscopic devices, an effective mass approximation can be used where the valence band (VB) and conduction band (CB) are approximated using the parabolic function. However, these models are not good enough to capture all physical effects at the nanoscale. At the time of writing of this thesis, two models are most popular to describe Hamiltonian of the system. The first model is based on *ab initio* density functional theory (DFT) which is a method that does not require outside parameters and is held as the theory with the highest accuracy to obtain the ground state of the nanostructure. DFT helps us to better understand the physics of such nanoscale devices and to predict device behavior. DFT is implemented in various programs such as Quantum Espresso [91], [92], VASP, SIESTA, ABINIT, QuantumATK, etc. However, depending on the parameters of the DFT, it has problems with evaluating the bandgap of the material which is one of the most important parameters when designing devices at the nanoscale. Furthermore, the computational burden is high and for more complex structures a supercomputer is needed. On the other hand, we have a tight-binding (TB) model which is an empirical model that is fitted on experimental results or *ab initio* DFT simulations results with the main advantage being much sparser matrices that enable simulation of a much higher number of atoms and consequently realistically sized devices even on desktop computers or workstations. To combine the accuracy of DFT and sparsity of the TB method, maximally localized Wannier functions can be used to transform DFT Hamiltonians into space-localized TB-like Hamiltonians. MLWF Hamiltonians are then used within NEGF formalism to describe the device at the atomic scale and obtain transport characteristics.

To simulate the transistor, the most advanced method is to solve NEGF in combination with the Poisson equation self-consistently. However, this method is computationally expensive and focusing on the ballistic performance of FET devices, the ballistic top-of-the-barrier model has proven to be good for assessing these devices. Although the TOB model only calculates thermionic current and tunneling current is neglected, studies have shown that for channels longer than 15 nm, it is good enough to study the performance. Under-the-barrier (UTB) model, an extension of the TOB model was developed to account for tunneling current. In this chapter simulation methods used to study nanoribbon-based FETs are explored where Hamiltonian is obtained using DFT and MLWF while the FET device is described and simulated using NEGF and TOB model.

3.2. Quantum Transport in Non-Equilibrium Green's Functions Formalism

Electrons, in quantum transport, are described fully quantum mechanically and injected into the simulation domain i.e. the studied nanostructure. After injection, some electrons are reflected while others are transmitted which causes current flow through the structure. Transport through the structure is only possible if the studied system is connected with the environment via electrical contacts, which is enabled by defining the open boundary conditions (OBCs). Therefore, non-equilibrium Green's functions (NEGF) formalism is employed to study the system by directly solving the Schrödinger equation with OBCs. The focus of this work is on coherent and ballistic transport in order to determine the upper intrinsic limits to device performance. Hence, it is assumed that the phase of the electron wavefunction is preserved through the device and all scattering processes that would cause decoherence, and momentum and energy relaxation, such as electron-phonon interactions, are neglected. The NEGF is implemented in QUDEN (from Quantum-Transport Device Engineering in Nanoelectronics), which is a legacy MATLAB code of the Computational Nanoelectronics Group at UNIZG-FER.

The NEGF is a known and widely used theory in physics that was based on the works of P. Martin and J. Schwinger in 1959 [93] and their PhD students L. P. Kadanoff and G. Baym in 1962 [94] and later formalized by L. P. Keldysh in 1965 [95]. More recently, the NEGF formalism has been adapted for applications in engineering fields by S. Datta [38], [40], Datta's simplified formulation yields the same results while being more accessible to electrical engineers [41] as there is no need to have previous knowledge in second quantization formalism and quantum statistical physics.

In order to introduce NEGF in a simplified manner, we focus on a nanosystem connected to external contacts or reservoirs which can be described as semi-infinite areas that are in local thermodynamic equilibrium with defined constant electrochemical potential or Fermi level. With details provided in [40], [41], the nanosystem with a single contact can be described using the non-homogenous differential equation

$$\left(E - H - \Sigma\right)\phi = S, \tag{1}$$

which resembles the Schrödinger equation with added terms that describe interaction with contacts. The Σ represents the contact self-energy which is a modification of the Hamiltonian to include interaction with connected contact. The S represents the source term or excitation of the nanosystem with electron waves from contact. This equation, unlike the Schrödinger equation with closed boundary conditions, is not an eigenvalue problem and therefore one needs to solve the equation (1) using Green's functions. Green's function is a mathematical construct used to solve non-homogenous differential equations where for linear differential operator $L(x)$ for which we can describe

$$L(x)\phi(x) = S(x). \tag{2}$$

Green's function $G(x, x')$ is every solution of

$$L(x)G(x,x') = \delta(x-x'), \tag{3}$$

where $\delta(x - x')$ is Dirac delta function. Solution of the eq. (2) using Green's function is then

$$\phi(x) = \int G(x,x')S(x')dx'. \tag{4}$$

Green function $G(x, x')$ in equation (4) can be observed as a propagator that propagates the influence of excitation or perturbation $S(x')$ from x' to x in which we evaluate the function $\phi(x)$. Also, $G(x, x')$ can be treated as a correlation function because if x and x' exhibit high correlation then $S(x')$ will have a strong impact on solution $\phi(x)$ while the opposite is true for low correlation.

Applying Green's function to solve equation (1) of a nanosystem with a single contact we obtain two solutions. The first solution is the retarded Green's function

$$\mathbf{G}^R(E) = \left[(E+i\eta)\mathbf{I} - \mathbf{H} - \mathbf{\Sigma}\right]^{-1}, \tag{5}$$

that represents the time-causal solution that ensures that response occurs after perturbation and therefore has a physical meaning. Obtaining a causal solution is assured by adding an infinitesimal positive imaginary constant $i\eta$, also called the convergence constant. Another solution is the advanced Green's function $\mathbf{G}^A = (\mathbf{G}^R)^\dagger$ which is also useful in NEGF calculations.

In further text, $\mathbf{G}^R$ and $\mathbf{G}^A$ will be simplified and represented with $\mathbf{G}$ and $\mathbf{G}^\dagger$, respectively. We start by defining two important parameters where the first is a spectral function

$$\mathbf{A}(E) = i\left[\mathbf{G}(E) - \mathbf{G}^\dagger(E)\right], \tag{6}$$

which provides information about the available electronic states and their broadening due to interaction with contacts. Diagonal elements of spectral function represent the local density of states (LDOS) per spin

$$g_L(\mathbf{r};E)=\frac{1}{2\pi}Diag\left[\mathbf{A}(E)\right], \tag{7}$$

while the trace of the density matrix

$$g(E)=\frac{1}{2\pi}Trace\left[\mathbf{A}(E)\right], \tag{8}$$

represents the density of states at the energy E per spin. The other important parameter is the broadening matrix

$$\boldsymbol{\Gamma}(E)=i\left[\boldsymbol{\Sigma}(E)-\boldsymbol{\Sigma}(E)^{\dagger}\right]=-2\,\mathrm{Im}\left[\boldsymbol{\Sigma}(E)\right], \tag{9}$$

that can be derived from the imaginary part of the contact self-energy that introduces broadening due to the coupling of the studied nanosystem with a contact. Also, the broadening matrix can be interpreted as a generalized energy-dependent escape rate of particle from the structure to the contact. The connection between the spectral function and the broadening matrix is given by

$$\mathbf{A}=i\left(\mathbf{G}-\mathbf{G}\right)^{\dagger}=\mathbf{G}\boldsymbol{\Gamma}\mathbf{G}^{\dagger}=\mathbf{G}^{\dagger}\boldsymbol{\Gamma}\mathbf{G}. \tag{10}$$

If we consider a system with two contacts, one can obtain the retarded Green's function of the system with two contacts as

$$\mathbf{G}(E)=\left[(E+i\eta)\mathbf{I}-\mathbf{H}-\boldsymbol{\Sigma}_1-\boldsymbol{\Sigma}_2\right]^{-1}. \tag{11}$$

where H is the device Hamiltonian while $\boldsymbol{\Sigma}_1$ and $\boldsymbol{\Sigma}_2$ are contact self-energy matrices. Electron density per energy and space can be marked as

$$\begin{aligned}\mathbf{G}^{n}(E)&=\mathbf{A}_1(E)f_1(E)+\mathbf{A}_2(E)f_2(E)\\&=\mathbf{G}(E)\left[\boldsymbol{\Gamma}_1(E)f_1(E)+\boldsymbol{\Gamma}_2(E)f_2(E)\right]\mathbf{G}^{\dagger}(E),\end{aligned} \tag{12}$$

where $f_1=f_1(E)=f_0(E-E_{F1})$ and $f_2=f_2(E)=f_0(E-E_{F2})$. Parameters E_{F1} and E_{F2} are Fermi levels of contacts 1 and 2 that are locally in thermodynamic equilibrium and act as reservoirs. Furthermore, the term in the middle of the equation can be marked as $\boldsymbol{\Sigma}^{in}$ and we can write

$$\mathbf{G}^{n}(E)=\mathbf{G}(E)\boldsymbol{\Sigma}^{in}\mathbf{G}^{\dagger}(E). \tag{13}$$

This term is also called the electron correlation function or non-equilibrium Green’s function from which the formalism got its name [38]. Non-equilibrium Green’s function in Datta’s formalism is similar to the original Keldysh quantum kinetic equation

$$\mathbf{G}^{<}(E) = \mathbf{G}(E)\mathbf{\Sigma}^{<}\mathbf{G}^{\dagger}(E), \tag{14}$$

where $\mathbf{G}^{<}(E) = i\mathbf{G}^{n}(E)$ is the lesser Green's function, and $\mathbf{\Sigma}^{<}(E) = i\mathbf{\Sigma}^{in}(E)$ is the lesser self-energy. Both the Keldysh quantum kinetic equation and retarded Green's function describe the system and its states while only the former incorporates information on the occupation of these states. The lesser Green's function $\mathbf{G}^{<}$ gives information about the occupation of the state which refers to electrons while greater Green's function $\mathbf{G}^{>}$ gives information about states that are not occupied and therefore refers to holes.

The current and its voltage dependence are determined by the electronic and transport properties of the simulated structure through the quantum transmission function calculated as

$$\overline{T}(E) = Trace\left[\mathbf{\Gamma}_1\mathbf{G}\mathbf{\Gamma}_2\mathbf{G}^{\dagger}\right], \tag{15}$$

where quantum transmission $\overline{T}(E)$ depends on device Green's function and interaction with contacts through broadening matrices. This equation represents the connection between the Landauer-Büttiker and NEGF formalism and it is valid only for coherent quantum transport, i.e. ballistic transport without any scattering considered.

Finally, in order to improve and optimize the previous version of the legacy code QUDEN, the NEGF equations are solved using the recursive Green's function (RGF) method [96]. Within RGF, the simulation domain is broken down from a complex system into smaller and more manageable parts which are called "slices". One of the computationally most demanding tasks in NEGF is a calculation of retarded Green's function as it includes the inversion of a huge matrix. However, the RGF approach can be employed for the calculation of transmission and density of states where only the diagonal, and edge sub-matrices are needed of the full retarded Green's function matrix, as it provides a significant speedup of simulation for large systems. The RGF computation time is $O(N^3/N_{SL}^2)$ while the direct method computation time is $O(N^3)$, where N is the size of the device matrix and N_{SL} is the number of slices. This implies that the maximum number of slices would drive the simulation time to a minimum, N_{SL} needs to be appropriate to include all relevant interaction information.

3.2.1. Surface Green's Function

Contacts, as previously defined, are semi-infinite leads of the same material as the channel and consequently, the Green's function of these contacts would be infinite in size. However, interaction with the full contacts can be reduced to surface-only interactions, and therefore we employ the surface Green's function approach, which considers only the overlap between the surface or edge elements of contacts and the main structure. Surface Green's function is a submatrix of a full contact Green's function, and using this simplification the contact self-energies of the left and right contacts can be written as

$$\mathbf{\Sigma}_L = \mathbf{T}_1 \mathbf{g}_L \mathbf{T}_1, \qquad \mathbf{\Sigma}_R = \mathbf{T}_2 \mathbf{g}_R \mathbf{T}_2^{\dagger}, \tag{16}$$

where $\mathbf{g}_L$ and $\mathbf{g}_R$ are the surface Green's functions of the left and right contact, respectively while $\mathbf{T}$ matrices describe the orbital or site overlap Hamiltonians between the contact and the nanosystem.

For ideal contacts, i.e. reservoirs made of the same material as the channel, the surface Green's function can be calculated using numerically efficient recursive methods. In these methods, layer by layer of contact regions is added until the difference between two sequential calculated surface Green's functions is smaller than a predetermined tolerance, which means that calculated contact Green's function is indistinguishable from Green's function of an infinite contact. This iterative method is simple [38] but very slow with $O(2^n)$ computational time where n is the number of layers. The most widely used method is the Sancho Rubio method [97] which has $O(n)$ computing time because the approach is constructed in such a manner that the number of included layers doubles in each iteration. The Sancho Rubio algorithm for the left contact is as follows

```
1. Initialize $\mathbf{A}_{old} = \mathbf{T}$, $\mathbf{B}_{old} = \mathbf{T}^{\dagger}$, $\mathbf{C}_{old} = \mathbf{D}_{old} = \mathbf{H}_0$, $\delta$(tolerance), $\varepsilon > \delta$
2. Iterate until $\varepsilon > \delta$
    a. Calculate $\mathbf{X} = [(E+i\eta)\mathbf{I}-\mathbf{C}_{old}]^{-1}$
    b. Calculate $\mathbf{A}_{new} = \mathbf{A}_{old}\mathbf{X}\mathbf{A}_{old}$, $\mathbf{A}_{new} = \mathbf{A}_{old}\mathbf{X}\mathbf{A}_{old}$
       $\mathbf{C}_{new} = \mathbf{C}_{old} + \mathbf{A}_{old}\mathbf{X}\mathbf{B}_{old} + \mathbf{B}_{old}\mathbf{X}\mathbf{A}_{old}$
       $\mathbf{D}_{new} = \mathbf{D}_{old} + \mathbf{B}_{old}\mathbf{X}\mathbf{A}_{old}$
    c. $\varepsilon_1 = \max[\mathrm{abs}(\mathbf{A}_{new}-\mathbf{A}_{old})]$, $\varepsilon_2 = \max[\mathrm{abs}(\mathbf{B}_{new}-\mathbf{B}_{old})]$,
       $\varepsilon_3 = \max[\mathrm{abs}(\mathbf{C}_{new}-\mathbf{C}_{old})]$, $\varepsilon_4 = \max[\mathrm{abs}(\mathbf{D}_{new}-\mathbf{D}_{old})]$,
       $\varepsilon = \max(\varepsilon_1, \varepsilon_2, \varepsilon_3, \varepsilon_4)$
    d. $\mathbf{A}_{old} = \mathbf{A}_{new}$, $\mathbf{B}_{old} = \mathbf{B}_{new}$, $\mathbf{C}_{old} = \mathbf{C}_{new}$, $\mathbf{D}_{old} = \mathbf{D}_{new}$,
3. $\mathbf{g}_L = [(E+i\eta)\mathbf{I}-\mathbf{D}_{new}]^{-1}$
4. $\mathbf{\Sigma}_L = \mathbf{T}^{\dagger}\mathbf{g}_L\mathbf{T}$
```

while for the right contact, we need to make two small changes in 2.b) $\mathbf{D}_{new} = \mathbf{D}_{old} + \mathbf{A}_{old}\mathbf{X}\mathbf{B}_{old}$ and in 4. $\mathbf{\Sigma}_R = \mathbf{T}\mathbf{g}_R\mathbf{T}^\dagger$. In the Sancho Rubio algorithm, $\mathbf{H}_0$ is the diagonal element of the total Hamiltonian block matrix while $\mathbf{T}$ and $\mathbf{T}^\dagger$ matrices describe the overlap to the right and left neighboring blocks, respectively. These matrices are illustrated later in the text in Section 3.5.1 and Figure 3.2 where $\mathbf{T}$ and $\mathbf{T}^\dagger$ matrices are denoted as $\mathbf{H}_1$ and $\mathbf{H}_{-1}$, respectively. In the following sections, total Hamiltonian (**H**) of the device will be obtained using DFT and transformed into a localized basis using MLWFs to obtain Hamiltonians suitable for NEGF and consequently Sancho Rubio calculations.

3.3. Top-of-the-Barrier and Under-the-Barrier Models

To explore the ballistic device performance of FETs with nanoribbon channel we employ the top-of-the-barrier (TOB) model to account for thermionic current and its extension, the under-the-barrier (UTB) model to include the direct source-to-drain tunneling current [98]. Within the TOB model, FET is modeled with three points: the potential at the top-of-the-barrier (U_{SC}), and source and drain Fermi levels. Furthermore, the transmission and DOS are obtained from NEGF and then used as inputs to the TOB module of QUDEN. The thermionic current flows only above the U_{SC}, as shown in Figure 3.1, and no tunneling is included at this point.

Mobile charge density at the top of the barrier is defined by local density at the top of the barrier, source and drain quasi-Fermi levels, and self-consistent TOB potential (U_{scf}). In equilibrium, i.e. for $V_G = V_D = V_S = 0$, charge density at the top of the barrier is described with

$$N_0 = \int_{-\infty}^{\infty} D(E)\left[f\left(E - E_F\right)\right] dE, \tag{17}$$

where $D(E)$ is the local density of states at the top of the barrier, while $f(E - E_F)$ is the Fermi-Dirac function.

The consequences of applying a bias to the gate and drain, while the source is grounded ($V_S = 0$ V), are: first, U_{scf} becomes self-consistent potential at the top of the barrier and, second, states at the top of the barrier are populated by two reservoirs with their respective Fermi levels. The positive velocity states in the channel are filled by the source with N_+ states, while the negative velocity states are filled by the drain with N_-, as follows

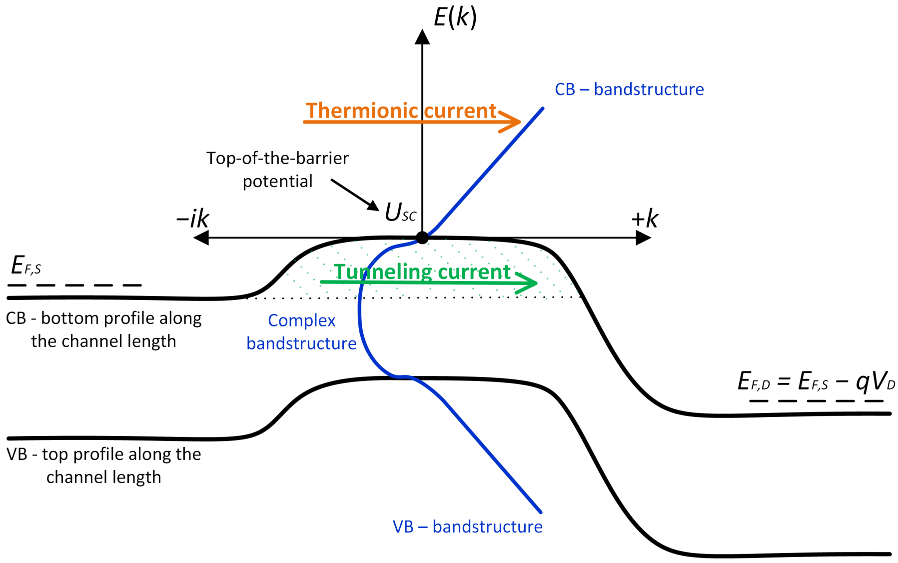

Figure 3.1. Profile of the conduction and valence bands along the channel length with quasi-Fermi levels in the source and drain. The *E*-*k* diagram is superimposed to illustrate the inclusion of real and complex parts of the bandstructure in FET simulations.[98]

$$\begin{aligned} N_+ &= \frac{1}{2}\int_{-\infty}^{\infty} D(E) f_1(E)\,dE, \\ N_- &= \frac{1}{2}\int_{-\infty}^{\infty} D(E) f_2(E)\,dE, \end{aligned} \tag{18}$$

where

$$\begin{aligned} f_1(E) &\equiv f\left(E - E_{FS} - U_{scf}\right), \\ f_2(E) &\equiv f\left(E - E_{FD} - U_{scf}\right), \end{aligned} \tag{19}$$

where the source Fermi level equals $E_{FS} = E_F$ and the drain Fermi level is defined as $E_{FD} = E_{FS} - qV_{DS}$.

To obtain the electron density at the top of the barrier, i.e. $N = N_+ + N_-$, we need to know the self-consistent potential U_{scf}. To find the U_{scf}, the 2D Poisson equation needs to be solved for a system that is represented by the three capacitors with the bias-induced charge $\Delta N = (N_+ + N_-) - N_0$ at the common terminal. The solution is obtained by superposition where first we ignore the mobile charge and calculate Laplace potential at the top-of-the-barrier as a result of terminal biases

$$U_L = -q\left(\alpha_G V_G + \alpha_D V_D + \alpha_S V_S\right). \tag{20}$$

In this equation, α_G, α_D, and α_S represent the influence of the gate, drain and source electrodes through capacitors C_G, C_D, and C_S in Laplace solution, and are given as

$$\alpha_G = \frac{C_G}{C_\Sigma} \qquad \alpha_D = \frac{C_D}{C_\Sigma} \qquad \alpha_S = \frac{C_S}{C_\Sigma}. \tag{21}$$

where C_Σ is the parallel combination of the three capacitors. The second part of the solution is mobile charge ΔN due to introduced biases. If we ground all three electrodes and calculate potential due to mobile charge at the top-of-the-barrier we get

$$U_P = \frac{q^2}{C_\Sigma} \Delta N. \tag{22}$$

Positive drain and gate voltages lower the top of the barrier potential energy, described with U_L but due to mobile charge it rises and the U_{scf} equation is given as follows

$$U_{scf} = U_P + U_L = -q\left(\alpha_G V_G + \alpha_D V_D + \alpha_S V_S\right) + \frac{q^2}{C_\Sigma} \Delta N. \tag{23}$$

To maintain charge neutrality in the highly doped source and drain regions under high bias conditions, a floating source potential is needed for ballistic transport. An increase in gate voltage decreases the number of electrons reflected from the barrier and consequently source potential needs to decrease to restore space-charge neutrality in the source. With the source potential decreasing the U_{scf} potential at the top of the barrier also decreases and this floating source effect results in an increased carrier density at the top of the barrier. In the analytical model, when the barrier height is high enough, i.e. when $U_{scf} >> E_{CS}$, where E_{CS} is the conduction band minimum in the source, both positive and negative velocity states are filled according to the source Fermi level

$$N_{SD} = \int_{-\infty}^{\infty} D\left(E - E_{CS}\right) f\left(E - E_{FS}\right) dE, \tag{24}$$

where N_{SD} is source doping density. When high bias is applied at the gate and drain, three distinct groups of carriers are present:

1) carriers with energy lower than the barrier reflected by the barrier
2) carriers with energy higher than the barrier with positive velocity
3) carriers with energy higher than the barrier with negative velocity

Groups 1) and 2) are in equilibrium with E_{FS} while group 3) is in equilibrium with E_{FD}. The sum of these populations is lower than the equilibrium carrier density and to maintain charge neutrality ($E_{FS} - E_{CS}$) needs to be increased. Although E_{FS} is fixed while E_{CS} floats down, in this model we keep E_{CS} fixed while E_{FS} floats up to E'_{FS}. From this, we can obtain charge neutrality condition in the source

$$\begin{aligned} N_{SD} = &\int_{-\infty}^{U_{scf}} D\left(E-E_{CS}\right) f\left(E-E'_{FS}\right) dE \\ &+ \int_{U_{scf}}^{\infty} D\left(E-E_{CS}\right)\left[f\left(E-E'_{FS}\right)+f\left(E-E'_{FS}+qV_{DS}\right)\right] dE. \end{aligned} \tag{25}$$

After the self-consistent U_{scf} is obtained, the thermionic current can be calculated. The difference between contact quasi-Fermi energies gives rise to the flow of current which can be calculated using Landauer's equation [38]

$$I_{th} = \frac{q}{h}\int_{-\infty}^{\infty} \bar{T}\left(E\right)\left[f_1\left(E\right)-f_2\left(E\right)\right] dE, \tag{26}$$

where I_{th} is calculated per spin. f_1 and f_2 represent source and drain Fermi functions defined in eq. (19) while $T(E)$ is obtained from NEGF via eq. (15).

Finally, to account for tunneling effects, the under-the-barrier model [99] is used as an extension of the TOB model. Complex bandstructure inside the bandgap is obtained, belonging to the evanescent electron waves in contrast to travelling electron waves in the real part of the bandstructure. This dispersion characteristic is approximated by a parabolic function that represents an energy-dependent electron decay rate or tunneling attenuation ($\kappa(E)$). The Wentzel-Kramers-Brillouin (WKB) approximation is used to obtain the transmission probability below the conduction band minimum (CBM) or above the valence band maximum (VBM) according to

$$T_{WKB}\left(E\right) = \sum_{n} \exp\left[-2l(E)\kappa(E)\right], \tag{27}$$

where n is a number of complex subbands of the channel material, i.e. respective nanoribbon, and $l(E)$ is the energy-dependent tunneling barrier length. The tunneling current is calculated per spin using the Landauer formula

$$I_{tun} = \frac{q}{h}\int_{E_{F,S}}^{Usc} T_{WKB}\left(E\right)\left[f\left(E-E_{F,S}\right)-f\left(E-E_{F,D}\right)\right] dE, \tag{28}$$

where $f(E - E_{F,S})$ and $f(E - E_{F,D})$ are source and drain Fermi-Dirac functions, respectively, and $E_{F,D} = E_{F,S} - qV_D$. Tunneling occurs only between the source CBM/VBM and top-of-the-barrier potential (U_{SC}), and mainly around $E_{F,S}$, as illustrated in Figure 3.1.

Finally, we can find the total current as

$$I_{tot} = I_{th} + I_{tun}, \tag{29}$$

which means a combination of TOB and UTB serves as an important tool to study FET devices with sub-15 nm gate lengths where the tunneling current cannot be ignored.

3.4. Density Functional Theory

To study nanoscale devices such as FETs with nanoribbons where strong quantum effects cannot be ignored, we need to use methods that are based on laws on physics and therefore do not use any fitting parameters from experimental data as for small and complex structures such as nanoribbons experimental data is limited to a few distinct materials and configurations due to complexity and price of fabrication. These methods are called first-principles or *ab initio* methods. Early *ab initio* methods that tried to solve the Schrödinger equation such as the Hartree method [100] in 1928 which introduced mean-field approximation and Hartree-Fock (HF) method [101] in 1930 that added Slater determinant for the wave function to the Hartree method relied on the $3N$ dimensional wave equation of N electrons which made these models practical only for few dozens of atoms. The breakthrough in *ab initio* methods came when Hohenberg and Kohn in 1964 [102] presented two theorems:

1. The energy ground state is a unique electron density functional: $E = E\ [(\rho(\mathbf{r})]$
2. Electron density which minimizes total functional is the real ground state of electron density $E\ [(\rho(\mathbf{r})] > E_0\ [(\rho_0(\mathbf{r})]$.

This was the ground for Kohn and Sham [103] in 1965 to develop a method called Density Functional Theory (DFT). DFT is an *ab initio* computational quantum mechanical method used to study the electronic structure of materials by solving the Schrödinger equation of the investigated system. The central quantity in DFT is electron density $\rho(\mathbf{r})$ which is defined as the sum of a set of squares of noninteracting orbitals

$$\rho(\mathbf{r}) = \sum_i |\phi_i(\mathbf{r})|^2 = 2\sum_i^{occ} |\phi_i(\mathbf{r})|^2 \tag{30}$$

where ϕ_i are Kohn-Sham (KS) orbitals in a noninteracting reference system. Note that non-interacting KS orbitals replace interacting wavefunctions ψ. Electron density is introduced to reduce the problem from $3N$ to 3 dimensions without losing information. Many-particle problem is reduced to many single-particle problems and each electron is treated as a point charge in the field of other electrons.

The introduction of the Kohn-Sham approach that utilizes electron density made it possible to study realistic-sized nano devices with hundreds or even thousands of atoms. In short, starting from the initial atomic structure, DFT iteratively optimizes structure geometry and electronic density until forces on atoms are low enough for it to be considered close enough to the true ground state. In the geometry part of the optimization process, atoms are moved to minimize forces on atoms. On the other hand, electronic density optimization relies on structure geometry and solving the Schrödinger equation.

3.4.1. The Kohn-Sham Approach

Firstly, the focus is on a stationary problem of n particles by neglecting the time-dependence of the Schrödinger equation whose full Hamiltonian of n particle system is

$$\hat{H} = -\frac{1}{2}\sum_{i=1}^{n}\nabla_i^2 - \sum_{I=1}^{N}\sum_{j=1}^{n}\frac{Z_I}{\left|\mathbf{R}_I - \mathbf{r}_j\right|} + \frac{1}{2}\sum_{i\neq j}^{n}\frac{1}{\left|\mathbf{r}_i - \mathbf{r}_j\right|} \tag{31}$$

where $\mathbf{r}_i$ and $\mathbf{r}_j$ are coordinates of electrons, $\mathbf{R}_I$ are coordinates of nuclei while Z_I are charges of the nuclei. The equation consists of three terms where the first term represents kinetic energy, the second term external potential and the last term is Hartree potential. Hartree potential includes coupled interactions between all n particles that are difficult to formulate in this form and therefore Kohn and Sham derived a different approach.

Kohn and Sham assumed that each electron is noninteracting. They decomposed the energy of n-electron into energy of n one-electrons and mapped the n-electron interacting system to a noninteracting system of n one-electrons. Total energy E in DFT framework can be written as

$$E = E_{kin}^{non} + E_{ext} + E_H + E_{xc} \tag{32}$$

where E_{kin}^{non} is non-interacting kinetic energy, E_{ext} is external potential, E_H is Hartree energy while the last term is exchange-correlation (XC) energy E_{xc}. Energy functionals in terms of electron density dependence can be written as follows. The kinetic energy E_{kin}^{non} in Kohn-Sham equations is defined as

$$E_{kin}^{non} = -\frac{1}{2}\sum_{i=1}^{n}\phi_i^*(\mathbf{r})\nabla^2\phi_i(\mathbf{r})d\mathbf{r}. \tag{33}$$

where ϕ_i are Kohn-Sham (KS) orbitals in a noninteracting system. Although orbitals are involved in this equation, it is directly correlated to electron density via eq. (30). External energy E_{ext} represents the interaction between electrons and other nuclei and can be written as

$$E_{ext} = \int\phi_i^*(\mathbf{r})U_{ext}\phi_i(\mathbf{r})d\mathbf{r} = \int U_{ext}\rho(\mathbf{r})d\mathbf{r}, \tag{34}$$

where U_{ext} (**r**) is external potential. Hartree energy E_H accounts for Coulomb interaction between electrons with

$$E_H = \frac{1}{2}\iint\frac{\rho(\mathbf{r})\rho(\mathbf{r}')}{|\mathbf{r}-\mathbf{r}'|}d\mathbf{r}\,d\mathbf{r}', \tag{35}$$

where ½ is for double counting. Furthermore, this term includes unphysical self-interactions of electrons which is corrected in the exchange energy term.

The final term is the exchange-correlation (XC) energy E_{xc} whose one-to-one relationship to the ground state was formalized by Hohenberg and Kohn [102]. It consists of all quantum effects and can be divided into exchange energy E_x and correlation energy E_c components where $E_{xc} = E_x + E_c$. E_x accounts for the exchange between electrons with the same spin while E_c is the correlation between electrons with a different spin. Exchange energy can be calculated as the sum of four-center integrals as a function of the single particle KS orbitals

$$E_x = -\frac{1}{2}\sum_{ij}^{n}\iint\frac{\phi_i^*(\mathbf{r})\phi_j^*(\mathbf{r})\phi_i(\mathbf{r})\phi_j(\mathbf{r})}{|\mathbf{r}-\mathbf{r}'|}d\mathbf{r}d\mathbf{r}', \tag{36}$$

which leads to less overlapping between electron densities and consequently a reduction in repulsion energy between electrons. Although E_x can be calculated directly with equation (36) for small systems, due to bad scaling and high computational cost E_x is always approximated. On the other hand, we have an electronic correlation where electrons with different spins can occupy the same orbital but also repel each other as they exhibit the same negative charges. Like E_x, the E_c results in less overlapping of electron densities. This is the unknown *n*-electron effect that is subject to an approximation. Correlation energy is an important component, especially for low electron densities where exchange energy becomes much lower due to lower interaction.

For small systems, XC-functional can be calculated but for bigger systems must be approximated. The simplest XC-functional approximations are local density approximation (LDA) and generalized gradient approximation (GGA). LDA depends only on the value of electronic density at each point in space. Electronic density is assumed to be the same everywhere and because of this assumption LDA often underestimates the bandgap of most semiconductors. The GGA improves upon LDA by taking into account the non-homogeneity of electron density. Perdew, Burke, and Ernzerhof (PBE) [104] parametrized GGA functional which significantly improved accuracy in the single electron orbital energies. Additionally, using hybrid functionals can reproduce band gaps even more accurately. The exchange part of the hybrid functional is calculated as a linear combination of GGA and Hartree-Fock exchange parts. The most widely used hybrid functional is HSE06, parametrized by Heyd, Scuseria, and Ernzerhof [105]. While highly precise, especially for band gap prediction, due to the high computational cost of using the Hartree-Fock method [106], the scalability of hybrid functional simulations is limited.

3.4.2. DFT for Crystalline Solids

The simulation path can be further narrowed because DFT is used to simulate crystalline solids. Crystal structures have a periodic arrangement of atoms and consequently periodic potential. Electrons in a periodic potential are Bloch waves which can be expanded into Fourier series and treated as a sum of plane waves with different kinetic energies. Ideally, an infinite range of plane waves with different energies should be considered but due to computational limits, a cutoff energy must be introduced. Cutoff energy must be high enough for total energy to converge within the given maximum error. The cutoff energy minimum for each atom type and used XC-functional is usually tested and attached to the materials pseudopotential (PP) file. Material properties are mainly characterized by valence electrons, so PPs are used to replace the core electrons and true potential with smoother and more effective potential. There are three common types of PPs: norm-conserving PPs, ultrasoft PPs and projector-augmented wave (PAW) PPs. Crystal structures are simulated by choosing a primitive unit cell that repeats infinitely in all directions. It is convenient to use reciprocal space because wavevectors **k** are defined in reciprocal space. In reciprocal space, the primitive unit cell is called the 1st Brillouin

Zone (BZ). Numerical calculations must be evaluated only in the 1st BZ and an appropriate of number *k*-points have to be chosen to sample the 1st BZ.

3.5. Maximally Localized Wannier Functions

Plane waves are used by most DFT codes to expand the single-particle Kohn-Sham wavefunctions. Plane-wave basis set enables highly accurate calculation of electronic states, but they are localized in energy and represented with dense Hamiltonians. For atomistic quantum transport simulations space-localized basis set is desired. In the 1930s, Wannier [107] introduced a localized real-space representation of Bloch states. Building upon Wannier work, Marzari and Vanderbilt [39] developed a computational method with maximal localization criteria for the construction of Wannier functions (WFs) which are represented with maximally sparse block-tridiagonal matrix. The usage of sparse matrices enables the simulation of nanodevices with realistic physical sizes. Marzari and Vanderbilt method was implemented in the Wannier90 [108] program and is compatible with a variety of DFT programs. In the following sections, only the basic concepts of maximally localized Wannier functions (MLWFs) will be outlined, while extensive theory can be found in [109].

Electronic structure calculations are often performed with periodic boundary conditions to study perfect crystal structures, while it is also common to study non-periodic systems such as liquids, molecules, interfaces, and defects. Bloch orbitals ($\psi_{n\mathbf{k}}$) can be chosen as common eigenstates of Hamiltonian in periodic systems

$$\psi_{n\mathbf{k}}(\mathbf{r}) = u_{n\mathbf{k}}(\mathbf{r})e^{i\mathbf{k}\cdot\mathbf{r}}, \tag{37}$$

where $u_{n\mathbf{k}}(\mathbf{r})$ includes the periodicity of the Hamiltonian, while $e^{i\mathbf{k}\cdot\mathbf{r}}$ can be interpreted as an envelope function where Bloch functions for different wave-vectors (**k**) exhibit different envelopes. Bloch functions are delocalized and spread over the entire space, but it is possible to construct a localized wave packet from Bloch functions by superimposing the contributions of different **k** values. If we switch to bra-ket notation where **R***n* refers to the Wannier function $w_{n\mathbf{R}}$ in cell **R** and band *n*, we can construct WFs according to

$$|\mathbf{R}n\rangle = \frac{V}{(2\pi)^3}\int_{BZ} d\mathbf{k}e^{-i\mathbf{k}\cdot\mathbf{R}}\sum_{m=1}^{J} U_{mn}^{(\mathbf{k})}|\psi_{n\mathbf{k}}\rangle, \tag{38}$$

where V is the volume of real-space primitive unit-cell, $e^{-i\mathbf{k}\cdot\mathbf{R}}$ is phase factor while $U_{mn}^{(\mathbf{k})}$ is unitary rotation matrix that can be interpreted as a gauge transformation used to deal with any discontinuity and ensure smoothness of $\psi_{n\mathbf{k}}$ in $\mathbf{k}$-space. This equation has a form of Fourier transform, and we can obtain its inverse transform as

$$\left|\psi_{n\mathbf{k}}\right\rangle = \sum_{\mathbf{R}} e^{-i\mathbf{k}\cdot\mathbf{R}} \left|\mathbf{R}n\right\rangle. \tag{39}$$

With transformations in equations (38) and (39) there is a unitary transformation between Bloch and Wannier basis and consequently, both sets of states provide an equally valid descriptions of the band subspace, although WFs are not Hamiltonian eigenstates. Manifest of the equivalence can be seen by expressing the band projection operator (P) in both Bloch and Wannier representations

$$P = \frac{V}{(2\pi)^3} \int_{BZ} \left|\psi_{n\mathbf{k}}\right\rangle \left\langle\psi_{n\mathbf{k}}\right| = \sum_{\mathbf{R}} \left|\mathbf{R}n\right\rangle \left\langle\mathbf{R}n\right|. \tag{40}$$

The WFs are not unique due to the gauge freedom in the definition of the Bloch functions and replacements

$$\begin{aligned} \left|\tilde{\psi}_{n\mathbf{k}}\right\rangle &= e^{i\varphi_n(\mathbf{k})} \left|\psi_{n\mathbf{k}}\right\rangle, \\ \left|\tilde{u}_{n\mathbf{k}}\right\rangle &= e^{i\varphi_n(\mathbf{k})} \left|u_{n\mathbf{k}}\right\rangle, \end{aligned} \tag{41}$$

in both Bloch and Wannier space can be made without changing the description of the system. $\varphi_n(\mathbf{k})$ is any real function periodic in reciprocal space.

For NEGF simulations, maximum localization is desired as it results in maximally sparse matrices. Real-space Wannier functions localization is linked to the smoothness of Bloch functions in reciprocal space and one of the simplest and most effective ways to construct a smooth gauge can be found by starting from the already localized trial orbitals ($g_n(\mathbf{r})$), usually atomic orbitals that represent a rough guess for home unit cell WFs, and projecting them on the Bloch manifold

$$\left|\phi_{n\mathbf{k}}\right\rangle = \sum_{m=1}^{J} \left|\psi_{m\mathbf{k}}\right\rangle \left\langle\psi_{m\mathbf{k}} \middle| g_n\right\rangle, \tag{42}$$

where the inner product matrix can be written as $\left(A_{\mathbf{k}}\right)_{mn} = \left\langle\psi_{m\mathbf{k}} \middle| g_n\right\rangle$ and used to compute the overlap matrix $\left(S_{\mathbf{k}}\right)_{mn} = \left\langle\phi_{m\mathbf{k}} \middle| \phi_{m\mathbf{k}}\right\rangle_V = \left(A_{\mathbf{k}}{}^{\dagger} A_{\mathbf{k}}\right)_{mn}$ .The result of projecting localized trial orbitals are usually functions that are smooth in the **k** space, but not orthonormal and applying the Löwdin orthonormalization technique [110] can fix this problem

$$\left|\tilde{\psi}_{n\mathbf{k}}\right\rangle = \sum_{m=1}^{J} \left|\phi_{m\mathbf{k}}\right\rangle \left(S_{\mathbf{k}}^{-1/2}\right)_{mn}, \tag{43}$$

at the expense of the resulting states not giving exactly the same description of the original system. The WFs obtained by the trial orbital projection are not maximally localized and well-defined localization criteria are needed to find MLWFs. Marzari and Vanderbilt [39] introduced localization criteria within the unit cell which reduces the problem of finding a gauge transformation ($U_{mn}^{(\mathbf{k})}$) that minimizes the localization functional

$$\Omega = \sum_{n} \left[\left\langle \mathbf{0}n \right| r^2 \left| \mathbf{0}n \right\rangle - \left\langle \mathbf{0}n \right| \mathbf{r} \left| \mathbf{0}n \right\rangle^2 \right] = \sum_{n} \left[\left\langle r^2 \right\rangle_n - \bar{\mathbf{r}}_n^2 \right], \tag{44}$$

described by the quadratic spread sum of the WFs in the home unit cell. Localization functional can be split into a sum of gauge invariant and gauge dependent parts where gauge-invariant part

$$\Omega_I = \sum_{n} \left[\left\langle \mathbf{0}n \right| r^2 \left| \mathbf{0}n \right\rangle - \sum_{\mathbf{R}m} \left| \left\langle \mathbf{R}m \right| \mathbf{r} \left| \mathbf{0}n \right\rangle \right|^2 \right], \tag{45}$$

cannot be minimized, while the gauge-dependent part

$$\tilde{\Omega} = \sum_{n} \sum_{\mathbf{R}m \neq \mathbf{0}n} \left| \left\langle \mathbf{R}m \right| \mathbf{r} \left| \mathbf{0}n \right\rangle \right|^2, \tag{46}$$

is further minimized.

The energy window around the bandgap of each material must be defined in which the accompanying bands are kept in MLWF Hamiltonian. The MLWF Hamiltonian is diagonalized along the same k-point path as in the DFT calculation. The MLWFs are localized around atom centers and the MLWF Hamiltonian matrix elements decay quickly when the distance between the WFs increases. To exclude interactions between the WFs that may be considered redundant, cutoff distance can be set.

3.5.1. Nanoribbon Hamiltonian Construction

After obtaining the MLFW Hamiltonian it must be converted into a suitable form that enables it to be upscaled to create a device Hamiltonian. There are two main outputs of the MLWF procedure: The first is $\mathbf{H}_{mn}(\mathbf{R})$ matrix where $\mathbf{R}$ are lattice vectors $(i,j,k) \in \mathbb{Z}$ which represents the interaction of the m-th WF in the home unit cell $\mathbf{R}(0,0,0)$ to n-th WF in the unit cell with indices $\mathbf{R}(i,j,k)$ as shown in Figure 3.2a. The second output are Wannier centers and their spreads within home unit cell. One can match the WFs to their centers in the home unit cell and construct various structures on an atom basis. This procedure is described in detail in [111] for various cases such as ideal scaling by repeating the unit cell N times where N is an integer, fractional scaling where one can determine the Hamiltonian of the device of desired length per atom basis and not per unit cell basis which is the case for ideal scaling. Nonetheless, in this work, the problem is simplified as we consider only the ideal upscaling procedure. Furthermore, the focus is on nanoribbons that are structures confined in a single direction and simulated in whole in DFT which means we can consider $\mathbf{R}$ in only a single direction, and we can write $\mathbf{H}_i \equiv \mathbf{H}_{mn}(\mathbf{R}(i,0,0))$ where $(i) \in \mathbb{Z}$.

With the inclusion of only the nearest-neighbor cell interactions and neglecting all other interactions between the WFs, we only need to consider $\mathbf{H}_i$ with lattice vectors $\mathbf{R}(i,0,0)$ where $i = \{-1,0,1\}$. The nanoribbon structure is shown in Figure 3.2b with depicted interactions within home unit cell $\mathbf{H}_0$, interactions of the home unit cell with first left unit cell with $\mathbf{H}_{-1}$ and first right unit cell with $\mathbf{H}_1$ where $\mathbf{H}_{-1} = \mathbf{H}_1^T$. Now that all needed interactions are described, we can use them to generate a super-cell Hamiltonian of a nanoribbon with the desired length in terms

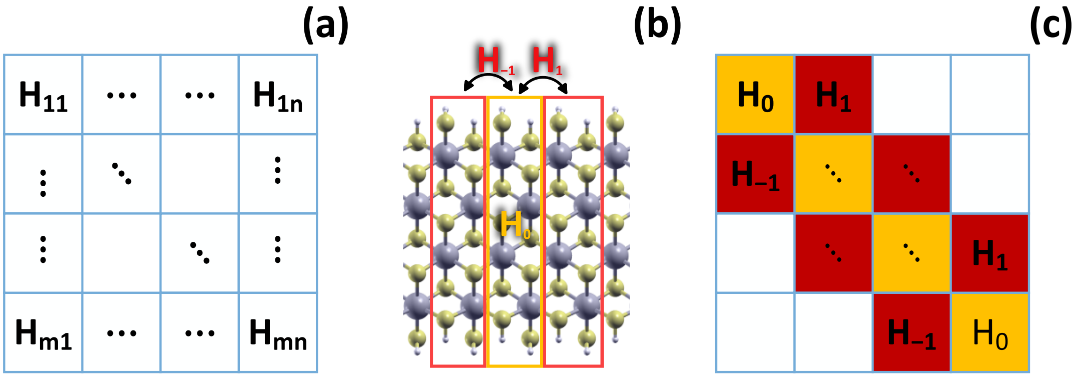

Figure 3.2. (a) Hamiltonian matrix $\mathbf{H}_{\mathbf{mn}}$, (b) nanoribbon structure with depicted interactions, (c) device Hamiltonian

of a number of unit cells N_L. The total Hamiltonian **H** of the nanoribbon is constructed as a block-tridiagonal matrix with $\mathbf{H}_0$ on the main diagonal repeated by the number of cells along the nanoribbon length N_L, $\mathbf{H}_1$ on the first super-diagonal, and $\mathbf{H}_{-1}^\dagger$ on the first sub-diagonal as shown in Figure 3.2c. If we designate the number of WFs in the unit-cell with N_{WANN}, the total Hamiltonian size is then $(N_{WANN} \times N_L) \times (N_{WANN} \times N_L)$. The obtained **H** is then used as an input for NEGF equations, i.e. for the retarded Green's function of the device.

3.6. Summary of the Workflow

A summary of the workflow used for device simulations reported in this thesis is shown in Figure 3.3. The simulation process starts with a definition of the initial nanoribbon structure that is imported into the DFT to optimize the geometry and find the electronic structure of the material, i.e. DFT Hamiltonian. Energy-localized DFT Hamiltonian, represented with a dense matrix, is transformed into a localized basis using MLWFs to obtain sparse MLWF Hamiltonians appropriate for quantum transport simulations. MLWF Hamiltonians are upscaled to create a total channel Hamiltonian (**H**) which serves as the main input into the NEGF code. Within NEGF, the device is described using the total channel Hamiltonian and $\mathbf{\Sigma}$ matrices that represent the interaction of the device with two contacts. The NEGF is used to obtain the transport properties, including transmission and DOS in equilibrium, which serve as an input for the TOB module of the overall code. The TOB and its extension UTB are used to calculate the current-voltage characteristics of single-gate ballistic NR FETs and obtain all relevant device figures of merit.

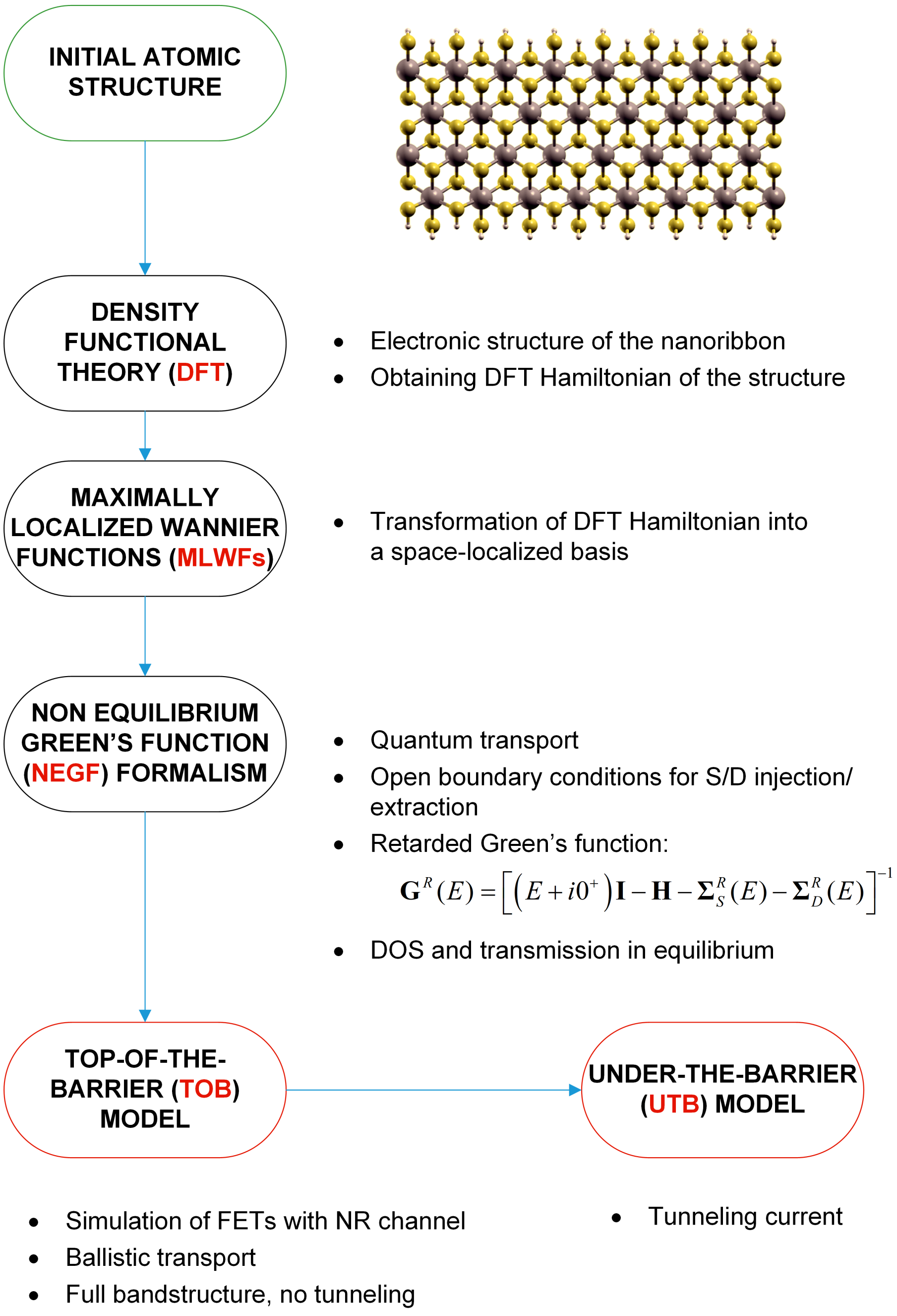

Figure 3.3 Summary of the simulation workflow used in this thesis to study nanoribbon FETs

Chapter 4

Main Scientific Contribution of the Thesis

The aim of this thesis is to develop a method based on the *ab initio* quantum transport calculations to analyze the electronic and transport properties of nanoribbons based on novel 2D materials, and to investigate the performance of respective 2D material NR FETs. The scientific contribution of this thesis can be divided into three main parts. The first part deals with the *ab initio* quantum transport method developed to study nanoribbon-based FETs from an atomistic material definition to fully quantum-mechanical quantum transport simulations. The second part deals with the application of the developed method to study the impact of quantum mechanical effects and dimensional scaling on the electronic and transport properties, as well as on the performance of NR FETs made of novel 2D materials. The last part provides optimum configurations of novel NR FETs and assesses their feasibility for future logic devices. The following subsections briefly discuss the main scientific contribution of the research for each of the three main parts.

1. **Self-consistent method for simulations of quantum transport in nanoelectronic devices based on nanoribbons of novel 2D materials**

To properly study nanoscale electronic devices, the simulation process needs to incorporate all relevant physics. Therefore, a method is developed that utilizes multiple advanced theoretical and computational techniques which can be divided into two parts. The first part is the atomistic construction of the studied nanoribbons of novel 2D materials and obtaining the electronic structure and the Hamiltonian of the material. The second part represents the quantum transport simulation of transistors which uses as input the mentioned Hamiltonian. The first part starts with an initial structure where the unit cell of a 2D material is used to construct nanoribbons of various widths and edge configurations. Once edges are passivated, nanoribbon is constructed and DFT is used to obtain electronic structure. Furthermore, the obtained DFT Hamiltonian is transformed into a space-localized basis using MLWFs which is one of the main inputs to quantum transport simulations. The quantum transport simulations utilize NEGF in combination with the TOB model for self-consistent calculation of the device current-voltage characteristics. Both NEGF and TOB modules of the total code are adapted and optimized for quasi-1D materials with DFT-MLWF Hamiltonian inputs. The NEGF is used in equilibrium to obtain transmission and density of states which serve as an input to TOB. TOB is used to model a single gate FET with three points, S/D Fermi level and TOB potential which represents barrier height between S/D. Although this model is simple, for devices with channels longer than 15 nm it showed similar results compared to the more advanced method that employs a full numerical solution of the Poisson equation, as reported in [Pub 5]. One of the biggest strengths of the developed and implemented DFT-MLWF-NEGF-TOB approach is the low computational time which is several orders of magnitude lower compared to full 3D Poisson simulation in commercial software. As a result, the implemented method can be used for fast screening of a variety of novel 2D materials patterned into nanoribbons with physical correctness and high accuracy.

2. Analysis of quantum-mechanical and scaling effects on the electronic and transport properties and on the performance of transistors based on nanoribbons of novel 2D materials using *ab initio* bandstructure calculations

Due to their size, the studied nanoribbons experience strong quantum confinement effects that modify the material properties, which consequently affects the performance of transistors based on such nanostructures. The analysis of quantum-mechanical and scaling effects is carried out by exploring the relationship between the ON-state current (I_{ON}) of NR FETs and the electronic, transport and device properties. Some of the physical variables and observables studied in this work include the bandstructure, bandstructure effective mass, bandgap, DOS, transmission, injection velocity, charge density, band decomposed charge density, effective transport mass, and current density. All these properties are extracted and analyzed separately for given nanoribbon material, width, and carrier type, while collectively they give a clear picture of the underlying physics behind the impact of quantum-mechanical and scaling effects.

Nanoribbons of novel 2D materials are studied in this thesis, specifically armchair and zigzag MX_2NRs where M = {Hf, Zr} and X = {S, Se} in [Pub 1], [Pub 2], [Pub 5] armchair and zigzag GeSNRs in [Pub 2], [Pub 3], and MoS_2NRs [Pub 6], [Pub 7], are atomically thin with widths in range from ~ 0.8 nm to ~ 7 nm. Analysis of the ON-state current shows that I_{ON} for most devices deteriorates with downscaling to the value of 50% to 95% of the widest observed nanoribbon compared to the narrowest. However, FETs of some materials show an unexpected increase with downscaling with up to 70% increase for zigzag MX_2NR NFETs, up to 20% increase for armchair MX_2NR PFETs and up to 6× for zigzag GeSNR PFETs. Interestingly, the I_{ON} of all devices whose performance increases with downscaling reaches a maximum when nanoribbon width is downscaled to ~ 2 nm.

3. Optimum configurations of transistors based on nanoribbons of novel 2D materials for future extremely scaled semiconductor electronic technologies

Optimum configurations of transistors based on nanoribbons of novel 2D materials are found by comparison with IEEE IRDS requirements for future technological nodes. The main IRDS requirements for this thesis are the ballistic I_{ON} and injection velocity (v_{inj}) which incorporate all the material and device physics. Material properties such as material composition, crystal phase, and edge configuration are predetermined by the material itself and therefore the optimization of NR FET performance can be achieved by tweaking nanoribbon width, S/D doping, gate oxide material, and gate oxide thickness. Nevertheless, all tunable properties in the simulation environment must stay within the physical limits of possible configurations in future devices.

Comparing the performance of studied NR FETs to IRDS I_{ON} requirement of ~2 mA/µm for future technology nodes shows that most zigzag MX_2NRs satisfy the requirement for both NFET and PFET devices. Out of zigzag MX_2NRs reported in [Pub 1], ZZ-HfS_2NRs and ZZ-$HfSe_2$NRs fulfill the requirement for all NR widths while for Zr-based zigzag MX_2NRs the criteria is met only for ZZ-ZrS_2NRs with $W < 3$ nm and ZZ-$ZrSe_2$NRs with $W < 6$ nm. In contrast, only the performance of PFETs with armchair MX_2NR channel is high enough to meet the IRDS requirement. Furthermore, AC-GeSNRs with $W \geq 1.86$ nm in [Pub 3] meet the I_{ON} criteria for both NFET and PFET devices while MoS_2NRs do not meet the IRDS I_{ON} requirement for any configuration, as reported in [Pub 6]. Comparison with IRDS affirms the potential of some Zr- and Hf-based MX_2NR and GeSNR configurations for future FETs.

Chapter 5

Overview of Scientific Work of the Thesis

5.1. List of Scientific Qualification Articles

The main scientific publications, both journals and conferences, related to the dissertation and included in this thesis are listed here.

5.1.1. Journal Publications

[Pub 1] M. Matić and M. Poljak, “Intrinsic performance limits of extremely scaled field-effect transistors based on MX_2 ($M = \{Zr, Hf\}$, $X = \{S, Se\}$) nanoribbons,” *Journal of Applied Physics*, vol. 136, no. 8, p. 084307, Aug. 2024, doi: 10.1063/5.0224088.

[Pub 2] M. Matić and M. Poljak, “Ballistic Performance of Quasi-One-Dimensional Hafnium Disulfide Field-Effect Transistors,” *Electronics*, vol. 13, no. 6, p. 1048, 2024. doi: 10.3390/electronics13061048

[Pub 3] M. Matić and M. Poljak, “Electronic, transport and ballistic device properties of quasi-one-dimensional GeS,” *Journal of Computational Electronics*, vol. 22, no. 5, pp. 1350–1362, 2023. doi: 10.1007/s10825-023-02054-4

[Pub 4] M. Matić and M. Poljak, “Ab initio quantum transport simulations of monolayer GeS nanoribbons,” *Solid-State Electronics*, vol. 197, p. 108460, 2022. doi: 10.1016/j.sse.2022.108460

5.1.2. Conference Publications

[Pub 5] M. Matić and M. Poljak, “Validity of the Ballistic Top-of-the-Barrier Model for FETs Based on 2D Material Nanoribbons,” in *2024 47th MIPRO ICT and Electronics Convention (MIPRO)*, 2024, pp. 1596–1601. doi: 10.1109/MIPRO60963.2024.10569245

[Pub 6] M. Matić and M. Poljak, “Transport Properties and Device Performance of Quasi-One-Dimensional MoS_2 FETs,” in *2023 46th MIPRO ICT and Electronics Convention (MIPRO)*, 2023, pp. 168–172. doi: 10.23919/MIPRO57284.2023.10159951

[Pub 7] I. Prevarić, M. Matić, and M. Poljak, “Tunneling Attenuation and Leakage Current in MoS_2 Nanoribbon MOSFETs,” in *2023 46th MIPRO ICT and Electronics Convention (MIPRO)*, 2023, pp. 163–167. doi: 10.23919/MIPRO57284.2023.10159745

5.2. Author’s Contribution to the Publications

The results presented in this thesis are based on the research conducted in the period from 2020 to 2024 at the University of Zagreb Faculty of Electrical Engineering and Computing, Department of Electronics, Microelectronics, Computer and Intelligent Systems (Unska 3, 10000 Zagreb, Croatia) under the supervision of Associate Professor Mirko Poljak, PhD. The work is the result of research within the project “Computational design of nanotransistors based on novel 2D materials” under the acronym CONAN2D, funded by the Croatian Science Foundation under grant number UIP-2019-04-3493.

The thesis includes four journal publications and three conference publications written in collaboration with coauthors of the published papers, while the author is listed as the first author on all journal papers and most conference papers. The author’s contribution to each paper consists of the manuscript conceptualization, methodology, software implementation, data curation, and formal analysis and interpretation of the results. The author’s contribution in the specific publication is detailed in the following list:

[Pub 1] In the journal paper **“*Intrinsic Performance Limits of Extremely Scaled Field-Effect Transistors Based on MX_2 (M = {Zr, Hf}, X = ({S, Se}) Nanoribbons*”** [34]: obtaining Hamiltonians of the armchair and zigzag MX_2 (M = {Zr, Hf}, X = {S, Se}) nanoribbons of various widths using DFT and MLWF, analyzing the effects of nanoribbon edge configuration and width scaling on the bandstructure and bandgap, device performance analysis of MX_2NR FETs by evaluating the ON-state current scaling behavior using DOS, transmission, injection velocity, charge density, bandstructure effective mass and effective transport mass, assessment of MX_2NR FETs and potential of MX_2NRs as channel materials for future logic devices by comparison with IRDS I_{ON} requirement, data visualization and writing the paper.

[Pub 2] In the journal paper **“*Ballistic Performance of Quasi-One-Dimensional Hafnium Disulfide Field-Effect Transistors*”** [82]: obtaining Hamiltonians of zigzag HfS_2 nanoribbons of various widths using DFT and MLWF, analysis of NR width scaling behavior of bandstructure, bandgap, and bandstructure effective mass, analysis of the nanoribbon width scaling on the ON-state current performance of ZZ-HfS_2NR FETs via DOS, injection velocity, current density and band-decomposed charge density, assessment of the potential of ZZ-HfS_2NR FETs for future logic devices by comparison with IRDS I_{ON} and injection velocity requirements, data visualization and writing the paper.

[Pub 3] In the journal paper: **“*Electronic, transport and ballistic device properties of quasi-one-dimensional GeS*”** [112]: upgrading the QUDEN quantum transport simulator to assess both N- and P-type FET devices, obtaining Hamiltonians of the armchair and zigzag GeS nanoribbons of various widths using DFT and MLWFs, analysis and interpretation of nanoribbon scaling impact on bandstructure evolution, bandgap, and bandstructure effective mass, analysis and interpretation of the ON-state current width dependence of AC and ZZ GeSNR FETs using DOS, transmission, charge density and injection velocity, optimization of GeSNR FETs via oxide thickness variation, data visualization and writing the paper.

[Pub 4] In the journal paper **“*Ab initio quantum transport simulations of monolayer GeS nanoribbons*”** [113]: creating the extension of the QUDEN quantum transport simulator to input DFT-MLWF Hamiltonians, obtaining DFT-MLWF Hamiltonians of armchair GeSNRs of various widths, analysis of bandstructure and electron effective mass evolution with scaling NR width, analysis of the ON-state current of armchair GeSNR NFETs using DOS and transmission, data visualization and writing the paper.

[Pub 5] In the conference paper: "***Validity of the Ballistic Top-of-the-Barrier Model for FETs Based on 2D Material Nanoribbons***" [114]: assessment and validation of the QUDEN quantum transport simulator by comparison with commercial QuantumATK software that utilizes a combination of NEGF and 3D Poisson, comparison of ZrS_2NR FET and graphene nanoribbon FET current performance by analysis of bandstructure, DOS and transmission, data visualization, writing the paper and oral presentation.

[Pub 6] In the conference paper "***Transport Properties and Device Performance of Quasi-One-Dimensional MoS_2 FETs***" [115]: obtaining Hamiltonians of MoS_2 nanoribbons of various widths using DFT and MLWF, analysis of bandstructure and bandgap, analysis of the ON-state current nanoribbon width scaling behavior, analysis and interpretation of DOS, transmission, charge density, injection velocity, and current density of MoS_2NRs and MoS_2NR FETs, data visualization, writing the paper and oral presentation.

[Pub 7] In the conference paper "***Tunneling Attenuation and Leakage Current in MoS_2 Nanoribbon MOSFETs***" [116]: conceptualization, methodology, obtaining DFT-MLWF Hamiltonians of MoS_2NRs of various widths, analysis of complex bandstructure evolution with NR width scaling, analysis of the OFF-state tunneling current of single-gate FETs for various channel lengths, cowriting the paper.

Chapter 6

Conclusions and Future Work

The gate-all-around (GAA) field-effect transistors (FETs) with nanosheets and nanowires represent the future of logic device technology with industry leaders already including 2D materials in their roadmap as early as late 2020s. However, there is an ongoing search for best-performing materials and device architectures due to the high number of possible candidates. While some experimental studies are present in the literature, they are limited to only a few materials due to the high cost and complexity of fabrication, which renders a need to study and identify the potential materials using an advanced computational design methodology which is the focus of this thesis. The main goals of this research are achieved by developing an advanced *ab initio* quantum transport method and applying it to investigate the feasibility of using nanoribbons of novel 2D materials as channel materials alternative to silicon-based devices.

Firstly, an *ab initio* quantum transport method is implemented which employs density functional theory (DFT) and maximally localized Wannier functions (MLWFs) to obtain the electronic structure of nanoribbons, whereas quantum transport simulations based on the non-equilibrium Green's function (NEGF) formalism in combination with the top-of-the-barrier (TOB) model are used to simulate ballistic single-gate FETs with a nanoribbon channel. Quantum transport simulator is implemented in QUDEN (from Quantum-Transport Device Engineering in Nanoelectronics) which is a legacy MATLAB code of the Computational Nanoelectronics Group at UNIZG-FER. For this research, QUDEN was heavily upgraded and extended to study both N- and P-type FETs and use DFT-MLWF Hamiltonians as an input, while its performance is boosted by using a much more numerically efficient recursive Green's function method. The simulator is validated by comparison with a commercial simulator which employs more advanced calculations that include solving a full 2D or 3D Poisson equation for device electrostatics. The implemented simulator is used to evaluate the electronic and transport properties of nanoribbons, and device properties of NR FETs, with the motivation of employing such nanoribbons as foreseeable replacements for "nanosheet structures" in MBC FETs and RibbonFETs that stand as industry-relevant GAA FET implementations.

The detailed study reported in this thesis has investigated the following nanoribbon candidates for future logic devices: (i) armchair (AC) and zigzag (ZZ) MX_2NRs where M = {Hf, Zr} and X = {S, Se}, (ii) AC and ZZ GeSNRs, and (iii) MoS_2NRs. Nanoribbon widths are designated based on the number of unit cells along the nanoribbon width (ranging from 2 to 10), which results in NR widths in the range from ~ 7 nm down to only ~ 0.8 nm. The studied materials exhibit a strong influence of atomistic and quantum-mechanical effects on the electronic and transport properties and, consequently, on the performance of ultra-scaled NR FET devices. Material properties are largely determined by material composition, crystal phase, and edge configuration and, for example, similar structures in terms of crystal phase and edge configuration with different material composition exhibit similar width scaling properties.

The bandstructure of the nanoribbon evolves with downscaling, and so do device properties and performance. Due to the mentioned quantum-mechanical effects whose effect on material properties increases as nanoribbon width decreases, the bandstructure of narrower NRs is significantly altered and exhibits a lower number of available subbands due to a lower number of orbitals. For most devices, the evolution of the bandstructure with downscaling leads to lower curvature of dominant subbands near the CBM/VBM, i.e. an increase of electron/hole bandstructure effective mass is observed. Consequently, electron or hole injection velocity is reduced in narrower nanoribbons and the respective NR FETs exhibit lower ON-state current (I_{ON}). Interestingly, some materials show an unexpected I_{ON} increase with downscaling. Specifically, armchair MX_2NR PFETs, zigzag MX_2NR NFETs, and zigzag GeSNR PFETs display improved I_{ON} when nanoribbon width is downscaled to ~ 2 nm. Although bandstructure evolution with nanoribbon width downscaling is different for each configuration, all devices that exhibit an increase in FET performance show an emergence of a subband with higher curvature (i.e. lower effective mass), which induces an increase in injection velocity and. ON-state current. The maximum I_{ON} is reported for FETs with ~ 2 nm-wide NR channels, while for narrower nanoribbons the strong quantum-confinement effects deteriorates the current-driving capabilities.

The potential of studied nanoribbon FETs for future technology nodes is assessed by comparing their performance with the IEEE International Roadmap for Devices and Systems (IRDS) requirements which specify the I_{ON} of ~2 mA/µm for '3 nm' node and beyond. The comparison shows that most zigzag MX_2NRs and AC-GeSNRs with $W \geq 1.86$ nm meet criteria for both NFET and PFET devices. As for the zigzag MX_2NRs, the requirement is met for all studied Hf-based MX_2NRs and some Zr-based zigzag MX_2NRs, i.e. sub-3 nm-wide ZZ-ZrS_2NRs and sub-6 nm-wide ZZ-$ZrSe_2NRs$. In contrast, only PFETs with an armchair MX_2NR channel fulfill the I_{ON} requirement. Finally, MoS_2NRs, which are nanoribbons of one of the most researched 2D materials after graphene, do not meet the IRDS requirement in any configuration. Nonetheless, our results indicate that certain Zr- and Hf-based MX_2NRs and GeSNRs have the potential to be employed as channel materials for future high-density and high-performance logic FETs, especially in multiple nanowire/nanosheet architectures such as MBC FETs and RibbonFETs.

This work establishes the computational design framework needed for the assessment of the upper ballistic performance limits and provides an assessment of potential nanoribbon candidates for future nanoscale logic devices. To build upon this research and extend its impact on more realistic devices, future research should deal with fully self-consistent NEGF and Poisson simulations while including carrier scattering. This approach could provide a way to explore a variety of structures by providing physical insights into realistic devices with dissipative transport. Furthermore, the high contact resistance in FETs with 2D materials could be addressed by analyzing the impact of various metallic contacts and different configurations for a comprehensive evaluation of nanoribbon FET devices. This direction could possibly be used to find optimal configurations and metals to minimize contact resistance in future logic devices. Further research could also be directed at assessing hundreds of other 2D materials that have not yet been studied, neither theoretically nor experimentally, in FET configurations but can be, in principle, cut into quasi-1D nanostructures. Some of these nanostructured materials could provide unexpected but useful properties that are suitable for future electron devices.

Bibliography

[1] N. Loubet *et al.*, "Stacked nanosheet gate-all-around transistor to enable scaling beyond FinFET," in *2017 Symposium on VLSI Technology*, Jun. 2017, pp. T230–T231. doi: 10.23919/VLSIT.2017.7998183.

[2] G. Bae *et al.*, "3nm GAA Technology featuring Multi-Bridge-Channel FET for Low Power and High Performance Applications," in *2018 IEEE International Electron Devices Meeting (IEDM)*, Dec. 2018, p. 28.7.1-28.7.4. doi: 10.1109/IEDM.2018.8614629.

[3] N. Singh *et al.*, "High-performance fully depleted silicon nanowire (diameter ≤ 5 nm) gate-all-around CMOS devices," *IEEE Electron Device Lett.*, vol. 27, no. 5, pp. 383–386, May 2006, doi: 10.1109/LED.2006.873381.

[4] K. Uchida, H. Watanabe, A. Kinoshita, J. Koga, T. Numata, and S. Takagi, "Experimental study on carrier transport mechanism in ultrathin-body SOI n and p-MOSFETs with SOI thickness less than 5 nm," in *Digest. International Electron Devices Meeting,* Dec. 2002, pp. 47–50. doi: 10.1109/IEDM.2002.1175776.

[5] C. Klinkert, Á. Szabó, C. Stieger, D. Campi, N. Marzari, and M. Luisier, "2-D Materials for Ultrascaled Field-Effect Transistors: One Hundred Candidates under the *Ab Initio* Microscope," *ACS Nano*, vol. 14, no. 7, pp. 8605–8615, Jul. 2020, doi: 10.1021/acsnano.0c02983.

[6] K. J. Kuhn, "Considerations for Ultimate CMOS Scaling," *IEEE Trans. Electron Devices*, vol. 59, no. 7, pp. 1813–1828, Jul. 2012, doi: 10.1109/TED.2012.2193129.

[7] M. C. Lemme, D. Akinwande, C. Huyghebaert, and C. Stampfer, "2D materials for future heterogeneous electronics," *Nat. Commun.*, vol. 13, no. 1, p. 1392, Mar. 2022, doi: 10.1038/s41467-022-29001-4.

[8] G. Fiori *et al.*, "Electronics based on two-dimensional materials," *Nat. Nanotechnol.*, vol. 9, no. 10, pp. 768–779, Oct. 2014, doi: 10.1038/nnano.2014.207.

[9] F. Schwierz, J. Pezoldt, and R. Granzner, "Two-dimensional materials and their prospects in transistor electronics," *Nanoscale*, vol. 7, no. 18, pp. 8261–8283, Apr. 2015, doi: 10.1039/C5NR01052G.

[10] F. Urban, G. Lupina, A. Grillo, N. Martucciello, and A. D. Bartolomeo, "Contact resistance and mobility in back-gate graphene transistors," *Nano Express*, vol. 1, no. 1, p. 010001, Mar. 2020, doi: 10.1088/2632-959X/ab7055.

[11] A. Allain, J. Kang, K. Banerjee, and A. Kis, "Electrical contacts to two-dimensional semiconductors," *Nat. Mater.*, vol. 14, no. 12, pp. 1195–1205, Dec. 2015, doi: 10.1038/nmat4452.

[12] M. Poljak, M. Matić, and A. Zeljko, "Minimum Contact Resistance in Monoelemental 2D Material Nanodevices With Edge-Contacts," *IEEE Electron Device Lett.*, vol. 42, no. 8, pp. 1240–1243, Aug. 2021, doi: 10.1109/LED.2021.3087908.

[13] J. Hong *et al.*, "Exploring atomic defects in molybdenum disulphide monolayers," *Nat. Commun.*, vol. 6, no. 1, p. 6293, May 2015, doi: 10.1038/ncomms7293.

[14] N. Ma and D. Jena, "Charge Scattering and Mobility in Atomically Thin Semiconductors," *Phys. Rev. X*, vol. 4, no. 1, p. 011043, Mar. 2014, doi: 10.1103/PhysRevX.4.011043.

[15] Z.-Y. Ong and M. V. Fischetti, "Mobility enhancement and temperature dependence in top-gated single-layer MoS_2," *Phys. Rev. B*, vol. 88, no. 16, p. 165316, Oct. 2013, doi: 10.1103/PhysRevB.88.165316.

[16] A. Penumatcha *et al.*, "High Mobility TMD NMOS and PMOS Transistors and GAA Architecture for Ultimate CMOS Scaling," in *2023 International Electron Devices Meeting (IEDM)*, Dec. 2023, pp. 1–4. doi: 10.1109/IEDM45741.2023.10413662.

[17] S. Hitesh, P. Dasika, K. Watanabe, T. Taniguchi, and K. Majumdar, "Integration of 3-Level MoS Multibridge Channel FET With 2D Layered Contact and Gate Dielectric," *IEEE Electron Device Lett.*, vol. 43, no. 11, pp. 1993–1996, Nov. 2022, doi: 10.1109/LED.2022.3206866.

[18] A. Provias *et al.*, "Reliability Assessment of Double-Gated Wafer-Scale MoS_2 Field Effect Transistors through Hysteresis and Bias Temperature Instability Analyses," in *2023 International Electron Devices Meeting (IEDM)*, Dec. 2023, pp. 1–4. doi: 10.1109/IEDM45741.2023.10413755.

[19] C. J. Dorow *et al.*, "Exploring manufacturability of novel 2D channel materials: 300 mm wafer-scale 2D NMOS & PMOS using MoS_2, WS_2, & WSe_2," in *2023 International Electron Devices Meeting (IEDM)*, Dec. 2023, pp. 1–4. doi: 10.1109/IEDM45741.2023.10413874.

[20] N. Mounet *et al.*, "Two-dimensional materials from high-throughput computational exfoliation of experimentally known compounds," *Nat. Nanotechnol.*, vol. 13, no. 3, pp. 246–252, Mar. 2018, doi: 10.1038/s41565-017-0035-5.

[21] B. Radisavljevic, A. Radenovic, J. Brivio, V. Giacometti, and A. Kis, "Single-layer MoS_2 transistors," *Nat. Nanotechnol.*, vol. 6, no. 3, pp. 147–150, Mar. 2011, doi: 10.1038/nnano.2010.279.

[22] Y. Huang *et al.*, "Tin Disulfide—An Emerging Layered Metal Dichalcogenide Semiconductor: Materials Properties and Device Characteristics," *ACS Nano*, vol. 8, no. 10, pp. 10743–10755, Oct. 2014, doi: 10.1021/nn504481r.

[23] D. Ovchinnikov, A. Allain, Y.-S. Huang, D. Dumcenco, and A. Kis, "Electrical Transport Properties of Single-Layer WS_2," *ACS Nano*, vol. 8, no. 8, pp. 8174–8181, Aug. 2014, doi: 10.1021/nn502362b.

[24] M. Poljak, "Electron Mobility in Defective Nanoribbons of Monoelemental 2D Materials," *IEEE Electron Device Lett.*, vol. 41, no. 1, pp. 151–154, Jan. 2020, doi: 10.1109/LED.2019.2952661.

[25] L. Tao *et al.*, "Silicene field-effect transistors operating at room temperature," *Nat. Nanotechnol.*, vol. 10, no. 3, pp. 227–231, Mar. 2015, doi: 10.1038/nnano.2014.325.

[26] S. Kaneko, H. Tsuchiya, Y. Kamakura, N. Mori, and M. Ogawa, "Theoretical performance estimation of silicene, germanene, and graphene nanoribbon field-effect transistors under ballistic transport," *Appl. Phys. Express*, vol. 7, no. 3, p. 035102, Mar. 2014, doi: 10.7567/APEX.7.035102.

[27] S. Zhang *et al.*, "Recent progress in 2D group-VA semiconductors: from theory to experiment," *Chem. Soc. Rev.*, vol. 47, no. 3, pp. 982–1021, 2018, doi: 10.1039/C7CS00125H.

[28] W. Zhou *et al.*, "Two-Dimensional Pnictogen for Field-Effect Transistors," *Research*, vol. 2019, pp. 1–21, Oct. 2019, doi: 10.34133/2019/1046329.

[29] M. Poljak, "Material and device properties of bismuthene nanoribbons from multi-orbital quantum transport simulations," in *2020 43rd International Convention on Information, Communication and Electronic Technology (MIPRO)*, Opatija, Croatia: IEEE, Sep. 2020, pp. 34–38. doi: 10.23919/MIPRO48935.2020.9245365.

[30] G. Fiori and G. Iannaccone, "Simulation of Graphene Nanoribbon Field-Effect Transistors," *IEEE Electron Device Lett.*, vol. 28, no. 8, pp. 760–762, Aug. 2007, doi: 10.1109/LED.2007.901680.

[31] Y. Ouyang, Y. Yoon, and J. Guo, "Scaling Behaviors of Graphene Nanoribbon FETs: A Three-Dimensional Quantum Simulation Study," *IEEE Trans. Electron Devices*, vol. 54, no. 9, pp. 2223–2231, Sep. 2007, doi: 10.1109/TED.2007.902692.

[32] M. Poljak and M. Matić, "DFT-Based Tight-Binding Model for Atomistic Simulations of Phosphorene Nanoribbons," in *2021 44th International Convention on Information, Communication and Electronic Technology (MIPRO)*, Sep. 2021, pp. 80–84. doi: 10.23919/MIPRO52101.2021.9596745.

[33] J. Appenzeller, J. Knoch, M. T. Bjork, H. Riel, H. Schmid, and W. Riess, "Toward Nanowire Electronics," *IEEE Trans. Electron Devices*, vol. 55, no. 11, pp. 2827–2845, Nov. 2008, doi: 10.1109/TED.2008.2008011.

[34] M. Matić and M. Poljak, "Intrinsic performance limits of extremely scaled field-effect transistors based on MX_2 (M = {Zr, Hf}, X = {S, Se}) nanoribbons," *J. Appl. Phys.*, vol. 136, no. 8, p. 084307, Aug. 2024, doi: 10.1063/5.0224088.

[35] M. Luisier *et al.*, "First-principles simulations of 2-D semiconductor devices: Mobility, I-V characteristics, and contact resistance," in *2016 IEEE International Electron Devices Meeting (IEDM)*, San Francisco, CA, USA: IEEE, Dec. 2016, p. 5.4.1-5.4.4. doi: 10.1109/IEDM.2016.7838353.

[36] W. Kohn and L. J. Sham, "Self-Consistent Equations Including Exchange and Correlation Effects," *Phys. Rev.*, vol. 140, no. 4A, pp. A1133–A1138, Nov. 1965, doi: 10.1103/PhysRev.140.A1133.

[37] A. Rahman, Jing Guo, S. Datta, and M. S. Lundstrom, "Theory of ballistic nanotransistors," *IEEE Trans. Electron Devices*, vol. 50, no. 9, pp. 1853–1864, Sep. 2003, doi: 10.1109/TED.2003.815366.

[38] S. Datta, *Quantum Transport: Atom to Transistor*. Cambridge: Cambridge University Press, 2005. doi: 10.1017/CBO9781139164313.

[39] N. Marzari and D. Vanderbilt, "Maximally localized generalized Wannier functions for composite energy bands," *Phys. Rev. B*, vol. 56, no. 20, pp. 12847–12865, Nov. 1997, doi: 10.1103/PhysRevB.56.12847.

[40] S. Datta, *Electronic Transport in Mesoscopic Systems*, 1st ed. Cambridge University Press, 1995. doi: 10.1017/CBO9780511805776.

[41] M. Poljak, *Kvantni transport na nanoskali*. Zagreb: Element, 2023.

[42] M. Pourfath, *The Non-Equilibrium Green's Function Method for Nanoscale Device Simulation*. in Computational Microelectronics. Vienna: Springer Vienna, 2014. doi: 10.1007/978-3-7091-1800-9.

[43] D. Ryndyk, *Theory of Quantum Transport at Nanoscale: An Introduction*, vol. 184. in Springer Series in Solid-State Sciences, vol. 184. Cham: Springer International Publishing, 2016. doi: 10.1007/978-3-319-24088-6.

[44] P. R. Wallace, "The Band Theory of Graphite," *Phys. Rev.*, vol. 71, no. 9, pp. 622–634, May 1947, doi: 10.1103/PhysRev.71.622.

[45] K. S. Novoselov, "Electric Field Effect in Atomically Thin Carbon Films," *Science*, vol. 306, no. 5696, pp. 666–669, Oct. 2004, doi: 10.1126/science.1102896.

[46] K. S. Novoselov *et al.*, "Two-dimensional atomic crystals," *Proc. Natl. Acad. Sci. U. S. A.*, vol. 102, no. 30, pp. 10451–10453, Jul. 2005, doi: 10.1073/pnas.0502848102.

[47] S. Zeng, Z. Tang, C. Liu, and P. Zhou, “Electronics based on two-dimensional materials: Status and outlook,” *Nano Res.*, vol. 14, no. 6, pp. 1752–1767, Jun. 2021, doi: 10.1007/s12274-020-2945-z.

[48] Y. Ouyang, Y. Yoon, and J. Guo, “Scaling Behaviors of Graphene Nanoribbon FETs: A Three-Dimensional Quantum Simulation Study,” *Electron Devices IEEE Trans. On*, vol. 54, no. 9, pp. 2223–2231, Sep. 2007, doi: 10.1109/TED.2007.902692.

[49] A. Betti, G. Fiori, and G. Iannaccone, “Atomistic Investigation of Low-Field Mobility in Graphene Nanoribbons,” *IEEE Trans. Electron Devices*, vol. 58, no. 9, pp. 2824–2830, Sep. 2011, doi: 10.1109/TED.2010.2100045.

[50] S. Kaneko, H. Tsuchiya, Y. Kamakura, N. Mori, and M. Ogawa, “Theoretical performance estimation of silicene, germanene, and graphene nanoribbon field-effect transistors under ballistic transport,” *Appl. Phys. Express*, vol. 7, no. 3, p. 035102, Mar. 2014, doi: 10.7567/APEX.7.035102.

[51] M. Poljak, “Electron Mobility in Defective Nanoribbons of Monoelemental 2D Materials,” *IEEE Electron Device Lett.*, vol. 41, no. 1, pp. 151–154, Jan. 2020, doi: 10.1109/LED.2019.2952661.

[52] M. Poljak and M. Matić, “Bandstructure and Size-Scaling Effects in the Performance of Monolayer Black Phosphorus Nanodevices,” *Materials*, vol. 15, no. 1, p. 243, Dec. 2021, doi: 10.3390/ma15010243.

[53] T. Chowdhury, E. C. Sadler, and T. J. Kempa, “Progress and Prospects in Transition-Metal Dichalcogenide Research Beyond 2D,” *Chem. Rev.*, vol. 120, no. 22, pp. 12563–12591, Nov. 2020, doi: 10.1021/acs.chemrev.0c00505.

[54] C. Chen *et al.*, “Sub-10-nm graphene nanoribbons with atomically smooth edges from squashed carbon nanotubes,” *Nat. Electron.*, vol. 4, no. 9, pp. 653–663, Sep. 2021, doi: 10.1038/s41928-021-00633-6.

[55] H. S. Wang *et al.*, “Towards chirality control of graphene nanoribbons embedded in hexagonal boron nitride,” *Nat. Mater.*, vol. 20, no. 2, pp. 202–207, Feb. 2021, doi: 10.1038/s41563-020-00806-2.

[56] M. C. Watts *et al.*, “Production of phosphorene nanoribbons,” *Nature*, vol. 568, no. 7751, pp. 216–220, Apr. 2019, doi: 10.1038/s41586-019-1074-x.

[57] “‘IEEE Intl. Roadmap for Devices and Systems (IRDS), 2022 Update.’ https://irds.ieee.org/.”

[58] I. Meric, M. Y. Han, A. F. Young, B. Ozyilmaz, P. Kim, and K. L. Shepard, “Current saturation in zero-bandgap, top-gated graphene field-effect transistors,” *Nat. Nanotechnol.*, vol. 3, no. 11, pp. 654–659, Nov. 2008, doi: 10.1038/nnano.2008.268.

[59] M. Lukosius *et al.*, “Metal-Free CVD Graphene Synthesis on 200 mm Ge/Si(001) Substrates,” *ACS Appl. Mater. Interfaces*, vol. 8, no. 49, pp. 33786–33793, Dec. 2016, doi: 10.1021/acsami.6b11397.

[60] J. Xi, M. Long, L. Tang, D. Wang, and Z. Shuai, “First-principles prediction of charge mobility in carbon and organic nanomaterials,” *Nanoscale*, vol. 4, no. 15, p. 4348, 2012, doi: 10.1039/c2nr30585b.

[61] F. Schwierz, “Graphene transistors,” *Nat. Nanotechnol.*, vol. 5, no. 7, pp. 487–496, Jul. 2010, doi: 10.1038/nnano.2010.89.

[62] Y.-W. Son, M. L. Cohen, and S. G. Louie, “Energy Gaps in Graphene Nanoribbons,” *Phys. Rev. Lett.*, vol. 97, no. 21, p. 216803, Nov. 2006, doi: 10.1103/PhysRevLett.97.216803.

[63] Z. Wu and J. Hao, “Electrical transport properties in group-V elemental ultrathin 2D layers,” *Npj 2D Mater. Appl.*, vol. 4, no. 1, pp. 1–13, Mar. 2020, doi: 10.1038/s41699-020-0139-x.

[64] H. Liu *et al.*, “Phosphorene: An Unexplored 2D Semiconductor with a High Hole Mobility,” *ACS Nano*, vol. 8, no. 4, pp. 4033–4041, Apr. 2014, doi: 10.1021/nn501226z.
[65] M. Pumera and Z. Sofer, “2D Monoelemental Arsenene, Antimonene, and Bismuthene: Beyond Black Phosphorus,” *Adv. Mater.*, vol. 29, no. 21, p. 1605299, 2017, doi: 10.1002/adma.201605299.
[66] J. Qiao, X. Kong, Z.-X. Hu, F. Yang, and W. Ji, “High-mobility transport anisotropy and linear dichroism in few-layer black phosphorus,” *Nat. Commun.*, vol. 5, no. 1, p. 4475, Dec. 2014, doi: 10.1038/ncomms5475.
[67] G. Pizzi, M. Gibertini, E. Dib, N. Marzari, G. Iannaccone, and G. Fiori, “Performance of arsenene and antimonene double-gate MOSFETs from first principles,” *Nat. Commun.*, vol. 7, no. 1, p. 12585, Nov. 2016, doi: 10.1038/ncomms12585.
[68] S. Zhang *et al.*, “Recent progress in 2D group-VA semiconductors: from theory to experiment,” *Chem. Soc. Rev.*, vol. 47, no. 3, Art. no. 3, 2018, doi: 10.1039/C7CS00125H.
[69] S. Zhang *et al.*, “Semiconducting Group 15 Monolayers: A Broad Range of Band Gaps and High Carrier Mobilities,” *Angew. Chem.*, vol. 128, no. 5, pp. 1698–1701, Jan. 2016, doi: 10.1002/ange.201507568.
[70] J.-A. Yan, M. A. D. Cruz, B. Cook, and K. Varga, “Structural, electronic and vibrational properties of few-layer 2H- and 1T-TaSe2,” *Sci. Rep.*, vol. 5, no. 1, p. 16646, Nov. 2015, doi: 10.1038/srep16646.
[71] Q. H. Wang, K. Kalantar-Zadeh, A. Kis, J. N. Coleman, and M. S. Strano, “Electronics and optoelectronics of two-dimensional transition metal dichalcogenides,” *Nat. Nanotechnol.*, vol. 7, no. 11, pp. 699–712, Nov. 2012, doi: 10.1038/nnano.2012.193.
[72] Q. Zhao, Y. Guo, K. Si, Z. Ren, J. Bai, and X. Xu, “Elastic, electronic, and dielectric properties of bulk and monolayer ZrS_2, $ZrSe_2$, HfS_2, $HfSe_2$ from van der Waals density-functional theory,” *Phys. Status Solidi B*, vol. 254, no. 9, p. 1700033, 2017, doi: 10.1002/pssb.201700033.
[73] W. Zhang, Z. Huang, W. Zhang, and Y. Li, “Two-dimensional semiconductors with possible high room temperature mobility,” *Nano Res.*, vol. 7, no. 12, pp. 1731–1737, Dec. 2014, doi: 10.1007/s12274-014-0532-x.
[74] A. Afzalian and G. Pourtois, “ATOMOS: An ATomistic MOdelling Solver for dissipative DFT transport in ultra-scaled $HfS\ _2$ and Black phosphorus MOSFETs,” in *2019 International Conference on Simulation of Semiconductor Processes and Devices (SISPAD)*, Udine, Italy: IEEE, Sep. 2019, pp. 1–4. doi: 10.1109/SISPAD.2019.8870436.
[75] T. Kanazawa *et al.*, “Few-layer HfS_2 transistors,” *Sci. Rep.*, vol. 6, no. 1, p. 22277, Mar. 2016, doi: 10.1038/srep22277.
[76] K. Xu *et al.*, “Toward High-Performance Top-Gate Ultrathin HfS_2 Field-Effect Transistors by Interface Engineering,” *Small*, vol. 12, no. 23, pp. 3106–3111, Jun. 2016, doi: 10.1002/smll.201600521.
[77] M. J. Mleczko *et al.*, “$HfSe_2$ and $ZrSe_2$: Two-dimensional semiconductors with native high-κ oxides,” *Sci. Adv.*, vol. 3, no. 8, p. e1700481, Aug. 2017, doi: 10.1126/sciadv.1700481.
[78] K. Xu *et al.*, “Toward High-Performance Top-Gate Ultrathin HfS_2 Field-Effect Transistors by Interface Engineering,” *Small*, vol. 12, no. 23, pp. 3106–3111, 2016, doi: 10.1002/smll.201600521.
[79] H. Y. Lv *et al.*, “Edge-controlled half-metallic ferromagnetism and direct-gap semiconductivity in ZrS_2 nanoribbons,” *RSC Adv.*, vol. 7, no. 53, pp. 33408–33412, Jun. 2017, doi: 10.1039/C7RA05362B.

[80] M. Ghaedsharafi, M. R. Moslemi, and F. Pesaran, “The Influence of Edge Atoms and Vacancy Defects on Different Types of $HfSe_2$ Nanoribbons,” *J. Electron. Mater.*, vol. 53, no. 2, pp. 969–978, Feb. 2024, doi: 10.1007/s11664-023-10787-y.

[81] S. Eskandari, S. K. Khorrami, and M. Berahman, “Field-effect transistor based on the zigzag $ZrSe_2$ nanoribbons,” *Appl. Phys. A*, vol. 129, no. 12, p. 823, Nov. 2023, doi: 10.1007/s00339-023-07057-3.

[82] M. Matić and M. Poljak, “Ballistic Performance of Quasi-One-Dimensional Hafnium Disulfide Field-Effect Transistors,” *Electronics*, vol. 13, no. 6, Art. no. 6, Jan. 2024, doi: 10.3390/electronics13061048.

[83] F. Li, X. Liu, Y. Wang, and Y. Li, “Germanium monosulfide monolayer: a novel two-dimensional semiconductor with a high carrier mobility,” *J. Mater. Chem. C*, vol. 4, no. 11, pp. 2155–2159, 2016, doi: 10.1039/C6TC00454G.

[84] Y. Ding *et al.*, “High-Performance Ballistic Quantum Transport of Sub-10 nm Monolayer GeS Field-Effect Transistors,” *ACS Appl. Electron. Mater.*, vol. 3, no. 3, pp. 1151–1161, Mar. 2021, doi: 10.1021/acsaelm.0c01019.

[85] M. Nakamura, H. Nakamura, Y. Matsushita, K. Shimamura, and N. Ohashi, “Growth of germanium monosulfide (GeS) single crystal by vapor transport from molten GeS source using a two-zone horizontal furnace,” *J. Cryst. Growth*, vol. 547, p. 125813, Oct. 2020, doi: 10.1016/j.jcrysgro.2020.125813.

[86] Y. Mao, N. Chen, T. Deng, and Z. Lan, “Two-dimensional GeS synthesized by one-step space-confined APCVD and its self-powered photodetector,” *Phys. B Condens. Matter*, vol. 685, p. 415984, Jul. 2024, doi: 10.1016/j.physb.2024.415984.

[87] M. Matić and M. Poljak, “*Ab Initio* Quantum Transport Simulations of Monolayer GeS Nanoribbons,” *Solid-State Electron.*, p. 108460, 2022, doi: https://doi.org/10.1016/j.sse.2022.108460.

[88] M. Matić and M. Poljak, “Electronic, transport and ballistic device properties of quasi-one-dimensional GeS,” *J. Comput. Electron.*, May 2023, doi: 10.1007/s10825-023-02054-4.

[89] R. Li, H. Cao, and J. Dong, “Electronic properties of group-IV monochalcogenide nanoribbons: Studied from first-principles calculations,” *Phys. Lett. A*, vol. 381, no. 44, pp. 3747–3753, Nov. 2017, doi: 10.1016/j.physleta.2017.09.048.

[90] W. Van Roosbroeck, “Theory of the flow of electrons and holes in germanium and other semiconductors,” *Bell Syst. Tech. J.*, vol. 29, no. 4, pp. 560–607, Oct. 1950, doi: 10.1002/j.1538-7305.1950.tb03653.x.

[91] P. Giannozzi *et al.*, “QUANTUM ESPRESSO: a modular and open-source software project for quantum simulations of materials,” *J. Phys. Condens. Matter*, vol. 21, no. 39, p. 395502, Sep. 2009, doi: 10.1088/0953-8984/21/39/395502.

[92] P. Giannozzi *et al.*, “Advanced capabilities for materials modelling with Quantum ESPRESSO,” *J. Phys. Condens. Matter*, vol. 29, no. 46, p. 465901, Nov. 2017, doi: 10.1088/1361-648X/aa8f79.

[93] P. C. Martin and J. Schwinger, “Theory of Many-Particle Systems. I,” *Phys. Rev.*, vol. 115, no. 6, pp. 1342–1373, Sep. 1959, doi: 10.1103/PhysRev.115.1342.

[94] L. P. Kadanoff and G. Baym, *Quantum statistical mechanics: Green’s function methods in equilibrium and nonequilibrium problems*. W.A. Benjamin, New York, 1962.

[95] L. V. Keldysh, “Diagram technique for nonequilibrium processes,” in *Selected Papers of Leonid V Keldysh*, WORLD SCIENTIFIC, 2023, pp. 47–55. doi: 10.1142/9789811279461_0007.

[96] D. J. Thouless and S. Kirkpatrick, “Conductivity of the disordered linear chain,” *J. Phys. C Solid State Phys.*, vol. 14, no. 3, p. 235, Jan. 1981, doi: 10.1088/0022-3719/14/3/007.

[97] M. P. L. Sancho, J. M. L. Sancho, and J. Rubio, “Quick iterative scheme for the calculation of transfer matrices: application to Mo (100),” *J. Phys. F Met. Phys.*, vol. 14, no. 5, p. 1205, May 1984, doi: 10.1088/0305-4608/14/5/016.

[98] M. Matic, M. Leljak, and M. Poljak, “Estimating OFF-state Leakage in Silicene Nanoribbon MOSFETs from Complex Bandstructure,” in *2021 44th International Convention on Information, Communication and Electronic Technology (MIPRO)*, Opatija, Croatia: IEEE, Sep. 2021, pp. 85–89. doi: 10.23919/MIPRO52101.2021.9596876.

[99] A. Szabo and M. Luisier, “Under-the-Barrier Model: An Extension of the Top-of-the-Barrier Model to Efficiently and Accurately Simulate Ultrascaled Nanowire Transistors,” *IEEE Trans. Electron Devices*, vol. 60, no. 7, pp. 2353–2360, Jul. 2013, doi: 10.1109/TED.2013.2263386.

[100] D. R. Hartree, “The Wave Mechanics of an Atom with a Non-Coulomb Central Field. Part I. Theory and Methods,” *Math. Proc. Camb. Philos. Soc.*, vol. 24, no. 1, pp. 89–110, Jan. 1928, doi: 10.1017/S0305004100011919.

[101] V. Fock, “Näherungsmethode zur Lösung des quantenmechanischen Mehrkörperproblems,” *Z. Für Phys.*, vol. 61, no. 1, pp. 126–148, Jan. 1930, doi: 10.1007/BF01340294.

[102] P. Hohenberg and W. Kohn, “Inhomogeneous Electron Gas,” *Phys. Rev.*, vol. 136, no. 3B, pp. B864–B871, Nov. 1964, doi: 10.1103/PhysRev.136.B864.

[103] W. Kohn and L. J. Sham, “Self-Consistent Equations Including Exchange and Correlation Effects,” *Phys. Rev.*, vol. 140, no. 4A, pp. A1133–A1138, Nov. 1965, doi: 10.1103/PhysRev.140.A1133.

[104] J. P. Perdew, K. Burke, and M. Ernzerhof, “Generalized Gradient Approximation Made Simple,” *Phys. Rev. Lett.*, vol. 77, no. 18, pp. 3865–3868, Oct. 1996, doi: 10.1103/PhysRevLett.77.3865.

[105] J. Heyd, G. E. Scuseria, and M. Ernzerhof, “Erratum: ‘Hybrid functionals based on a screened Coulomb potential’ [J. Chem. Phys. 118, 8207 (2003)],” *J. Chem. Phys.*, vol. 124, no. 21, p. 219906, Jun. 2006, doi: 10.1063/1.2204597.

[106] J. C. Slater, “A Simplification of the Hartree-Fock Method,” *Phys. Rev.*, vol. 81, no. 3, pp. 385–390, Feb. 1951, doi: 10.1103/PhysRev.81.385.

[107] G. H. Wannier, “The Structure of Electronic Excitation Levels in Insulating Crystals,” *Phys. Rev.*, vol. 52, no. 3, pp. 191–197, Aug. 1937, doi: 10.1103/PhysRev.52.191.

[108] A. A. Mostofi, J. R. Yates, Y.-S. Lee, I. Souza, D. Vanderbilt, and N. Marzari, “wannier90: A tool for obtaining maximally-localised Wannier functions,” *Comput. Phys. Commun.*, vol. 178, no. 9, pp. 685–699, May 2008, doi: 10.1016/j.cpc.2007.11.016.

[109] N. Marzari, A. A. Mostofi, J. R. Yates, I. Souza, and D. Vanderbilt, “Maximally localized Wannier functions: Theory and applications,” *Rev. Mod. Phys.*, vol. 84, no. 4, pp. 1419–1475, Oct. 2012, doi: 10.1103/RevModPhys.84.1419.

[110] P. Löwdin, “On the Non-Orthogonality Problem Connected with the Use of Atomic Wave Functions in the Theory of Molecules and Crystals,” *J. Chem. Phys.*, vol. 18, no. 3, pp. 365–375, Mar. 1950, doi: 10.1063/1.1747632.

[111] C. Stieger and M. Luisier, “Winterface: An Interface from Wannier90 to Quantum Transport,” Jul. 12, 2020, *arXiv*: arXiv:2007.04268. doi: 10.48550/arXiv.2007.04268.

[112] M. Matić and M. Poljak, “Electronic, transport and ballistic device properties of quasi-one-dimensional GeS,” *J. Comput. Electron.*, vol. 22, no. 5, pp. 1350–1362, Oct. 2023, doi: 10.1007/s10825-023-02054-4.

[113] M. Matić and M. Poljak, "*Ab initio* quantum transport simulations of monolayer GeS nanoribbons," *Solid-State Electron.*, vol. 197, p. 108460, Nov. 2022, doi: 10.1016/j.sse.2022.108460.

[114] M. Matić and M. Poljak, "Validity of the Ballistic Top-of-the-Barrier Model for FETs Based on 2D Material Nanoribbons," in *2024 47th MIPRO ICT and Electronics Convention (MIPRO)*, May 2024, pp. 1596–1601. doi: 10.1109/MIPRO60963.2024.10569245.

[115] M. Matić and M. Poljak, "Transport Properties and Device Performance of Quasi-One-Dimensional MoS_2 FETs," in *2023 46th MIPRO ICT and Electronics Convention (MIPRO)*, May 2023, pp. 168–172. doi: 10.23919/MIPRO57284.2023.10159951.

[116] I. Prevarić, M. Matić, and M. Poljak, "Tunneling Attenuation and Leakage Current in MoS_2 Nanoribbon MOSFETs," in *2023 46th MIPRO ICT and Electronics Convention (MIPRO)*, May 2023, pp. 163–167. doi: 10.23919/MIPRO57284.2023.10159745.

Abbreviations

1D	One-Dimensional
2D	Two-Dimensional
2DM	Two-Dimensional Material
AC	Armchair
BTE	Boltzmann Transport Equation
BZ	Brillouin Zone
CBM	Conduction Band Minimum
CMOS	Complementary-Metal-Oxide-Semiconductor
DD	Drift-Diffusion
DFT	Density Functional Theory
DOS	Density of States
FET	Field-Effect Transistor
GAA	Gate-All-Around
GGA	Generalized Gradient Approximation
IRDS	International Roadmap for Devices and Systems
KS	Kohn-Sham
LDA	Local Density Approximation
LDOS	Local Density of States
MBC	Multi-Bridge-Channel
MLWF	Maximally Localized Wannier Functions
MX_2	Transition Metal Dichalcogenide
MX_2NR	Transition Metal Dichalcogenide Nanoribbon

NEGF	Non-Equilibrium Green's Function
OBC	Open Boundary Condition
PBE	Perdew-Burke-Ernzerhof
PP	Pseudo-Potential
QUDEN	Quantum-transport Device Engineering in Nanoelectronics
S/D	Source and Drain
TMD	Transition Metal Dichalcogenide
TOB	Top-Of-The-Barrier
UTB	Under-The-Barrier
VBM	Valence Band Maximum
WF	Wannier Functions
WKB	Wentzel–Kramers–Brillouin
XC	Exchange-Correlation
ZZ	Zigzag

Publications

Publication 1

Intrinsic Performance Limits of Extremely Scaled Field-Effect Transistors Based on MX_2 (M = {Zr, Hf}, X = {S, Se}) Nanoribbons

M. Matić and M. Poljak, “Intrinsic performance limits of extremely scaled field-effect transistors based on MX_2 (M = {Zr, Hf}, X = {S, Se}) nanoribbons,” *Journal of Applied Physics*, vol. 136, no. 8, p. 084307, Aug. 2024.
doi: 10.1063/5.0224088

– 10 pages

Journal of
Applied Physics
ARTICLE
pubs.aip.org/aip/jap

Intrinsic performance limits of extremely scaled field-effect transistors based on MX_2 (M = {Zr, Hf}, X = {S, Se}) nanoribbons

Cite as: J. Appl. Phys. **136**, 084307 (2024); doi: 10.1063/5.0224088
Submitted: 19 June 2024 · Accepted: 15 August 2024 ·
Published Online: 28 August 2024

Mislav Matić and Mirko Poljak[a)]

AFFILIATIONS

University of Zagreb, Faculty of Electrical Engineering and Computing, Computational Nanoelectronics Group,
Unska 3, 10000 Zagreb, Croatia

[a)]**Author to whom correspondence should be addressed:** mirko.poljak@fer.unizg.hr

ABSTRACT

We investigate the MX_2 (M = {Hf, Zr}, X = {S, Se}) transition metal dichalcogenides patterned into armchair (AC) and zigzag (ZZ) nanoribbons (NRs) as potential channel materials in future logic field-effect devices. *Ab initio* quantum transport simulations are employed to assess the electronic, transport, and ballistic field-effect transistor (FET) properties of devices with such quasi-one-dimensional channels. We report a non-monotonic scaling behavior of MX_2NR properties due to strong quantum confinement effects, which is reflected in a strong dependence of the ON-state current (I_{ON}) of MX_2NR FETs on the nanoribbon configuration. The ~2 nm-wide $HfSe_2$ and $ZrSe_2$ AC-PFETs have the highest I_{ON} of up to 2.6 mA/μm at 10 nA/μm OFF-state current. Surprisingly, MX_2NR ZZ-NFETs exhibit a current increase of up to 70% when channel width is scaled down, with I_{ON} reaching 2.2 mA/μm in ~2 nm-wide devices. The high ON-state performance is a direct consequence of high carrier injection velocity, which is explained by analyzing the band structure, transmission, and density of states. We demonstrate that nanostructured MX_2 materials can be promising candidates for future logic transistors based on multi-nanowire architectures.

I. INTRODUCTION

Multi-bridge channel (MBC) FETs with bulk-silicon nanosheets or nanowires represent current state-of-the-art device technology.[1–3] However, silicon is reaching its limits and new materials are needed to extend Moore's law. 2D materials (2DMs) are one of the most promising candidates to replace silicon due to excellent electronic and transport properties,[4,5] despite the currently unresolved problem of high contact resistance, which greatly affects the device performance.[6–8] The 2DMs can be patterned into quasi-one-dimensional (quasi-1D) nanoribbons (NRs),[9,10] which could be used in MBC FETs[11] [see Fig. 1(a)] and enable high integration density with additional performance tuning by quantum confinement effects. Experimental work on NRs is limited to a few materials due to the high complexity of fabrication with the main challenge being the reliable control of crystal phase, edge structure, and dimensionality.[12] Nevertheless, continuous progress in this field affirms fabrication potential and makes nanoribbons interesting structures for future nanodevices.[13–15] In this work, we focus on transition metal dichalcogenides (TMDs) MX_2 (M = {Zr, Hf}, X = {S, Se}) as some of the most promising 2DMs,[16–18] with a reported high compatibility of Hf- and Zr-based TMDs to high-*k* oxides (HfO_2, ZrO_2).[19,20] Potential of 2D MX_2 TMDs has been studied in depth[17,21,22] by advanced theoretical calculations and experimental work was reported in Refs. 23 and 24. The MX_2 nanoribbon (MX_2NR) research is quite limited with electronic properties studied for ZrS_2NRs,[25] $HfSe_2NRs$.[26] As for MX_2NR FETs, only single $ZrSe_2NR$ FET was studied in Ref. 27 with our group's initial study on zigzag HfS_2NR FETs reported in Ref. 28, which showed potential of these devices for future logic devices. Therefore, we expand our research to study all potential TMD materials similar to HfS_2NRs that show semiconducting behavior. We report in detail the electronic, transport, and ballistic device characteristics, as intrinsic upper limits to device performance, for

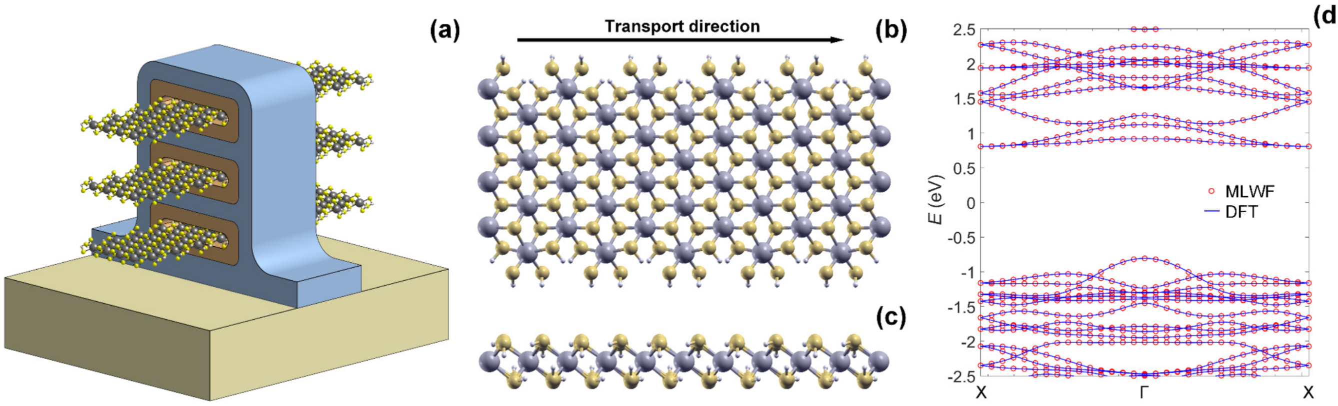

FIG. 1. (a) Model of a MBC FET with nanoribbon channel. (b) Top view and (c) side view of AC-MX_2NR. (d) MLWF and DFT bandstructure of AC-ZrS_2NR.

armchair (AC) and zigzag (ZZ) MX_2NR FETs in eight different configurations defined by the NR material and edge type. We show AC-PFETs and ZZ-NFETs driving current increases with downscaling with maximum for ∼2 nm-wide NRs while AC-NFET and ZZ-PFET show performance degradation with downscaling. To explore these findings, we investigate the density of states, transmission, and injection velocity of AC MX_2NRs since ZZ-counterparts were explored previously in detail.[28] Furthermore, we explore interdependence of current to various properties such as charge density, injection velocity, band structure effective mass and effective transport mass where we show that the performance is mostly determined by injection velocity and transport effective mass. Finally, we compare AC- and ZZ- MX_2NR NFETs and PFETs to the requirements of the International Roadmap of Devices and Systems (IRDS) and other 2DMs. We show that IRDS current requirement for both N- and PFET is met by ZZ-FETs with HfS_2NR and $HfSe_2NR$ channel of all widths, ZZ-ZrS_2NRs with $W < 3$ nm and ZZ-$ZrSe_2NRs$ with $W < 6$ nm while only PFET devices with AC nanoribbons meet IRDS I_{ON} requirements.

II. METHODOLOGY

Supercells of AC-MX_2NRs [Figs. 1(b) and 1(c)] and ZZ-MX_2NRs are constructed based on the number of 2D MX_2 unit cells (NW, from 2 to 10) repeated along the nanoribbon width (W). This results in W from 0.9 to 4 nm for AC-MX_2NRs, and 1.3 to 6.7 nm for ZZ-MX_2NRs. The Hamiltonians are found using the *ab initio* density functional theory (DFT) Quantum Espresso (QE) program[29] with plane-augmented wave (PAW) pseudopotentials and Perdew, Burke, and Ernzerhof (PBE)[30] exchange correlation (XC) functional. Interactions between the layers are excluded by adding a vacuum of 20 Å in confined directions. A $1 \times 15 \times 1$ Monkhorst–Pack k-point grid[31] with 15 points in the transport direction is used to sample the Brillouin zone. The kinetic energy cutoff is set at 1360 eV, while the convergence threshold for the ionic forces is set to 10^{-3} eV/Å and 10^{-4} eV for the total energy. The DFT Hamiltonians are then transformed into a space-localized basis using maximally-localized Wannier functions (MLWFs)[32] implemented in the Wannier90 tool.[33] Within Wannier90, trial orbitals are d orbitals for Zr/Hf atoms and p orbitals for S/Se atoms. The MLWF Hamiltonians are assessed by comparison of band structure calculated with DFT and MLWF, as reported in Fig. 1(d). The MLWF Hamiltonian matrices of MX_2NR supercells are extended in the transport direction to construct the total Hamiltonian of ∼15 nm-long nanoribbons that serve as the channel of MX_2NR FETs.

The ballistic top-of-the-barrier (ToB) FET model[34] is used to simulate N- and P-type single gate FETs with MX_2NR channels. The ToB model calculates the thermionic current while direct tunneling is negligible for a 15 nm-long device. Furthermore, as intrinsic limit is explored, there is no scattering and dissipation included in the simulation with contact resistance neglected as source and drain channels are considered ideal, i.e., of the same material as the channel. Although dissipative transport simulation is necessary for a complete assessment of device performance, previous studies show that carrier transport in sub-15 nm-long FETs is expected to be 75%–90% ballistic.[35–37] The transmission function and the density of states (DOS), which are the main inputs of the ToB FET model, are calculated using the non-equilibrium Green's function (NEGF) formalism[38,39] as implemented in our in-house code.[40,41] Main term in NEGF formalism is the retarded Green's function

$$G^R(E) = [(E + i0^+)I - H - \Sigma_S^R(E) - \Sigma_D^R(E)]^{-1}, \tag{1}$$

where H is the total channel Hamiltonian, while Σ_S^R and Σ_D^R are source/drain (S/D) contact self-energy matrices calculated using the Sancho–Rubio method.[42,43] Transmission is obtained using

$$T(E) = tr[\Gamma_S(E) G^R(E) \Gamma_D(E) G^A(E)], \tag{2}$$

where $\Gamma_{S,D} = -2\ \mathrm{Im}(\Sigma^R)$ are S/D contact broadening matrices. On the other hand, density of states is calculated using

$$DOS(E) = \frac{1}{\pi} tr[-2\mathrm{Im}(G^R(E))]. \tag{3}$$

The N- and PFETs with AC- and ZZ-MX_2NR channels are simulated with an ideal electrostatic gate control assumed for these atomically-thin channels leading to an ideal subthreshold slope (60 mV/dec at 300 K), an equivalent oxide thickness (EOT) of 1 nm, an S/D doping of 0.01 areal molar fraction, and a supply voltage (V_{DD}) of 0.7 V. The simulations of the MX_2NR FETs are performed with a common OFF-state current (I_{OFF}) of 10 nA/μm, as defined by the IEEE International Roadmap for Devices and Systems (IRDS) for high-performance logic devices.[44] The ON-state current (I_{ON}) is extracted at $V_{GS} = V_{DS} = V_{DD} = 0.7$ V. Finally, we set the EOT to 0.6 nm and compare the I_{ON} performance of MX_2NR FETs to maximum IRDS I_{ON} requirement with $I_{ON} = 1.979$ mA/μm, and other quasi-1D materials studied by either our or other groups.

III. RESULTS AND DISCUSSION

The band structure of the widest ($NW = 10$) and narrowest ($NW = 2$) MX_2NRs with AC and ZZ nanoribbons are shown in Figs. 2 and 3, respectively. The AC-MX_2NRs (Fig. 2) have an indirect bandgap and show qualitatively similar evolution of the band structure width and W downscaling which is accompanied by a decrease in the number of subbands near the conduction band minimum (CBM) and valence band maximum (VBM). On the other hand, ZZ-MX_2NRs (Fig. 3) exhibit a direct bandgap with subband crowding in the conduction band at the CBM for wider NRs. Moreover, two degenerate subbands are formed in the valence band of the 10-ZZ-MX_2NR due to edge effects,[28] and this degeneracy is generally broken in the narrowest ZZ-MX_2NRs due to strong quantum confinement. Our DFT calculations show that all AC and ZZ MX_2NRs are semiconductors which show qualitatively similar dispersions and band structure evolution features with W downscaling for the two (AC and ZZ) categories.

The bandgap (E_g) is extracted from the dispersions and its width-scaling dependence in AC and ZZ-MX_2NRs is shown in Fig. 4. E_g of all AC-MX_2NRs [Fig. 4(a)] increases by ∼0.45 eV when W is scaled from ∼4 to ∼1 nm. In terms of bandgap values, a ∼0.7 eV higher E_g is observed for S-based AC-MX_2NRs compared to their Se-based counterparts with the highest $E_g = 1.85$ eV observed for 1 nm-wide AC-HfS_2NR and lowest $E_g = 0.55$ eV for AC-$ZrSe_2$NRs with $W = 4$ nm. On the other hand, the bandgap of ZZ nanoribbons [Fig. 4(b)] is immune to width scaling, making it a good choice for robust NR FET design. Similarly to AC-MX_2NRs, S-based ZZ-MX_2NRs exhibit ∼0.5 eV higher E_g compared to Se-based ZZ-MX_2NRs with maximum of 1 eV for ZZ-HfS_2NRs and minimum of 0.35 eV for ZZ-$ZrSe_2$NRs.

The S-based MX_2NRs of both edge types exhibit bandgaps of at least 0.9 eV, which is enough to suppress band-to-band tunneling (BTBT) for V_{DD} under 0.7 V. On the other hand, Se-based MX_2NRs with ZZ edges exhibit a rather constant E_g of about

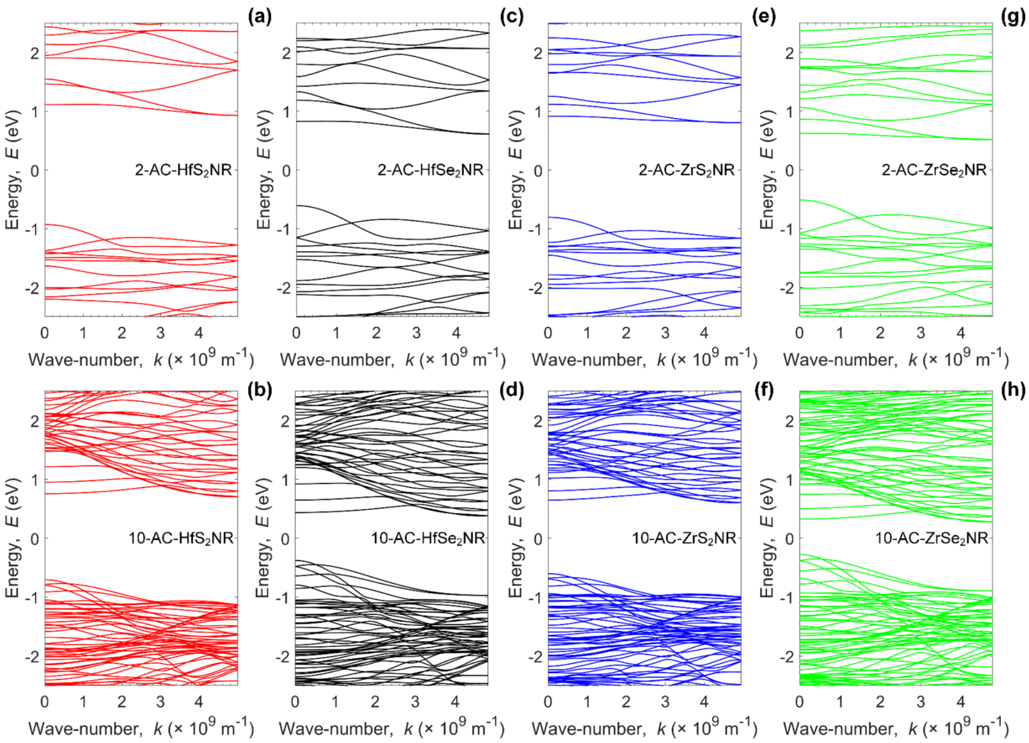

FIG. 2. Bandstructure of the (a) 2- and (b) 10-unit-cell-wide armchair HfS_2NR, (c) 2- and (d) 10-unit-cell-wide armchair $HfSe_2$NR, (e) 2- and (f) 10-unit-cell-wide armchair ZrS_2NR, and (g) 2- and (h) 10-unit-cell-wide armchair $ZrSe_2$NR.

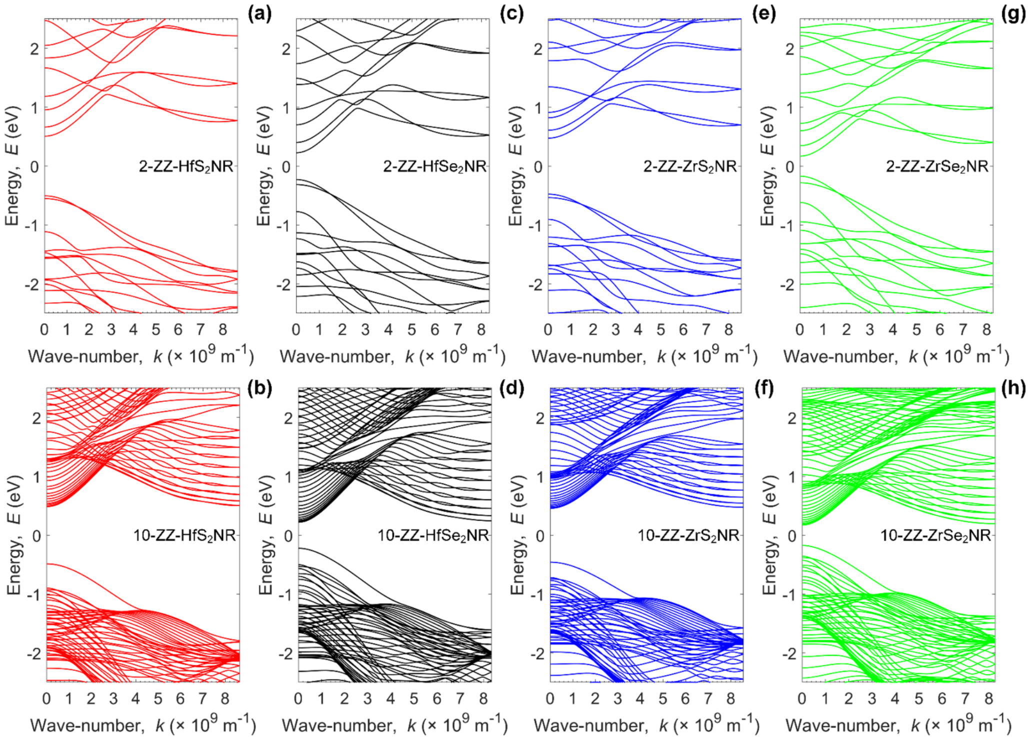

FIG. 3. Bandstructure of the (a) 2- and (b) 10-unit-cell-wide zigzag HfS$_2$NR, (c) 2- and (d) 10-unit-cell-wide zigzag HfSe$_2$NR, (e) 2- and (f) 10-unit-cell-wide zigzag ZrS$_2$NR, and (g) 2- and (h) 10-unit-cell-wide zigzag ZrSe$_2$NR.

0.4 eV, whereas for Se-based AC nanoribbons, one needs ultra-narrow widths to reach appropriate bandgaps. Nevertheless, we consider all these materials as potential candidates for future logic FETs in the following paragraphs because it is well established in the literature that PBE functionals underestimate the bandgap. A recent study[18] has shown that E_g obtained using the HSE06 functional is at least ~0.6 eV higher for S- and Se-based MX$_2$-enes than E_g calculated with the PBE functional.

The performance of N- and PFETs with AC- and ZZ-MX$_2$NR channels is evaluated through the ON-state current, which is shown in Fig. 5 for AC-MX$_2$NR FETs (AC-FETs) and ZZ-MX$_2$NR FETs (ZZ-FETs). All AC-NFETs exhibit I_{ON} of ~1 mA/μm for NRs with $W > 2.4$ nm, while downscaling decreases the I_{ON} up to 50% due to strong quantum confinement effects [Fig. 5(a)] with an exception for the narrowest HfX$_2$NRs which show surprising increase up to 30% due to quantum confinement effects. On the other hand, the I_{ON} of AC-PFETs [Fig. 5(b)] depends mostly on the chalcogenide, i.e., S and Se as their AC-PFET configurations show similar I_{ON} performance. We note that PFETs with AC HfSe$_2$ and ZrSe$_2$ nanoribbons as channels have ~30% higher I_{ON} than the S-based AC-PFETs. I_{ON} is relatively constant for $W > 3$ nm with ~2.4 mA/μm for Se-based and ~1.9 mA/μm for S-based devices. Scaling down the W shows surprising I_{ON} increase with the maximum for W of 2–2.5 nm, depending on the device with ~2.6 mA/μm for HfSe$_2$ and ZrSe$_2$ nanoribbon devices with ~2.1 mA/μm for HfS$_2$ and ZrS$_2$ nanoribbon devices. Further reduction in width decreases I_{ON} by ~30% in all AC-PFETs.

I_{ON} of ZZ-NFETs, reported in Fig. 5(c), shows that all devices exhibit surprising I_{ON} increase with downscaling. I_{ON} increases

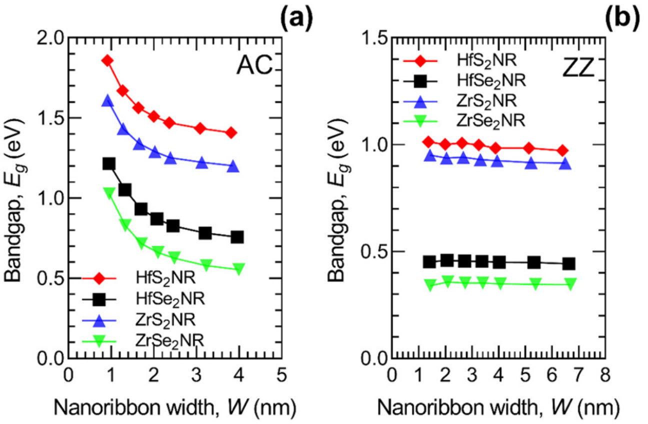

FIG. 4. Bandgap dependence on nanoribbon width of the investigated (a) armchair and (b) zigzag MX$_2$NRs.

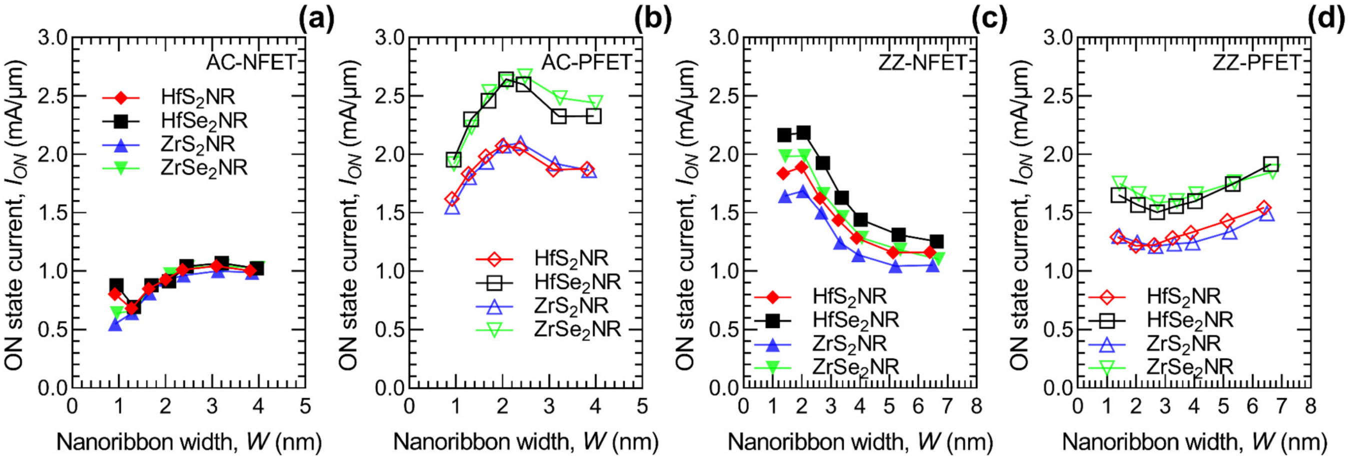

FIG. 5. ON-state current of armchair (a) NFETs and (b) PFETs, and zigzag (c) NFETs and (d) PFETs with various MX$_2$NR channels.

slightly for $W > 4$ nm with I_{ON} in the 1–1.25 mA/μm range. Further NR width scaling from 4 to 2 nm shows significant increase of I_{ON} up to 70% while for the narrowest ZZ-NFETs with 1 nm-wide MX$_2$NR channel performance marginally degrades. ZZ-HfSe$_2$NR NFETs exhibit the highest performance at given W and maximum I_{ON} of 2.2 mA/μm reported for ∼1–2 nm-wide ZZ-HfSe$_2$NR NFETs. ZZ-NFETs with HfS$_2$ and ZrSe$_2$ nanoribbon channels show similar I_{ON} performance, which is ∼10% lower compared to ZZ-NFETs with HfSe$_2$NR channels. The ZZ-ZrS$_2$NR NFETs exhibit the lowest I_{ON} with a maximum of 1.7 mA/μm for $W = 2$ nm. In contrast, as reported in Fig. 5(d) the ZZ-PFETs have a weakly decreasing I_{ON} when W is downscaled up to $W = 3$ nm and a slight increase of ∼10% when W is scaled from 3 to 1 nm. In the widest examined ZZ-NRs the drive current is 1.9 mA/μm for Se-based ZZ-PFETs and 1.5 mA/μm in S-based devices. The lowest performance is reported for $W = 3$ nm where HfSe$_2$ and ZrSe$_2$ exhibit I_{ON} ∼1.5 mA/μm while their S-based counterparts I_{ON} is ∼1.2 mA/μm. Similar to AC-PFETs, Se-based ZZ-PFETs exhibit 25% higher I_{ON} compared to devices with HfS$_2$ and ZrS$_2$ nanoribbon channels. The results show that the I_{ON} scaling behavior is mainly determined by the edges, i.e., the AC and ZZ edges. Therefore, the performance MX$_2$NR FETs and the I_{ON} behavior within each group are governed by the same physical effects with the only real difference being the magnitude.

The same principles apply to ZZ-MX$_2$NRs as to the previously studied ZZ-HfS$_2$NRs in Ref. 28. In short, we have shown that for ZZ-NFETs current of the wider NRs is mainly determined by the higher energy subbands, while for the narrower ones it is determined by single subband nearest to the CBM due to lower number of subbands near the CBM. On the other hand, the PFET performance is mainly attributed to two degenerate subbands in the VB of wide nanoribbons, which are dominant due to edge effects. Furthermore, scaling down NR width breaks the degeneracy and lowers the ZZ-PFET performance. Therefore, we focus on AC-MX$_2$NRs in this work.

We investigate the transport properties of AC-MX$_2$NRs on an example of HfSe$_2$NRs by studying the density of states, transmission and injection velocity. The DOS and transmission in CB and VB of HfSe$_2$NRs with various widths are shown in Fig. 6. The HfSe$_2$NR NFETs exhibit dense DOS in CB, as shown in Fig. 6(a), and scaling down the NR width increases the overall DOS near CBM which is accompanied by decrease of the number of Van Hove singularities (VHS) due to the lower number of available bands. Although the DOS is higher in narrower NRs, it is not supported by higher transmission [see Fig. 6(b)]. This is a direct consequence of lower curvature of dominant subbands (i.e., higher effective mass) in narrower NRs which ultimately lowers the performance of NFETs with AC edges. Wide HfSe$_2$NRs with $W > 3$ nm show interesting transmission near the CBM where it is 2 at the CBM which sharply decreases to 1 and again increases back to two within CBM + 0.01 eV. The narrowest NR with $W = 0.95$ nm has transmission 1 at the CBM which quickly rises to 2 at CBM + 0.01 eV. On the other hand, DOS curves in VB for AC-HfSe$_2$NRs exhibit much lower number of bands near VBM compared to CB. Scaling down the nanoribbon width decreases VHS number while DOS [see Fig. 6(c)] near VBM increases. Transmission is unity for all NRs up to VBM + 0.07 eV. The NRs with $W = 2.08$ nm and $W = 2.46$ nm have the lowest overall DOS up to VBM + 0.1 eV which is the most relevant region for transport.

Although the density of states and transmission encompass all the physics that governs the performance of AC NFETs and PFETs, differences in device behavior are not necessarily easy to explain using barely these two features. Therefore, we extract and examine the figures-of-merit that incorporate the DOS and transmission such as injection velocity, charge density, band structure effective mass and effective transport mass. First, we explore on the dependence of the injection velocity (v_{inj}) on the gate voltage (V_{GS}) in the range between the threshold voltage (∼0.2 V) and the supply voltage (0.7 V) for AC-NFETs and AC-PFETs with HfSe$_2$NR channel in Figs. 7(a) and 7(b), respectively. The AC-NFETs show almost no modulation with V_{GS} with the magnitude being directly correlated with the I_{ON} performance. For NRs with $W > 3$ nm, v_{inj} is ∼0.75×10^7 cm/s while for the $W = 1.33$ nm, which has the

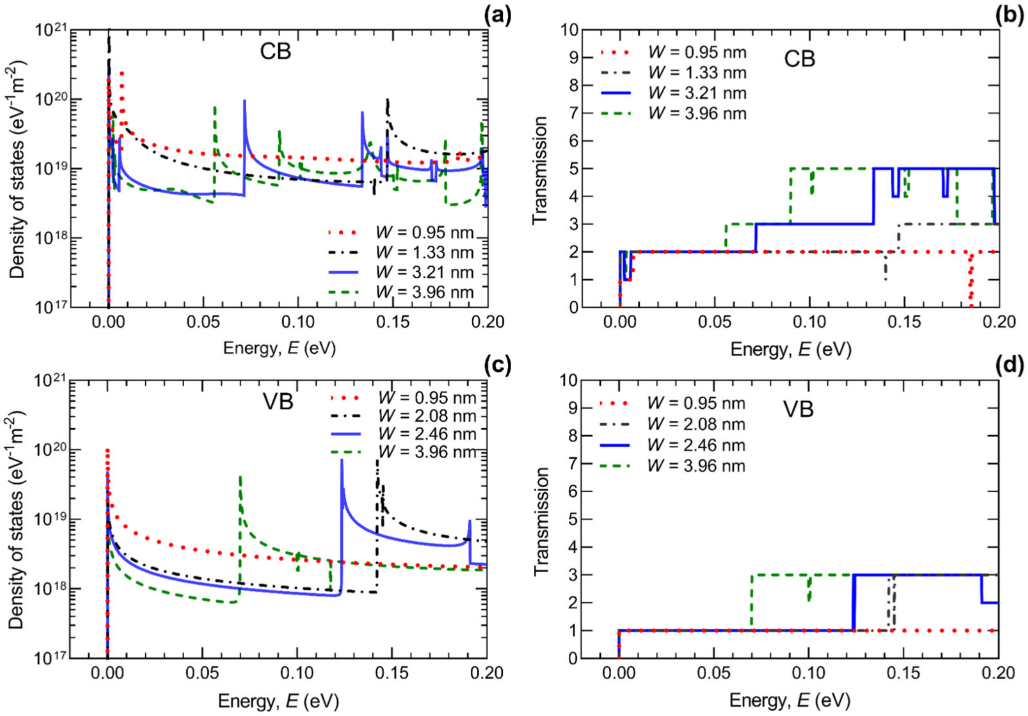

FIG. 6. DOS and transmission for (a), (b) CB and (c), (d) VB of AC-HfSe$_2$NRs of various widths.

lowest I_{ON}, $v_{inj} = 0.5 \times 10^7$ cm/s. The AC-PFETs show much more interesting v_{inj}. At threshold voltage, NRs with $W > 2$ nm show a similar v_{inj} of $\sim 1.45 \times 10^7$ cm/s while v_{inj} modulation with V_{GS} increase results with highest v_{inj} $\sim 2.05 \times 10^7$ cm/s at supply voltage for $W = 2.08$ nm and $W = 2.46$ nm. The narrowest NRs with $W = 0.95$ nm show the lowest v_{inj} and the lowest modulation with V_{GS} where v_{inj} is $\sim 1.5 \times 10^7$ cm/s at $V_{GS} = 0.7$ V. Similarly to AC-NFETs, I_{ON} directly corresponds to v_{inj} in the ON-state for AC-PFETs.

To affirm this, we plot the interdependence of the ON-state current, the ON-state charge density and the ON-state injection velocity in Fig. 8(a). I_{ON} is proportional to the ON-state injection velocity and inversely proportional to the ON-state charge density. PFETs generally exhibit higher v_{inj} and consequently higher I_{ON}

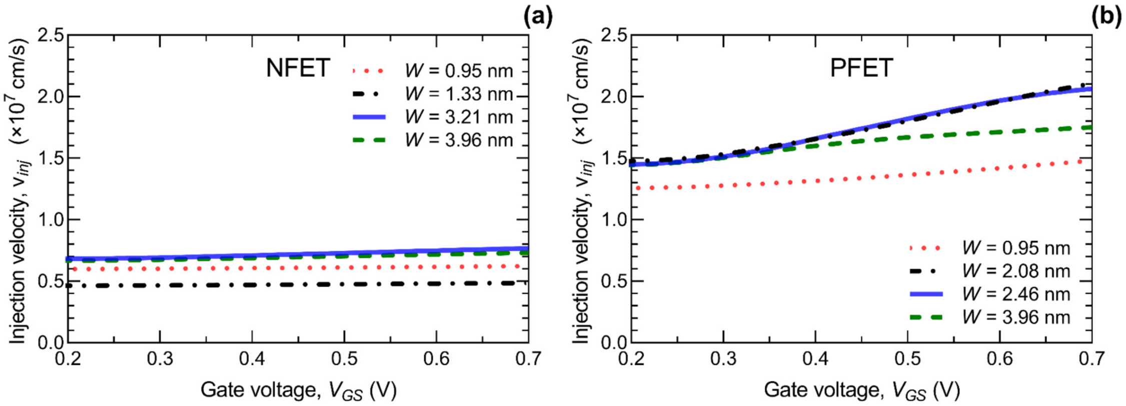

FIG. 7. Injection velocity gate voltage dependence of (a) n-type and (b) p-type armchair HfSe$_2$NR FETs for various widths.

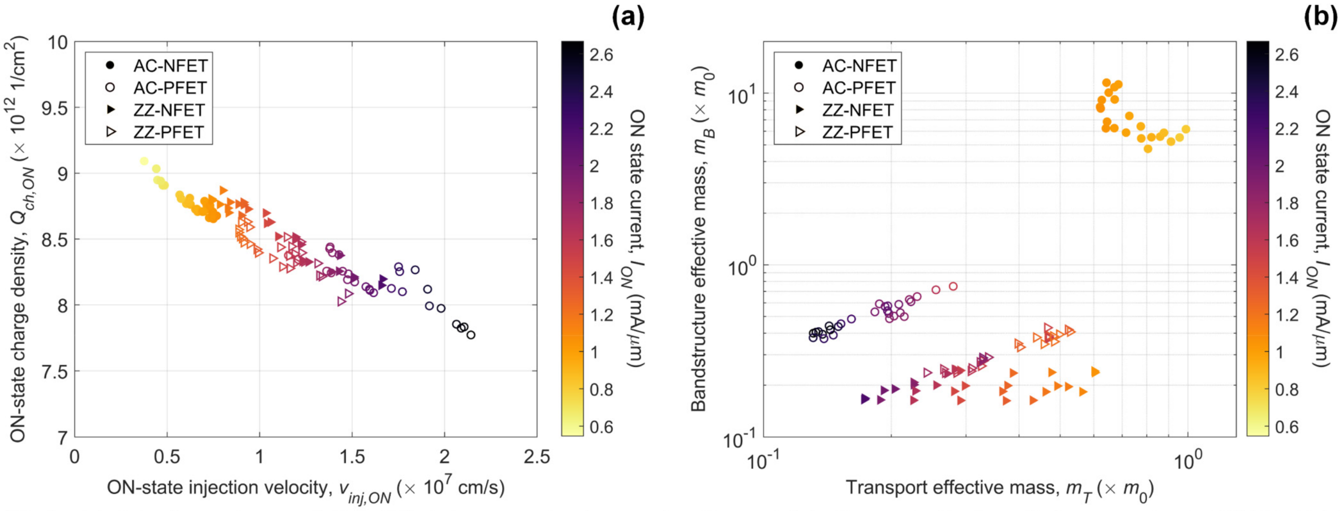

FIG. 8. (a) Interdependence of the ON-state current, charge density and injection velocity for all the examined MX_2NR FETs. (b) Interdependence of the ON-state current, bandstructure, and effective transport mass for all the examined MX_2NR FETs.

compared to NFETs with both AC and ZZ edges. Furthermore, in Fig. 8(b), we plot the interdependence of I_{ON}, band structure effective mass (m_B), and the effective transport mass (m_T). m_B of electrons and holes is extracted by a parabolic approximation of the subband closest to the CBM and VBM. m_T is calculated from the average thermal velocity that is extracted from the bias-dependence of the injection velocity in the quasi-1D channel,[45] as done in our previous work.[46] The low I_{ON} of AC-NFETs is directly caused by the highest m_T and m_B among all the studied devices, whereas the better performance of AC-PFETs is due to moderate m_B of 0.4–0.8m_0 combined with low $m_T < 0.3m_0$ and minimum of 0.14m_0 .On the other hand, most N- and PFETs with the ZZ-MX_2NR channels generally have lower m_B compared to their AC counterparts, and exhibit m_T in the 0.2–0.6m_0 range. The narrowest ZZ-NFETs in which I_{ON} increases considerably [Fig. 4(c)] also exhibit the smallest m_T of only 0.18m_0. This discussion demonstrates that m_T and m_B of all MX_2NR FETs, in combination with the 15-nm-long channel, should be large enough to suppress tunneling, which makes the ballistic I_{ON} a reliable figure-of-merit for these devices.

The comparison of our results with the IRDS I_{ON} requirement minimum of ∼2 mA/μm shows that most Se-based AC-PFETs with $W > 1.2$ nm and sub-2 nm-wide Se-based ZZ-NFETs meet the IRDS requirement. These devices are studied with EOT set to 1 nm and using high-κ dielectrics such as HfO_2 and ZrO_2 that exhibit $\epsilon_r > 20$ should enable EOT up to 0.5. Furthermore, these dielectrics have shown high compatibility with studied MX_2NRs which affirms the potential of these materials as logic device candidates. We compare I_{ON} of NFETs and PFETs with AC- and ZZ- MX_2NR channels in Fig. 9 with one hundred 2D potential candidates for logic devices studied in Ref. 17, AC- and ZZ GeSNRs,[40,41] and AC-MoS_2NRs[47] studied by our group. For a fair comparison, all devices are single-gate FETs with an EOT value of 0.6 nm, i.e., the same value used in previous comparisons and referenced literature. We group the data according to the MX_2NR channel material, as shown in Fig. 9.

None of the studied FETs with AC-MX_2NR channel fulfill the IRDS I_{ON} requirements for both N- and PFET devices. Although AC-PFETs exhibit $I_{ON} > 2.5$ mA/μm which is sufficient to meet the IRDS I_{ON} requirement, none of the AC-NFETs meet I_{ON} IRDS requirement. On the other hand, all NFETs and PFETs with Hf-based ZZ-MX_2NR channel meet the IRDS requirement while only ZZ-ZrS_2NRs with $W < 3$ nm and ZZ-$ZrSe_2$NRs with $W < 6$ nm meet the requirement with limiting factor being low performance of wide ZZ-NFETs. Furthermore, we compare studied devices to our previous works. Compared to AC and ZZ GeSNRs, only AC-GeSNRs with $W > 3$ nm show better NFET and PFET I_{ON} performance than most MX_2NR devices with the only exception of Se-based ZZ-MX_2NRs with $W < 3$ nm. In addition, the I_{ON} performance of all AC or ZZ MX_2NR FETs is superior to any AC-MoS_2NR FET. Finally, compared to 2D materials, AC and ZZ MX_2NR FETs perform better than ∼90% of the studied 2D materials. Compared to the 2D counterparts of the studied nanoribbons, e.g., HfS_2 and ZrS_2, the I_{ON} performance of nanoribbon FETs cannot match the 2D FETs. However, this is to be expected due to the strong quantum confinement effects along the width in ultra-narrow NRs. The performance is especially poor when compared against other most promising 2D materials such WS_2, Ge_2S_2, arsenene (As_4) and phosphorene (P_4). Nevertheless, MX_2NR FETs show adequate performance that affirms the potential of MX_2NRs as channel materials for future ultra-scaled FETs if the issues of high contact resistance in low-dimensional materials are solved.[48,49]

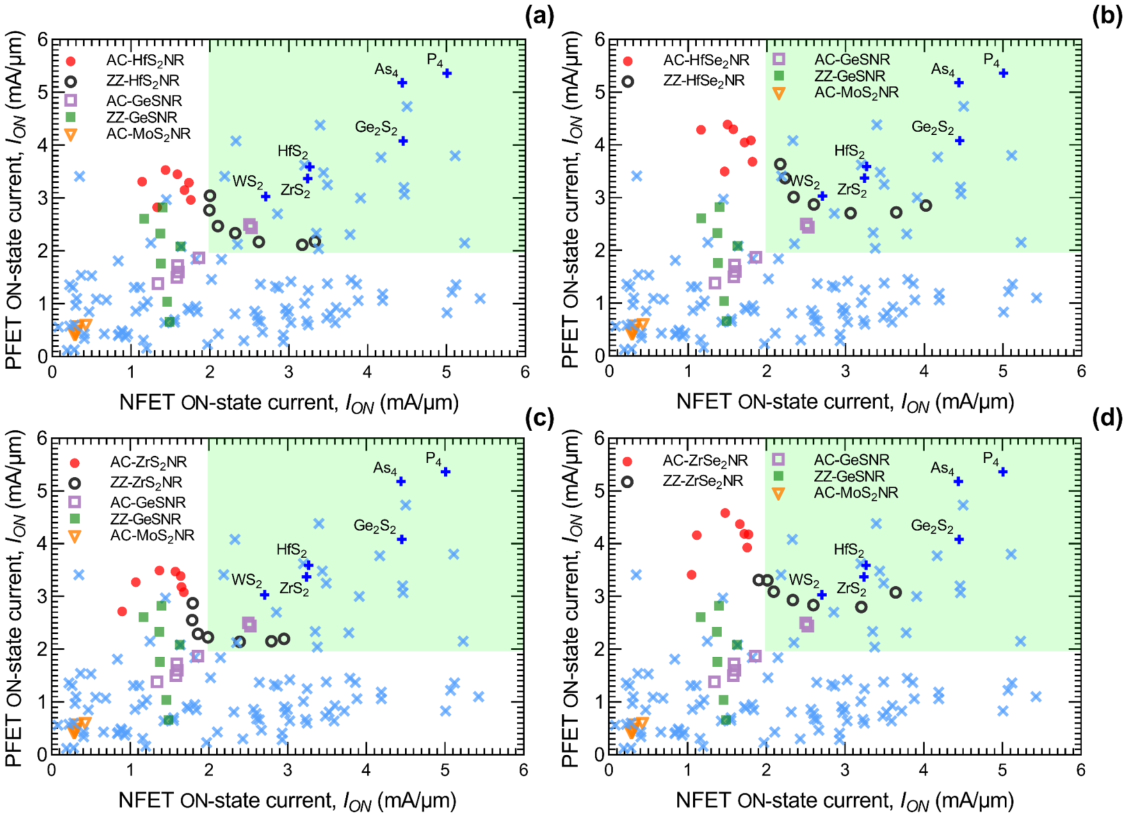

FIG. 9. nFET vs pFET ON-state current of devices with (a) AC and ZZ-HfS$_2$NR, (b) AC and ZZ-HfSe$_2$NR, (c) AC and ZZ-ZrS$_2$NR, and (d) AC and ZZ-ZrSe$_2$NR channel. Green area represents IRDS I_{ON} requirement with $I_{ON} = 1.979$ mA/μm. The 100 2DMs reported in Ref. 12 are included in graphs with the most relevant materials directly named and marked with blue plus signs, while the unnamed 2DMs are shown with light blue crosses.

IV. CONCLUSIONS

Transition metal dichalcogenides (TMDs) MX$_2$ (M = {Hf, Zr}, X = {S, Se}) are patterned into armchair and zigzag quasi-1D semiconductor nanoribbons and investigated using *ab initio* quantum transport simulations. The bandgap width-dependence characteristics can be divided into two groups, namely, in AC-MX$_2$NRs E_g increases by ∼0.45 eV when W is scaled from ∼4 nm to ∼1 nm, while ZZ-MX$_2$NRs exhibit bandgap immunity to nanoribbon width downscaling. By studying FETs with MX$_2$NR channel and EOT of 1 nm, we show that AC-NFETs have the lowest performance with $I_{ON} < 1$ mA/μm, while AC-PFETs are the best-performing devices with I_{ON} of up to 2.6 mA/μm. On the other hand, ZZ-PFETs are relatively immune to W downscaling as I_{ON} decreases only slightly, whereas ZZ-NFETs exhibit a surprising I_{ON} increase of up to 70% when the channel width decreases to ∼2 nm. We report that the ON-state performance of all devices is directly proportional to the ON-state injection velocity and effective transport mass, with v_{inj} reaching $\sim 2.1 \times 10^7$ cm/s and m_T being as low as $0.14 m_0$. Finally, we show that FETs with Hf-based MX$_2$ ZZ nanoribbons, ZZ-ZrS$_2$NRs with $W < 3$ nm and ZZ-ZrSe$_2$NRs with $W < 6$ nm, meet the IRDS requirements for both NFET and PFET devices. In contrast, for AC-MX$_2$NRs only the p-channel devices meet the I_{ON} provision as stated in the IRDS. Our work presents the upper ballistic limits to the potential device performance on the nanoscale, whereas further work is needed on addressing the contact resistance and carrier scattering for a detailed assessment of MX$_2$NR FETs. Nevertheless, our results demonstrate that certain Zr- and Hf-based MX$_2$ nanoribbons could serve as high-performing channel materials in future high-density and high-performance logic FETs based on multiple-nanowire/nanosheet architectures such as MBC FETs.

ACKNOWLEDGMENTS

This work was supported by the Croatian Science Foundation under the project CONAN2D (Grant No. UIP-2019-04-3493).

AUTHOR DECLARATIONS

Conflict of Interest

The authors have no conflicts to disclose.

Author Contributions

Mislav Matić: Conceptualization (equal); Data curation (equal); Formal analysis (equal); Methodology (equal); Software (equal); Writing – original draft (equal). **Mirko Poljak:** Funding acquisition (equal); Methodology (equal); Supervision (equal); Writing – review & editing (equal).

DATA AVAILABILITY

The data that support the findings of this study are available within the article and from the corresponding author upon reasonable request.

REFERENCES

[1] N. Loubet, T. Hook, P. Montanini, C.-W. Yeung, S. Kanakasabapathy, M. Guillom, T. Yamashita, J. Zhang, X. Miao, J. Wang, A. Young, R. Chao, M. Kang, Z. Liu, S. Fan, B. Hamieh, S. Sieg, Y. Mignot, W. Xu, S.-C. Seo, J. Yoo, S. Mochizuki, M. Sankarapandian, O. Kwon, A. Carr, A. Greene, Y. Park, J. Frougier, R. Galatage, R. Bao, J. Shearer, R. Conti, H. Song, D. Lee, D. Kong, Y. Xu, A. Arceo, Z. Bi, P. Xu, R. Muthinti, J. Li, R. Wong, D. Brown, P. Oldiges, R. Robison, J. Arnold, N. Felix, S. Skordas, J. Gaudiello, T. Standaert, H. Jagannathan, D. Corliss, M.-H. Na, A. Knorr, T. Wu, D. Gupta, S. Lian, R. Divakaruni, T. Gow, C. Labelle, S. Lee, V. Paruchuri, H. Bu, and M. Khare, "Stacked nanosheet gate-all-around transistor to enable scaling beyond FinFET," in *2017 Symposium VLSI Technology* (IEEE, 2017), pp. T230–T231.

[2] G. Bae, D.-I. Bae, M. Kang, S.M. Hwang, S.S. Kim, B. Seo, T.Y. Kwon, T.J. Lee, C. Moon, Y.M. Choi, K. Oikawa, S. Masuoka, K.Y. Chun, S.H. Park, H.J. Shin, J.C. Kim, K.K. Bhuwalka, D.H. Kim, W.J. Kim, J. Yoo, H.Y. Jeon, M.S. Yang, S.-J. Chung, D. Kim, B.H. Ham, K.J. Park, W.D. Kim, S.H. Park, G. Song, Y.H. Kim, M.S. Kang, K.H. Hwang, C.-H. Park, J.-H. Lee, D.-W. Kim, S.-M. Jung, and H.K. Kang, "3 nm GAA technology featuring multi-bridge-channel FET for low power and high performance applications," in *2018 IEEE International Electron Devices Meeting IEDM* (IEEE, 2018), pp. 28.7.1–28.7.4.

[3] N. Singh, A. Agarwal, L. K. Bera, T. Y. Liow, R. Yang, S. C. Rustagi, C. H. Tung, R. Kumar, G. Q. Lo, N. Balasubramanian, and D.-L. Kwong, "High-performance fully depleted silicon nanowire (diameter /spl les/ 5 nm) gate-all-around CMOS devices," IEEE Electron Device Lett. **27**(5), 383–386 (2006).

[4] G. Fiori, F. Bonaccorso, G. Iannaccone, T. Palacios, D. Neumaier, A. Seabaugh, S. K. Banerjee, and L. Colombo, "Electronics based on two-dimensional materials," Nat. Nanotechnol. **9**(10), 768–779 (2014).

[5] F. Schwierz, J. Pezoldt, and R. Granzner, "Two-dimensional materials and their prospects in transistor electronics," Nanoscale **7**(18), 8261–8283 (2015).

[6] F. Urban, G. Lupina, A. Grillo, N. Martucciello, and A. Di Bartolomeo, "Contact resistance and mobility in back-gate graphene transistors," Nano Express **1**(1), 010001 (2020).

[7] A. Allain, J. Kang, K. Banerjee, and A. Kis, "Electrical contacts to two-dimensional semiconductors," Nat. Mater. **14**(12), 1195–1205 (2015).

[8] M. Poljak, M. Matić, and A. Zeljko, "Minimum contact resistance in monoelemental 2D material nanodevices with edge-contacts," IEEE Electron Device Lett. **42**(8), 1240–1243 (2021).

[9] G. Fiori and G. Iannaccone, "Simulation of graphene nanoribbon field-effect transistors," IEEE Electron Device Lett. **28**(8), 760–762 (2007).

[10] Y. Ouyang, Y. Yoon, and J. Guo, "Scaling behaviors of graphene nanoribbon FETs: A three-dimensional quantum simulation study," Electron Devices IEEE Trans. On **54**(9), 2223–2231 (2007).

[11] S. Hitesh, P. Dasika, K. Watanabe, T. Taniguchi, and K. Majumdar, "Integration of 3-level MoS multibridge channel FET with 2D layered contact and gate dielectric," IEEE Electron Device Lett. **43**(11), 1993–1996 (2022).

[12] T. Chowdhury, E. C. Sadler, and T. J. Kempa, "Progress and prospects in transition-metal dichalcogenide research beyond 2D," Chem. Rev. **120**(22), 12563–12591 (2020).

[13] C. Chen, Y. Lin, W. Zhou, M. Gong, Z. He, F. Shi, X. Li, J. Z. Wu, K. T. Lam, J. N. Wang, F. Yang, Q. Zeng, J. Guo, W. Gao, J.-M. Zuo, J. Liu, G. Hong, A. L. Antaris, M.-C. Lin, W. L. Mao, and H. Dai, "Sub-10-nm graphene nanoribbons with atomically smooth edges from squashed carbon nanotubes," Nat. Electron. **4**(9), 653–663 (2021).

[14] H. S. Wang, L. Chen, K. Elibol, L. He, H. Wang, C. Chen, C. Jiang, C. Li, T. Wu, C. X. Cong, T. J. Pennycook, G. Argentero, D. Zhang, K. Watanabe, T. Taniguchi, W. Wei, Q. Yuan, J. C. Meyer, and X. Xie, "Towards chirality control of graphene nanoribbons embedded in hexagonal boron nitride," Nat. Mater. **20**(2), 202–207 (2021).

[15] M. C. Watts, L. Picco, F. S. Russell-Pavier, P. L. Cullen, T. S. Miller, S. P. Bartuś, O. D. Payton, N. T. Skipper, V. Tileli, and C. A. Howard, "Production of phosphorene nanoribbons," Nature **568**(7751), 216–220 (2019).

[16] Q. H. Wang, K. Kalantar-Zadeh, A. Kis, J. N. Coleman, and M. S. Strano, "Electronics and optoelectronics of two-dimensional transition metal dichalcogenides," Nat. Nanotechnol. **7**(11), 699–712 (2012).

[17] C. Klinkert, Á. Szabó, C. Stieger, D. Campi, N. Marzari, and M. Luisier, "2-D materials for ultrascaled field-effect transistors: One hundred candidates under the *A\ab initio* microscope," ACS Nano **14**(7), 8605–8615 (2020).

[18] Q. Zhao, Y. Guo, K. Si, Z. Ren, J. Bai, and X. Xu, "Elastic, electronic, and dielectric properties of bulk and monolayer ZrS$_2$, ZrSe$_2$, HfS$_2$, HfSe$_2$ from van der Waals density-functional theory," Phys. Status Solidi B **254**(9), 1700033 (2017).

[19] M. J. Mleczko, C. Zhang, H. R. Lee, H.-H. Kuo, B. Magyari-Köpe, R. G. Moore, Z.-X. Shen, I. R. Fisher, Y. Nishi, and E. Pop, "Hfse$_2$ and ZrSe$_2$: Two-dimensional semiconductors with native high-κ oxides," Sci. Adv. **3**(8), e1700481 (2017).

[20] K. Xu, Y. Huang, B. Chen, Y. Xia, W. Lei, Z. Wang, Q. Wang, F. Wang, L. Yin, and J. He, "Toward high-performance top-gate ultrathin HfS$_2$ field-effect transistors by interface engineering," Small **12**(23), 3106–3111 (2016).

[21] A. Afzalian and G. Pourtois, "ATOMOS: An ATomistic MOdelling solver for dissipative DFT transport in ultra-scaled HfS$_2$ and black phosphorus MOSFETs," in *2019 International Conference on Simulation of Semiconductor Processes and Devices SISPAD* (IEEE, Udine, 2019), pp. 1–4.

[22] W. Zhang, Z. Huang, W. Zhang, and Y. Li, "Two-dimensional semiconductors with possible high room temperature mobility," Nano Res. **7**(12), 1731–1737 (2014).

[23] T. Kanazawa, T. Amemiya, A. Ishikawa, V. Upadhyaya, K. Tsuruta, T. Tanaka, and Y. Miyamoto, "Few-layer HfS$_2$ transistors," Sci. Rep. **6**(1), 22277 (2016).

[24] K. Xu, Y. Huang, B. Chen, Y. Xia, W. Lei, Z. Wang, Q. Wang, F. Wang, L. Yin, and J. He, "Toward high-performance top-gate ultrathin HfS$_2$ field-effect transistors by interface engineering," Small **12**(23), 3106–3111 (2016).

[25] H. Y. Lv, W. J. Lu, J. Y. Li, R. C. Xiao, M. J. Wei, P. Tong, X. B. Zhu, and Y. P. Sun, "Edge-controlled half-metallic ferromagnetism and direct-gap semiconductivity in ZrS$_2$ nanoribbons," RSC Adv. **7**(53), 33408–33412 (2017).

[26] M. Ghaedsharafi, M. R. Moslemi, and F. Pesaran, "The influence of edge atoms and vacancy defects on different types of HfSe$_2$ nanoribbons," J. Electron. Mater. **53**(2), 969–978 (2024).

[27] S. Eskandari, S. K. Khorrami, and M. Berahman, "Field-effect transistor based on the zigzag ZrSe$_2$ nanoribbons," Appl. Phys. A **129**(12), 823 (2023).

[28] M. Matić and M. Poljak, "Ballistic performance of quasi-one-dimensional hafnium disulfide field-effect transistors," Electronics **13**(6), 1048 (2024).

[29] P. Giannozzi, S. Baroni, N. Bonini, M. Calandra, R. Car, C. Cavazzoni, D. Ceresoli, G. L. Chiarotti, M. Cococcioni, I. Dabo, A. Dal Corso, S. de Gironcoli, S. Fabris, G. Fratesi, R. Gebauer, U. Gerstmann, C. Gougoussis, A. Kokalj, M. Lazzeri, L. Martin-Samos, N. Marzari, F. Mauri, R. Mazzarello, S. Paolini, A. Pasquarello, L. Paulatto, C. Sbraccia, S. Scandolo, G. Sclauzero, A. P. Seitsonen, A. Smogunov, P. Umari, and R. M. Wentzcovitch, "QUANTUM ESPRESSO: A modular and open-source software project for quantum simulations of materials," J. Phys.: Condens. Matter **21**(39), 395502 (2009).

[30]J. P. Perdew, K. Burke, and M. Ernzerhof, "Generalized gradient approximation made simple," Phys. Rev. Lett **77**(18), 3865–3868 (1996).
[31]H. J. Monkhorst and J. D. Pack, "Special points for Brillouin-zone integrations," Phys. Rev. B **13**(12), 5188–5192 (1976).
[32]N. Marzari and D. Vanderbilt, "Maximally localized generalized Wannier functions for composite energy bands," Phys. Rev. B **56**(20), 12847–12865 (1997).
[33]G. Pizzi, V. Vitale, R. Arita, S. Blügel, F. Freimuth, G. Géranton, M. Gibertini, D. Gresch, C. Johnson, T. Koretsune, J. Ibañez-Azpiroz, H. Lee, J.-M. Lihm, D. Marchand, A. Marrazzo, Y. Mokrousov, J. I. Mustafa, Y. Nohara, Y. Nomura, L. Paulatto, S. Poncé, T. Ponweiser, J. Qiao, F. Thöle, S. S. Tsirkin, M. Wierzbowska, N. Marzari, D. Vanderbilt, I. Souza, A. A. Mostofi, and J. R. Yates, "Wannier90 as a community code: New features and applications," J. Phys.: Condens. Matter **32**(16), 165902 (2020).
[34]A. Rahman, J. Guo, S. Datta, and M. S. Lundstrom, "Theory of ballistic nanotransistors," IEEE Trans. Electron Devices **50**(9), 1853–1864 (2003).
[35]A. Szabo, R. Rhyner, H. Carrillo-Nunez, and M. Luisier, "Phonon-limited performance of single-layer, single-gate black phosphorus n- and p-type field-effect transistors," in *2015 IEEE International Electron Devices Meeting IEDM* (IEEE, Washington, DC, 2015), pp. 12.1.1–12.1.4.
[36]J. S. Martin, A. Bournel, and P. Dollfus, "On the ballistic transport in nanometer-scaled DG MOSFETs," IEEE Trans. Electron Devices **51**(7), 1148–1155 (2004).
[37]J. S. Martin, V. Aubry-Fortuna, A. Bournel, P. Dollfus, S. Galdin, and C. Chassat, "Influence of ballistic effects in ultra-small MOSFETs," J. Comput. Electron. **3**(3–4), 207–210 (2004).
[38]S. Datta, *Electronic Transport in Mesoscopic Systems* (Cambridge University Press, Cambridge, 1995).
[39]M. Poljak, *Kvantni transport na nanoskali [Quantum Transport on the Nanoscale]*, 1st ed. (Element, Zagreb, 2023).
[40]M. Matić and M. Poljak, "*Ab initio* quantum transport simulations of monolayer GeS nanoribbons," Solid-State Electron. **197**, 108460 (2022).
[41]M. Matić and M. Poljak, "Electronic, transport and ballistic device properties of quasi-one-dimensional GeS," J. Comput. Electron. **22**, 1350–1362 (2023).
[42]M. Pourfath, *The Non-Equilibrium Green's Function Method for Nanoscale Device Simulation* (Springer-Verlag, Wien, 2014).
[43]M. P. L. Sancho, J. M. L. Sancho, and J. Rubio, "Quick iterative scheme for the calculation of transfer matrices: Application to Mo (100)," J. Phys. F: Met. Phys. **14**(5), 1205–1215 (1984).
[44]"IEEE International Roadmap for Devices and Systems (IRDS), 2022 Update," see https://irds.ieee.org/ (n.d.).
[45]M. S. Lundstrom and J. Guo, *Nanoscale Transistors: Device Physics, Modeling and Simulation* (Springer, New York, 2006).
[46]M. Poljak, M. Matić, I. Prevarić, and K. Japec, "Ballistic performance and overshoot effects in gallenene nanoribbon field-effect transistors," J. Appl. Phys. **135**(7), 074302 (2024).
[47]M. Matić and M. Poljak, "Transport Properties and Device Performance of Quasi-One-Dimensional MoS_2 FETs," 184–188 (2023).
[48]L. Wang, I. Meric, P. Y. Huang, Q. Gao, Y. Gao, H. Tran, T. Taniguchi, K. Watanabe, L. M. Campos, D. A. Muller, J. Guo, P. Kim, J. Hone, K. L. Shepard, and C. R. Dean, "One-dimensional electrical contact to a two-dimensional material," Science **342**(6158), 614–617 (2013).
[49]A. Jain, Á Szabó, M. Parzefall, E. Bonvin, T. Taniguchi, K. Watanabe, P. Bharadwaj, M. Luisier, and L. Novotny, "One-dimensional edge contacts to a monolayer semiconductor," Nano Lett. **19**(10), 6914–6923 (2019).

Publication 2

Ballistic Performance of Quasi-One-Dimensional Hafnium Disulfide Field-Effect Transistors

M. Matić and M. Poljak, “Ballistic Performance of Quasi-One-Dimensional Hafnium Disulfide Field-Effect Transistors,” *Electronics*, vol. 13, no. 6, p. 1048, 2024.
doi: 10.3390/electronics13061048

– 11 pages

electronics

MDPI

Article

Ballistic Performance of Quasi-One-Dimensional Hafnium Disulfide Field-Effect Transistors

Mislav Matić and Mirko Poljak *

Computational Nanoelectronics Group, Faculty of Electrical Engineering and Computing, University of Zagreb, HR 10000 Zagreb, Croatia; mislav.matic@fer.hr
* Correspondence: mirko.poljak@fer.hr; Tel.: +385-1-6129-924

Abstract: Hafnium disulfide (HfS_2) monolayer is one of the most promising two-dimensional (2D) materials for future nanoscale electronic devices, and patterning it into quasi-one-dimensional HfS2 nanoribbons (HfS_2NRs) enables multi-channel architectures for field-effect transistors (FETs). Electronic, transport and ballistic device characteristics are studied for sub-7 nm-wide and ~15 nm-long zigzag HfS_2NR FETs using non-equilibrium Green's functions (NEGF) formalism with density functional theory (DFT) and maximally localized Wannier functions (MLWFs). We provide an in-depth analysis of quantum confinement effects on ON-state performance. We show that bandgap and hole transport mass are immune to downscaling effects, while the ON-state performance is boosted by up to 53% but only in n-type devices. Finally, we demonstrate that HfS_2NR FETs can fulfill the industry requirements for future technology nodes, which makes them a promising solution for FET architectures based on multiple nanosheets or nanowires.

Keywords: density functional theory (DFT); hafnium disulfide (HfS_2); nanoribbon; non-equilibrium Green's function (NEGF); quantum transport; quasi-one-dimensional

check for updates

Citation: Matić, M.; Poljak, M. Ballistic Performance of Quasi-One-Dimensional Hafnium Disulfide Field-Effect Transistors. *Electronics* **2024**, *13*, 1048.https://doi.org/10.3390/electronics13061048

Academic Editors: Jae-Hyung Jang, Tao Wang, Frédérique Ducroquet, Yi Gu and Hongtao Li

Received: 2 February 2024
Revised: 4 March 2024
Accepted: 8 March 2024
Published: 11 March 2024

1. Introduction

Atomically thin two-dimensional (2D) materials (2DMs) have arisen as potential candidates for future transistor channel materials [1–3] since the discovery of graphene in 2004 [4]. The 2DMs exhibit near-ballistic transport properties and show potential for future high-performance electronic devices due to atomic thickness and dangling-bond-free surfaces [5]. Despite their promising characteristics, the 2DM devices are severely limited by the high contact resistance that degrades the device performance [6–8]. After graphene, more than 1800 2DMs have been predicted to be stable [9], and many of them have shown promise as channel material with transition metal dichalcogenides (TMDs), such as MoS_2, $MoTe_2$, WS_2, WSe_2, SnS_2, etc. [10–12], being among the most promising for future FETs. One hundred 2DMs were studied recently in [13] for future logic devices where monolayer hafnium disulfide (HfS_2) is reported to be one of the best-performing 2DMs for future ultra-scaled FETs due to a combination of electronic and transport properties such as low effective mass and high injection velocity that result in high ON-state current for both n- and p-FETs. The electronic, transport, and device properties of 2D HfS_2 were studied in detail in [13–15] by advanced theoretical calculations, whereas experimental work on few-layer HfS_2 FETs was reported in [16,17] where integration compatibility of monolayer HfS_2 with HfO_2 high-*k* dielectric was emphasized as one the biggest strengths of realization of devices with HfS_2.

With current state-of-the-art multi-bridge channel (MBC) FETs with silicon nanosheets or nanowires gaining momentum in the industry, 2DMs patterned into quasi-one-dimensional (quasi-1D) structures such as nanoribbons could replace silicon and extend Moore's law by offering higher integration density [18–20]. Additionally, quantum confinement effects provide avenues for tuning the material properties, which could benefit the performance of such electronic nanodevices. Recently, various nanoribbons with ultimately downscaled widths were experimentally reported, including graphene nanoribbons (GNRs) [21,22] and phosphorene nanoribbons (PNRs) [23,24], which affirms the possibility of constructing MBC FETs, at least in principle, with quasi-1D 2DM nanostructures. Therefore, given the promising performance of 2D HfS_2 FETs, it is imperative to systematically explore the electronic, transport, and device properties of quasi-1D nanoribbons of HfS_2 (HfS_2NRs) about which nothing is currently known in the literature.

In this paper, we present an ab initio study on HfS_2NRs using density functional theory (DFT) to obtain the electronic structure, and maximally localized Wannier functions (MLWFs) to transform DFT Hamiltonians into localized basis suitable for quantum transport simulation. The MLWF Hamiltonians are then coupled to our in-house non-equilibrium Green's function (NEGF)-based quantum transport [25,26] solver to obtain the relevant properties of HfS_2NRs and HfS_2NR FETs. Most importantly, we report the degradation of pFET performance while scaling down the nanoribbon width; however, the driving current in HfS_2NR nFETs is surprisingly boosted in ~2 nm-wide transistors by the quantum confinement effects. These findings are further explained by investigating the bandgap, density of states and carriers, current density, and injection velocity. Finally, we compare HfS_2NR n- and p-type FETs to other 2DMs and to the requirements set in the International Roadmap for Devices and Systems (IRDS). We show that both n- and p-type HfS_2NR FETs with nanoribbon widths in the range from ≈2 nm to ≈5 nm can fulfil the goals set for future logic devices.

2. Methods

The unit cell of monolayer HfS_2 (Figure1a) is obtained from the Materials Cloud [27] and scaled to construct the supercells of zigzag HfS_2 nanoribbons with hydrogen-passivated edges. The nanoribbon structure from the top and side views is shown in Figures1b and1c, respectively. The zigzag direction exhibits the highest curvature of the dominant subbands in the valence and conduction bands, which hints at excellent carrier transport in these devices. The HfS_2NR supercells are constructed with respect to the number of HfS_2 unit cells repeated along the nanoribbon width (W). This number ranges from 2 to 10 unit cells, which corresponds to W from 1.36 nm to 6.39 nm. After defining the initial structure, we employ an ab initio plane-wave DFT, implemented in the Quantum Espresso (QE) program package (v.6.8) [28], to relax the nanoribbon structure and obtain the Hamiltonians. A 20 Å vacuum is added in confined directions to exclude any interactions between layers. The DFT calculations use Perdew–Burke–Ernzerhof generalized gradient approximation (PBE-GGA) [29] as the exchange–correlation functional with plane augmented wave (PAW) pseudopotentials. The Brillouin zone is sampled with $1 \times 15 \times 1$ Monkhorst–Pack k-point grid [30] where 15 k-points are in transport direction, and the cutoff energy is set to 1360 eV. Convergence thresholds for ionic forces are fixed to 10^{-3} eV/Å, while 10^{-4} eV is used for total energy.

Energy-localized plane-wave Hamiltonians from QE are then converted into a space-localized basis using MLWFs [31] implemented in the Wannier90 (v.3.1.0) program package [32,33]. The main input into the Wannier90 tool are the trial orbitals that are used for Wannier transformation, and here we use d orbitals for Hf atoms and p orbitals for S atoms. The band structure calculated with MLWF and DFT Hamiltonians shows good agreement in the relevant energy region around the bandgap, as seen in Figure1d that reports the dispersion of the 3.25 nm wide HfS_2NR. Finally, the supercell MLWF Hamiltonian matrices are upscaled to construct the total HfS_2NR Hamiltonian, where the ~15 nm-long nanoribbon represents the channel of the HfS_2NR FET.

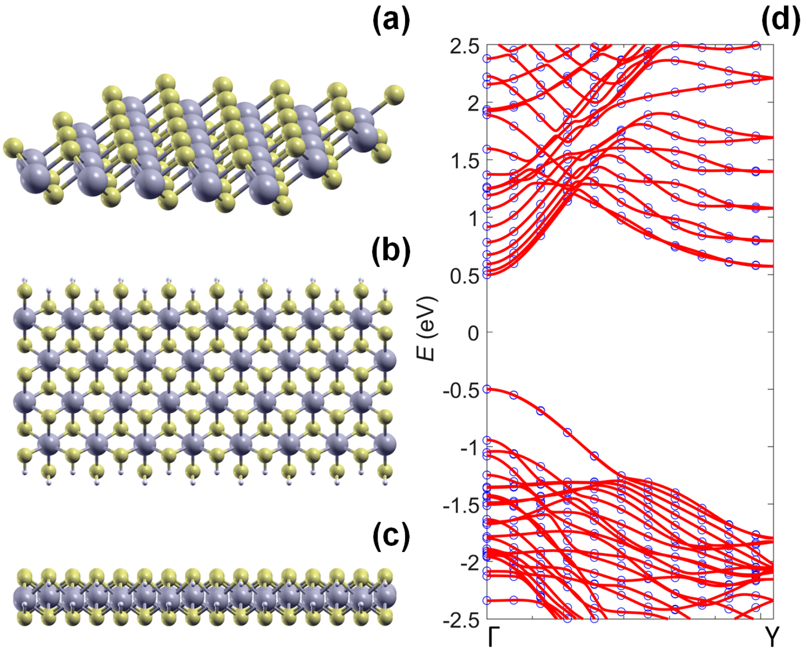

Figure 1. Illustration of (**a**) HfS_2 monolayer. (**b**) Top and (**c**) side view of the monolayer HfS_2 nanoribbon with zigzag edges. (**d**) Band structure obtained from DFT (blue dots) and MLWF (red lines).

Being primarily interested in the ON-state performance, we use the top-of-the-barrier (ToB) ballistic FET model [34] to simulate single gate n- and p-type FETs with HfS_2NR channel. Within the ToB model, only the thermionic current is calculated, which is reasonable because the assumed 15 nm long channel is long enough for negligible tunnelling. The main inputs of the ToB FET model are transmission and density of states (DOS) calculated using the NEGF formalism implemented in our in-house code [35,36]. Within NEGF, the channel is described with the total HfS_2NR Hamiltonian and source/drain (S/D) contacts are described with S/D self-energy matrices calculated using the numerically efficient Sancho–Rubio method [37,38]. The n- and p-type FETs with zigzag HfS_2NR channels are simulated with ideal electrostatic control by the gate, resulting in a perfect subthreshold slope, equivalent oxide thickness (EOT) of 1 nm, S/D doping set at 0.01 areal molar fraction or $\approx 2.7 \times 10^{13}$ cm^{-2}, and supply voltage (V_{DD}) set to 0.7 V. To provide a meaningful comparison between various HfS_2NR devices, simulations are performed with a common OFF-state current (I_{OFF}) set to 10 nA/µm as defined by IRDS for high performance (HP) devices [39].The setting of I_{OFF} is performed by adjusting the gate work function for each device automatically within our code. The ballistic ON-state current (I_{ON}) and the ON-state charge density at ToB are extracted when both gate and drain are biased at the supply voltage. Finally, we set EOT to 0.6 nm and compare I_{ON} and injection velocity to our previous work on GeS nanoribbon devices, in addition to one hundred 2DMs reported in [13].

3. Results and Discussion

Band structure of HfS_2NRs with various widths is reported in Figure2a–d. All HfS_2NRs exhibit a direct bandgap at the Γ point and we observe an immunity of bandgap (E_g) to width scaling. The bandgap keeps a constant value of ≈1 eV in all nanoribbons, as reported in Figure2e, which is slightly smaller than the 1.3 eV reported in [13] for the HfS_2 monolayer. As W is scaled down, the conduction band (CB) exhibits fewer bands near the CB minimum (CBM), while the dominant subband qualitatively remains the same. On the other hand, two degenerate subbands are visible in the valence band (VB) of wide HfS_2NRs with $W > 4$ nm, and this degeneracy is broken in narrower nanoribbons due to strong quantum confinement effect. Namely, two-hole subbands separate and this separation increases with W downscaling, which is followed by an increase in the curvature of the second subband near the VB maximum (VBM). To further investigate the quantum confinement effects on the band structure of all HfS_2NR widths, we extract the electron and hole–band structure effective mass of the dominant subband, closest to the CBM or VBM, from the band structure by fitting its curvature with a parabolic approximation (Figure2f). Electron effective mass (m_e*) is immune to scaling with $m_e^* \approx 0.2m_0$ for all nanoribbon widths. In contrast, hole effective mass (m_h*) experiences a significant width-scaling effect. Namely, m_h* is $\approx 0.37m_0$ for HfS_2NRs with $W \geq 3.25$ nm; while scaling down the width linearly decreases m_h* to $0.33m_0$ when $W = 1.36$ nm. Considering only the observed differences in CB and VB, where the m_h* of the dominant (highest) subband is at least 1.6 × lower than the m_e* for all observed HfS_2NRs, we expect a considerable difference in the performance of n- and p-FETs with HfS_2NR channels. However, this metric does not take into account degeneracy in VB or the higher number of subbands near CBM in wider nanoribbons.

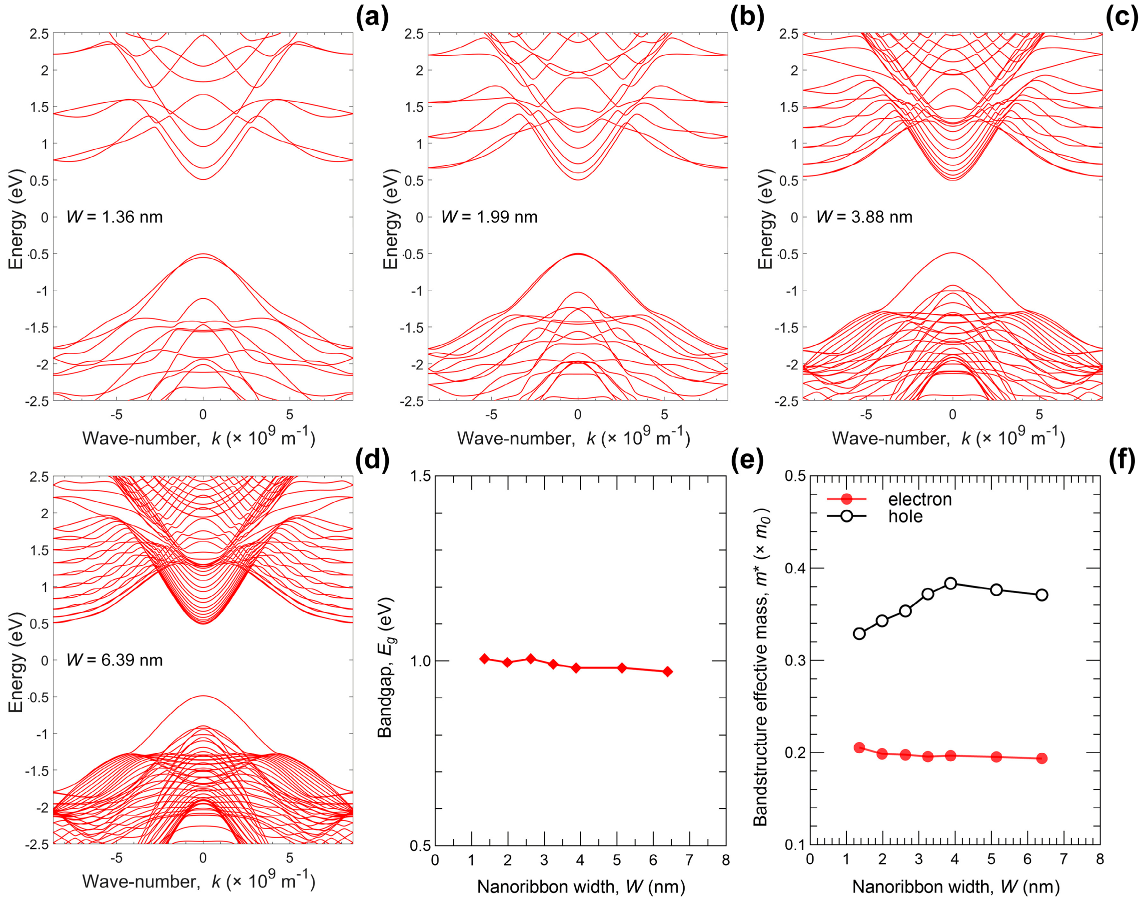

Figure 2. Band structure of zigzag HfS_2NRs with the widths of (**a**) 1.36 nm, (**b**) 1.99 nm, (**c**) 3.88 nm and (**d**) 6.39 nm. (**e**) Impact of nanoribbon width-scaling on the bandgap of zigzag HfS_2NRs. (**f**) Electron and hole band structure effective mass dependence on nanoribbon width. Effective masses are extracted for the lowest (highest) subband in the CB (VB).

To assess the performance of n- and p-type HfS_2NR FETs in Figure3a, we plot the nanoribbon width dependence of the width-normalized ON-state current. The HfS_2NR pFETs exhibit a monotonic I_{ON} decrease from 1.5 mA/µm to 1.12 mA/µm when the width is downscaled. The only exception is the narrowest pFET that shows a slight I_{ON} increase to 1.18 mA/µm. On the other hand, for HfS_2NR nFETs, we surprisingly observe a generally monotonic increase of I_{ON} when HfS_2NR width decreases. The ON-state performance is enhanced from 1.14 mA/µm to 1.74 mA/µm when the width is downscaled from 6.39 nm to 1.99 nm, whereas the narrowest nanoribbon with W = 1.36 nm exhibits a slight decrease of I_{ON} to 1.66 mA/µm. Therefore, quantum confinement effects induce a current boosting of 53% for nFETs with the ≈2 nm wide HfS$_2$NR channel. Since the performance of HfS$_2$NR FETs shows no correlation to the band structure effective mass, in the following paragraphs, we explore the features of charge density, density of states, and carrier injection velocity.

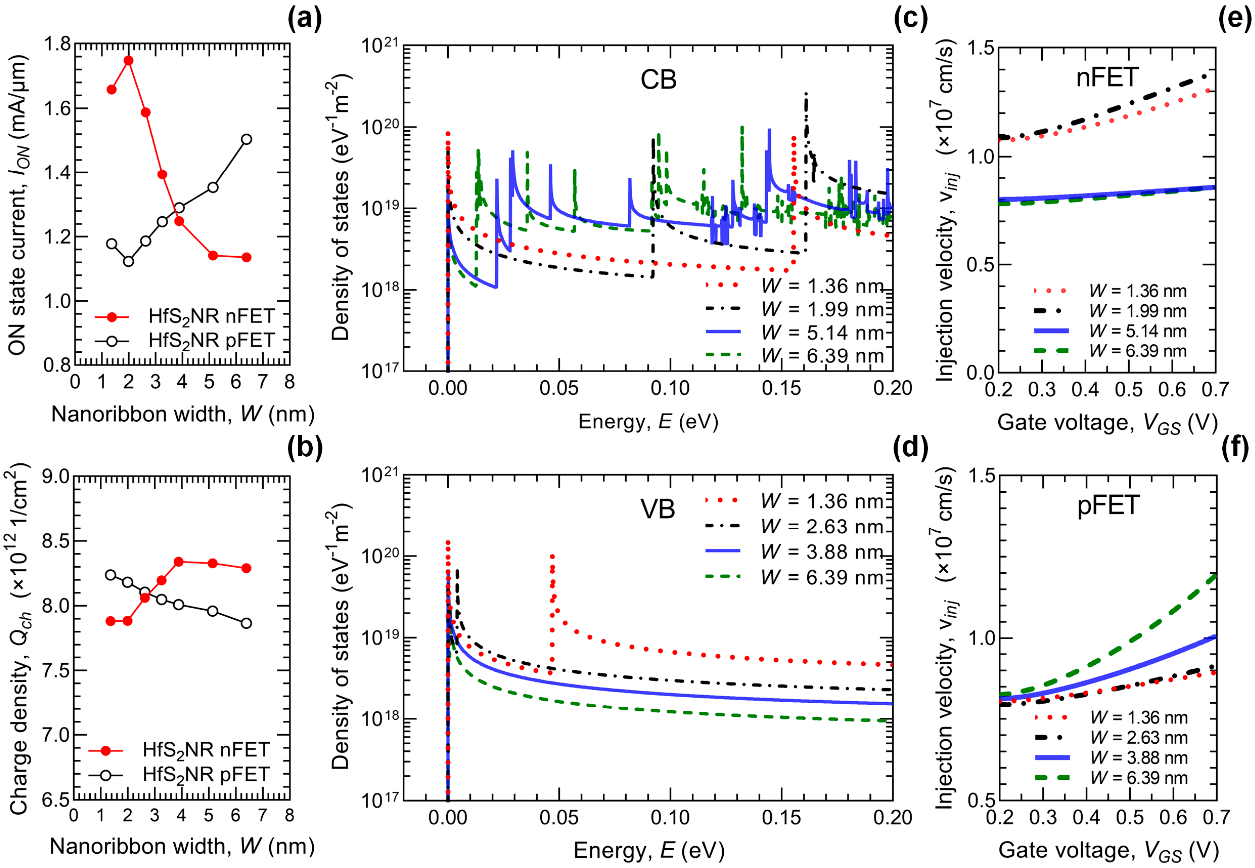

Figure 3. (**a**) ON-state current and (**b**) charge density at ToB width dependence in n- and p-type zigzag HfS$_2$NR FETs. I_{ON} and Q_{ch} are extracted at $V_{GS} = V_{DS} = V_{DD}$ = 0.7 V with a common I_{OFF} = 10 nA for all devices. Comparison of DOS in (**c**) conduction and (**d**) valence band of HfS$_2$NR FETs. All DOS and transmission plots are shifted so that the CBM and VBM are positioned at 0 eV. Dependence of injection velocity on gate voltage in (**e**) n-type and (**f**) p-type zigzag HfS$_2$NR FETs for various nanoribbon widths.

Charge density at the top-of-the-barrier extracted in the ON-state (Q_{CH}) for various HfS$_2$NR widths is plotted in Figure3b. For HfS$_2$NR nFETs, we report $Q_{CH} \approx 8.3 \times 10^{12}$ cm^{-2} for $W \geq 3.88$ nm, while scaling down decreases Q_{CH} to 7.88×10^{12} cm^{-2} in the 1.36 nm wide device. On the other hand, in pFETs, charge density increases monotonically from $Q_{CH} = 7.87 \times 10^{12}$ cm^{-2} for W = 6.39 nm to $Q_{CH} = 8.24 \times 10^{12}$ cm^{-2} for W = 1.36 nm. Charge density at the top-of-the-barrier depends on DOS near the CBM or VBM. Therefore, we plot DOS near the CBM (VBM) for various HfS$_2$NR widths in Figure3c,d. The HfS$_2$NR nFETs exhibit a dense DOS with a high number of Van Hove singularities (VHS) near the CBM. Scaling down, HfS$_2$NR width reduces the number of available bands in the CB, decreases the overall DOS in the 100 meV window, and, therefore, lowers the charge density in narrower HfS$_2$NRs. However, VB DOS that is relevant for HfS$_2$NR pFETs shows an increase from a single VHS to two VHSs near the VBM due to band separation of the two dominant subbands (see Figure2a) which increases the DOS near the VBM and Q_{CH} when nanoribbon width is scaled down.

Since the trends in I_{ON} and Q_{CH} behavior, reported in Figure 3a,b, are qualitatively opposite, the only reasonable explanation for I_{ON} trends should be found in the carrier transport properties, i.e., injection velocity. Injection velocity (v_{inj}) represents the average carrier velocity at the top-of-the-barrier under the ballistic limit and it is shown in Figure 3e,f for n- and p-type HfS$_2$NR FETs, i.e., electrons and holes, respectively. The plots report a gate voltage (V_{GS}) dependence of v_{inj} in the range from the threshold voltage ($V_{GS} \approx 0.2$ V) to the supply voltage ($V_{GS} = 0.7$ V). The nFETs with $W \geq 5.14$ nm show almost no modulation by V_{GS} with electron v_{inj} being $\approx 0.8 \times 10^7$ cm/s. In contrast, v_{inj} increases with increasing bias in the 1.36 nm and 1.99 nm wide HfS$_2$NR nFETs. These two devices exhibit similar v_{inj} at the threshold voltage; however, HfS$_2$NR nFETs with $W = 1.99$ nm exhibit a stronger bias modulation and a higher maximum electron v_{inj} of 1.39×10^7 cm/s. The best observed v_{inj} coincides with the best reported I_{ON} in nFETs for the 1.99 nm wide HfS$_2$NR nFET. We attribute the optimum performance and highest electron v_{inj} for $W \approx 2$ nm to the band structure evolution, especially to the second CB subband visible in Figure 2b. Namely, for this nanoribbon, the subband crowding is not as dense as for wider HfS$_2$NRs, which means that higher subbands with heavier carriers do not contribute significantly to the current-carrying process. As for pFETs, hole v_{inj} at the threshold equals $\approx 0.8 \times 10^7$ cm/s for all HfS$_2$NR pFETs. Scaling down, HfS$_2$NR width decreases the strength of V_{GS} modulation of the hole v_{inj}, and devices with $W \leq 2.63$ nm show almost no bias modulation. The widest observed HfS$_2$NR ($W = 6.39$ nm) shows a 49% increase of hole v_{inj} to 1.2×10^7 cm/s in the ON-state. As the width is downscaled, the hole v_{inj} decreases monotonically, which agrees with the I_{ON} behavior reported in Figure 3a.

We further explore the current and transport properties in ultra-scaled HfS$_2$NR nanodevices by analyzing the current energy density (J_{de}) in the ON-state. The J_{de} results are shown for n- and pFETs in Figures 4a and 4b, respectively. In all devices, the current is mainly contained in the energy window up to ≈100 meV from the CBM/VBM. The nFETs exhibit J_{de} maximum at the CBM for the narrowest HfS$_2$NR, but wider HfS$_2$NRs exhibit a slight shift of the maximum by 20–30 meV, due to the higher number of occupied subbands. Namely, setting a common I_{OFF} for all devices results in different S/D Fermi levels (E_F) depending on device width, with a greater E_F shift upward generally observed for wider HfS$_2$NRs. Consequently, there are more current-carrying subbands, and the current density at the CBM is lower in wider HfS$_2$NR nFETs. The 1.36 nm wide HfS$_2$NR shows maximum current density near the CBM, with only a single dominant subband. In contrast, for $W = 1.99$ nm, the second subband carries current as well, with the second-subband current density surpassing that of the first subband above CBM + 90 meV, which leads to the maximum I_{ON} for the 2 nm wide device among all the studied HfS$_2$NR nFETs.

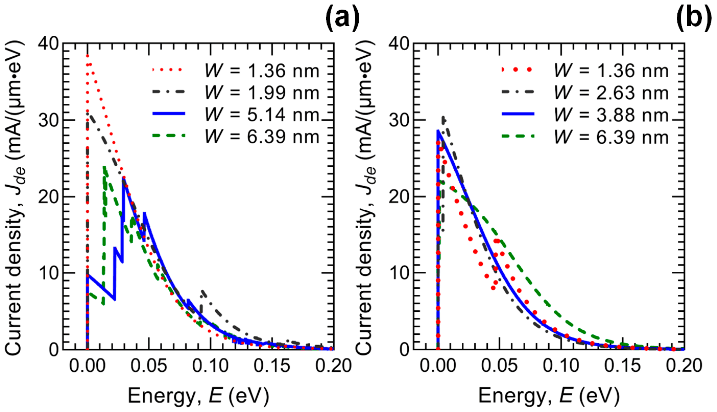

Figure 4. Current energy density at ToB in the ON-state for HfS$_2$NR (**a**) n-type and (**b**) p-type FETs with different nanoribbon channel widths.

In addition to the current density, band decomposed charge density (BDCD) of nanoribbons with the widths of 1.36 nm and 6.39 nm is plotted in Figures 5a and 5b, respectively.

The BDCD is shown for subbands at the CBM/VBM, along with the nearest next subbands that are denoted as next-CBM/next-VBM. Figure5a shows that the electron current in the narrowest nanoribbon, mainly determined by the first CB subband (see Figure4a), is distributed almost through the whole nanoribbon width, except for edge S atoms. On the other hand, electron current in the widest HfS_2NR is mostly determined by the next-CBM subband (see Figure4a), so that the current flows away from the edges and somewhat through the middle, as shown in Figure5b. As for HfS_2NR pFETs with current density reported in Figure4b, J_{de} is localized near the VBM due to the dominant first subband in the VB with a considerable contribution of the second subband in some devices. The lowest two VB subbands are slightly separated, i.e., degeneracy is broken, only in the narrowest HfS_2NR (see Figure2a), and this split results in lower transmission probability near the VBM and, therefore, lower J_{de} in pFETs with the narrowest 1.36 nm wide channel. As shown in the BDCD plots in Figure5a,b, now addressing the situation for the VBM subband, we observe that the hole current is expected to flow exclusively along nanoribbon edges. Furthermore, for wide HfS_2NRs where two degenerate subbands are dominant near the VBM, we observe that the current flows through separate edges in VBM and next-VBM, as seen in Figure5b, due to zero overlap between the edges. Scaling down the nanoribbon width decreases the distance between the edges, which increases the overlap of the edge states and, therefore, causes the separation of degenerate subbands near the VBM, as seen in Figure2. Increasing the current by increasing the width would be limited due to edge transport; hence, the narrowest HfS_2NR pFETs exhibit a decreasing drive current (Figure3a) due to higher DOS in S/D regions and related E_F downshift.

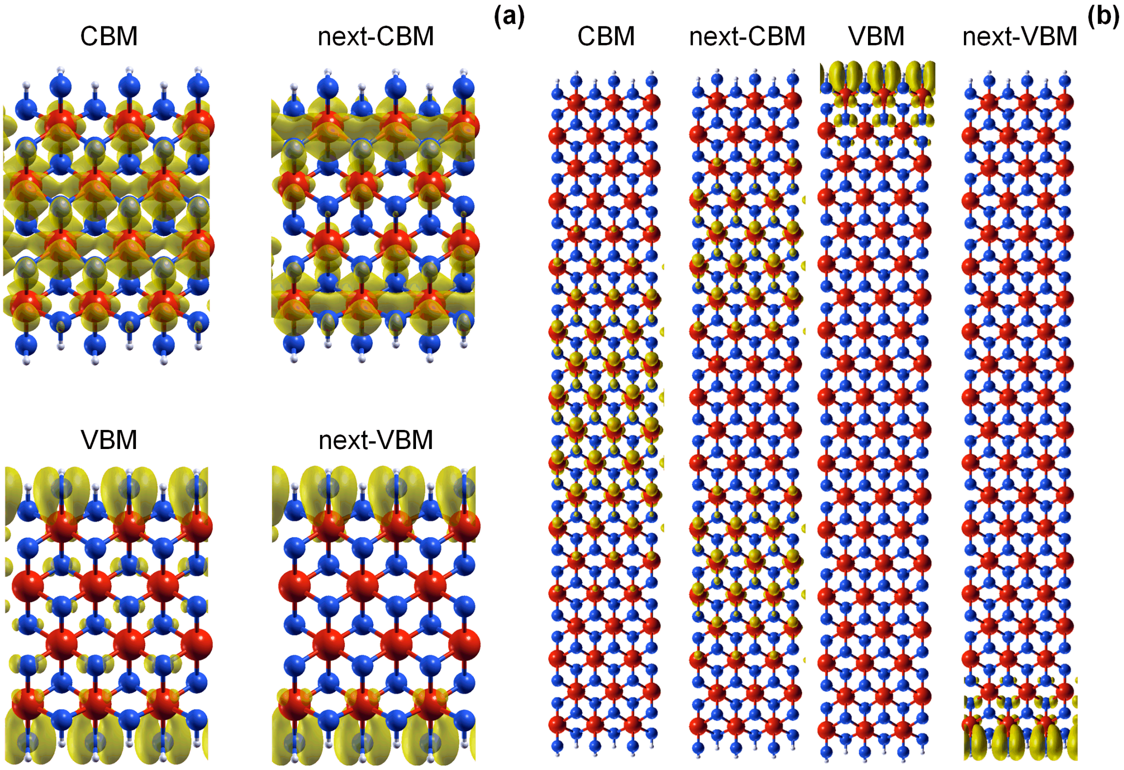

Figure 5. Band-decomposed charge density of CBM, next-CBM, VBM and next-VBM subbands of (**a**) 1.39 nm and (**b**) 6.39 nm wide HfS_2NRs. Isovalue is set at 0.001 q/bohr^3.

Finally, we compare the ON-state performance of HfS_2NR FETs with one hundred 2DMs analyzed in [13], to the armchair and zigzag GeSNRs from our previous work [36,40], and to the IRDS requirements for future logic nodes [39]. For a proper comparison with the literature data, we set the EOT to 0.6 nm (HfO_2 with ε_r = 20, t_{ox} = 3 nm) as in [13]. The injection velocity in the ON-state for nFET and pFETs is shown in Figure6a. All HfS_2NR n- and pFETs exhibit v_{inj} close to, or higher, than the IRDS requirement (0.9×10^7 cm/s), while achieving comparable v_{inj} values to those in 2D HfS_2 along the zigzag direction. Furthermore, only a few other large-area 2D materials such as Ge_2S_2, As_4 and P_4 exhibit higher v_{inj} compared to HfS_2NRs. This is noteworthy because HfS_2NRs are quasi-1D nanostructures with additional quantum confinement in comparison to 2DMs that are infinite 2D sheets.

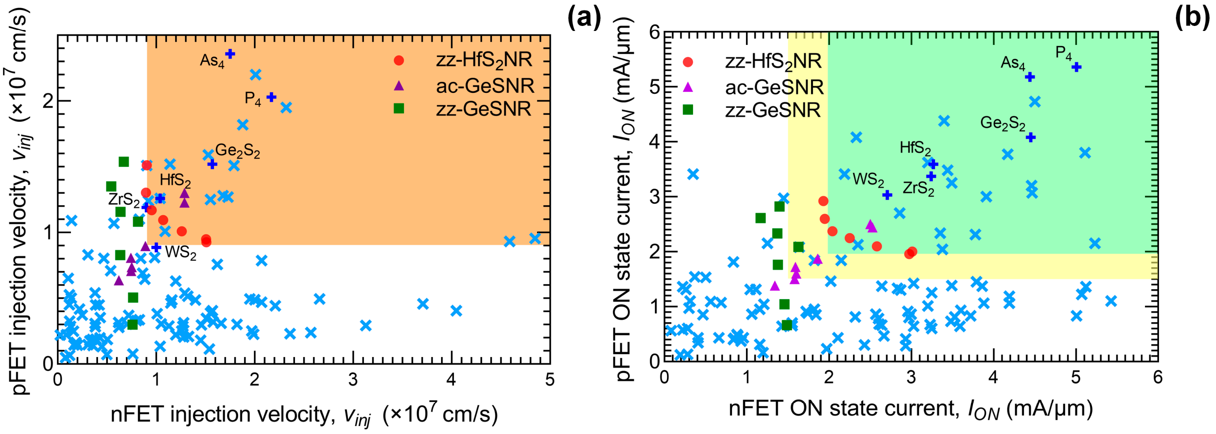

Figure 6. (**a**) nFET vs. pFET ON-state injection velocity with orange area denoting injection velocity higher than 0.9×10^7 cm/s set by IRDS 2022 for future logic nodes. (**b**) nFET vs. pFET ON-state current with a green area representing IRDS 2021 maximum I_{ON} requirement with I_{ON} = 1.979 mA/µm, and a yellow area representing the minimum I_{ON} requirement for future logic devices with I_{ON} = 1.504 mA/µm. The 100 2DMs reported in [13] are included in graphs with the most relevant materials named directly and denoted with blue plus signs, while the unnamed 2DMs are presented with light blue crosses.

The ON-state current is compared in Figure6b again for HfS $_2$NR FETs from this work and one hundred 2DMs reported in [13]. We compare the data against IRDS 2021 [41] because the IRDS 2022 version, which we have used for all previous comparisons, does not provide I_{ON} requirements with zero series or contact resistance. We observe that HfS_2NR FETs exhibit a relatively high I_{ON} and all devices meet the minimum IRDS I_{ON} for both nFET and pFET devices. On the other hand, the maximum IRDS I_{ON} specification is met only by HfS_2NR FETs with W in the range from 1.99 nm to 5.14 nm. The remaining HfS_2NR FETs are close but are nevertheless beyond the edges of the acceptable I_{ON} window. Compared to the armchair and zigzag GeSNRs, only armchair GeSNRs with $W > 3$ nm show better I_{ON} performance than HfS_2NR devices in both n- and p-FET configurations. Finally, in comparison to 2D HfS_2 and other 2D materials such as WS_2, ZrS_2, Ge_2S_2, arsenene and phosphorene, all HfS_2NR FETs perform relatively poorly. Nevertheless, we stress that HfS_2NRs are quasi-1D nanostructures with strong quantum confinement effects along the width, so a direct comparison to 2D monolayers is not completely fair.

The usage of zigzag HfS_2NR for future FET architectures based on multiple parallel nanosheets or nanowires is plausible, given their fulfilment of the IRDS requirements for the ON-state current and injection velocity and, moreover, given the possibility of a matched performance of n- and p-channel devices. Although several monoelemental 2D materials and TMDs outperform hafnium disulphide nanoribbon devices, the HfS_2NR FETs still outperform most of the previously studied 2DMs when both n- and p-FET devices and their performance are considered. Meeting the IRDS requirements for the ON-state current is obtained here for the ideal single-gate FET structure, whereas the usage of multi-channel architectures such as MBC FETs could provide opportunities for further improvements in performance. Additionally, we note that this study deals with purely ballistic devices so only the upper ballistic performance limits are explored in this work, while taking into account realistic effects like carrier scattering in quasi-ballistic transport and contact resistance would deteriorate the reported HfS_2NR FET performance. While investigating the impact of these issues is important, it is also out of the scope of the current manuscript and will be addressed in future work. Nevertheless, the potential of using ultra-scaled HfS_2NRs as a channel material in future logic devices is evident.

4. Conclusions

We present a comprehensive study on the electronic, transport and ballistic device characteristics for HfS_2 nanoribbons with a length of 15 nm and widths under 7 nm. We show that HfS_2NRs and HfS_2NR FETs exhibit promising transport properties and ON-state performance combined with an immunity of bandgap to nanoribbon width downscaling. Moreover, an unexpected and significant I_{ON} increase of up to 53% is observed in n-type FETs with HfS_2NR width of $\approx$2 nm. Concerning the industry goals for future technology nodes, we demonstrate that HfS_2NR FETs with nanoribbon widths in the range from 1.99 nm to 5.14 nm meet all IRDS requirements when EOT is set to 0.6 nm. Therefore, just like 2D HfS_2, quasi-1D nanostructures of monolayer HfS_2 present a promising candidate material system for ultra-scaled logic devices, especially for multi-channel nanosheet or nanowire nFETs, in which the ~2 nm wide HfS_2NRs could provide a significant performance boost due to the strong quantum confinement effect on the band structure.

Author Contributions: Conceptualization, M.M. and M.P.; methodology, M.M.; software, M.M.; validation, M.M. and M.P.; formal analysis, M.M. and M.P.; investigation, M.M.; resources, M.P.; data curation, M.M.; writing—original draft preparation, M.M.; writing—review and editing, M.P.; visualization, M.M.; supervision, M.P.; project administration, M.P.; funding acquisition, M.P. All authors have read and agreed to the published version of the manuscript.

Funding: This research was funded by Croatian Science Foundation under the project CONAN2D, grant number UIP-2019-04-3493.

Data Availability Statement: The data that support the findings of this study are available from the corresponding author, M.P., upon reasonable request.

Conflicts of Interest: The authors declare no conflicts of interest.

References

1. Fiori, G.; Bonaccorso, F.; Iannaccone, G.; Palacios, T.; Neumaier, D.; Seabaugh, A.; Banerjee, S.K.; Colombo, L. Electronics Based on Two-Dimensional Materials. *Nat. Nanotechnol.* **2014**, *9*, 768–779. [CrossRef] [PubMed]
2. Schwierz, F.; Pezoldt, J.; Granzner, R. Two-Dimensional Materials and Their Prospects in Transistor Electronics. *Nanoscale* **2015**, *7*, 8261–8283. [CrossRef] [PubMed]
3. Iannaccone, G.; Bonaccorso, F.; Colombo, L.; Fiori, G. Quantum Engineering of Transistors Based on 2D Materials Heterostructures. *Nat. Nanotechnol.* **2018**, *13*, 183–191. [CrossRef] [PubMed]
4. Novoselov, K.S.; Geim, A.K.; Morozov, S.V.; Jiang, D.; Zhang, Y.; Dubonos, S.V.; Grigorieva, I.V.; Firsov, A.A. Electric Field Effect in Atomically Thin Carbon Films. *Science* **2004**, *306*, 666–669. [CrossRef]
5. Zeng, S.; Tang, Z.; Liu, C.; Zhou, P. Electronics Based on Two-Dimensional Materials: Status and Outlook. *Nano Res.* **2021**, *14*, 1752–1767. [CrossRef]
6. Allain, A.; Kang, J.; Banerjee, K.; Kis, A. Electrical Contacts to Two-Dimensional Semiconductors. *Nat. Mater.* **2015**, *14*, 1195–1205. [CrossRef] [PubMed]
7. Gahoi, A.; Kataria, S.; Driussi, F.; Venica, S.; Pandey, H.; Esseni, D.; Selmi, L.; Lemme, M.C. Dependable Contact Related Parameter Extraction in Graphene–Metal Junctions. *Adv. Electron. Mater.* **2020**, *6*, 2000386. [CrossRef]
8. Poljak, M.; Matić, M.; Zeljko, A. Minimum Contact Resistance in Monoelemental 2D Material Nanodevices with Edge-Contacts. *IEEE Electron. Dev. Lett.* **2021**, *42*, 1240–1243. [CrossRef]
9. Mounet, N.; Gibertini, M.; Schwaller, P.; Campi, D.; Merkys, A.; Marrazzo, A.; Sohier, T.; Castelli, I.E.; Cepellotti, A.; Pizzi, G.; et al. Two-Dimensional Materials from High-Throughput Computational Exfoliation of Experimentally Known Compounds. *Nat. Nanotech.* **2018**, *13*, 246–252. [CrossRef]
10. Radisavljevic, B.; Radenovic, A.; Brivio, J.; Giacometti, V.; Kis, A. Single-Layer MoS_2 Transistors. *Nat. Nanotech.* **2011**, *6*, 147–150. [CrossRef]
11. Huang, Y.; Sutter, E.; Sadowski, J.T.; Cotlet, M.; Monti, O.L.A.; Racke, D.A.; Neupane, M.R.; Wickramaratne, D.; Lake, R.K.; Parkinson, B.A.; et al. Tin Disulfide—An Emerging Layered Metal Dichalcogenide Semiconductor: Materials Properties and Device Characteristics. *ACS Nano* **2014**, *8*, 10743–10755. [CrossRef]

12. Ovchinnikov, D.; Allain, A.; Huang, Y.-S.; Dumcenco, D.; Kis, A. Electrical Transport Properties of Single-Layer WS $_2$. *ACS Nano* **2014**, *8*, 8174–8181. [CrossRef]
13. Klinkert, C.; Szabó, Á.; Stieger, C.; Campi, D.; Marzari, N.; Luisier, M. 2-D Materials for Ultrascaled Field-Effect Transistors: One Hundred Candidates under the *Ab Initio* Microscope. *ACS Nano* **2020**, *14*, 8605–8615. [CrossRef]
14. Afzalian, A.; Pourtois, G. ATOMOS: An ATomistic MOdelling Solver for Dissipative DFT Transport in Ultra-Scaled HfS $_2$ and Black Phosphorus MOSFETs. In Proceedings of the 2019 International Conference on Simulation of Semiconductor Processes and Devices (SISPAD), Udine, Italy, 4–6 September 2019; IEEE: Udine, Italy, 2019; pp. 1–4.
15. Zhang, W.; Huang, Z.; Zhang, W.; Li, Y. Two-Dimensional Semiconductors with Possible High Room Temperature Mobility. *Nano Res.* **2014**, *7*, 1731–1737. [CrossRef]
16. Kanazawa, T.; Amemiya, T.; Ishikawa, A.; Upadhyaya, V.; Tsuruta, K.; Tanaka, T.; Miyamoto, Y. Few-Layer HfS2 Transistors. *Sci. Rep.* **2016**, *6*, 22277. [CrossRef]
17. Xu, K.; Huang, Y.; Chen, B.; Xia, Y.; Lei, W.; Wang, Z.; Wang, Q.; Wang, F.; Yin, L.; He, J. Toward High-Performance Top-Gate Ultrathin HfS$_2$ Field-Effect Transistors by Interface Engineering. *Small* **2016**, *12*, 3106–3111. [CrossRef]
18. Fiori, G.; Iannaccone, G. Simulation of Graphene Nanoribbon Field-Effect Transistors. *IEEE Electron. Device Lett.* **2007**, *28*, 760–762. [CrossRef]
19. Li, X.; Wang, X.; Zhang, L.; Lee, S.; Dai, H. Chemically Derived, Ultrasmooth Graphene Nanoribbon Semiconductors. *Science* **2008**, *319*, 1229–1232. [CrossRef] [PubMed]
20. Poljak, M.; Song, E.B.; Wang, M.; Suligoj, T.; Wang, K.L. Influence of Edge Defects, Vacancies, and Potential Fluctuations on Transport Properties of Extremely Scaled Graphene Nanoribbons. *IEEE Trans. Electron. Devices* **2012**, *59*, 3231–3238. [CrossRef]
21. Chen, C.; Lin, Y.; Zhou, W.; Gong, M.; He, Z.; Shi, F.; Li, X.; Wu, J.Z.; Lam, K.T.; Wang, J.N.; et al. Sub-10-Nm Graphene Nanoribbons with Atomically Smooth Edges from Squashed Carbon Nanotubes. *Nat. Electron.* **2021**, *4*, 653–663. [CrossRef]
22. Wang, H.S.; Chen, L.; Elibol, K.; He, L.; Wang, H.; Chen, C.; Jiang, C.; Li, C.; Wu, T.; Cong, C.X.; et al. Towards Chirality Control of Graphene Nanoribbons Embedded in Hexagonal Boron Nitride. *Nat. Mater.* **2021**, *20*, 202–207. [CrossRef] [PubMed]
23. Watts, M.C.; Picco, L.; Russell-Pavier, F.S.; Cullen, P.L.; Miller, T.S.; Bartuś, S.P.; Payton, O.D.; Skipper, N.T.; Tileli, V.; Howard, C.A. Production of Phosphorene Nanoribbons. *Nature* **2019**, *568*, 216–220. [CrossRef] [PubMed]
24. Zhang, W.; Enriquez, H.; Tong, Y.; Mayne, A.J.; Bendounan, A.; Smogunov, A.; Dappe, Y.J.; Kara, A.; Dujardin, G.; Oughaddou, H. Flat Epitaxial Quasi-1D Phosphorene Chains. *Nat. Commun.* **2021**, *12*, 5160. [CrossRef] [PubMed]
25. Datta, S. *Electronic Transport in Mesoscopic Systems*; Cambridge University Press: Cambridge, UK, 1997; ISBN 978-0-521-59943-6.
26. Poljak, M. *Kvantni Transport na Nanoskali [Quantum Transport on the Nanoscale]*, 1st ed.; Element: Zagreb, Croatia, 2023; ISBN 978-953-250-236-7.
27. Talirz, L.; Kumbhar, S.; Passaro, E.; Yakutovich, A.V.; Granata, V.; Gargiulo, F.; Borelli, M.; Uhrin, M.; Huber, S.P.; Zoupanos, S.; et al. Materials Cloud, a Platform for Open Computational Science. *Sci. Data* **2020**, *7*, 299. [CrossRef] [PubMed]
28. Giannozzi, P.; Baroni, S.; Bonini, N.; Calandra, M.; Car, R.; Cavazzoni, C.; Ceresoli, D.; Chiarotti, G.L.; Cococcioni, M.; Dabo, I.; et al. QUANTUM ESPRESSO: A Modular and Open-Source Software Project for Quantum Simulations of Materials. *J. Phys. Condens. Matter.* **2009**, *21*, 395502. [CrossRef]
29. Perdew, J.P.; Burke, K.; Ernzerhof, M. Generalized Gradient Approximation Made Simple. *Phys. Rev. Lett.* **1996**, *77*, 3865–3868. [CrossRef]
30. Monkhorst, H.J.; Pack, J.D. Special Points for Brillouin-Zone Integrations. *Phys. Rev. B* **1976**, *13*, 5188–5192. [CrossRef]
31. Marzari, N.; Vanderbilt, D. Maximally Localized Generalized Wannier Functions for Composite Energy Bands. *Phys. Rev. B* **1997**, *56*, 12847–12865. [CrossRef]
32. Pizzi, G.; Vitale, V.; Arita, R.; Blügel, S.; Freimuth, F.; Géranton, G.; Gibertini, M.; Gresch, D.; Johnson, C.; Koretsune, T.; et al. Wannier90 as a Community Code: New Features and Applications. *J. Phys. Condens. Matter* **2020**, *32*, 165902. [CrossRef]
33. Calderara, M.; Brück, S.; Pedersen, A.; Bani-Hashemian, M.H.; VandeVondele, J.; Luisier, M. Pushing Back the Limit of *Ab-Initio* Quantum Transport Simulations on Hybrid Supercomputers. In Proceedings of the International Conference for High Performance Computing, Networking, Storage and Analysis, Austin, TX, USA, 15–20 November 2015; pp. 1–12.
34. Rahman, A.; Guo, J.; Datta, S.; Lundstrom, M.S. Theory of Ballistic Nanotransistors. *IEEE Trans. Electron. Devices* **2003**, *50*, 1853–1864. [CrossRef]
35. Matić, M.; Župančić, T.; Poljak, M. Parallelized Ab Initio Quantum Transport Simulation of Nanoscale Bismuthene Devices. In Proceedings of the 2022 45th Jubilee International Convention on Information, Communication and Electronic Technology (MIPRO), Opatija, Croatia, 23–27 May 2022; pp. 118–123.
36. Matić, M.; Poljak, M. Ab Initio Quantum Transport Simulations of Monolayer GeS Nanoribbons. *Solid-State Electron.* **2022**, *197*, 108460. [CrossRef]
37. Pourfath, M. *The Non-Equilibrium Green's Function Method for Nanoscale Device Simulation*; Springer: Wien, Austria, 2014; ISBN 978-3-7091-1799-6.
38. Sancho, M.P.L.; Sancho, J.M.L.; Rubio, J. Quick Iterative Scheme for the Calculation of Transfer Matrices: Application to Mo (100). *J. Phys. F Met. Phys.* **1984**, *14*, 1205–1215. [CrossRef]
39. IEEE International Roadmap for Devices and Systems (IRDS), 2022 Update. Available online:https://Irds.Ieee.Org/editions/2022/more-moore(accessed on 15 January 2024).

40. Matić, M.; Poljak, M. Electronic, Transport and Ballistic Device Properties of Quasi-One-Dimensional GeS. *J. Comput. Electron.* **2023**, *22*, 1350–1362. [CrossRef]
41. IEEE International Roadmap for Devices and Systems (IRDS), 2021 Update. Available online:https://Irds.Ieee.Org/editions/2021/more-moore(accessed on 17 January 2024).

Publication 3

Electronic, transport and ballistic device properties of quasi-one-dimensional GeS

M. Matić and M. Poljak, "Electronic, transport and ballistic device properties of quasi-one-dimensional GeS," *Journal of Computational Electronics*, vol. 22, no. 5, pp. 1350–1362, 2023. doi:10.1007/s10825-023-02054-4

– 13 pages

Journal of Computational Electronics (2023) 22:1350–1362
https://doi.org/10.1007/s10825-023-02054-4

Electronic, transport and ballistic device properties of quasi-one-dimensional GeS

Mislav Matić[1] · **Mirko Poljak**[1]

Received: 31 January 2023 / Accepted: 11 May 2023 / Published online: 23 May 2023

Abstract

Monolayer germanium monosulfide (GeS) is among the most promising two-dimensional (2D) materials for applications in electron devices at the nanoscale. Quasi-one-dimensional GeS nanoribbons (GeSNRs) allow a high-density integration and provide an additional avenue for tuning the material and device properties. In this work we study electronic, transport and ballistic device characteristics of sub-5 nm-wide and ~ 15 nm-long armchair and zigzag GeSNRs using quantum transport simulations based on Green's functions, and atomically and orbitally resolved Hamiltonians obtained with density functional theory that are transformed using maximally localized Wannier functions. The evolution of bandstructure, effective mass, charge density, injection velocity, and ON-state drain current (I_{ON}) of GeSNRs and GeSNR-based field-effect transistors (FETs) are studied with respect to GeSNR width downscaling. We show that GeSNRs and GeSNR FETs experience strikingly different consequences of scaling and confinement depending on carrier type and edge configuration, with e.g. I_{ON} behavior including monotonic decrease (n- and p-type FETs with armchair GeSNRs), nearly no change (nFETs with zigzag GeSNR), and appearance of local minima and maxima (pFETs with zigzag GeSNR channels). By comparing device performance to specifications set by a technology roadmap, we demonstrate that certain GeSNR FETs can fulfil the requirements and, moreover, we provide the ranges of acceptable nanoribbon widths and equivalent oxide thickness values depending on channel type and edge configuration.

Keywords Quantum transport · Non-equilibrium Green's function (NEGF) · Density functional theory (DFT) · Maximally-localized Wannier functions (MLWF) · Germanium monosulfide (GeS) · Nanoribbon · Quasi-one-dimensional

1 Introduction

The tremendous growth of the semiconductor industry over the past 60 years has been driven by the miniaturization and optimization of transistors. Due to the challenges to suppress short channel effects (SCEs) at gate lengths below 20 nm, new materials and device architectures are needed to enable further transistor scaling and enhance device performance. Since the discovery of graphene in 2004 [1], atomically-thin two-dimensional (2D) materials (2DMs) arose as potential candidates for future transistor channel materials [2–4]. With projected sub-15 nm channel lengths in future FETs in combination with atomic thickness and dangling-bond-free surfaces [5], 2DMs can exhibit near-ballistic transport properties that can be utilized for high-performance electron devices. Nevertheless, high contact resistance is still an obstacle to their use in nanodevices [6–8]. Recently, hundreds of 2DMs were studied in detail in [9], and monolayer germanium monosulfide (GeS) was identified as one of the most promising 2DMs for ultra-scaled FETs. The 2D GeS is a member of monolayer group IV-VI monochalcogenides, MXs ($M \in \{Ge, Si, Sn\}$ and $X \in \{S, Se\}$) with phosphorene-like buckled orthorhombic lattice which indicates anisotropic transport [10]. As other 2DMs, the 2D GeS can in principle be patterned into quasi-one-dimensional (quasi-1D) nanoribbons, which enables an additional way of tuning of electronic, transport and device properties that include e.g. bandgap, effective mass, injection velocity, etc. [11–14].

A recent quantum transport study of sub-10 nm monolayer GeS FETs [15] showed great potential of GeS as a material for future short-channel transistors. However, very little is known about quasi-1D GeS nanoribbon (GeSNR)

✉ Mirko Poljak
mirko.poljak@fer.hr

[1] Computational Nanoelectronics Group, Faculty of Electrical Engineering and Computing, University of Zagreb, 10000 Zagreb, Croatia

devices, with the information being limited to electronic bandstructure [16] and some transport and n-channel transistor (nFET) properties for GeSNRs with armchair edges (ac-GeSNR) from our previous work [17]. Electronic properties of armchair and zigzag GeSNRs with bare and H-terminated edges were studied in [16]. This study demonstrated a high dependence of electronic properties on edge termination as zigzag GeSNRs (zz-GeSNR) with bare edges show metallic properties while all bare-edge ac-GeSNRs exhibit semiconducting behavior. On the other hand, termination by H atoms is presented as a good option to stabilize the ac- and zz-GeSNRs that exhibit semiconducting behavior. In the literature, there is currently no information about the scaling effects on the performance of ac-GeSNR p-channel transistors (pFETs) and zz-GeSNR-based FETs for both carrier types, i.e. zz-GeSNR nFET and pFET. Therefore, in this work we study in detail the electronic and transport properties, and ballistic device performance of ultra-scaled GeS nanodevices down to the 1D structure limit.

In order to properly account for the atomistic resolution and strong quantum effects in nanodevices, advanced modeling is necessary for the simulation of materials and FETs at the nanoscale [18, 19]. Ab initio density functional theory (DFT) is used in this study to calculate the electronic structure, and maximally-localized Wannier functions (MLWFs) are used to convert DFT Hamiltonians into a localized basis, preserving the precision of the bandstructure and enabling transport calculations for realistically-sized devices. Afterward, ballistic quantum transport simulations are then performed using the non-equilibrium Green's function (NEGF) formalism, which includes the MLWF Hamiltonians. The GeSNR FETs are analyzed using our in-house DFT-MLWF-NEGF solver that is described in [20]. We demonstrate strong bandstructure effects that occur in GeSNRs when their width is downscaled from ~ 4.2–0.7 nm, with considerable impact on bandgap, electron and hole effective masses, transmission, charge densities and carrier injection velocities. Finally, we show that scaling down the equivalent oxide thickness (EOT) enables various ac- and zz-GeSNR FETs to meet the requirements of the International Roadmap for Devices and Systems (IRDS) for logic technology beyond the "3 nm" node [21].

2 Methodology

We start by obtaining the Hamiltonian of the GeSNR using ab initio plane-wave DFT and transforming the DFT Hamiltonian into a localized basis using the MLWFs [9, 22]. The GeSNR FET structure is then simulated using several results obtained by NEGF simulations that are fed into the top-of-the-barrier (ToB) model to obtain ballistic performance of n- and p-type GeSNR FETs with armchair and zigzag edges.

The GeS nanoribbon super-cell is constructed from the 2D GeS unit cell (obtained from Materials Cloud [23]) that is repeated along the nanoribbon width 2–10 times, which translates to nanoribbon widths (*W*) from 0.76 to 3.70 nm for ac-GeSNRs and from 0.67 to 4.18 nm for zz-GeSNRs. Hydrogen atoms are used to passivate the edges of the nanoribbons. After constructing the super-cell, Quantum Espresso (QE) program package [24] is used to perform DFT calculations that include relaxation and electronic structure calculations. Since DFT assumes a periodic structure in all three directions, a vacuum layer of 20 Å is added to exclude any interactions in confined directions. Generalized gradient approximation parameterized by Perdew-Burke-Ernzerhof (PBE-GGA) [25] is used as the exchange–correlation functional in the simulations due to good evaluation of bandstructure, with a downside of underestimating the bandgap. In DFT simulations the cut-off energy is set to at least 1.5 × the suggested minimum cut-off provided in pseudopotential file for each element, i.e. 1360 eV in this study. Convergence threshold is set to 10^{-3} eV/Å for the ionic forces, and to 10^{-4} eV for the total energy. A 15-point equally-spaced Monkhorst–Pack grid [26] is used to sample the *k*-space in the transport direction with single point in the confined directions. Figure 1 shows a zz-GeSNR structure relaxed using DFT, with a top view in Fig. 1a and a side view in Fig. 1b, and we observe a slight shift of the edge atoms for both Ge and S atoms.

Due to the plane-wave basis of DFT in QE, output DFT Hamiltonians are localized in energy, but for NEGF calculations a spatially-localized basis is desired. Transformation of DFT Hamiltonians into spatially-localized basis is done using maximally-localized Wannier functions (MLWFs) [27], which results in much sparser tight-binding like matrices. The process of obtaining MLWF based Hamiltonians is implemented in Wannier90 program package [28–30]. The main component for the wannierization process are trial orbitals that are projected onto the Bloch manifold where localization in real space is linked to smoothness

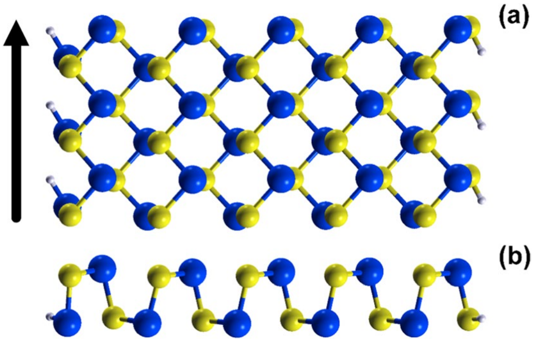

Fig. 1 **a** Top and **b** side view of the monolayer GeS nanoribbon with zigzag edges. Transport direction is designated with an arrow

in reciprocal Bloch space. Atomic orbitals are smooth in reciprocal space and are used as trial orbitals in this work. For ac-GeSNRs we choose *s* and *p* atomic orbitals as trial orbitals for both Ge and S atoms. On the other hand, *s*, *p* and *d* orbitals are chosen for Ge atoms and *s* and *p* orbitals for S atoms in the case of zz-GeSNRs. In Fig. 2 we compare the bandstructure plots obtained using DFT and MLWF and we observe a good agreement for energies around the Fermi level for both nanoribbon types, i.e. for ac-GeSNR in Fig. 2a and zz-GeSNR in Fig. 2b. After transformation to a localized basis, MLWF Hamiltonian matrices are used to construct the total GeSNR Hamiltonians of ~ 15 nm-long ac- and zz-GeSNRs with various widths which represent the channel of the device.

In our in-house code [14, 20] we employ the NEGF formalism to obtain electronic and transport properties of the device attached to two contacts, e.g. source and drain (S/D). Within NEGF, the device is described with the total GeSNR Hamiltonian representing the channel of the device and S/D self-energy matrices that account for contacts, i.e. open boundary conditions at S/D. While metallic S/D contacts can be included into NEGF [8, 31], here we assume ideal contacts, i.e. semi-infinite regions of the same material as the channel and calculated using the numerically efficient Sancho-Rubio method [19, 32]. Therefore, the resulting density of states (DOS) will exhibit van Hove singularities, whereas S/D transmission will be a step-like curve.

The top-of-the-barrier (ToB) model, as described in [33], is used to study ballistic device characteristics. Within the ToB model a FET is defined by three potential/energy points, i.e. S/D quasi Fermi levels and the self-consistently calculated barrier height between S/D, denoted as the ToB potential (Fig. 3a). The main inputs to ToB are DOS and

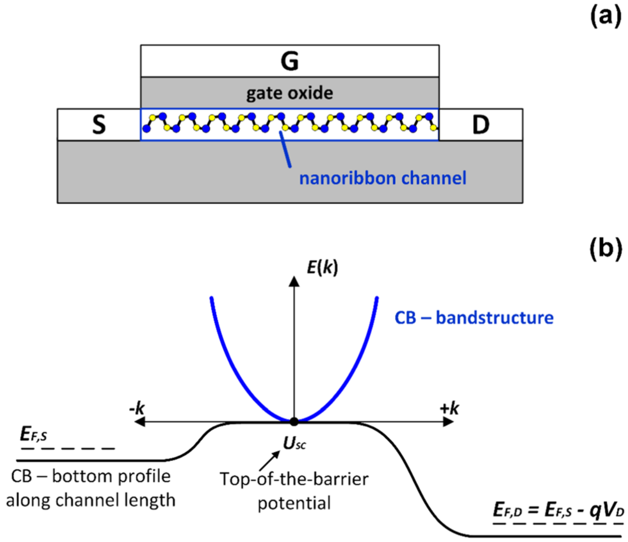

Fig. 3 **a** Illustration of a FET with a GeSNR channel. **b** Conduction band profile along the channel length with S/D quasi-Fermi levels and an illustration of the channel material bandstructure

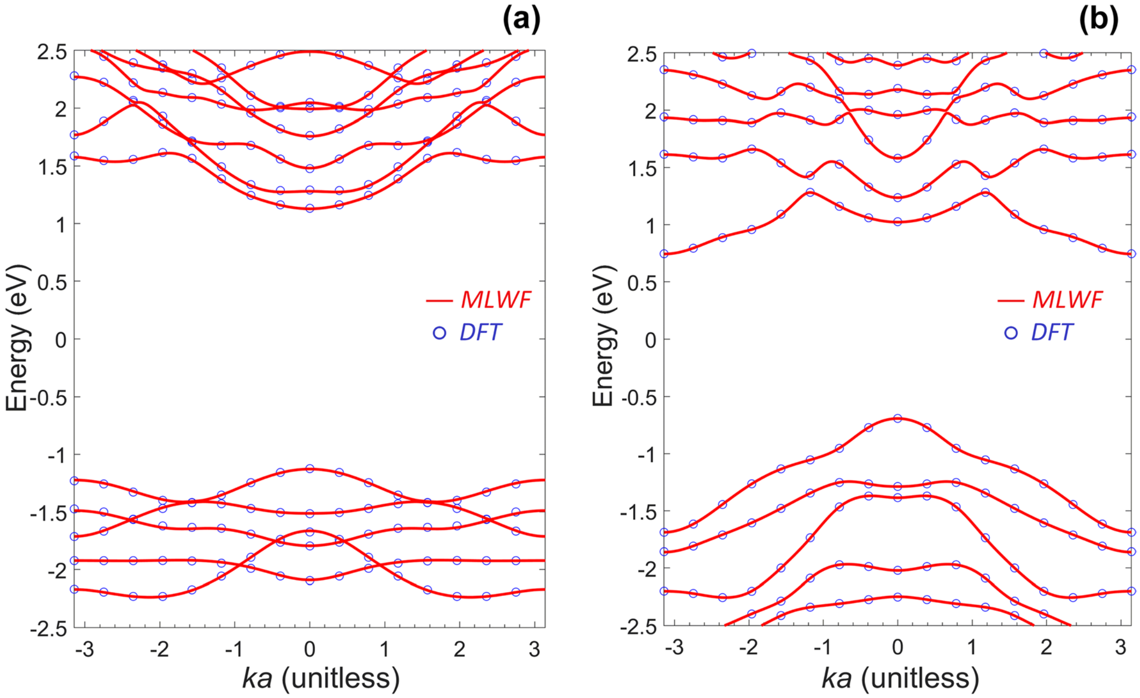

Fig. 2 Bandstructure obtained from DFT and MLWF for **a** ac-GeSNR, **b** zz-GeSNR

transmission calculated in equilibrium using NEGF, gate oxide material and thickness, and S/D Fermi levels due to doping. To illustrate the ToB model and the inclusion of orbitally-resolved bandstructure, conduction band profile along channel length is plotted in Fig. 3b. The ToB model finds only the thermionic current above the S/D barrier. Nevertheless, this approach is a dependable method for FETs where direct S/D tunneling and band to band tunneling (BTBT) are negligible, i.e. for channel lengths larger than ~ 15 nm, and materials with a bandgap wider than ~ 0.5 eV, respectively.

In this study, we simulate n- and p-type FETs with armchair and zigzag GeSNR channels. Simulation parameters are set to comply with IRDS for generations beyond the “3 nm” logic node [21]. In ToB FET model, channel control by the gate is assumed to be ideal, S/D doping is set at 0.01 molar fraction of the GeS areal density, and an initial EOT is set to 1 nm. Supply voltage is $V_{DD} = 0.7$ V, which is slightly higher than 0.65 V that is predicted by IRDS for "2.1 nm" and "1.5 nm" logic nodes. The ballistic ON-state current (I_{ON}) and ON-state charge density at ToB (Q_{CH}) are extracted when both gate and drain are biased at the supply voltage. Simulations are done with a common OFF-state current (I_{OFF}) for all devices to provide a fair and meaningful comparison between various GeS quasi-1D nanodevices. The I_{OFF} is set to 10 nA/μm so the study deals with high performance (HP) devices as defined by IRDS.

3 Results and discussion

Bandstructure of various zz-GeSNRs is shown in Fig. 4, and generally we observe that zz-GeSNRs exhibit an indirect bandgap for all nanoribbon widths. Conduction band (CB)

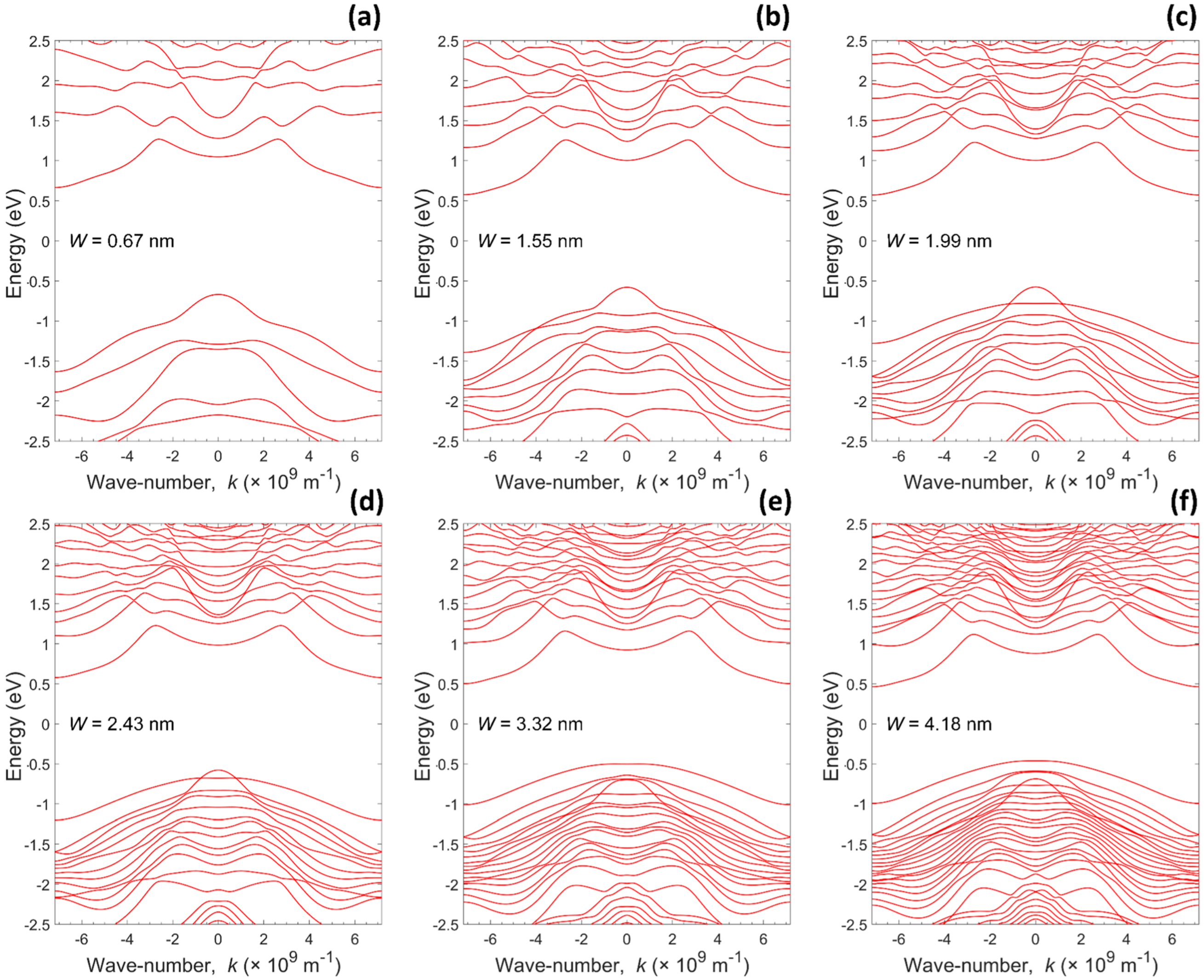

Fig. 4 Bandstructure of zigzag GeSNRs with the widths of **a** 0.67 nm, **b** 1.55 nm, **c** 1.99 nm, **d** 2.43 nm, **e** 3.32 nm, and **f** 4.18 nm

near the bandgap shows almost no change while scaling down nanoribbon width, i.e. the lowest CB subband is not affected by width scaling. On the other hand, in valence band (VB) a subband with a higher curvature, i.e. lower effective mass, emerges for nanoribbon widths below 3.32 nm. In order to provide a full picture, here we refer to our previous work where the bandstructure of various ac-GeSNRs was studied [17]. Notably, ac-GeSNRs with the widths below 1.86 nm transition from an indirect to a direct semiconductor. Additionally, for $W = 1.86$ nm the subband with lower effective mass for both conduction and valence bands becomes dominant in ac-GeSNRs.

From the bandstructure we extract the bandgap (E_g) and plot it in Fig. 5 for the examined ac- and zz-GeSNRs with the widths ranging from ~ 4.2 to ~ 0.6 nm. Scaling down the width of ac-GeSNRs changes the bandgap from indirect to direct, as it increases from 1.73 eV for $W = 3.70$ nm to 1.94 eV for $W = 1.86$ nm. The direct bandgap in sub-1.86 nm-wide ac-GeSNRs shows a similar scaling effect with the maximum direct E_g of 2.24 eV obtained for the 0.76 nm-wide ac-GeSNR. On the other hand, all zz-GeSNRs have an indirect bandgap but the Eg scaling law is different in two width regions, depending on the behavior of the highest subband in VB. In wider GeSNRs with zigzag edges the bandgap change is limited, i.e. E_g increases from 0.91 eV for $W = 4.18$ nm to 0.99 eV for the 3.32 nm-wide zz-GeSNR. Scaling the width below 3.32 nm changes the bandstructure so that the highest subband in VB is the one with a lower curvature (see Fig. 4d and e). Hence, bandgap increase to 1.12 eV for the 2.43 nm-wide zz-GeSNR, and reaches the maximum of 1.33 eV in the 0.67 nm-wide zz-GeSNR due to the strong quantum confinement in this nearly 1D nanostructure. For the large-area 2D GeS we obtain $E_g = 1.69$ eV, which is similar to the value of 1.65 eV reported in [15]. The bandgap of the 2D material is lower than in ac-GeSNRs due to quantum confinement, but higher than in zz-GeSNRs. The latter is unsurprising due to the existence of a subband in CB that belongs to edge states.

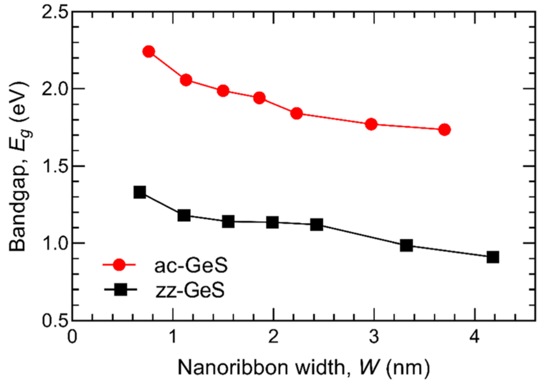

Fig. 5 Impact of nanoribbon width-scaling on the bandgap of armchair and zigzag GeSNRs

Effective mass (m^*) is a good indicator of device properties and can be obtained near bandstructure minima/maxima by a parabolic approximation. The effective mass of the lowest conduction subband, i.e. electron effective mass m_e^*, and highest valence subband, i.e. hole effective mass m_h^*, for ac- and zz-GeSNRs are reported in Fig. 6. The effective mass in ac-GeSNRs (Fig. 4a) for both electrons and holes increase while scaling down nanoribbon width. The m_e^* increases from 0.33 m_0 for $W = 3.70$ nm to 1.37 m_0 for $W = 0.76$ nm, whereas m_h^* increases from 0.34 m_0 for $W = 3.70$ nm to 1.09 m_0 for $W = 0.76$ nm. The effective masses for both holes and electrons in ac-GeSNRs are higher than in 2D GeS in the armchair direction. The difference is larger than ~ 1.4 × because in [34] the authors obtained $m_e^* = 0.23\ m_0$ and $m_h^* = 0.25\ m_0$. Therefore, transport properties of ac-GeSNRs relevant for device applications are

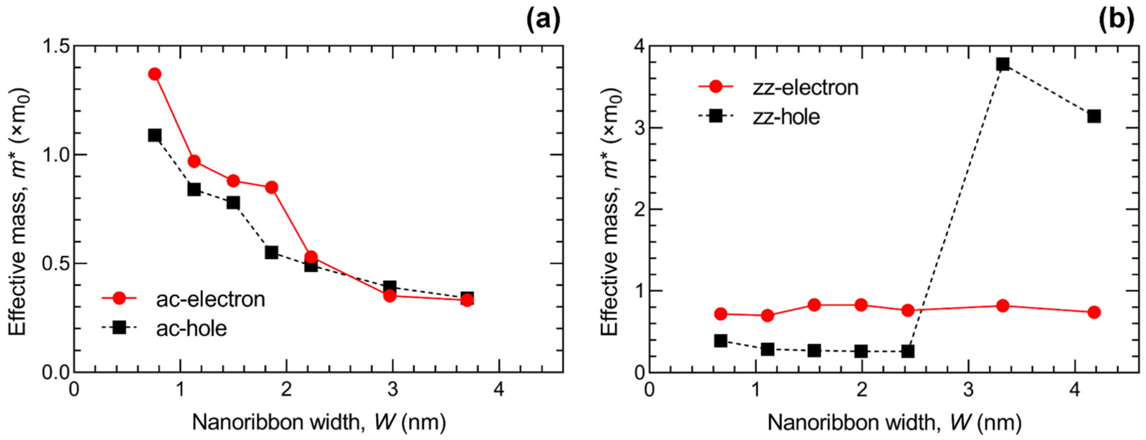

Fig. 6 Dependence of electron and hole effective masses on nanoribbon width for **a** armchair and **b** zigzag GeSNRs. Effective masses are extracted for the lowest (highest) subband in the conduction (valence) band

expected to suffer significantly from downscaling and confinement effects. On the other hand, in zz-GeSNRs (Fig. 4b) the effective mass of electrons is almost constant for all GeSNR widths, varying slightly from $m_e^* = 0.70\ m_0$ for $W = 1.11$ nm to $m_e^* = 0.83\ m_0$ for $W = 1.99$ nm. In contrast to m_e^*, hole effective mass is $> 3\ m_0$ for $W \geq 3.32$ nm. We note that the extraction of m_h^* is much less accurate due to the existence of a subband with two barely noticeable peaks near the Γ point with high effective mass. Scaling down zz-GeSNR width below $W = 3.32$ nm gives rise to subband with much lower effective mass with minimum obtained for $W = 1.99$ nm where $m_h^* = 0.26\ m_0$. As for the 2D GeS in zigzag direction, as reported in [34], electron effective mass of 0.55 m_0 in 2D GeS is ~ 1.3 × smaller than the minimum value obtained for m_e^* in zz-GeSNRs. On the other hand, holes are lighter in zz-GeSNRs than in the 2D counterpart, i.e. $m_h^* = 0.67\ m_0$ is reported for 2D GeS in the zigzag direction, which is ~ 2.6 × larger than the minimum hole effective mass obtained for zz-GeSNRs with $W \leq 2.43$ nm.

Effective mass in the transport direction can help roughly predict device performance so, for example, the results provided in Fig. 5 indicate promising zz-GeSNR FETs if nanoribbon width is kept under 2.43 nm. However, the rough prediction can be improved by simulating the ON-state current to assess device performance in more detail. The I_{ON} is plotted for n- and p-channel GeSNR FETs for GeSNRs with armchair (Fig. 7a) and zigzag (Fig. 7b) edges. The ON-state current of the ac-GeSNR nFETs decreases monotonically while scaling down the channel width, from 1.52 mA/µm for $W = 3.70$ nm to $I_{ON} = 0.82$ mA/µm for $W = 0.76$ nm. Similarly, the I_{ON} of pFETs with armchair GeSNRs also decreases monotonically while scaling down the channel width, from 1.55 mA/µm for $W = 3.70$ nm to 0.77 mA/µm in the 0.76 nm-wide nanoribbon. On the other hand, the ON-state current exhibits qualitatively different behavior in FETs with zz-GeSNRs. Namely, in zz-GeSNR nFETs the I_{ON} is relatively constant with respect to width scaling, and ranges between 0.96 and 0.80 mA/µm. However, in zz-GeSNR pFETs the driving current exhibits a local maximum for the 1.99 nm-wide device with $I_{ON} = 1.62$ mA/µm, and a local minimum of 0.32 mA/µm for $W = 3.32$ nm. Digital switching capabilities of GeSNR FETs for logic applications can be assessed by the I_{ON}/I_{OFF} ratio. Both ac- and zz-GeSNR FETs show good switching capabilities with ac-GeSNR FETs showing I_{ON}/I_{OFF} higher than 7.7×10^4 while zz-GeSNR FETs show I_{ON}/I_{OFF} higher than 3.2×10^4. Maximum I_{ON}/I_{OFF} value of 1.62×10^5 is obtained for zz-GeSNR FETs with $W = 1.99$ nm.

The ON-state performance for both zigzag and armchair GeSNR FETs is directly correlated to the bandstructure along the transport direction. Namely, the current depends on the amount of charge in the channel and its transport properties, i.e. carrier charge density at ToB depends on DOS and transport probability for each conducting mode is represented by the transmission characteristics. The ON-state current is mainly determined by the subbands that are the nearest to the conduction band minimum (CBM) for nFETs, and valence band maximum (VBM) for pFETs. Higher effective mass correlates directly to lower I_{ON} which can be seen by comparing e.g. the effective mass in Fig. 6a and current in Fig. 7a for GeSNRs with armchair edges. Here we can see that the downscaling of ac-GeSNR width increases the effective mass and decreases the I_{ON}, both monotonically. Additionally, a considerable drop in hole effective mass in zz-GeSNRs when going from the 3.3 nm to 2.4 nm-wide nanoribbons (Fig. 6b) translates into a significant I_{ON} increase for zz-GeSNRs pFETs in the same width range (Fig. 7b).

To further analyze the ON-state performance of FETs with quasi-1D GeS channels we investigate the features of DOS, transmission, charge density and injection velocity. Transmission and DOS of ac-GeSNRs are discussed

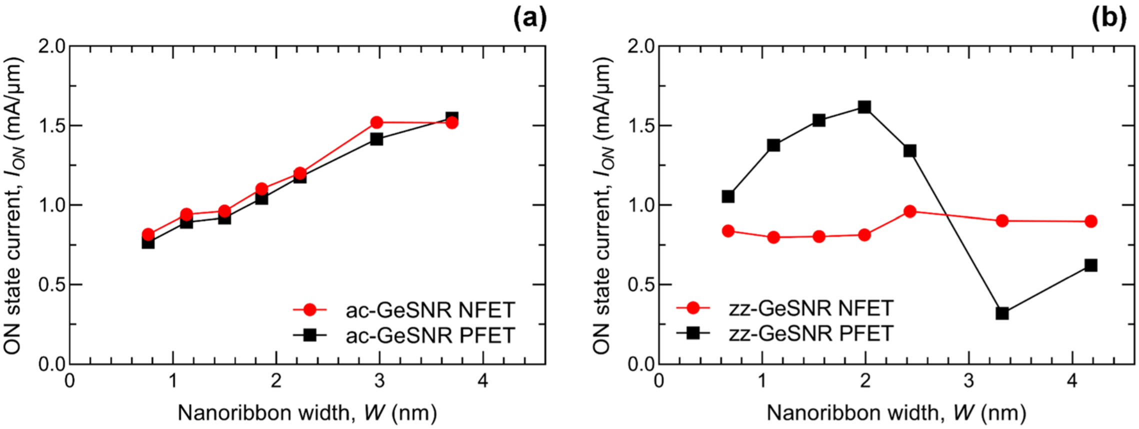

Fig. 7 Width-dependence of the ON-state current in n- and p-type **a** armchair and **b** zigzag GeSNR FETs. I_{ON} is extracted at $V_{GS} = V_{DS} = V_{DD} = 0.7$ V with a common $I_{OFF} = 10$ nA for all devices

previously in [17], but only for electrons in the CB. In short, we showed that scaling down the width increases DOS near the CBM (due to emergence of subbands with lower curvature, i.e. higher effective mass), and decreases the number of Van Hove singularities (VHS) due to a lower number of conducting modes in narrower nanoribbons. Moreover, transmission equals unity near the CBM for all ac-GeSNR widths and rises for wider ac-GeSNRs due to higher number of subbands near CBM. Figure 8 reports the DOS and transmission near the CBM, VBM, or both for ac- or zz-GeSNRs of various widths. Since the characteristics of CB are already known, for ac-GeSNRs we plot only the DOS and transmission in the VB in Fig. 8(a,b). For zz-GeSNRs, the properties in the CB and VB are plotted in Fig. 8(c,d) and (e,f), respectively.

The DOS in ac-GeSNRs near the VBM is rather high with a high number of densely spaced Van Hove singularities. Scaling down nanoribbon width decreases the transmission near the VBM from 2 for $W = 3.70$ nm to 1 for $W < 1.86$ nm, which is where ac-GeSNRs transition from indirect to direct

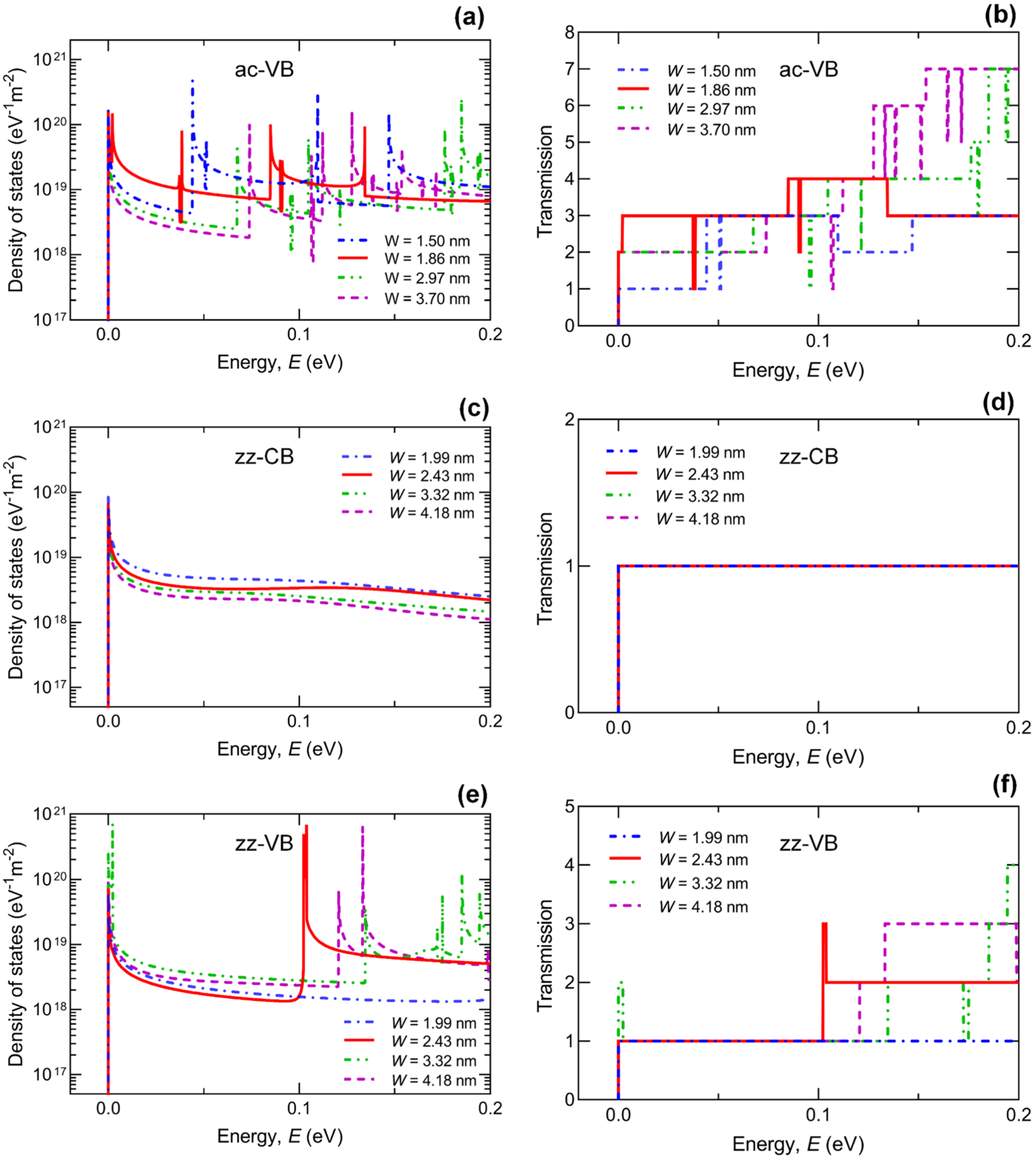

Fig. 8 Comparison of DOS and transmission in **a**, **b** valence band of ac-GeSNRs, **c**, **d** conduction band of zz-GeSNRs and **e**, **f** valence band of zz-GeSNRs for various nanoribbon widths. All DOS and transmission plots are shifted so that the CBM and VBM are positioned at 0 eV

semiconductor. For 1.86 nm-wide ac-GeSNR, transmission quickly rises to 3 at VBM – 0.002 eV because a subband emerges at the Γ point. The DOS curves in CB for zz-GeSNRs have a similar magnitude with a single dominant band. This is also visible in the transmission plot where CB transmission is unity near the CBM for all zz-GeSNR widths. The immunity of electron bands in zz-GeSNRs to width-scaling confinement effects observed for transmission in Fig. 8d is in qualitative agreement with I_{ON} behavior of zz-GeSNR nFETs reported in Fig. 7b. On the other hand, transmission and DOS in VB of zz-GeSNR exhibit a bit more interesting characteristics than in the CB. The widest zz-GeSNRs with $W = 3.32$ nm and $W = 4.18$ nm have higher DOS near the VBM due to the low-curvature and high-m^* in the highest VB subband (see Fig. 4e and f). The 3.32 nm-wide zz-GeSNR also shows a secondary VHS at an energy 0.002 eV away from the VBM because of the shape of the top subband that has two barely noticeable peaks near Γ point. This effect is also seen in the transmission plot in Fig. 8f where the transmission equals 2 in the narrow energy range near the VBM and decreases to unity at higher energies. The similar transmission values in VB of zz-GeSNRs (Fig. 8f) stand in contrast with a strongly nonmonotonic I_{ON} behavior in zz-GeSNR pFETs reported in Fig. 7b. Therefore, in this case key information is contained in effective masses along the transport direction which, in turn, are visible in the properties of channel charge density and carrier injection velocity.

The stark differences in DOS reported in Fig. 8 should translate into considerable variations of Q_{CH} in various GeSNR devices. The ON-state charge density is plotted for n- and p- type FETs for various widths of ac-GeSNRs and zz-GeSNRs in Fig. 9a and b, respectively. Scaling down ac-GeSNR width shows similar scaling properties for both n- and p-type FETs. The nFET charge density slightly increases from 8.03×10^{12} cm^{-2} for the GeSNR width of 3.70 nm to 8.37×10^{12} cm^{-2} for the 0.76 nm-wide ac-GeSNR. Similarly, in pFETs with armchair GeSNRs charge density increases from 7.99×10^{12} cm^{-2} for $W = 3.70$ nm to 8.43×10^{12} cm^{-2} for $W = 1.50$ nm. To accommodate for the increase of bandgap in the narrowest nanoribbons and setting a proper I_{OFF}, charge density is the highest in the narrowest nanoribbons where the ON-state current is the lowest. On the other hand, scaling down zz-GeSNR width (Fig. 9b) increase the ToB charge density in nFETs from 7.77×10^{12} cm^{-2} in the 4.18 nm-wide zz-GeSNR up to 8.26×10^{12} cm^{-2} for $W = 0.67$ nm. While the ON-state current has similar values for all nFETs with zz-GeSNR channel, charge density is the highest for the narrowest nanoribbons due to the increase of bandgap and setting of a common I_{OFF}. In the case of pFETs with zz-GeSNR channels we can split the devices into three groups. The first group includes zz-GeSNRs with $W > 2.43$ nm where charge density is the highest among all simulated GeSNRs with the maximum value obtained for $W = 4.18$ nm where $Q_{CH} = 8.81 \times 10^{12}$ cm^{-2}. This occurs due to the subband with high DOS near the VBM, as seen in Fig. 4e and f and Fig. 8e, which in turn gives rise to more mobile charge at the ToB for the same applied voltage. A local minimum in hole density of $Q_{CH} = 7.86 \times 10^{12}$ cm^{-2} is reached for $W = 1.99$ nm after which the hole density increases to 8.19×10^{12} cm^{-2} in the 0.67 nm-wide zz-GeSNR. Charge density is of the same magnitude for all ac- and zz-GeSNR FETs, agreeing with the obtained magnitude of the ON-state current, and with a scaling behavior qualitatively comparable to effective mass scaling shown in Fig. 6.

Injection velocity (v_{inj}) dependence on V_{GS} in the range from the threshold voltage to the supply voltage (~ 0.2 V to 0.7 V) for n- and p-type GeSNR FETs with armchair (Fig. 10) and zigzag edges (Fig. 11). Nanoribbon widths are the same as in Fig. 8. For each device, a relative v_{inj} increase

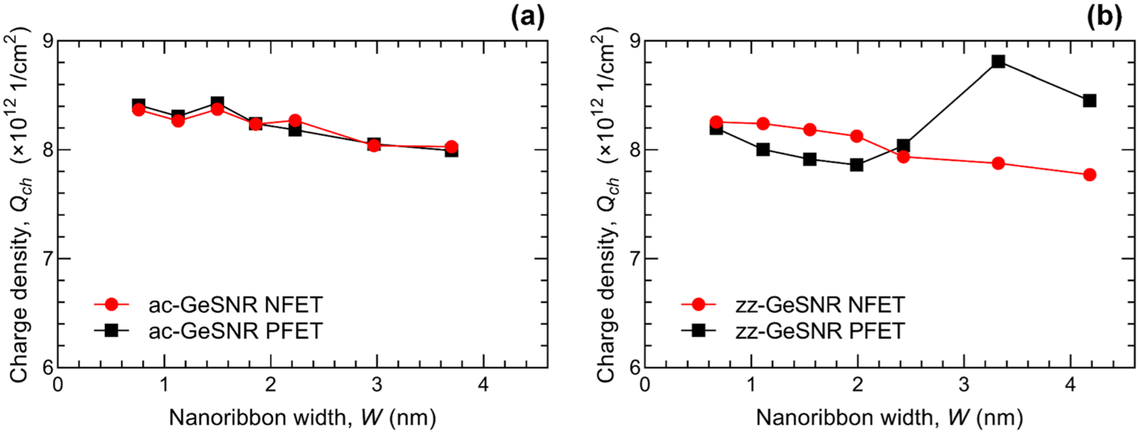

Fig. 9 Width-dependence of charge density at ToB in n- and p-type **a** armchair and **b** zigzag GeSNR FETs. Charge density is extracted in the ON-state, i.e. for $V_{GS} = V_{DS} = V_{DD} = 0.7$ V

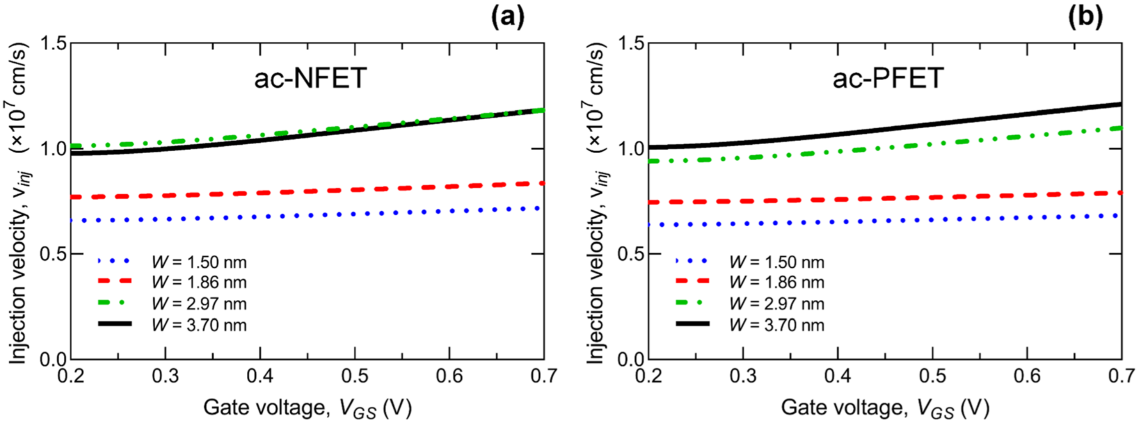

Fig. 10 Dependence of injection velocity on gate voltage in **a** n-type and **b** p-type armchair GeSNR FETs for various nanoribbon widths

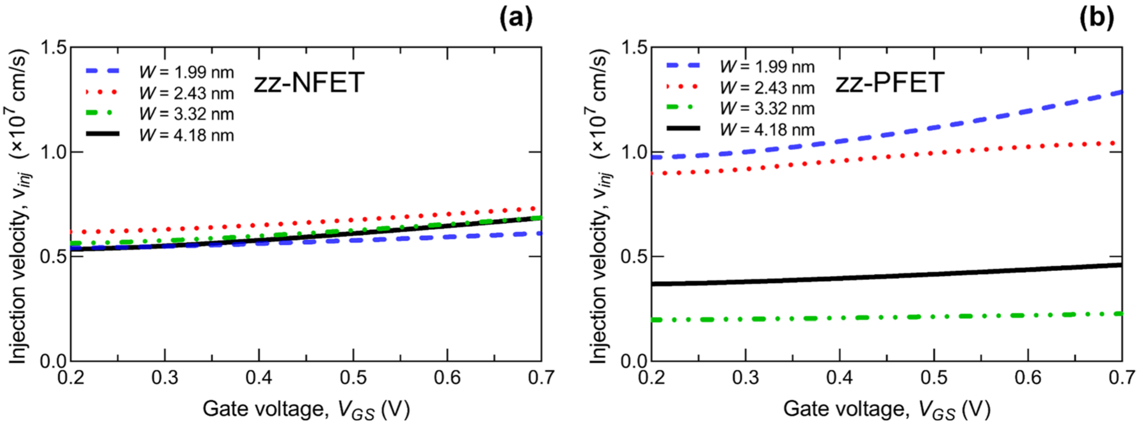

Fig. 11 Injection velocity vs. gate voltage for **a** n-type and **b** p-type zigzag GeSNR FETs with different nanoribbon widths

is defined as an increase of injection velocity extracted at 0.7 V compared to the value at 0.2 V. As shown in Fig. 10a, scaling down the width of ac-GeSNR nFETs decreases the electron v_{inj} from 1.18×10^7 cm/s for $W = 3.70$ nm to 0.72×10^7 cm/s for $W = 1.50$ nm. Injection velocity noticeably rises with increasing V_{GS} only in wider nanoribbons because wider GeSNRs exhibit a denser bandstructure near the CBM, and therefore higher modulation of v_{inj} with the applied bias. The relative v_{inj} increase equals 20% for $W = 3.70$ nm, while the smallest relative increase is 9% and is obtained for $W = 1.50$ nm. The hole injection velocity in ac-GeSNR pFETs (Fig. 10b) shows comparable values and nearly identical scaling properties as electron v_{inj} in nFETs with ac-GeSNR channels. On the other hand, electron injection velocity in zz-GeSNR nFETs changes very little for different nanoribbon widths and various gate bias. The v_{inj} ranges from 0.61×10^7 cm/s to 0.73×10^7 cm/s, with the highest value obtained for the 2.43 nm-wide zz-GeSNR due to the existence of a single dominant subband in CB that is resistant to scaling. Unlike nFETs, the hole injection velocity in zz-GeSNR pFETs varies considerably with the width downscaling and exhibits bias-dependence, especially for the ~ 2 nm-wide device. The maximum hole v_{inj} equals 1.29×10^7 cm/s that is obtained in the 1.99 nm-wide zz-GeSNR, whereas the minimum v_{inj} is only 0.23×10^7 cm/s for $W = 3.32$ nm. This ~ 5.6 × difference is caused by the emergence of a subband in VB of zz-GeSNRs with a higher curvature, as seen in Fig. 3 and discussed in related text. Contrary to other ac- and zz-GeSNR FETs in which the widest nanoribbons exhibit the highest relative v_{inj} increase, the largest improvement of hole injection velocity in zz-GeSNRs is 32% and occurs in the 1.99 nm-wide device. The findings related to the injection velocity are in line with the reported bandstructure, effective mass and current modulation with width scaling. For example, lower effective mass leads to a higher v_{inj} and this relationship can be clearly seen when comparing effective mass in Fig. 6a and v_{inj} in Fig. 10, i.e. monotonic increase of m^* leads to v_{inj} decrease when the width is scaled down in ac-GeSNRs. The ON-state current is proportional to v_{inj} and Q_{CH}, and while v_{inj} shows similar scaling laws compared to I_{ON}, Q_{CH} exhibits an inverse scaling behavior as discussed earlier. Therefore, the injection velocity is a dominant factor that determines the values and trends of drain current in GeSNR FETs.

In order to benchmark GeSNR devices against relevant digital logic technology goals, we compare our results to the ON-state current requirements of IRDS for HP devices for two future nodes, i.e. “2.1 nm” node with $I_{ON} = 1.79$ mA/µm and “1.5 nm” node with $I_{ON} = 1.98$ mA/µm. Initially in the simulations the EOT is set to 1 nm that results in I_{ON} values reported in Fig. 7, and none of these GeSNR FETs meets the IRDS requirements for either node. Nevertheless, using high-κ dielectrics such as HfO_2 with a relative dielectric constant of ~ 20 enables further oxide thickness scaling down to ~ 0.5 nm. Hence, we simulate the ON-state for n- and p-channel, ac- and zz-GeSNR FETs again for various nanoribbon widths and different EOT values ranging from 0.5 to 1 nm. The I_{OFF} is common for all devices and is again set to 10 nA/µm in order to assess GeSNR FETs as potential HP transistors. The results are plotted in Fig. 12 and Fig. 13 for GeSNR FETs with armchair and zigzag edges, respectively. In the plots, light blue squares indicate that a specific combination of width and EOT meets the “2.1 nm” node goal, while darker blue squares indicate the same for both the “2.1 nm” and “1.5 nm” technology node.

The results for armchair n-type (Fig. 12a) and p-type (Fig. 12b) GeSNR FETs show that width-scaling decreases the EOT needed to meet the requirements for “2.1 nm” and “1.5 nm” nodes. The ac-GeSNR nFETs with the widths of 3.70 nm and 2.97 nm fulfil the “2.1 nm” node requirements for EOT < 0.85 nm, while EOT < 0.77 nm is needed for the “1.5 nm” node. The narrowest ac-GeSNR nFETs that meet IRDS requirements are those with $W = 1.13$ nm and $W = 1.50$ nm, but a small EOT ~ 0.5 nm is needed in these devices. Similarly, for pFETs wider ac-GeSNRs also allow a thicker oxide, which benefits the fabrication process complexity. For example, the 3.70 nm-wide ac-GeSNR pFET exhibits the largest allowed EOT of 0.86 nm and 0.78 nm, depending on the desired node. The narrowest ac-GeSNRs that meet IRDS requirements as p-channel devices are those with EOT ~ 0.5 nm, with the width of 1.13 nm for “2.1 nm” node, and $W = 1.86$ nm for “1.5 nm” node. The 0.76 nm-wide ac-GeSNR n- and p-type FETs do not meet IRDS specification for either node even with a downscaled oxide thickness, which is expected given the bandstructure and confinement effects explained earlier in the text.

Devices with zigzag edges, i.e. zz-GeSNR n-type FETs shown in Fig. 13a and p-type FETs reported in Fig. 13b, experience remarkably different scaling effects compared to their armchair-edge counterparts. The nFETs with $W \geq 2.43$ nm and with EOT up to ~ 0.55 nm meet IRDS goals for the “2.1 nm” node, whereas only the 2.43 nm-wide and 4.18 nm-wide devices with EOT ~ 0.5 nm meet the requirements for “1.5 nm” node. The zz-GeSNR nFETs with sub-1.99 nm widths do not meet IRDS specifications for either node. These results indicate that 2D GeS nFETs in the zz-direction should meet IRDS requirements because the large-area GeS does not have the subband that is dominant near the CBM. However, the influence of this subband seems to be a bottleneck for nFETs with a zz-GeSNR channel. In

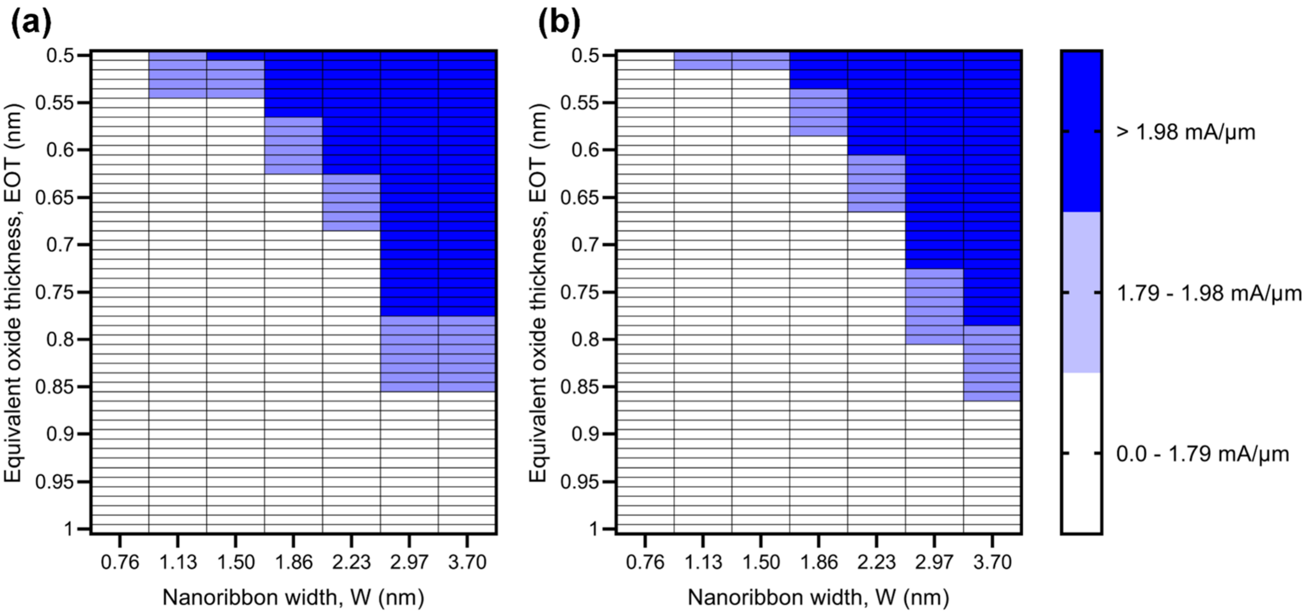

Fig. 12 ON-state current dependence on equivalent oxide thickness and nanoribbon width in **a** n-type and **b** p-type armchair GeSNR FETs

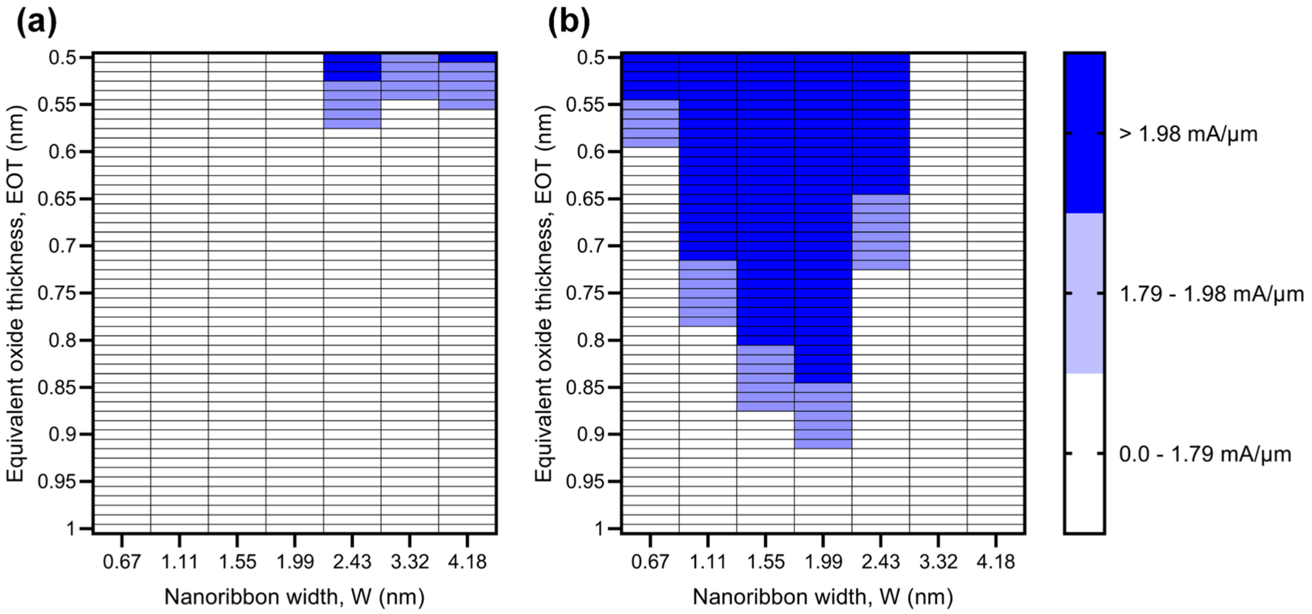

Fig. 13 ON-state current dependence on equivalent oxide thickness and nanoribbon width in **a** n-type and **b** p-type zigzag GeSNR FETs

contrast, the situation looks more optimistic for zz-GeSNR pFETs. Namely, some of these devices with $W \leq 2.43$ nm meet IRDS requirements for both nodes. These results correspond to those in Fig. 7b where maximum I_{ON} is reported for ~ 2 nm-wide zigzag GeSNR pFETs, and is caused by the emergence of sub-band with lower effective mass. In turn, this effect creates a region of high I_{ON} that is centered around W ~ 1.55 nm and EOT ~ 0.65 nm in the EOT-W plane visible in Fig. 13b. For example, within this region the 1.99 nm-wide zz-GeSNR pFET meets the IRDS requirements for both nodes when EOT < 0.85 nm. Beyond this region, i.e. for $W \geq 3.32$ nm, IRDS specifications are not fulfilled for either node. We expect the same to be true for 2D GeS pFETs in the zigzag direction, irrespective of node and EOT employed in the device.

The results obtained for armchair and zigzag GeS nanoribbon FETs are promising when compared to the IRDS requirements, however, we note that the upper ballistic limits are explored in this work. Clearly, taking realistic metal contacts and carrier scattering would deteriorate the reported GeSNR FET performance. For example, due to polar nature of GeS the mobility decreases by ~ 4 × when polarization effects on carrier transport are taken into account as shown in [34]. Another potential problem for realistic GeSNR devices is edge roughness, which greatly depends on advancements in manufacturing of such devices at the nanoscale. While some of these issues such as elastic defect scattering, inelastic phonon scattering, and the impact of metal contacts and contact resistance will be addressed in future work, we nevertheless stress the potential of GeSNRs for future multi-bridge-channel FETs as reported in our study.

4 Conclusions

We presented an in-depth study on the electronic, transport and ballistic device characteristics of quasi-1D GeS nanostructures. We investigated sub-5 nm-wide and ~ 15 nm-long armchair and zigzag GeSNRs and GeSNR n- and p- type FETs by combining DFT, MLWF, NEGF and ToB modeling and numerical simulations. Starting from the bandstructure, and analyzing DOS, transmission, carrier effective mass and injection velocity, we show that some ac- and zz-GeSNR FETs show promising ON-state performance when benchmarked against IRDS requirements. Moreover, IRDS specifications are fulfilled for “2.1 nm” and “1.5 nm” nodes with realistic and technologically relevant EOT values. In both n- and p-type FETs with ac-GeSNR channels the I_{ON} monotonically decreases while scaling down nanoribbon width due to increase of m^* and, consequently, reduction of electron and hole injection velocity. Although ac-GeSNR FETs exhibit a deteriorating performance with the width-downscaling, for $W > 1.13$ nm and by extension for 2D GeS in armchair direction a device that meets IRDS specifications is possible for both n- and p-type FETs. In contrast, all zz-GeSNR have a relatively high electron m^*, which results in low electron v_{inj} and poor ON-state performance of zz-GeSNR nFETs. The IRDS goals are met only for the widest analyzed nanoribbons and with an EOT close to 0.5 nm, which disqualifies zz-GeSNR as a plausible solution for ultra-scaled nFETs. The most interesting characteristics are provided by zz-GeSNR pFETs that exhibit nonmonotonic behavior of hole density, effective mass, injection velocity, and ON-state current. Namely, for $W \leq 2.43$ nm a subband with low effective mass appears in zz-GeSNRs at the top of VB that results in high hole v_{inj} and good ON-state performance of zz-GeSNR pFETs. For these devices, a region of acceptable EOT and W values exists where IRDS specifications are fulfilled. The zz-GeSNR pFETs with $W > 2.43$ nm, and by extension 2D GeS pFETs with channel oriented along the zigzag direction, do not meet IRDS requirements. Finally, the I_{ON}/I_{OFF} ratio of at least ~ 7.7×10^4 and ~ 3.2×10^4 is reported for GeSNR FETs with armchair and zigzag nanoribbons, respectively, which indicates good digital switching performance for logic devices. Therefore, our work demonstrates that quasi-1D GeS nanostructures offer interesting and promising electronic and ballistic transport properties with potential applications in future extremely-scaled transistors.

Acknowledgements This work was supported by the Croatian Science Foundation under the project CONAN2D (Grant No. UIP-2019-04-3493).

Author contribution All authors contributed to the study conception and design. Material preparation, data collection and analysis were performed by MM and MP. The first draft of the manuscript was written by MM and all authors commented on previous versions of the manuscript. All authors read and approved the final manuscript. The datasets generated during and/or analyzed during the current study are available from the corresponding author on reasonable request.

Funding This work was supported by the Croatian Science Foundation under the project CONAN2D (Grant No. UIP2019-04-3493). The authors have no relevant financial or non-financial interests to disclose.

Data availability Enquiries about data availability should be directed to the authors.

Competing interests The authors have not disclosed any competing interests.

References

1. Novoselov, K.S., Geim, A.K., Morozov, S.V., Jiang, D., Zhang, Y., Dubonos, S.V., Grigorieva, I.V., Firsov, A.A.: Electric field effect in atomically thin carbon films. Science **306**, 666–669 (2004). https://doi.org/10.1126/science.1102896
2. Fiori, G., Bonaccorso, F., Iannaccone, G., Palacios, T., Neumaier, D., Seabaugh, A., Banerjee, S.K., Colombo, L.: Electronics based on two-dimensional materials. Nat. Nanotechnol. **9**, 768–779 (2014). https://doi.org/10.1038/nnano.2014.207
3. Schwierz, F., Pezoldt, J., Granzner, R.: Two-dimensional materials and their prospects in transistor electronics. Nanoscale **7**, 8261–8283 (2015). https://doi.org/10.1039/C5NR01052G
4. Iannaccone, G., Bonaccorso, F., Colombo, L., Fiori, G.: Quantum engineering of transistors based on 2D materials heterostructures. Nat. Nanotech. **13**, 183–191 (2018). https://doi.org/10.1038/s41565-018-0082-6
5. Zeng, S., Tang, Z., Liu, C., Zhou, P.: Electronics based on two-dimensional materials: Status and outlook. Nano Res. **14**, 1752–1767 (2021). https://doi.org/10.1007/s12274-020-2945-z
6. Allain, A., Kang, J., Banerjee, K., Kis, A.: Electrical contacts to two-dimensional semiconductors. Nat. Mater. **14**, 1195–1205 (2015). https://doi.org/10.1038/nmat4452
7. Gahoi, A., Kataria, S., Driussi, F., Venica, S., Pandey, H., Esseni, D., Selmi, L., Lemme, M.C.: Dependable contact related parameter extraction in graphene-metal junctions. Adv. Electron. Mater. **6**, 2000386 (2020). https://doi.org/10.1002/aelm.202000386
8. Poljak, M., Matić, M., Zeljko, A.: Minimum contact resistance in monoelemental 2D material nanodevices with edge-contacts. IEEE Electron Device Lett. **42**, 1240–1243 (2021). https://doi.org/10.1109/LED.2021.3087908
9. Klinkert, C., Szabó, Á., Stieger, C., Campi, D., Marzari, N., Luisier, M.: 2-D Materials for ultrascaled field-effect transistors: one hundred candidates under the ab initio microscope. ACS Nano **14**, 8605–8615 (2020). https://doi.org/10.1021/acsnano.0c02983
10. Carvalho, A., Wang, M., Zhu, X., Rodin, A.S., Su, H., Castro Neto, A.H.: Phosphorene: from theory to applications. Nat. Rev. Mater. **1**, 16061 (2016). https://doi.org/10.1038/natrevmats.2016.61
11. Betti, A., Fiori, G., Iannaccone, G.: Atomistic investigation of low-field mobility in graphene nanoribbons. IEEE Trans. Electron Devices **58**, 2824–2830 (2011). https://doi.org/10.1109/TED.2010.2100045
12. Kaneko, S., Tsuchiya, H., Kamakura, Y., Mori, N., Ogawa, M.: Theoretical performance estimation of silicene, germanene, and graphene nanoribbon field-effect transistors under ballistic transport. Appl. Phys. Express. **7**, 035102 (2014). https://doi.org/10.7567/APEX.7.035102
13. Poljak, M.: Electron mobility in defective nanoribbons of monoelemental 2D materials. IEEE Electron Dev. Lett. **41**, 151–154 (2020). https://doi.org/10.1109/LED.2019.2952661
14. Poljak, M., Matić, M.: Bandstructure and size-scaling effects in the performance of monolayer black phosphorus nanodevices. Materials. **15**, 243 (2021). https://doi.org/10.3390/ma15010243
15. Ding, Y., Liu, Y.-S., Yang, G., Gu, Y., Fan, Q., Lu, N., Zhao, H., Yu, Y., Zhang, X., Huo, X., Chen, G.: High-performance ballistic quantum transport of sub-10 nm monolayer GeS field-effect transistors. ACS Appl. Electron. Mater. **3**, 1151–1161 (2021). https://doi.org/10.1021/acsaelm.0c01019
16. Li, R., Cao, H., Dong, J.: Electronic properties of group-IV monochalcogenide nanoribbons: studied from first-principles calculations. Phys. Lett. A **381**, 3747–3753 (2017). https://doi.org/10.1016/j.physleta.2017.09.048
17. Matić, M., Poljak, M.: Ab initio quantum transport simulations of monolayer GeS nanoribbons. Solid-State Electron. (2022). https://doi.org/10.1016/j.sse.2022.108460
18. Vasileska, D., Goodnick, S.M., Klimeck, G.: Computational Electronics: Semiclassical and Quantum Device Modeling and Simulation. CRC Press, Boca Raton (2010)
19. Pourfath, M.: The Non-Equilibrium Green's Function Method for Nanoscale Device Simulation. Springer, Wien (2014)
20. Matić, M., Župančić, T., Poljak, M.: Parallelized ab initio quantum transport simulation of nanoscale bismuthene devices. In: 2022 45th Jubilee International Convention on Information, Communication and Electronic Technology (MIPRO). pp. 118–123 (2022)
21. "IEEE Intl. Roadmap for Devices and Systems (IRDS), 2019 Update." https://irds.ieee.org/.
22. Afzalian, A.: Ab initio perspective of ultra-scaled CMOS from 2D-material fundamentals to dynamically doped transistors. Npj 2D Mater. Appl. **5**, 1–13 (2021). https://doi.org/10.1038/s41699-020-00181-1
23. Talirz, L., Kumbhar, S., Passaro, E., Yakutovich, A.V., Granata, V., Gargiulo, F., Borelli, M., Uhrin, M., Huber, S.P., Zoupanos, S., Adorf, C.S., Andersen, C.W., Schütt, O., Pignedoli, C.A., Passerone, D., VandeVondele, J., Schulthess, T.C., Smit, B., Pizzi, G., Marzari, N.: Materials Cloud, a platform for open computational science. Sci. Data. **7**, 299 (2020). https://doi.org/10.1038/s41597-020-00637-5

24. Giannozzi, P., Baroni, S., Bonini, N., Calandra, M., Car, R., Cavazzoni, C., Ceresoli, D., Chiarotti, G.L., Cococcioni, M., Dabo, I., Dal Corso, A., de Gironcoli, S., Fabris, S., Fratesi, G., Gebauer, R., Gerstmann, U., Gougoussis, C., Kokalj, A., Lazzeri, M., Martin-Samos, L., Marzari, N., Mauri, F., Mazzarello, R., Paolini, S., Pasquarello, A., Paulatto, L., Sbraccia, C., Scandolo, S., Sclauzero, G., Seitsonen, A.P., Smogunov, A., Umari, P., Wentzcovitch, R.M.: QUANTUM ESPRESSO: a modular and open-source software project for quantum simulations of materials. J. Phys. Condens. Matter. **21**, 395502 (2009). https://doi.org/10.1088/0953-8984/21/39/395502
25. Perdew, J.P., Burke, K., Ernzerhof, M.: Generalized Gradient approximation made simple. Phys. Rev. Lett. **77**, 3865–3868 (1996). https://doi.org/10.1103/PhysRevLett.77.3865
26. Monkhorst, H.J., Pack, J.D.: Special points for Brillouin-zone integrations. Phys. Rev. B. **13**, 5188–5192 (1976). https://doi.org/10.1103/PhysRevB.13.5188
27. Marzari, N., Vanderbilt, D.: Maximally localized generalized Wannier functions for composite energy bands. Phys. Rev. B. **56**, 12847–12865 (1997). https://doi.org/10.1103/PhysRevB.56.12847
28. Pizzi, G., Vitale, V., Arita, R., Blügel, S., Freimuth, F., Géranton, G., Gibertini, M., Gresch, D., Johnson, C., Koretsune, T., Ibañez-Azpiroz, J., Lee, H., Lihm, J.-M., Marchand, D., Marrazzo, A., Mokrousov, Y., Mustafa, J.I., Nohara, Y., Nomura, Y., Paulatto, L., Poncé, S., Ponweiser, T., Qiao, J., Thöle, F., Tsirkin, S.S., Wierzbowska, M., Marzari, N., Vanderbilt, D., Souza, I., Mostofi, A.A., Yates, J.R.: Wannier90 as a community code: new features and applications. J. Phys. Condens. Matter. **32**, 165902 (2020). https://doi.org/10.1088/1361-648X/ab51ff
29. Calderara, M., Brück, S., Pedersen, A., Bani-Hashemian, M.H., VandeVondele, J., Luisier, M.: Pushing back the limit of *ab-initio* quantum transport simulations on hybrid supercomputers. In: Proceedings of the International Conference for High Performance Computing, Networking, Storage and Analysis. pp. 1–12. ACM, Austin Texas (2015)
30. Klimeck, G., Luisier, M.: Atomistic modeling of realistically extended semiconductor devices with NEMO and OMEN. Comput. Sci. Eng. **12**, 28–35 (2010). https://doi.org/10.1109/MCSE.2010.32
31. Fediai, A., Ryndyk, D.A., Seifert, G., Mothes, S., Claus, M., Schröter, M., Cuniberti, G.: Towards an optimal contact metal for CNTFETs. Nanoscale **8**, 10240–10251 (2016). https://doi.org/10.1039/C6NR01012A
32. Sancho, M.P.L., Sancho, J.M.L., Rubio, J.: Quick iterative scheme for the calculation of transfer matrices: application to Mo (100). J. Phys. F: Met. Phys. **14**, 1205–1215 (1984). https://doi.org/10.1088/0305-4608/14/5/016
33. Rahman, A., Jing Guo, D.S., Lundstrom, M.S.: Theory of ballistic nanotransistors. IEEE Trans. Electron Devices. **50**, 1853–1864 (2003). https://doi.org/10.1109/TED.2003.815366
34. Yang, M., Cao, S., You, Q., Shi, L.-B., Qian, P.: Intrinsic carrier mobility of monolayer GeS and GeSe: first-principles calculation. Physica E Low-dimens. Syst. Nanostruct. **118**, 113877 (2020). https://doi.org/10.1016/j.physe.2019.113877

Publication 4

Ab initio quantum transport simulations of monolayer GeS nanoribbons

M. Matić and M. Poljak, "*Ab initio* quantum transport simulations of monolayer GeS nanoribbons," *Solid-State Electronics*, vol. 197, p. 108460, 2022.
doi:10.1016/j.sse.2022.108460

– 4 page

Solid-State Electronics 197 (2022) 108460

Contents lists available at ScienceDirect

Solid State Electronics

journal homepage: www.elsevier.com/locate/sse

Ab initio quantum transport simulations of monolayer GeS nanoribbons

Mislav Matić, Mirko Poljak [*]

Computational Nanoelectronics Group, Micro and Nano Electronics Laboratory, Faculty of Electrical Engineering and Computing, University of Zagreb, Zagreb HR 10000, Croatia

ARTICLE INFO

Keywords:
Quantum transport
non-equilibrium Green's function (NEGF)
Density functional theory (DFT)
Maximally-localized Wannier functions (MLWF)
GeS
Nanoribbon

ABSTRACT

Monolayer germanium monosulfide (GeS) was recently identified as one of the most promising 2D materials for ultra-scaled FETs. While sub-10 nm monolayer GeS FETs were studied by quantum transport, very little is known about GeS nanoribbons (GeSNRs) or GeSNR FET performance. In this work, we employ quantum transport and Hamiltonians with an orbital resolution to study the electronic, transport, and ballistic device properties of sub-4 nm-wide and ~15 nm-long GeSNRs. While ultra-scaled GeSNR FETs exhibit I_{ON}/I_{OFF} of at least ~7×10^5, indicating good switching performance, they also offer modest ballistic I_{ON} values of up to ~1.2 mA/μm.

1. Introduction

Miniaturization and optimization of transistors have driven the tremendous development of the semiconductor industry in the last 60 years. Short channel effects (SCEs) suppression at gate lengths under ~20 nm is difficult and, on that account, new materials and device architectures are needed to enable further transistor scaling and improve device performance. Potential candidates for future transistor channel materials are atomically thin 2D materials (2DMs). Due to their atomic thickness and dangling-bond-free surfaces, 2DMs have high immunity to SCEs, and the near-ballistic transport properties are promising for high-performance devices [1], but the high contact resistance still remains a limiting factor for 2DMs application in nanodevices [2,3]. Patterning 2DMs into quasi–1D nanoribbons enables tuning of the electronic, transport, and device properties [4,5] such as bandgap, effective mass, injection velocity, etc., which makes these nanostructures of interest for nanoelectronic devices.

Monolayer germanium monosulfide (GeS) is a group-IV monochalcogenide 2D material with a buckled orthorhombic lattice. Monolayer GeS was recently examined along with hundreds of 2D materials as one of the most promising 2D materials for ultra-scaled FETs in [1], while a quantum transport study of sub-10 nm monolayer GeS FETs was reported in [6]. On the other hand, very little is known about GeS nanoribbons (GeSNRs) or GeSNR device performance, with the knowledge on the former being limited to electronic properties only, as reported in [7]. Concerning their electronic properties, armchair and zigzag GeSNRs were studied with armchair 2D GeS showing more promise for device applications due to lower electron and hole effective masses. Hence, in this work, we analyze GeSNRs with armchair edges.

Advanced modeling is needed for the simulation of transistors at the nanoscale due to the atomistic resolution of the material and strong quantum effects. Here we use *ab initio* density functional theory (DFT) to perform electronic structure calculations and maximally localized Wannier functions (MLWFs) are employed to transform DFT Hamiltonians into a localized basis, which preserves bandstructure accuracy and reduces the computational load for transport calculations. Next, non-equilibrium Green's function (NEGF) formalism, including the MLWF Hamiltonians, is used for ballistic quantum transport simulations [8–10]. In this work, our in-house DFT-MLWF-NEGF solver is employed to analyze the electronic, transport, and ballistic device properties of ultra-scaled armchair GeSNRs and GeSNR FETs that exhibit a direct bandgap for narrowest nanoribbons.

1.1. Methodology

The unit cell of the 2D GeS is obtained from the 2D materials database provided by Materials Cloud [11], which is then used to construct an armchair GeSNR super-cell along the nanoribbon width (*W*). Edges of the GeSNRs are passivated with H atoms and a vacuum of 20 Å is added in the confined directions to exclude any interactions (existing due to DFT that assumes periodicity in all three directions). We construct and perform DFT simulations for GeSNR super-cells for nanoribbon widths

---

[*] Corresponding author.
E-mail address: mirko.poljak@fer.hr (M. Poljak).

https://doi.org/10.1016/j.sse.2022.108460

from $W = 0.76$ nm to $W = 3.70$ nm. The DFT calculations are used to relax H-passivated GeSNRs structures and obtain the band structure with high accuracy. Plane-wave based Quantum Espresso program package [12] is used for DFT calculations, with Perdew-Burke-Ernzerhof generalized gradient approximation (PBE-GGA) [13] for the exchange-correlation (XC) functional. The plane-wave cutoff energy is set to 100 Ry, while the convergence threshold is set to 10^{-3} eV/Å for the ionic force, and to the value of 10^{-4} eV for energy. The k-points are sampled using an equally-spaced Monkhorst-Pack grid [14] in the transport direction and 1 k-point in the confined directions. The output of the DFT are dense Hamiltonians localized in energy, but NEGF simulations prefer spatially localized Hamiltonians. Maximally-localized Wannier functions (MLWFs) [15] are used to transform DFT Hamiltonians into a localized basis, which results in much sparser matrices and enables the simulation of devices consisting of thousands of atoms [8,16]. Wannier90 program package [17] is used to obtain the MLWF Hamiltonians. The MLWFs accuracy greatly depends on trial orbitals that are projected on the Bloch manifold. For GeSNRs we choose s, p_x, p_y, and p_z atomic orbitals as trial orbitals for both Ge and S atoms. The MLWF Hamiltonian matrices are then used to construct the total GeSNR channel Hamiltonians of ~15 nm long nanoribbons with different GeSNR widths.

Non-equilibrium Green's function (NEGF) formalism is used to directly solve the Schrödinger's equation with open boundary conditions (OBCs). Retarded Green's function, G^R, of the device is the central quantity of NEGF formalism and can be written as.

$$G^R(E) = \left[(E + i\eta)I - H - \Sigma_S^R(E) - \Sigma_D^R(E)\right]^{-1},$$

where H is the total GeSNR channel Hamiltonian, Σ matrices denote source (S) and drain (D) retarded contact self-energies that account for OBCs, and $i\eta$ is the infinitesimal positive imaginary convergence constant used to ensure the physically relevant causal result. The NEGF framework is implemented in our in-house code [4,5,10] which is used for the calculation of size-dependent properties of GeSNRs. Contacts are assumed to be ideal, i.e. semi-infinite regions made up of the same material as the channel, with the Sancho-Rubio method [18] employed for a numerically-efficient calculation of S/D contact self-energy matrices.

Electronic and transport properties are calculated using NEGF, including S/D transmission (T_{SD}) and density of states (DOS), which are used within the top-of-the-barrier (ToB) model [19] to study the ballistic performance of n-channel GeSNR MOSFETs. The ToB model provides the thermionic current and the calculations depend on the self-consistent ToB potential that represents the S/D barrier height, source and drain Fermi-Dirac functions, and Fermi levels for charge neutrality in S/D regions, DOS and T_{SD}. Since only the thermionic current above the ToB potential is calculated, the ToB model is a dependable method for FETs with channel lengths >15 nm where direct S/D tunneling is negligible [19]. Gate oxide has EOT = 1 nm, and S/D doping is set at 0.001 M fraction of the GeS areal density. In all devices, we set a common V_{TH} of 0.24 V as projected in the International Roadmap for Devices and Systems (IRDS) at the "3 nm" logic node [20]. In turn, this V_{TH} results in a very low OFF-state current (I_{OFF}) of 0.87 nA/μm due to the 60 mV/dec subthreshold slope and ideal gate control over the channel that are assumed in the ToB model. The ballistic ON-state current (I_{ON}) is extracted at $V_{GS} = V_{DS} = 0.7$ V, i.e. when both gate and drain are biased at the supply voltage.

2. Results and discussion

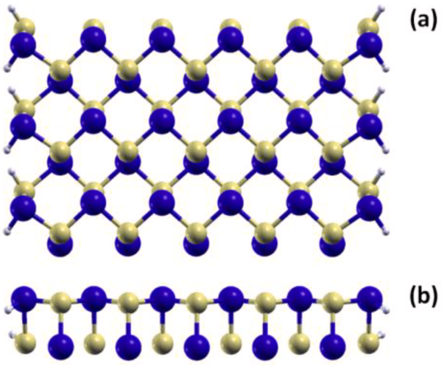

Fig. 1. (a) Top and (b) side view of the monolayer GeS nanoribbon with armchair edges.

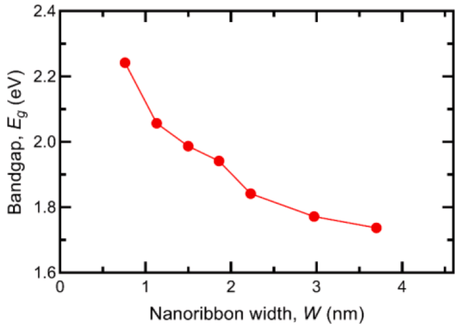

Fig. 2. Impact of width-scaling on the bandgap of armchair GeSNRs.

Fig. 1 shows the top (Fig. 1a) and side (Fig. 1b) view of a relaxed 1.86 nm-wide armchair GeS nanoribbon structure passivated with H atoms. GeS exhibits buckled orthorhombic structure and after relaxation, a slight shift of the edge Ge and S atoms are observed and visible in Fig. 1a. In Fig. 2 bandgap is shown for various nanoribbon widths. Scaling down nanoribbon width increases the bandgap (E_g) from 1.73 eV for $W = 3.70$ nm to 2.24 eV for $W = 0.76$ nm. The bandstructure plots for GeSNRs of various widths, reported in Fig. 3, show that E_g of wider GeSNRs is indirect while scaling down the nanoribbon width below $W = 2.23$ nm transitions GeSNRs into a direct semiconductor which agrees with the results in [7]. Effective mass (m^*, in units of m_0) of the lowest conduction band is calculated and reported in Fig. 3. Effective mass increases while scaling down nanoribbon width from $m^* = 0.276$ for $W = 3.70$ nm to $m^* = 1.143$ for $W = 0.76$ nm. The effective mass is high even for the widest nanoribbons when compared to m^* of the lowest conduction band in 2D GeS alongside armchair direction ($m^* = 0.2$ was reported in [21]). In Fig. 4 the width-dependence of the ON-state current for armchair GeSNR MOSFETs is shown. The ON-state current decreases monotonically while scaling down the GeSNR width, from $I_{ON} = 1.20$ mA/μm for $W = 3.70$ nm to $I_{ON} = 0.65$ mA/μm for $W = 0.76$ nm. The performance of GeSNR FETs is directly related to the channel bandstructure along nanoribbon transport direction, as reported in Fig. 3 since mobile charge density depends on the density of states (DOS), and the transmission function determines transport probability for each conducting mode. Subbands nearest to the conduction band minimum (CBM) have the highest influence on the ON-state current in n-channel FETs. For nanoribbons with $W = 2.97$ nm and $W = 3.70$ nm, I_{ON} values are approximately the same due to bandstructure similarity near the CBM for both GeSNRs. To further clarify the $I_{ON} - W$ curve, transmission and DOS are plotted in the ~200 meV energy range from the CBM, with CBM shifted to 0 eV for an easier comparison of different GeSNRs as shown in Fig. 5. Nanoribbons with $W = 3.70$ nm and $W = 2.97$ nm show DOS and transmission characteristics that match almost perfectly for energies up to 0.11 eV away from the CBM, where the contribution to the current is the highest, thus resulting in the same I_{ON}. The 2.23 nm-wide GeSNR presents a transitional nanoribbon because the lowest sub-bands nearest to the CBM start moving away from the CBM as W decreases further (e.g. compare Fig. 3c and d). This subband shift directly translates into the significant I_{ON} drop while scaling the GeSNR

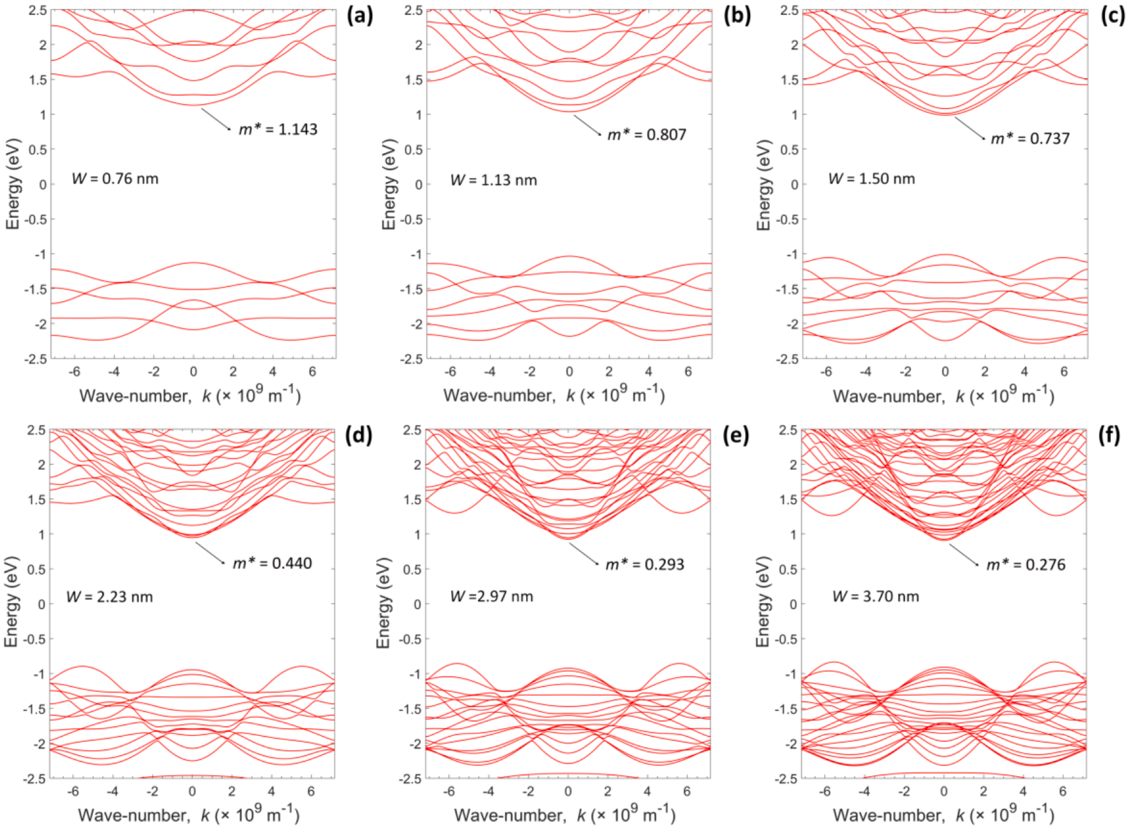

Fig. 3. Bandstructure of GeSNRs with the widths of (a) W = 0.76 nm, (b) W = 1.13 nm, (c) W = 1.50 nm, (d) W = 2.23 nm, (e) W = 2.97 nm, and (f) W = 3.70 nm with extracted effective mass (in units of m_0) of electrons in the lowest conduction band.

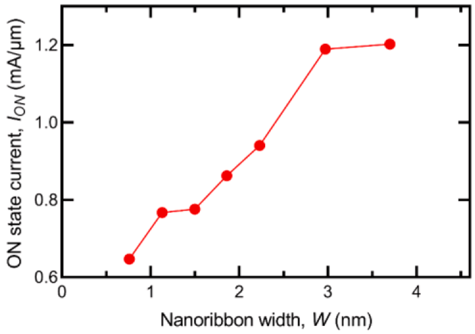

Fig. 4. Width-dependence of the ON-state current extracted at 0.7 V supply voltage in armchair GeSNR FETs.

width from 2.97 nm to 2.23 nm observed in Fig. 4. For GeSNRs with W <2.23 nm the subband with lower curvature, i.e. higher effective mass, becomes the lowest subband that dominantly determines the overall transport. This property, alongside the lower number of available bands/modes due to the lower number of available orbitals in narrower GeSNRs, further decreases I_{ON} in ultra-scaled GeSNR FETs. None of the analyzed devices fulfills IRDS specification for I_{ON} at the "3 nm" node, but the ON-state performance can be somewhat improved by optimizing the EOT, doping, etc., which is beyond the scope of this work. On the other hand, I_{ON}/I_{OFF} reaches ~7×10^5 even in the worst case, indicating good switching capabilities of GeSNR FETs for logic applications.

3. Conclusions

We employ NEGF with MLWF Hamiltonians to study the electronic, transport and ballistic device properties of sub-4 nm-wide and ~15 nm-

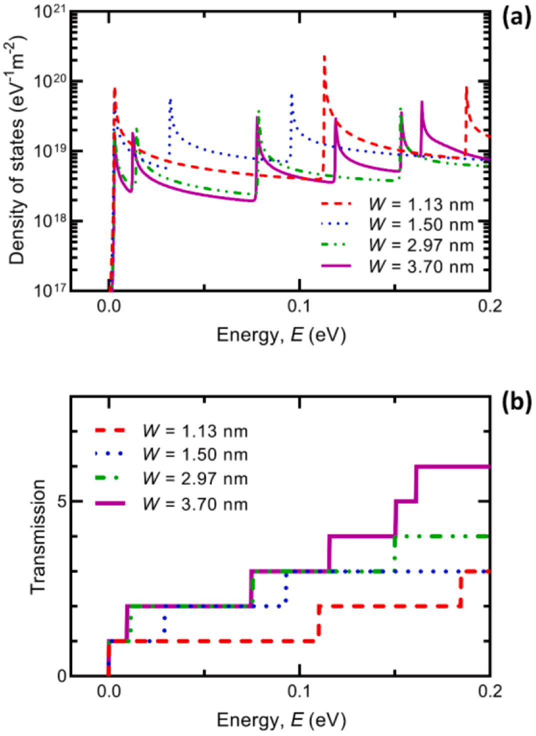

Fig. 5. (a) Density of states and (b) transmission comparison for armchair GeSNRs with the widths of W = 1.50 nm (dotted blue line), W = 1.86 nm (dashed red line), W = 2.97 nm (dot-dot-dashed green line), and W = 3.70 nm (purple line). (For interpretation of the references to colour in this figure legend, the reader is referred to the web version of this article.)

long GeSNRs. The I_{ON}/I_{OFF} ratio of at least $\sim 7\times10^5$ is observed for ultra-scaled GeSNR FETs, which indicates good switching performance for digital logic devices. The ON-state performance deteriorates as the GeSNR width is scaled down, with the maximum ballistic I_{ON} of ~1.20 mA/μm achieved for the widest analyzed GeSNR FET with $W = 3.70$ nm. While GeSNR FETs do not meet the IRDS requirements at the “3 nm” CMOS node and beyond, further performance improvement of GeS-based nanodevices is possible by doping and gate-stack engineering. Nevertheless, future work must also consider carrier scattering and dissipative transport for a realistic assessment. [9].

Declaration of Competing Interest

The authors declare that they have no known competing financial interests or personal relationships that could have appeared to influence the work reported in this paper.

Data availability

Data will be made available on request.

Acknowledgments

This work was supported by the Croatian Science Foundation under the project CONAN2D (Grant No. UIP-2019-04-3493).

References

[1] Klinkert C, Szabó Á, Stieger C, Campi D, Marzari N, Luisier M. 2-D Materials for Ultrascaled Field-Effect Transistors: One Hundred Candidates under the *Ab Initio* Microscope. ACS Nano Jul. 2020;14(7):8605–15. https://doi.org/10.1021/acsnano.0c02983.

[2] Poljak M, Matic M, Zeljko A. Minimum Contact Resistance in Monoelemental 2D Material Nanodevices with Edge-Contacts. IEEE Electron Device Lett 2021;42(8):1240–3.

[3] Allain A, Kang J, Banerjee K, Kis A. Electrical contacts to two-dimensional semiconductors. Nature Mater 2015;14(12):1195–205.

[4] Poljak M. Electron Mobility in Defective Nanoribbons of Monoelemental 2D Materials. IEEE Electron Device Lett 2020;41(1):151–4.

[5] Poljak M, Matić M. Bandstructure and Size-Scaling Effects in the Performance of Monolayer Black Phosphorus Nanodevices. Materials Dec. 2021;15(1):243. https://doi.org/10.3390/ma15010243.

[6] Ding Y, et al. High-Performance Ballistic Quantum Transport of Sub-10 nm Monolayer GeS Field-Effect Transistors. ACS Appl Electron Mater Mar. 2021;3(3):1151–61. https://doi.org/10.1021/acsaelm.0c01019.

[7] Li R, Cao H, Dong J. Electronic properties of group-IV monochalcogenide nanoribbons: Studied from first-principles calculations. Phys Lett A Nov. 2017;381(44):3747–53. https://doi.org/10.1016/j.physleta.2017.09.048.

[8] Klimeck G, Luisier M. Atomistic Modeling of Realistically Extended Semiconductor Devices with NEMO and OMEN. Comput Sci Eng Mar. 2010;12(2):28–35. https://doi.org/10.1109/MCSE.2010.32.

[9] A. Afzalian and G. Pourtois, “ATOMOS: An ATomistic MOdelling Solver for dissipative DFT transport in ultra-scaled HfS $_2$ and Black phosphorus MOSFETs,” in *2019 International Conference on Simulation of Semiconductor Processes and Devices (SISPAD)*, Udine, Italy, Sep. 2019, pp. 1–4. 10.1109/SISPAD.2019.8870436.

[10] M. Matić, T. Župančić, and M. Poljak, “Parallelized Ab Initio Quantum Transport Simulation of Nanoscale Bismuthene Devices,” in *2022 45th Jubilee International Convention on Information, Communication and Electronic Technology (MIPRO)*, 2022, pp. 118–123. 10.23919/MIPRO55190.2022.9803335.

[11] Talirz L, Kumbhar S, Passaro E, Yakutovich AV, Granata V, Gargiulo F, et al. Materials Cloud, a platform for open computational science. Sci Data 2020;7(1).

[12] Giannozzi P, Baroni S, Bonini N, Calandra M, Car R, Cavazzoni C, et al. QUANTUM ESPRESSO: a modular and open-source software project for quantum simulations of materials. J Phys: Condens Matter 2009;21(39):395502.

[13] Perdew JP, Burke K, Ernzerhof M. Generalized Gradient Approximation Made Simple. Phys Rev Lett 1996;77(18):3865–8.

[14] Monkhorst HJ, Pack JD. Special points for Brillouin-zone integrations. Phys Rev B 1976;13(12):5188–92.

[15] Marzari N, Vanderbilt D. Maximally localized generalized Wannier functions for composite energy bands. Phys Rev B 1997;56(20):12847–65.

[16] Calderara M, Brück S, Pedersen A, Bani-Hashemian MH, VandeVondele J, Luisier M. Pushing back the limit of ab-initio quantum transport simulations on hybrid supercomputers. In: Proceedings of the International Conference for High Performance Computing, Networking. Austin Texas: Storage and Analysis; 2015. p. 1–12. https://doi.org/10.1145/2807591.2807673.

[17] Pizzi G, Vitale V, Arita R, Blügel S, Freimuth F, Géranton G, et al. Wannier90 as a community code: new features and applications. J Phys: Condens Matter 2020;32(16):165902.

[18] Sancho MPL, Sancho JML, Rubio J. Quick iterative scheme for the calculation of transfer matrices: application to Mo (100). J Phys F: Met Phys 1984;14(5):1205–15.

[19] A. Rahman, Jing Guo, S. Datta, and M. S. Lundstrom, “Theory of ballistic nanotransistors,” *IEEE Trans. Electron Devices*, vol. 50, no. 9, pp. 1853–1864, Sep. 2003, 10.1109/TED.2003.815366.

[20] “‘IEEE Intl. Roadmap for Devices and Systems (IRDS), 2019 Update.’ https://irds.ieee.org/.”.

[21] Li F, Liu X, Wang Y, Li Y. Germanium monosulfide monolayer: a novel two-dimensional semiconductor with a high carrier mobility. J. Mater. Chem. C 2016;4:2155–9. https://doi.org/10.1039/C6TC00454G.

Publication 5

Validity of the Ballistic Top-of-the-Barrier Model for FETs Based on 2D Material Nanoribbons

M. Matić and M. Poljak, “Validity of the Ballistic Top-of-the-Barrier Model for FETs Based on 2D Material Nanoribbons,” in *2024 47th MIPRO ICT and Electronics Convention (MIPRO)*, 2024, pp. 1596–1601.
doi: 10.1109/MIPRO60963.2024.10569245

– 6 pages

MIPRO 2024, May 20 - 24, 2024, Opatija, Croatia

2024 47th MIPRO ICT and Electronics Convention (MIPRO) | 979-8-3503-8250-1/24/$31.00 ©2024 IEEE | DOI: 10.1109/MIPRO60963.2024.10569245

Validity of the Ballistic Top-of-the-Barrier Model for FETs Based on 2D Material Nanoribbons

M. Matić and M. Poljak[*]
Computational Nanoelectronics Group
Faculty of Electrical Engineering and Computing, University of Zagreb, Zagreb, Croatia
[*]Corresponding author: mirko.poljak@fer.unizg.hr

***Abstract*—We investigate our in-house implementation of the non-equilibrium Green's function (NEGF) formalism in combination with the top-of-the-barrier (ToB) ballistic model, as implemented in our QUDEN (from Quantum-transport Device Engineering in Nanoelectronics) simulator. We calibrate QUDEN on self-consistent NEGF-Poisson simulations of graphene nanoribbon (GNR) field-effect transistor (FET) with ~15 nm channel in the commercial software QuantumATK. It is demonstrated that QUDEN device predicting ability is adequate for nanoribbon-based FETs, except in materials with ultra-low effective mass. QUDEN is then employed to explore monolayer zirconium-disulfide (ZrS_2) nanoribbon (ZrS_2NR) nFETs, using Hamiltonians from density functional theory (DFT) calculations. We show that ZrS_2NR nFET exhibits 32% lower ON-state current compared to GNR nFET, which is attributed to 36% higher electron effective mass in ZrS_2NRs than in GNRs. Our results show that DFT-based Hamiltonians and NEGF-ToB model can be efficiently used for accurate investigation of nanoribbon-based devices.**

Keywords—Non-equilibrium Green's function (NEGF), top-of-the-barrier (ToB) model, zirconium-disulfide (ZrS_2), nanoribbon, density functional theory (DFT), QuantumATK

I. INTRODUCTION

Research focus on two-dimensional (2D) materials is growing at a fast pace since the discovery of graphene in 2004 [1]. Due to their superior electronic an transport properties, 2D materials are considered as potential candidates to replace silicon in future electronic devices [2], [3]. Recently, more than 1800 2D materials were discovered by *ab initio* calculations [4], with 100 of them studied in a search for the best performing 2D material for future logic field-effect transistors (FETs) [5]. Currently, research focus in the literature is on group-IV monolayers (graphene, silicene, germanene, stanene) [6], [7], [8], group-V monolayers (phosphorene, arsenene, antimonene) [9], [10], and transition metal dichalcogenides (TMDs, e.g. MoS_2, SnS_2, WS_2, etc.) [11], [12], [13]. Additionally, 2D materials can be configured in various structures such as nanoribbons [14], nanosheets [15], and nanowires [16], which gives additional degrees of freedom to engineer their properties.

Although many 2D materials have undergone theoretical and numerical studies, most have not yet been successfully experimentally isolated. Given the vast array of possibilities, advanced modeling and simulation are needed for future development of 2D material-based FETs and other devices [17]. The needed advanced approaches must incorporate the underlying electronic and transport physics of these materials. Currently, the best and most advanced numerical simulators are based on self-consistent solving of the non-equilibrium Green's function (NEGF) formalism equations in combination with solving the 3D Poisson equation, while the materials themselves are described using the *ab initio* density functional theory (DFT) or semiempirical tight-binding (TB) Hamiltonians. However, self-consistent NEGF-Poisson comes at an expense of a very high computational cost and that fact motivated the development of the top-of-the-barrier (ToB) model [18]. The ToB model was applied and investigated previously [19], [20] and it was proven useful for FETs with channel lengths above 15 nm where direct tunneling is negligible.

In this paper, we validate our implementation of the NEGF-ToB numerical model implemented in our MATLAB in-house simulator of nanoribbon FETs designated QUDEN (from Quantum-transport Device Engineering in Nanoelectronics). For a valid assessment of the QUDEN simulator, we compare the performance of a single-gate FET with a 1.11 nm-wide graphene nanoribbon (GNR) obtained in QUDEN with the results obtained by modeling the same device in the commercial software package QuantumATK (QATK) [21] that employs self-consistent NEGF-Poisson calculations. After validating and calibrating QUDEN, we investigate the ballistic performance of zirconium-disulfide (ZrS_2) nanoribbon (ZrS_2NR) FET with the channel length of ~15 nm and channel width of 1.42 nm.

II. METHODOLOGY

The assessment of QUDEN starts with the simulation of a single-gate GNR FET in QUDEN and QATK. For a fair comparison we set the same device parameters in both simulators with the GNR Hamiltonian based on the Hancock TB model [22]. After the verification, QUDEN is used to study device performance of a ZrS_2NR FET and material properties of ZrS_2NR. The ZrS_2NR Hamiltonian is obtained using *ab initio* DFT simulations and is then

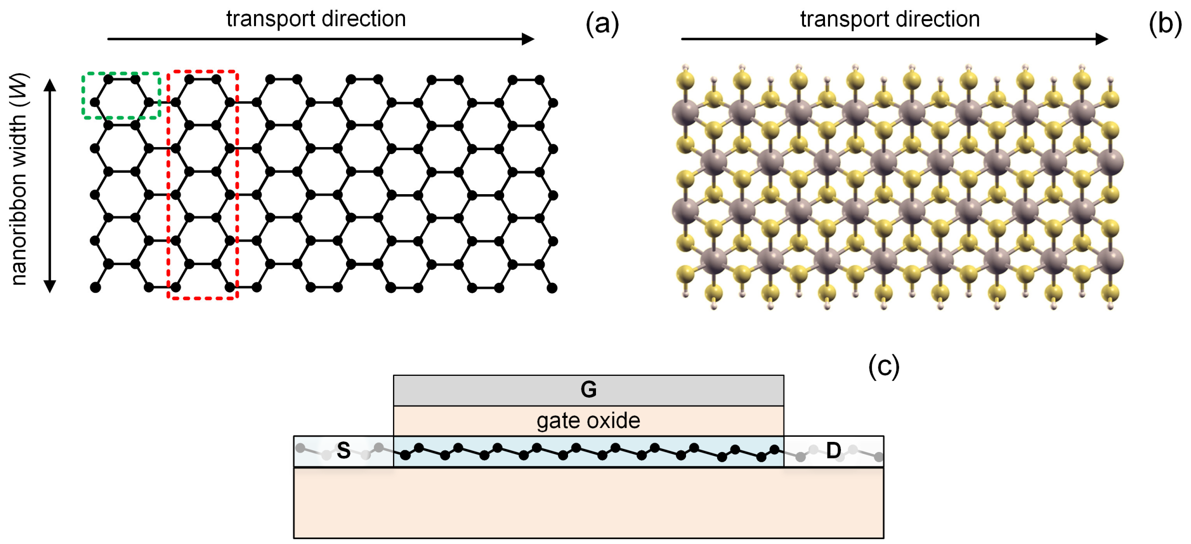

Fig. 1. Top view on the structure of (a) GNR with $W = 1.11$ nm, and (b) ZrS_2NR with $W = 1.42$ nm. Panel (a) also marks the unit cells used in the construction of the tight-binding GNR Hamiltonian. (c) Illustration of a single-gate FET with a nanoribbon channel.

transformed into a TB-like basis using the maximally-localized Wannier functions (MLWF) formalism.

A. Atomistic Nanoribbon Hamiltonians

The GNR Hamiltonian is constructed using the Hancock TB model with up to the third-nearest-neighbor interaction included, i.e. $t_1 = 2.7$ eV, $t_2 = 0.2$ eV, and $t_3 = 0.18$ eV. Construction of the GNR in QATK is straightforward using a built-in plugin designed to generate nanoribbons. On the other hand, in QUDEN the GNRs are constructed using a 4-atom unit cell (smaller green rectangle in Fig. 1a) that is repeated in the confined direction to construct a super-cell along the GNR width (larger red rectangle in Fig. 1a). To create the total channel Hamiltonian, the super-cell is repeated along the transport direction for the desired nanoribbon length. Later in the text we explore the properties of ZrS_2NR FETs, and the Hamiltonian of the 1.42 nm-wide ZrS_2NR with H-passivated edges (illustrated in Fig. 1b) is obtained by employing the plane-wave DFT, implemented in Quantum Espresso (QE) [23]. Transformation into MLWF Hamiltonians is done using Wannier90 software tool [24], which results in space-localized Hamiltonians suitable for quantum transport simulations. In QE, we use plane augmented wave (PAW) pseudopotential with the Perdew-Burke-Ernzerhof [25] (PBE) exchange-correlation functional. The MLWF localization depends mainly on trial orbitals that are set as follows: *d* orbitals for Zr atoms, *p* orbitals for S atoms and *s* orbitals for H atoms. Other main inputs together with simulation and parameter details are the same as in our previous work on hafnium-disulfide nanoribbons [26].

B. Brief Description of QUDEN

The NEGF formalism is used to directly solve the Schrödinger's equation with open boundary conditions for a system of choice [27], [28], i.e. a FET channel in the form of a nanoribbon in our case. The main term of the NEGF formalism is the energy-dependent retarded Green's function of the device defined as

$$G^R(E) = [(E + i\eta)I - H - \Sigma_S^R(E) - \Sigma_D^R(E)]^{-1}, \qquad (1)$$

where E is the energy, η is an infinitesimal number (convergence constant), H is total channel Hamiltonian, while interaction with source and drain contacts is represented with retarded contact self-energies, i.e. Σ_S^R and Σ_D^R. Contacts are assumed to be ideal, i.e. made of the same material as the channel, and hence the contact self-energy matrices are calculated using the iterative Sancho-Rubio method [29].

The ToB model [18] is used to assess the ballistic FET performance, with the device illustrated in Fig. 1c. The main inputs of the ToB model from NEGF are transmission and density of states (DOS). Within the ToB model, the transistor is modeled with only three points: top-of-the-barrier potential that represents the barrier height between the source and drain (S/D) regions, and with S/D Fermi levels. In ToB, carrier tunneling is not included and therefore only the thermionic component of current is calculated. Nevertheless, the potential points are calculated self-consistently along with charge density, and charge neutrality of S/D regions is maintained. Therefore, as shown previously [30], [31], [32], the NEGF-ToB approach presents a predictive model only for sufficiently long channels and wide bandgaps.

C. Brief Description of Quantum ATK

QATK simulations of GNR FETs are performed using the self-consistent solution of the 3D Poisson equation for electrostatics together with solving 1D NEGF equations for transport. Within QATK, the Poisson equation is

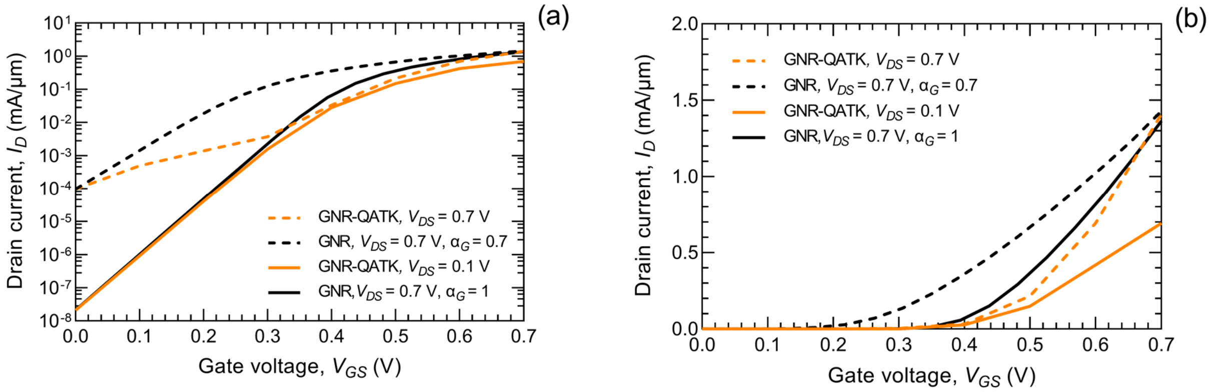

Fig. 2. Transfer characteristics of GNR FET with $W = 1.11$ nm in (a) logarithmic and (b) linear scale. Comparison is done between the results obtained by the commercial package QATK and by our in-house QUDEN code.

solved using the multigrid Poisson solver with Neuman boundary conditions (BCs) in the confined directions and Dirichlet BCs in the transport direction. The NEGF equations are calculated by separation into the equilibrium and non-equilibrium parts, with the equilibrium part being solved using a semi-circle double-contour on the imaginary axis method [33], [34], whereas the non-equilibrium part is solved on the real axis with a dense energy grid of $dE = 0.027$ eV.

III. RESULTS AND DISCUSSION

An identical single-gate GNR FET is defined in QATK and in our in-house QUDEN simulator. For all devices we set the same parameters as follows: channel length of ~15 nm, oxide thickness (t_{ox}) of 1 nm with $\varepsilon_r = 3.9$ (for SiO_2), and S/D doping is set to 0.01 molar fraction of the areal atom density of the channel material, i.e. $N_D = 4.3\times10^{12}$ cm^{-2}. To compare QUDEN to QATK, in Fig. 2 we report the transfer characteristics in the logarithmic and linear scale.

The GNR FET is simulated in QATK for V_{DS} set to 0.1 V and 0.7 V. For $V_{DS} = 0.1$ V we obtain a near ideal subthreshold swing (SS) of 62 mV/dec, while for $V_{DS} = 0.7$ V the SS increases significantly and reaches ~200 mV/dec. The observed very high SS is a result of significant increase of the drain current for gate bias below $V_{GS} = 0.3$ V due to direct and band-to-band tunneling (BTBT), which also results in a very high OFF-state current (I_{OFF}) of ~10^{-7} A/μm.

In the first QUDEN simulation we set the ideal gate control within the ToB model, as defined by parameter α_G [18], i.e. $\alpha_G = 1$, while the OFF-state current is set to the value obtained for QATK-GNR at $V_{DS} = 0.1$ V. This assumption is viable because under the threshold voltage (V_{th}) the BTBT is negligible and results in near ideal SS, as expected in the idealized ballistic ToB model. Comparison of the transfer characteristics of GNR FETs at $V_{DS} = 0.7$ V in QUDEN (with $\alpha_G = 1$) and QATK demonstrates the same V_{th} of 0.33 V, if calculated by the IRDS definition [35]. A great mismatch between QUDEN and QATK is clearly visible for $V_{GS} < 0.3$ V in Fig. 2a, and this is caused by stronger tunneling at higher drain bias, and QUDEN does not account for any type of tunneling. However, for $V_{GS} > 0.3$ V the transfer characteristics in Fig. 2b (full black line and dashed orange line) show near-perfect match for V_{GS} between 0.6 V and 0.7 V, i.e. in the ON-state current (I_{ON}). This bias range is the most relevant region because all future CMOS nodes are expected to feature the supply voltage values in the 0.6 - 0.7 V span. In the ON-state at $V_{DS} = V_{GS} = 0.7$ V, QATK simulation gives $I_{ON} = 1.41$ mA/μm, while QUDEN provides a somewhat lower I_{ON} of 1.37 mA/μm, i.e. a difference of 3 % compared to QATK.

For the second QUDEN simulation, we set the OFF-state current to that obtained by QATK at $V_{DS} = 0.7$ V, i.e. increased leakage visible in Fig. 2a, and find the α_G needed for the QUDEN simulation to match both the ON- and OFF-state current from the QATK simulation. We find $\alpha_G = 0.7$, and this value sets the correct I_{OFF} of ~10^{-7} A/μm, but also results in an unrealistically low SS of 85 mV/dec, much lower than ~200 mV/dec obtained in QATK. Furthermore, setting the α_G to 0.7 shifts the transfer characteristic current value up, which consequently lowers the threshold voltage from 0.33 V to 0.16 V, as seen in Fig. 2b. Nevertheless, for devices with similar bandgaps and effective transport mass, the choice of $\alpha_G = 0.7$ should result in similar BTBT and I_{OFF}. Therefore, the resulting ON-OFF current ratio, needed to assess the logic device switching performance, can be considered reliable. Finally, simulation wall-time to obtain a single 8-point *I-V* curve in QATK is 3 hours, while QUDEN provides the same in less than a minute, when the simulation is run on the same 8-core CPU. We argue that even for a FET with a very sparse Hamiltonian, as in the case of tight-binding GNR Hamiltonians, computational burden in QATK is very high. Additionally, simulation of devices in QATK with materials defined by DFT, which is also possible within the QATK package, would require prohibitive resources for our computational cluster.

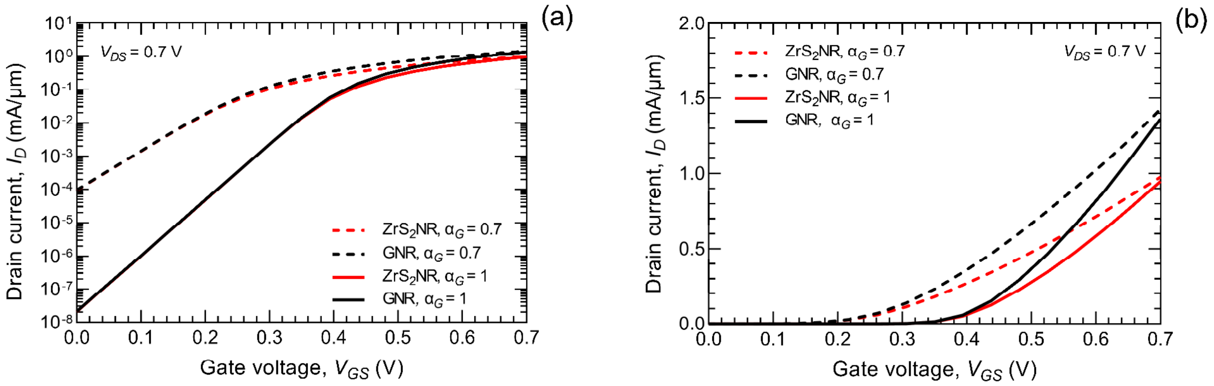

Fig. 3. Transfer characteristics of the ZrS_2NR FET with W = 1.42 nm and the GNR FET with W = 1.11 nm simulated in QUDEN. Logarithmic scale is used in (a), while a linear scale is shown in (b).

Now that we have shown that QUDEN can be used for the assessment of FETs with nanoribbon channels in the ON-state, we employ it to study the ZrS_2NR and the corresponding FET. The 2D material ZrS_2 is chosen since it has shown promise for 2D FETs in [5], whereas the one-dimensional counterparts such as ZrS_2NRs have not yet been studied. The ZrS_2NR width of 1.42 nm is chosen to have the same band gap as the previously mentioned and studied 1.11 nm-wide GNR. In Fig. 3 we compare the current-voltage characteristics of the ZrS_2NR FET with GNR FET simulated in QUDEN. Both devices are numerically investigated for two cases, i.e. two sets of I_{OFF} and α_G values discussed earlier. In the sub-threshold region, ZrS_2NR FET and GNR FET characteristics match perfectly for both α_G values, as shown in Fig. 3a. However, above V_{th} the ZrS_2NR FET performs worse than GNR FET with a 32% lower ON-state current in the ZrS_2NR FET than GNR FET. Similarly to GNR FETs, in the ZrS_2NR FET we also obtain a 3% higher I_{ON} for $\alpha_G = 0.7$ (0.978 mA/μm) compared to I_{ON} = 0.95 mA/μm when $\alpha_G = 1$. Threshold voltage is the same for the ZrS_2NR FET and GNR FET, with V_{th} = 0.33 V for α_G = 1 and lower V_{th} = 0.16 V for α_G = 0.7 as previously discussed. Finally, we calculate the I_{ON}/I_{OFF} ratio for the ZrS_2NR FET and obtain 10^4 and 4.5×10^7 for α_G of 0.7 and 1, respectively. These results show that ZrS_2NR FETs can fulfil IRDS requirements on the switching ratio if gate control over the channel is strong, i.e. if α_G is close to unity, which is feasible due to the quasi-one-dimensional nature of ZrS_2NRs.

Further insight into the material properties of the 1.42 nm-wide ZrS_2NR is obtained by plotting the band structure, density of states (DOS), and transmission. The band structure of studied GNR and ZrS_2NR is shown in Fig. 4. Both nanoribbons exhibit a direct bandgap (E_G) with E_G = 0.95 eV for the ZrS_2NR and E_G = 0.91 eV for the GNR. Bandstructure effective mass (m^*), extracted using a parabolic approximation, of the dominant (lowest) subband in the conduction band (CB) is $0.25m_0$ for the ZrS_2NR, while for the GNR we get $m^* = 0.16m_0$. The very low bandstructure effective mass in the GNR is the main reason for high BTBT at high drain bias in QATK simulations that account for tunneling. Due to the higher m^* and E_G in the ZrS_2NR, the tunneling in the ZrS_2NR FETs will be lower in ZrS_2NR FETs [5]. Hence, lower BTBT will result in much higher I_{ON}/I_{OFF} in ZrS_2NR FETs than in GNR FETs, with I_{ON}/I_{OFF} closer to the maximum I_{ON}/I_{OFF} of ~4.5×10^7 obtained for FET with an ideal electrostatic gate control over the channel.

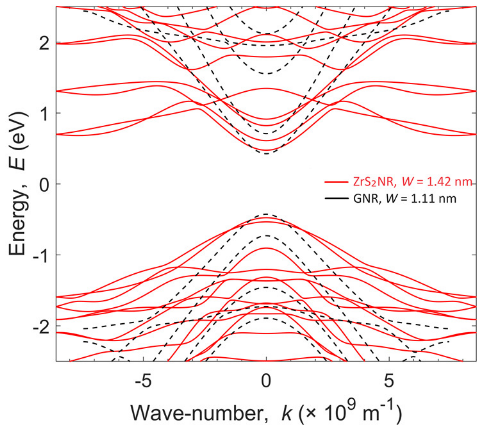

Fig. 4. Comparison of the bandstructure of the 1.42 nm-wide ZrS_2NR and 1.11 nm-wide GNR.

Finaly, we report the transmission and DOS in the conduction band of the 1.42 nm-wide ZrS_2NR and the 1.11 nm-wide GNR in Fig. 5a and b, respectively. In Fig. 5, the conduction band minimum (CBM) is set at 0 eV. Transmission is unity for both the GNR and ZrS_2NR up to the energy CBM + 0.13 eV, while for higher energies the ZrS_2NR exhibits higher transmission with the maximum of four for energies above CBM+0.2 eV. However, up to CBM + 0.1 eV, which presents the most important energy range for carrier transport, transmission is the same in both devices. Clearly, higher conducting subbands are not activated in ZrS_2NRs because GNR FET

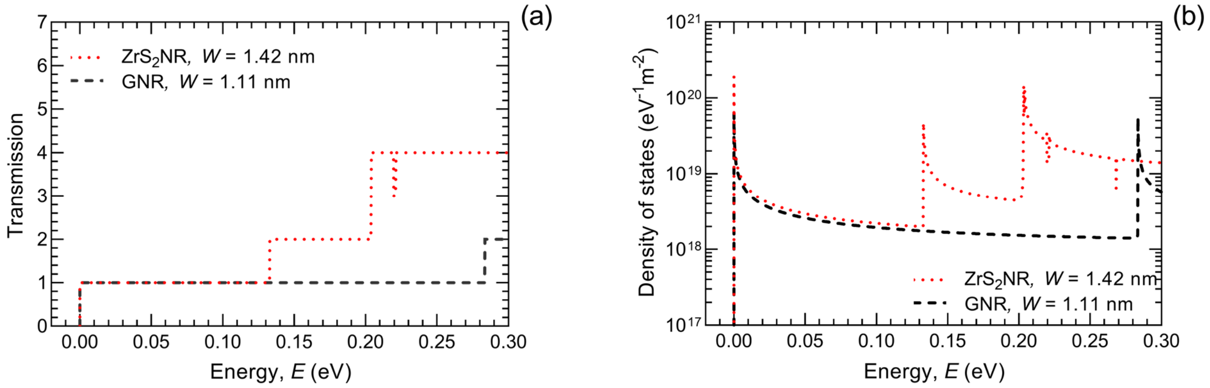

Fig. 5. (a) Transmission, and (b) density of states in the conduction band of ZrS$_2$NR with W = 1.42 nm and GNR with W = 1.11 nm. Conduction band minimum is set at 0 eV.

exhibits higher drain current than ZrS$_2$NR FET (see e.g. Fig. 3b). Additionally, we explore DOS in Fig. 5b in which the ZrS$_2$NR shows higher DOS generally near the CBM with a higher number of Van Hove singularities when compared to the GNR. While higher DOS leads to a higher density of conducting electrons and higher currents, the higher DOS in the ZrS$_2$NR (Fig. 5b) is also directly connected to the higher curvature of the lowest electronic subband, i.e. higher electron effective mass (Fig. 4). The lower ON-state performance of the ZrS$_2$NR FET can be attributed to the larger effective transport mass of electrons in the 1.42 nm-wide ZrS$_2$NR with respect to the GNR with W = 1.11 nm. We note that even though the ON-state performance of ZrS$_2$NR FETs is lower, the higher m^* in ZrS$_2$NRs can be beneficial for the applicability of the ToB model. Namely, larger effective transport mass decreases tunneling probability, thus suppressing the influence of BTBT, which enables NEGF-ToB to be a predictive tool over a wider range of biases.

IV. CONCLUSIONS

We assess the validity of our in-house implementation of the NEGF-ToB approach in QUDEN on a single-gate GNR FET by comparing it to the commercial software package QuantumATK. Transfer characteristics exhibit an excellent match for gate bias above 0.6 V, which indicates that QUDEN can properly assess the ON-state performance of nanoribbon devices with the gate-control parameter from the ToB model being $\alpha_G = 1$, while the OFF-state leakage can be adequately addressed with $\alpha_G = 0.7$ since the ToB model does not account for direct tunneling or BTBT. The verified QUDEN is then employed to explore the properties of the ZrS$_2$NR FET, in which the nanoribbon is 1.42 nm wide and with the same bandgap (~0.9 eV) as the GNR. We report a 32% lower ON-state current of the ZrS$_2$NR FET compared to the GNR FET, which we attribute mainly to the 36% higher effective electron mass in the ZrS$_2$NR. Nevertheless, a high I_{ON}/I_{OFF} of 4.5×10^7 is achievable in the ZrS$_2$NR FET, which makes it a plausible device for efficient digital switching according to IRDS requirements. Finally, our results on the GNR and ZrS$_2$NR FETs show that (1) DFT-MLWF Hamiltonians and NEGF are properly implemented in QUDEN, (2) predicting the subthreshold performance for materials with ultra-low effective mass is limited without adjusting the ToB model parameters, but (3) QUDEN can be used to determine the ON-state performance of nanoribbon-based FETs efficiently and accurately.

ACKNOWLEDGMENTS

This work was supported by the Croatian Science Foundation under the project CONAN2D (Grant No. UIP-2019-04-3493).

REFERENCES

[1] K. S. Novoselov *et al.*, “Electric Field Effect in Atomically Thin Carbon Films,” *Science*, vol. 306, no. 5696, pp. 666–669, Oct. 2004, doi: 10.1126/science.1102896.

[2] N. Briggs *et al.*, “A roadmap for electronic grade 2D materials,” *2D Mater.*, vol. 6, no. 2, p. 022001, Jan. 2019, doi: 10.1088/2053-1583/aaf836.

[3] G. Fiori *et al.*, “Electronics based on two-dimensional materials,” *Nature Nanotech*, vol. 9, no. 10, pp. 768–779, Oct. 2014, doi: 10.1038/nnano.2014.207.

[4] N. Mounet *et al.*, “Two-dimensional materials from high-throughput computational exfoliation of experimentally known compounds,” *Nature Nanotech*, vol. 13, no. 3, pp. 246–252, Mar. 2018, doi: 10.1038/s41565-017-0035-5.

[5] C. Klinkert, Á. Szabó, C. Stieger, D. Campi, N. Marzari, and M. Luisier, “2-D Materials for Ultrascaled Field-Effect Transistors: One Hundred Candidates under the Ab Initio Microscope,” *ACS Nano*, vol. 14, no. 7, pp. 8605–8615, Jul. 2020, doi: 10.1021/acsnano.0c02983.

[6] M. Poljak, “Electron Mobility in Defective Nanoribbons of Monoelemental 2D Materials,” *IEEE Electron Device Lett.*, vol. 41, no. 1, pp. 151–154, Jan. 2020, doi: 10.1109/LED.2019.2952661.

[7] L. Tao *et al.*, “Silicene field-effect transistors operating at room temperature,” *Nature Nanotech*, vol. 10, no. 3, pp. 227–231, Mar. 2015, doi: 10.1038/nnano.2014.325.

[8] S. Kaneko, H. Tsuchiya, Y. Kamakura, N. Mori, and M. Ogawa, “Theoretical performance estimation of silicene, germanene, and graphene nanoribbon field-effect transistors under ballistic transport,” *Appl. Phys. Express*, vol. 7, no. 3, p. 035102, Mar. 2014, doi: 10.7567/APEX.7.035102.

[9] S. Zhang *et al.*, “Recent progress in 2D group-VA semiconductors: from theory to experiment,” *Chem. Soc. Rev.*, vol. 47, no. 3, pp. 982–1021, 2018, doi: 10.1039/C7CS00125H.

[10] W. Zhou *et al.*, “Two-Dimensional Pnictogen for Field-Effect Transistors,” *Research*, vol. 2019, pp. 1–21, Oct. 2019, doi: 10.34133/2019/1046329.

[11] B. Radisavljevic, A. Radenovic, J. Brivio, V. Giacometti, and A. Kis, “Single-layer MoS2 transistors,” *Nature Nanotech*, vol. 6, no. 3, pp. 147–150, Mar. 2011, doi: 10.1038/nnano.2010.279.

[12] Y. Huang *et al.*, “Tin Disulfide—An Emerging Layered Metal Dichalcogenide Semiconductor: Materials Properties and Device Characteristics,” *ACS Nano*, vol. 8, no. 10, pp. 10743–10755, Oct. 2014, doi: 10.1021/nn504481r.

[13] D. Ovchinnikov, A. Allain, Y.-S. Huang, D. Dumcenco, and A. Kis, “Electrical Transport Properties of Single-Layer WS $_2$,” *ACS Nano*, vol. 8, no. 8, pp. 8174–8181, Aug. 2014, doi: 10.1021/nn502362b.

[14] C. Chen *et al.*, “Sub-10-nm graphene nanoribbons with atomically smooth edges from squashed carbon nanotubes,” *Nat. Electron.*, vol. 4, no. 9, Art. no. 9, Sep. 2021, doi: 10.1038/s41928-021-00633-6.

[15] N. Loubet *et al.*, “Stacked nanosheet gate-all-around transistor to enable scaling beyond FinFET,” in *2017 Symposium on VLSI Technology*, Kyoto, Japan: IEEE, Jun. 2017, pp. T230–T231. doi: 10.23919/VLSIT.2017.7998183.

[16] J. Appenzeller, J. Knoch, M. T. Bjork, H. Riel, H. Schmid, and W. Riess, “Toward Nanowire Electronics,” *IEEE Trans. Electron Devices*, vol. 55, no. 11, pp. 2827–2845, Nov. 2008, doi: 10.1109/TED.2008.2008011.

[17] M. Luisier *et al.*, “First-principles simulations of 2-D semiconductor devices: Mobility, I-V characteristics, and contact resistance,” in *2016 IEEE International Electron Devices Meeting (IEDM)*, San Francisco, CA, USA: IEEE, Dec. 2016, p. 5.4.1-5.4.4. doi: 10.1109/IEDM.2016.7838353.

[18] A. Rahman, Jing Guo, S. Datta, and M. S. Lundstrom, “Theory of ballistic nanotransistors,” *IEEE Trans. Electron Devices*, vol. 50, no. 9, pp. 1853–1864, Sep. 2003, doi: 10.1109/TED.2003.815366.

[19] A. Paul, S. Mehrotra, G. Klimeck, and M. Luisier, “On the Validity of the Top of the Barrier Quantum Transport Model for Ballistic Nanowire MOSFETs,” in *2009 13th International Workshop on Computational Electronics*, May 2009, pp. 1–4. doi: 10.1109/IWCE.2009.5091134.

[20] M. W. Chuan *et al.*, “A review of the top of the barrier nanotransistor models for semiconductor nanomaterials,” *Superlattices and Microstructures*, vol. 140, p. 106429, Apr. 2020, doi: 10.1016/j.spmi.2020.106429.

[21] S. Smidstrup *et al.*, “QuantumATK: an integrated platform of electronic and atomic-scale modelling tools,” *J. Phys.: Condens. Matter*, vol. 32, no. 1, p. 015901, Oct. 2019, doi: 10.1088/1361-648X/ab4007.

[22] Y. Hancock, A. Uppstu, K. Saloriutta, A. Harju, and M. J. Puska, “Generalized tight-binding transport model for graphene nanoribbon-based systems,” *Phys. Rev. B*, vol. 81, no. 24, p. 245402, Jun. 2010, doi: 10.1103/PhysRevB.81.245402.

[23] P. Giannozzi *et al.*, “QUANTUM ESPRESSO: a modular and open-source software project for quantum simulations of materials,” *J. Phys.: Condens. Matter*, vol. 21, no. 39, p. 395502, Sep. 2009, doi: 10.1088/0953-8984/21/39/395502.

[24] G. Pizzi *et al.*, “Wannier90 as a community code: new features and applications,” *J. Phys.: Condens. Matter*, vol. 32, no. 16, p. 165902, Apr. 2020, doi: 10.1088/1361-648X/ab51ff.

[25] J. P. Perdew, K. Burke, and M. Ernzerhof, “Generalized Gradient Approximation Made Simple,” *Phys. Rev. Lett.*, vol. 77, no. 18, pp. 3865–3868, Oct. 1996, doi: 10.1103/PhysRevLett.77.3865.

[26] M. Matić and M. Poljak, “Ballistic Performance of Quasi-One-Dimensional Hafnium Disulfide Field-Effect Transistors,” *Electronics*, vol. 13, no. 6, Art. no. 6, Jan. 2024, doi: 10.3390/electronics13061048.

[27] S. Datta, *Electronic Transport in Mesoscopic Systems*. Cambridge University Press, 1997.

[28] M. Poljak, *Kvantni transport na nanoskali [Quantum Transport on the Nanoscale]*, 1st ed. Zagreb, Croatia: Element, 2023.

[29] M. P. L. Sancho, J. M. L. Sancho, J. M. L. Sancho, and J. Rubio, “Highly convergent schemes for the calculation of bulk and surface Green functions,” *J. Phys. F: Met. Phys.*, vol. 15, no. 4, p. 851, 1985, doi: 10.1088/0305-4608/15/4/009.

[30] M. Poljak, M. Matić, and A. Zeljko, “Minimum Contact Resistance in Monoelemental 2D Material Nanodevices With Edge-Contacts,” *IEEE Electron Dev. Lett.*, vol. 42, no. 8, pp. 1240–1243, Aug. 2021, doi: 10.1109/LED.2021.3087908.

[31] M. Matić and M. Poljak, “Electronic, transport and ballistic device properties of quasi-one-dimensional GeS,” *J. Comput. Electron.*, vol. 22, no. 5, pp. 1350–1362, Oct. 2023, doi: 10.1007/s10825-023-02054-4.

[32] M. Poljak, M. Matić, I. Prevarić, and K. Japec, “Ballistic performance and overshoot effects in gallenene nanoribbon field-effect transistors,” *Journal of Applied Physics*, vol. 135, no. 7, p. 074302, Feb. 2024, doi: 10.1063/5.0188216.

[33] “QuantumATK Reference Manual — | QuantumATK V-2023.12 Documentation,” docs.quantumatk.com. Accessed: Jan. 14, 2024. [Online]. Available: https://docs.quantumatk.com/manual/NLRefMan.html

[34] M. Brandbyge, J.-L. Mozos, P. Ordejón, J. Taylor, and K. Stokbro, “Density-functional method for nonequilibrium electron transport,” *Phys. Rev. B*, vol. 65, no. 16, p. 165401, Mar. 2002, doi: 10.1103/PhysRevB.65.165401.

[35] “IRDS^{TM} 2022: More Moore - IEEE IRDS^{TM},” irds.ieee.org. Accessed: Jan. 01, 2024. [Online]. Available: https://irds.ieee.org/editions/2022/more-moore

Publication 6

Transport Properties and Device Performance of Quasi-One-Dimensional MoS$_2$ FETs

M. Matić and M. Poljak, “Transport Properties and Device Performance of Quasi-One-Dimensional MoS$_2$ FETs,” in *2023 46th MIPRO ICT and Electronics Convention (MIPRO)*, 2023, pp. 168–172.
doi: 10.23919/MIPRO57284.2023.10159951

– 5 pages

MIPRO 2023, May 22 - 26, 2023, Opatija, Croatia

Transport Properties and Device Performance of Quasi-One-Dimensional MoS_2 FETs

M. Matić and M. Poljak*
Computational Nanoelectronics Group
Micro and Nano Electronics Laboratory, Faculty of Electrical Engineering and Computing
University of Zagreb, HR-10000 Zagreb, Croatia
*E-mail: mirko.poljak@fer.hr

***Abstract*—We investigated the bandstructure, transport and device properties of semiconducting MoS_2 nanoribbons (MoS_2NR) with hybrid OH-passivated armchair edges using orbitally-resolved *ab initio* Hamiltonians and quantum transport simulations based on Green's functions. The impact of MoS_2NR width scaling on the bandstructure, transmission, bandgap, injection velocity, charge density and ON-state current are analyzed in detail using the ballistic FET model. We find that sub-3 nm-wide and ~15 nm-long MoS_2NR FETs offer low driving currents under 0.43 mA/µm for nFETs and under 0.6 mA/µm for pFETs. Moreover, the current is only weakly modulated by nanoribbon width downscaling due to immunity of the MoS_2NR bandstructure to quantum confinement effects.**

Keywords*—MoS_2, molybdenum disulfide, quasi-one-dimensional, nanoribbon, quantum transport, Green's function, NEGF, ab initio, DFT, MLWF

I. INTRODUCTION

Since the discovery of graphene in 2004, research focus on two-dimensional (2D) materials as potential candidates to replace silicon in future electronic devices is growing exponentially [1]–[3]. Atomically-thin and dangling-bond-free surfaces along with near-ballistic transport properties of some 2D materials are ideal for future field-effect transistors (FETs). After graphene, monolayer molybdenum disulfide (MoS_2) is one of the most studied 2D materials which showed promise due to high stability, compatibility with graphene, and exceptionally high ON/OFF current ratio > 10^8 [4]. The MoS_2 monolayer is a transition metal disulfide (TMD) with a sandwiched S-Mo-S structure, as shown in Fig. 1. Electronic, transport, and device properties of MoS_2 monolayer devices have been studied extensively and it is often used as a benchmark for other 2D materials [5]–[7]. On the other hand, patterning MoS_2 into quasi-one-dimensional (quasi-1D) nanoribbons, which are illustrated in Fig. 1, enables the tuning of electronic and transport properties, with a potential for beneficial adjustment of device properties as well. Although MoS_2 nanoribbons (MoS_2NRs) in armchair and zigzag directions have been studied previously [8]–[10], due to high influence of edge atoms on the device performance and wide range of possible edge passivation atoms, there are still interesting configurations that have not been explored such as MoS_2NRs with hybrid OH-passivated edges. Electronic properties study in [11] of the hybrid OH-passivated MoS_2NRs showed that this edge configuration is the most stable among all studied edge passivation configurations and, therefore, presents an interesting choice for future MoS_2 based nanodevices once fabrication becomes mature enough. Therefore, in this work we study the device performance of the hybrid OH-passivated MoS_2NRs.

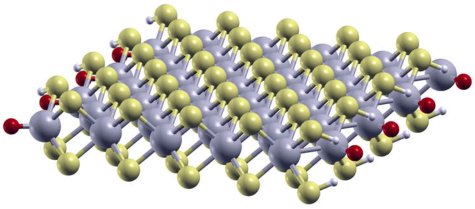

Figure 1. Illustration of an MoS_2 nanoribbon with OH-passivated armchair edges (Mo, S, O and H atoms are represented by grey, yellow, red and white balls, respectively).

Advanced modeling and simulations are used in this study to investigate MoS_2 nanoribbons and MoS_2NR FETs at an atomic level, which is necessary due to inherently strong quantum effects in 2D material nanostructures. Electronic band structure is calculated using the *ab initio* density functional theory (DFT) and, afterwards, maximally-localized Wannier functions (MLWFs) are employed to transform DFT Hamiltonians into a localized basis. The localized MLWF Hamiltonians are much sparser, thus enabling the simulations of realistically sized nanodevice. Quantum transport in such nanostructures is calculated by using the non-equilibrium Greens function (NEGF) formalism. In this paper, we analyze the electronic, transport and device properties of MoS_2NR and MoS_2NR FETs with OH-passivated edges by employing our in-house DFT-NEGF-MLWF solver [12], [13]. We report only a weak impact of MoS_2NR width scaling from ~3.0 nm to ~0.8 nm on the ballistic performance, which results in small degradation and robust performance of ultra-scaled MoS_2NR FETs.

II. METHODOLOGY

The MoS_2NR structure of various widths ranging from ~0.8 nm to ~3.0 nm is constructed along the armchair direction from a MoS_2 unit-cell obtained from Materials Cloud [14] and passivated with OH, as shown in Fig. 1. The Mo edge atoms are passivated with O atoms, while S atoms are passivated with H atoms. Plane-wave DFT is used to obtain highly accurate Hamiltonians of MoS_2 nanostructures investigated in this work. Since DFT calculations assumes periodicity in all three directions, we add a vacuum region of 20 Å in confined directions to exclude any interaction between adjacent layers. For DFT calculations we employ Quantum Espresso [15] with Perdew-Burke-Ernzerhof generalized gradient approximation (PBE-GGA) [16] exchange-correlation (XC) functional and projector augmented wave (PAW) pseudopotentials . The Brillouin zone (BZ) is sampled using an 15-point equally-spaced Monkhorst-Pack grid [17] in the transport direction and a single point in the confined directions. The plane-wave cutoff energy is set to 100 Ry, whereas the convergence threshold is set to 10^{-3} eV/Å for the ionic force and to 10^{-4} eV for energy.

Dense DFT Hamiltonians are localized in energy and are, therefore, not suitable for NEGF quantum transport simulations which prefer sparser matrices, i.e. space-localized Hamiltonians. Transformation into a space-localized basis is performed using the maximally-localized Wannier functions (MLWFs) [18] which results in tight-binding-like sparse matrices. To obtain MLWF Hamiltonians, we use the Wannier90 [19] program. The main inputs of Wannier90 are the trial orbital projections on Bloch manifold, and in this work the trial orbitals for MoS_2NRs are *d* orbitals for Mo atoms and *p* orbitals for O and S atoms. For all MoS_2NR widths the Wannier spread smaller than 2.5 Å^2 per atom is obtained. For each nanoribbon width, MLWF Hamiltonians of a MoS_2NR unit-cell are scaled in the transport direction to construct ~15 nm-long MoS_2NRs.

For quantum transport simulations we use the NEGF formalism [20]–[22], as implemented in our in-house code [12], [13], [23], [24]. Within NEGF, device is modeled with ideal contacts i.e. semi-infinite regions of the same material as the channel using the recursive Sancho-Rubio method [25]. Top-of-the-barrier (ToB) model [26] is used in combination with NEGF to assess ballistic device performance of ultra-scaled MoS_2NR FETs with n- and p-type channels. In ToB ballistic FET simulations, gate equivalent oxide thickness (EOT) is set to 1 nm, while source/drain (S/D) region doping levels are set at 0.01 molar fraction of the MoS_2NR areal atomic density. In all devices we set a common OFF-state current (I_{OFF}) of 10 nA/μm as projected in the International Roadmap for Devices and Systems (IRDS) for high-performance (HP) devices in future CMOS technology nodes [27]. Gate control over the channel in the ToB model devices is assumed ideal and, since no tunneling is included, ideal 60 mV/dec subthreshold slope is obtained in all devices. The ballistic ON-state current (I_{ON}) is extracted when both gate and drain are biased at the supply voltage, i.e. $V_{GS} = V_{DS} = 0.7$ V.

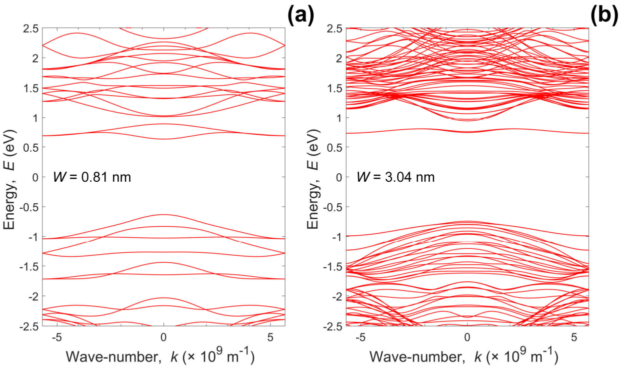

Figure 2. Bandstructure of armchair MoS_2NRs with the widths of (a) 0.81 nm and (b) 3.04 nm.

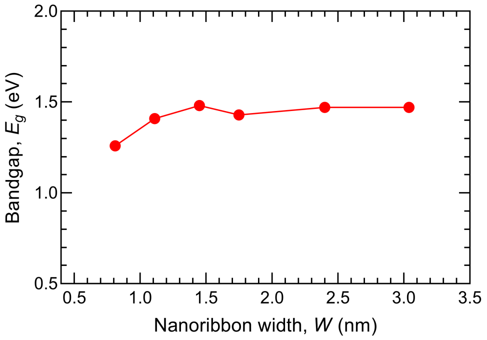

Figure 3. Impact of nanoribbon width scaling on the bandgap of armchair MoS_2NRs.

III. RESULTS AND DISCUSSION

In Figure 2 we plot the bandstructure of the widest (Fig. 2a) and the narrowest (Fig. 2b) analyzed MoS_2NR with the widths of $W = 3.04$ nm and $W = 0.81$ nm, respectively. Bandstructure plots contain two subbands that are isolated from the rest of the conduction band (CB). These subbands are isolated due to the influence of edge atoms, which also shift the bandgap from indirect to direct with no conclusive pattern. Scaling down nanoribbon width from 3.04 nm to 0.81 nm results in the separation of these two subbands in CB near the Γ point, which also results in higher curvature, i.e. lower electron effective mass, near CB minimum (CBM) for $W = 0.81$ nm. On the other hand, in the valence band (VB) a higher number of available bands in wider MoS_2NR results in higher number of bands near the VB maximum (VBM), but the narrowest MoS_2NR exhibits a higher curvature and lower hole effective mass in the dominant subband near VBM.

Width-dependence of the bandgap (E_g), extracted from the bandstructure of MoS_2NRs of various widths, is reported in Fig. 3. The plot show a nearly constant bandgap of ~1.47 eV for MoS_2NRs with $W > 1.4$ nm, while scaling down the width below 1.4 nm results in a sharp E_g decrease to 1.26 eV in the 0.81 nm-wide MoS_2NR. The OH-passivated MoS_2NRs exhibit a similar bandgap compared to 2D monolayer MoS_2 for which we obtain the bandgap of 1.7 eV. This value is in line with

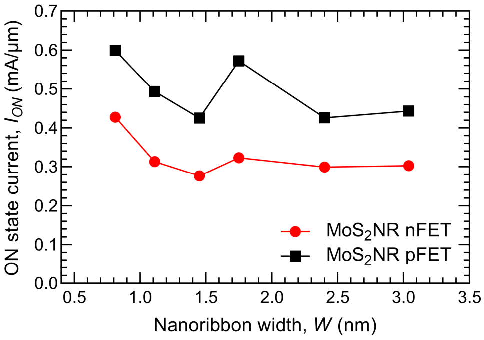

Figure 4. Width-dependence of the ON-state current in n- and p-type MoS$_2$NR FETs. I_{ON} extracted at $V_{GS} = V_{DS} = V_{DD} = 0.7$ V, with a common I_{OFF} = 10nA set for all devices.

$E_g = 1.67$ eV reported in [11] with the main difference coming from the isolated edge-state bands in the CB.

In order to assess the scaling and confinement effects on device performance, we plot the ON-state current in Fig. 4 for different widths and both device types. Both n- and pFETs exhibit similar scaling laws of I_{ON} with width-downscaling. Qualitatively, we can separate the plot into two groups or two width ranges. The first group includes MoS$_2$NR FETs with channel widths from $W = 3.04$ nm to $W = 1.75$ nm, which shows increase of I_{ON} while scaling down MoS$_2$NR width. The second group starts with $W = 1.45$ nm where the I_{ON} shows a sharp decrease compared to the $W = 1.75$ nm case, while further width downscaling results in an increase of I_{ON} down to the 0.81 nm-wide MoS$_2$NR FET. The maximum I_{ON} for both n- and pFETs is obtained for 0.81 nm-wide MoS$_2$NR transistor with $I_{ON} = 0.43$ mA/µm for the nFET and $I_{ON} = 0.60$ mA/µm for the pFET. Comparing the obtained I_{ON} results for MoS$_2$NR FETs to IRDS requirements at the "3 nm" and "2.1 nm" nodes, we conclude that the I_{ON} goal set at 1.9 mA/µm is fulfilled by none of the MoS$_2$NR devices explored in this paper.

To further understand the behavior of the ON-state current we plot density of states (DOS), transmission, the ON-state charge density (Q_s) and injection velocity (v_{inj}) at ToB, and the ON-state current energy-density. The DOS and transmission characteristics, plotted separately for electrons and holes i.e. in the CB and VB, are shown in Fig. 5. The DOS near the CBM is similar for all MoS$_2$NRs up to ~0.08 eV after which, due to the existence of isolated edge-state bands, there are no free states and DOS goes to zero. There is an exception for $W = 0.81$ nm where we previously in Fig. 2a observed the broadening of the isolated band near the Γ point. This band broadening results in a nonzero DOS in a broader energy range in comparison to wider nanoribbons. Transmission exhibits similar characteristics as DOS in the CB. At the CBM, transmission equals 1 for the widths of 0.81 nm and 1.75 nm, and sharply increases to 2 at an energy ~20 meV away from the CBM. Interestingly, these MoS$_2$NRs have a direct bandgap and show highest drain current of all the simulated MoS$_2$NR nFETs. On the other hand, the 1.45 nm-wide and 3.04 nm-wide MoS$_2$NRs have a higher transmission equal to 2 at the CBM. This is because these MoS$_2$NRs have an indirect bandgap with a lower curvature of the CB dispersion, which results in lower I_{ON}. On the other hand, in VB we observe that scaling down nanoribbon width decreases the number of Van Hove

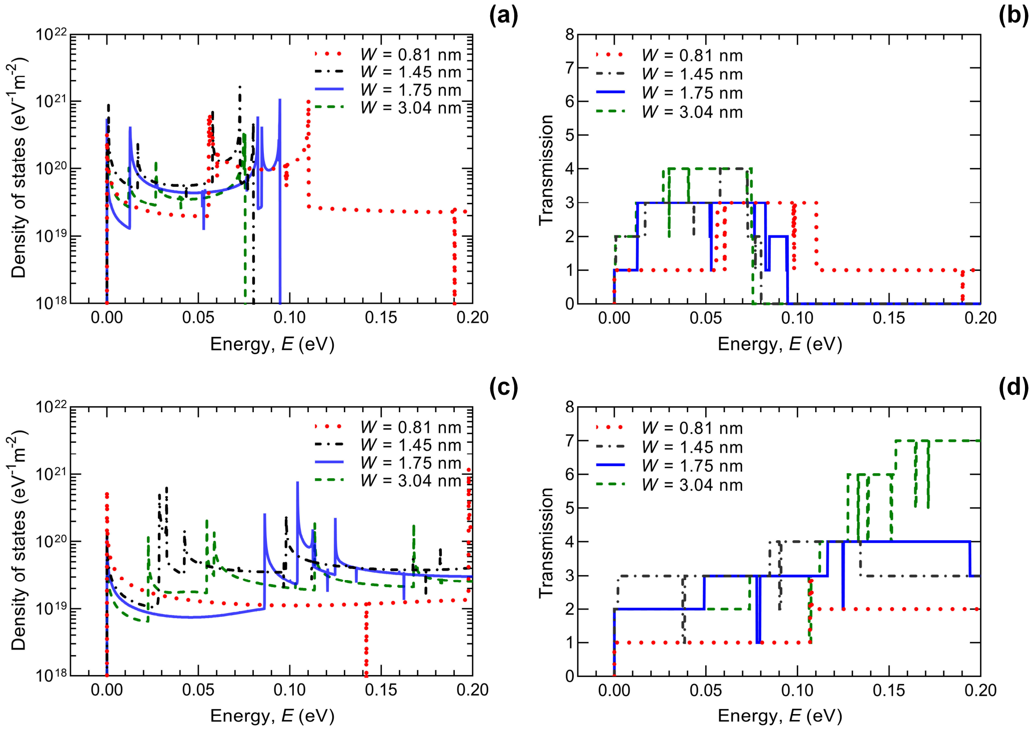

Figure 5. Comparison of DOS (panels on the left) and transmission (panels on the right) in (a, b) CB and (c, d) VB of MoS$_2$NRs of various widths.

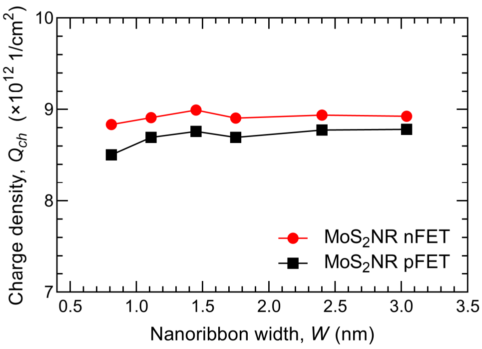

Figure 6. Width-dependence of the channel charge density at ToB in n- and p-type MoS$_2$NR FETs. The Q_s is extracted in the ON-state, i.e. $V_{GS} = V_{DS} = V_{DD} = 0.7$ V.

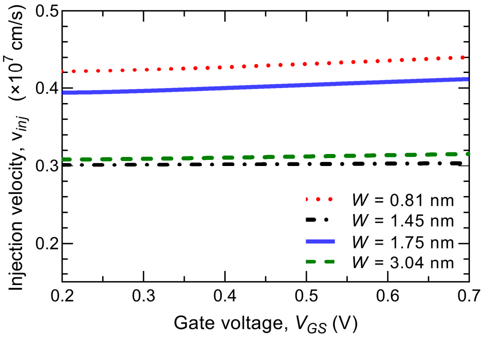

Figure 7. Hole injection velocity dependence on gate bias in MoS$_2$NR pFETs with various channel widths. $V_{DS} = V_{DD} = 0.7$ V.

singularities (VHS) in the hole DOS near the VBM due to the lower number of available subbands in narrower MoS$_2$NRs. For the same reason, transmission near the VBM decreases while scaling down MoS$_2$NR width. When comparing the transport of electrons and holes, we see that holes generally exhibit a higher transmission probability than electrons over the 200 meV energy range away from the VBM or CBM, respectively, which is partly responsible for the higher I_{ON} in p-type than in n-type MoS$_2$NR FETs reported in Fig. 4.

The DOS and transmission exhibit complex characteristics and are unable to provide a clear insight into FET performance. The influence of width scaling on the ON-state charge density at the ToB is plotted in Fig. 6. Despite considerable variations in the DOS, similar values of Q_s are obtained for all MoS$_2$NR nFETs and pFETs. On average over all nanoribbon widths, electron density is ~8.9×10^{12} cm^{-2}, while hole density is somewhat lower and equals ~8.7×10^{12} cm^{-2}. The impact of scaling and confinement is visible only in the 0.81 nm-wide MoS$_2$NRs that show slightly lower electron and hole density at 8.8×10^{12} cm^{-2} and 8.5×10^{12} cm^{-2}, respectively. This decrease is due to setting the common I_{OFF} value, because MoS$_2$NR with the width of 0.81 nm has the smallest bandgap and, therefore, the lowest applied bias is needed to set I_{OFF} which results in slightly lower Q_s at ToB.

Within the ballistic ToB model, we have $I_{ON} = Q_s \cdot v_{inj}$ at ToB in the ON-state and, hence, the peculiar I_{ON} - W characteristic in Fig. 4 is a consequence of the injection velocity behavior [13], [26]. In Fig. 7 we plot the gate bias dependence of v_{inj} in pFETs, with gate voltage ranging from the threshold voltage (~0.2 V) to supply voltage (0.7 V). Only the v_{inj} in pFETs is plotted because nFETs do not show any noticeable velocity modulation with the applied gate voltage. On the other hand, hole injection velocity in MoS$_2$NR pFETs with the widths of 0.81 nm and 1.75 nm show a slight increase of v_{inj} with increasing gate bias. The modulation is rather weak, equaling around 5% increase with maximum value obtained in the ON-state of 0.41×10^7 cm/s and 0.44×10^7 cm/s, respectively. With the proportional relationship of the ON-state current to v_{inj} and Q_s, and v_{inj} showing similar scaling laws as I_{ON} while Q_s being of the similar value for all MoS$_2$NR widths we determine that ON-state performance is dominantly determined by v_{inj}. In comparison to other contending 2D materials, MoS$_2$NR FETs exhibit significantly lower v_{inj} that deteriorates up to ~9× in comparison to graphene nanoribbons, and ~1.5× when compared against conventional Si MOSFETs [28]. Hence, it is no surprise that the I_{ON} of MoS$_2$NR FETs is lower than in other 2D material devices [28]–[31].

Finally, the ON-state current energy-density (J_{de}) for MoS$_2$NR nFET (Fig. 8a) and pFET (Fig. 8b) shows that the current flows mostly in the ~100 meV energy range above/under the CBM/VBM. This range coincides with the energy range of isolated bands in the CB and, therefore, only the isolated edge-state bands in the CB determine the performance of nFETs. On the other hand, VB offers higher number of available bands in the same energy

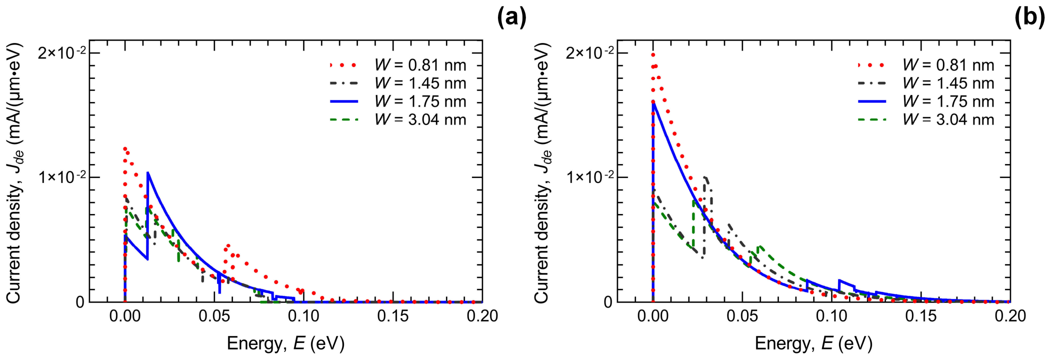

Figure 8. Current energy-density at ToB in the ON-state for MoS$_2$NR (a) nFETs and (b) pFETs with different nanoribbon channel widths.

range, which results in higher J_{de}, i.e. maxima of 1.2×10^{-2} mA/(eV·µm) for nFETs and 2×10^{-2} mA/(eV·µm) for pFETs, with both values reached at the CBM and VBM, respectively. Hence, any improvement of MoS$_2$NR nFET performance depends on the effective turn-off of the isolated band contribution.

IV. CONCLUSIONS

We studied the electronic, transport and ballistic device characteristics of sub-3 nm-wide and ~15 nm-long quasi-1D MoS$_2$ nanostructures with OH-passivated edges. We employed DFT and MLWFs to obtain the electronic structure, and NEGF simulations with the ToB model to assess the ballistic performance of armchair MoS$_2$NR FETs. We found that nFET is limited by the two isolated bands in the CB, which exist due to edge configuration or edge states. The analysis revealed that Q_s is similar for all MoS$_2$NR widths, and that I_{ON} - W dependence is mainly determined by the features of v_{inj}. The maximum ON-state current of 0.43 mA/µm is obtained for nFETs and 0.6 mA/µm for pFETs. Therefore, MoS$_2$NR FETs passivated with OH do not meet IRDS requirements for advanced nodes unless a method of eliminating edge states and associated isolated bands in the CB is found.

ACKNOWLEDGMENTS

This work was supported by the Croatian Science Foundation under the project CONAN2D (Grant No. UIP-2019-04-3493).

REFERENCES

[1] K. S. Novoselov *et al.*, "Electric Field Effect in Atomically Thin Carbon Films," *Science*, vol. 306, no. 5696, pp. 666–669, Oct. 2004, doi: 10.1126/science.1102896.

[2] G. Fiori *et al.*, "Electronics based on two-dimensional materials," *Nat. Nanotechnol.*, vol. 9, no. 10, pp. 768–779, Oct. 2014, doi: 10.1038/nnano.2014.207.

[3] N. Briggs *et al.*, "A roadmap for electronic grade 2D materials," *2D Mater.*, vol. 6, no. 2, p. 022001, Jan. 2019, doi: 10.1088/2053-1583/aaf836.

[4] B. Radisavljevic, A. Radenovic, J. Brivio, V. Giacometti, and A. Kis, "Single-layer MoS2 transistors," *Nature Nanotechnology*, vol. 6, no. 3, pp. 147–150, 2011, doi: 10.1038/nnano.2010.279.

[5] W. Cao, J. Kang, D. Sarkar, W. Liu, and K. Banerjee, "Performance evaluation and design considerations of 2D semiconductor based FETs for sub-10 nm VLSI," in *2014 IEEE International Electron Devices Meeting*, Dec. 2014, p. 30.5.1-30.5.4. doi: 10.1109/IEDM.2014.7047143.

[6] A. Nourbakhsh *et al.*, "MoS2 Field-Effect Transistor with Sub-10 nm Channel Length," *Nano Lett.*, vol. 16, no. 12, pp. 7798–7806, Dec. 2016, doi: 10.1021/acs.nanolett.6b03999.

[7] Y. Lee, S. Fiore, and M. Luisier, "Ab initio mobility of single-layer MoS2 and WS2: comparison to experiments and impact on the device characteristics," in *2019 IEEE International Electron Devices Meeting (IEDM)*, Dec. 2019, p. 24.4.1-24.4.4. doi: 10.1109/IEDM19573.2019.8993477.

[8] C. Ataca, H. Şahin, E. Aktürk, and S. Ciraci, "Mechanical and Electronic Properties of MoS2 Nanoribbons and Their Defects," *J. Phys. Chem. C*, vol. 115, no. 10, pp. 3934–3941, Mar. 2011, doi: 10.1021/jp1115146.

[9] K. Dolui, C. D. Pemmaraju, and S. Sanvito, "Electric Field Effects on Armchair MoS2 Nanoribbons," *ACS Nano*, vol. 6, no. 6, pp. 4823–4834, Jun. 2012, doi: 10.1021/nn301505x.

[10] Q. Yue *et al.*, "Bandgap tuning in armchair MoS2 nanoribbon," *J. Phys.: Condens. Matter*, vol. 24, no. 33, p. 335501, Jul. 2012, doi: 10.1088/0953-8984/24/33/335501.

[11] L. Zhang *et al.*, "Modulation of Electronic Structure of Armchair MoS $_2$ Nanoribbon," *J. Phys. Chem. C*, vol. 119, no. 38, pp. 22164–22171, Sep. 2015, doi: 10.1021/acs.jpcc.5b04747.

[12] M. Matić;, T. Župančić, and M. Poljak, "Parallelized Ab Initio Quantum Transport Simulation of Nanoscale Bismuthene Devices," in *2022 45th Jubilee International Convention on Information, Communication and Electronic Technology (MIPRO)*, 2022, pp. 118–123. doi: 10.23919/MIPRO55190.2022.9803335.

[13] M. Matić and M. Poljak, "Ab initio quantum transport simulations of monolayer GeS nanoribbons," *Solid-State Electronics*, vol. 197, p. 108460, Nov. 2022, doi: 10.1016/j.sse.2022.108460.

[14] L. Talirz *et al.*, "Materials Cloud, a platform for open computational science," *Sci Data*, vol. 7, no. 1, Art. no. 1, Dec. 2020, doi: 10.1038/s41597-020-00637-5.

[15] P. Giannozzi *et al.*, "QUANTUM ESPRESSO: a modular and open-source software project for quantum simulations of materials," *J. Phys.: Condens. Matter*, vol. 21, no. 39, Art. no. 39, Sep. 2009, doi: 10.1088/0953-8984/21/39/395502.

[16] J. P. Perdew, K. Burke, and M. Ernzerhof, "Generalized Gradient Approximation Made Simple," *Phys. Rev. Lett.*, vol. 77, no. 18, Art. no. 18, Oct. 1996, doi: 10.1103/PhysRevLett.77.3865.

[17] H. J. Monkhorst and J. D. Pack, "Special points for Brillouin-zone integrations," *Phys. Rev. B*, vol. 13, no. 12, Art. no. 12, Jun. 1976, doi: 10.1103/PhysRevB.13.5188.

[18] N. Marzari and D. Vanderbilt, "Maximally localized generalized Wannier functions for composite energy bands," *Phys. Rev. B*, vol. 56, no. 20, Art. no. 20, Nov. 1997, doi: 10.1103/PhysRevB.56.12847.

[19] G. Pizzi *et al.*, "Wannier90 as a community code: new features and applications," *J. Phys.: Condens. Matter*, vol. 32, no. 16, p. 165902, Apr. 2020, doi: 10.1088/1361-648X/ab51ff.

[20] S. Datta, *Electronic Transport in Mesoscopic Systems*. Cambridge University Press, 1997.

[21] M. Pourfath, *The Non-Equilibrium Green's Function Method for Nanoscale Device Simulation*. Wien: Springer-Verlag, 2014. doi: 10.1007/978-3-7091-1800-9.

[22] Y. He, T. Kubis, M. Povolotskyi, J. Fonseca, and G. Klimeck, "Quantum transport in NEMO5: Algorithm improvements and high performance implementation," in *2014 International Conference on Simulation of Semiconductor Processes and Devices (SISPAD)*, Sep. 2014, pp. 361–364. doi: 10.1109/SISPAD.2014.6931638.

[23] M. Poljak, "Electron Mobility in Defective Nanoribbons of Monoelemental 2D Materials," *IEEE Electron Dev. Lett.*, vol. 41, no. 1, pp. 151–154, Jan. 2020, doi: 10.1109/LED.2019.2952661.

[24] M. Poljak, M. Matić, and A. Zeljko, "Minimum Contact Resistance in Monoelemental 2D Material Nanodevices With Edge-Contacts," *IEEE Electron Device Letters*, vol. 42, no. 8, pp. 1240–1243, Aug. 2021, doi: 10.1109/LED.2021.3087908.

[25] M. P. L. Sancho, J. M. L. Sancho, and J. Rubio, "Quick iterative scheme for the calculation of transfer matrices: application to Mo (100)," *J. Phys. F: Met. Phys.*, vol. 14, no. 5, Art. no. 5, May 1984, doi: 10.1088/0305-4608/14/5/016.

[26] A. Rahman, Jing Guo, S. Datta, and M. S. Lundstrom, "Theory of ballistic nanotransistors," *IEEE Trans. Electron Devices*, vol. 50, no. 9, pp. 1853–1864, Sep. 2003, doi: 10.1109/TED.2003.815366.

[27] "'IEEE Intl. Roadmap for Devices and Systems (IRDS), 2019 Update.' https://irds.ieee.org/."

[28] G. Liang, N. Neophytou, D. E. Nikonov, and M. S. Lundstrom, "Performance Projections for Ballistic Graphene Nanoribbon Field-Effect Transistors," *IEEE Transactions on Electron Devices*, vol. 54, no. 4, pp. 677–682, Apr. 2007, doi: 10.1109/TED.2007.891872.

[29] S. Kaneko, H. Tsuchiya, Y. Kamakura, N. Mori, and M. Ogawa, "Theoretical performance estimation of silicene, germanene, and graphene nanoribbon field-effect transistors under ballistic transport," *Appl. Phys. Express*, vol. 7, no. 3, p. 035102, Mar. 2014, doi: 10.7567/APEX.7.035102.

[30] X. Cao and J. Guo, "Simulation of Phosphorene Field-Effect Transistor at the Scaling Limit," *IEEE Trans. Electron Devices*, vol. 62, no. 2, pp. 659–665, Feb. 2015, doi: 10.1109/TED.2014.2377632.

[31] M. Poljak and M. Matić, "Bandstructure and Size-Scaling Effects in the Performance of Monolayer Black Phosphorus Nanodevices," *Materials*, vol. 15, no. 1, Art. no. 1, Jan. 2022, doi: 10.3390/ma15010243.

Publication 7

Tunneling Attenuation and Leakage Current in MoS_2 Nanoribbon MOSFETs

I. Prevarić, M. Matić, and M. Poljak, “Tunneling Attenuation and Leakage Current in MoS_2 Nanoribbon MOSFETs,” in *2023 46th MIPRO ICT and Electronics Convention (MIPRO)*, 2023, pp. 163–167.
doi: 10.23919/MIPRO57284.2023.10159745

– 5 pages

MIPRO 2023, May 22 - 26, 2023, Opatija, Croatia

Tunneling Attenuation and Leakage Current in MoS_2 Nanoribbon MOSFETs

I. Prevarić, M. Matić, and M. Poljak[*]
Computational Nanoelectronics Group
Micro and Nano Electronics Laboratory, Faculty of Electrical Engineering and Computing
University of Zagreb, HR-10000 Zagreb, Croatia
[*]E-mail: mirko.poljak@fer.hr

***Abstract*—We study the OFF-state leakage current in quasi-one-dimensional MoS_2 nanoribbon (MoS_2NR) FETs using *ab initio* Hamiltonians and quantum transport simulations based on Green's functions. Complex band structure is computed for these devices and the energy-dependent tunneling attenuation inside the bandgap is obtained. We investigate the tunneling component of the OFF-state leakage for sub-20 nm long and sub-3 nm wide MoS_2NR FETs, using the under-the-barrier (UTB) and top-of-the-barrier (ToB) ballistic models. We report that using the parabolically-approximated attenuation overestimates the OFF-state leakage significantly. Furthermore, we demonstrate that all MoS_2NR FETs show good tunneling suppression due to high attenuation even for the shortest devices where the OFF-state leakage is under 16.5 nA/µm for nFETs and lower than 22 nA/µm for pFETs.**

Keywords*—*MoS_2, molybdenum disulfide, leakage current, complex bandstructure, tunneling, quasi-one-dimensional, nanoribbon, quantum transport, NEGF, ab initio, DFT

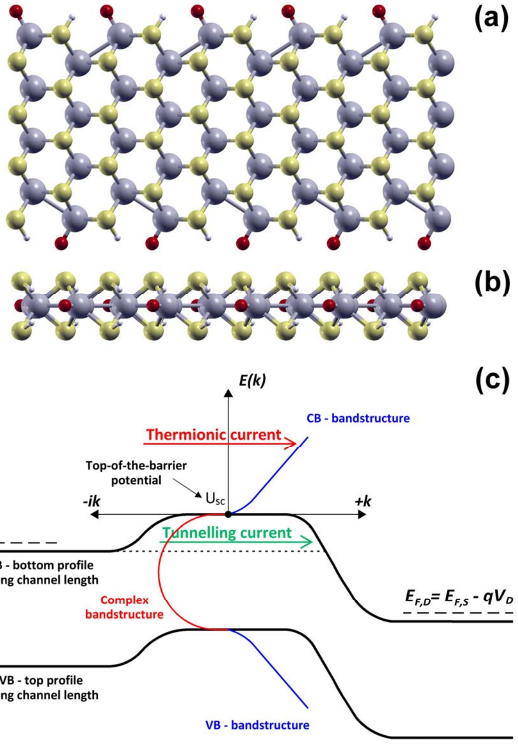

Fig. 1. (a) Top and (b) side view of MoS_2NR with OH passivation (explained in the text). (c) Conduction and valence band profiles along the channel length with an illustration of real and complex bandstructure used in UTB and TOB calculations.

I. INTRODUCTION

Monolayer molybdenum disulfide (MoS_2), alongside graphene, is one of the most promising two-dimensional (2D) materials for future field-effect transistors (FETs) due to high stability and very high ON-OFF current ratio [1]. The 2D MoS_2 is a transition metal dichalcogenide (TMD) that exhibits a sandwiched S-Mo-S structure as illustrated in Fig. 1a and b. The electronic, transport, and device properties of devices with 2D MoS_2 monolayer were comprehensively studied previously [2]–[4], however, patterning MoS_2 into quasi-one-dimensional (quasi-1D) structures such as nanoribbons provides an additional degree of freedom. This nanostructure enables the tuning of electron and transport properties via quantum confinement effects and allows a strong influence of edge atoms on the characteristics of MoS_2 nanoribbons (MoS_2NRs). Consequently, a high number of possible MoS_2NR configurations exists and many of them have been studied previously in both armchair and zigzag directions [5]–[7]. Nevertheless, there are some interesting configurations, such as MoS_2NRs with hybrid OH-passivated edges shown in Fig. 1a and b, whose transport and device properties have not yet been explored. Electronic properties of hybrid OH-passivated MoS_2NRs were studied in [8] where this configurations was proven to be one of the most stable edge passivation configurations for future MoS_2-based nanodevices.

In addition to stability, low OFF-state leakage current (I_{OFF}) is one of the critical requirements for future low power/high density devices. However, I_{OFF} has not yet been studied in ultra-scaled FETs with channels made of MoS_2NRs with hybrid OH passivation. In this paper, we present a study on I_{OFF} of MoS_2NR FETs using our in-house non-equilibrium Green's function (NEGF) formalism based quantum transport solver [9], [10]. The NEGF calculations are employed in conjunction with top-of-the-barrier (ToB) model [11] for the ballistic thermionic current and with the under-the-barrier (UTB) model [12],[13] that accounts for intra-band tunneling, as indicated in Fig. 1c. Highly accurate space-localized

Hamiltonians are obtained from *ab initio* plane-wave density functional theory (DFT) calculations using maximally-localized Wannier functions (MLWFs). We report strong suppression of tunneling for all the studied MoS_2NRs even in transistors with 5 nm-long channels, which indicates a robust performance and low I_{OFF} in ultra-scaled MoS_2NR FETs.

II. METHODOLOGY

Armchair MoS_2 nanoribbons passivated with OH of various widths (W) ranging from ~0.8 nm to ~3.0 nm are constructed for *ab initio* calculations. For example, the 1.11 nm-wide MoS_2NR is shown in the top (Fig. 1a) and side view (Fig. 1b) with the transport direction along the horizontal orientation. The hybrid OH passivation is achieved by terminating the edge Mo atoms with O atoms and S atoms with H atoms. Plane-wave DFT is employed in combination with transformation to tight-binding-like sparse matrices using MLWFs [14] that are suitable for NEGF simulations. Quantum Espresso [15] is used for DFT calculations, where a vacuum region of 20 Å is added in the confined directions due to the nature of DFT to assume periodicity in all three directions. The Brillouin zone (BZ) is sampled using an 1 × 15 × 1 Monkhorst-Pack grid [16], where 15 points are used in the transport direction. Perdew-Burke-Ernzerhof generalized gradient approximation (PBE-GGA) [17] exchange-correlation (XC) functional is used along projector augmented wave (PAW) pseudopotentials. The plane-wave cutoff energy is set to 1360 eV, whereas the convergence threshold is set to 10^{-3} eV/Å for the ionic force and to 10^{-4} eV for energy. Wannier90 program [18] is employed to transform the DFT Hamiltonians into the space-localized basis while preserving the accuracy of the DFT. The accuracy of transformation using MLWFs greatly depends on the trial projections on the Bloch manifold. In this work, for OH-passivated MoS_2NRs, *d* orbitals are chosen as trial orbitals for Mo atoms and *p* orbitals for S and O atoms. During wannierization, we obtain a Wannier spread lower than 2.5 Å^2 per atom for all MoS_2NR widths, which indicates successful transformation. After MLWF Hamiltonians of a MoS_2NR unit-cell are obtained, where the unit-cell designates a super-cell along the entire nanoribbon width, the cell is scaled in the transport direction to construct the total MLWF Hamiltonian of the given MoS_2NR with lengths (L) ranging from ~5 nm to ~20 nm.

The main topic of this paper is the study of I_{OFF} of n- and p- type MoS_2NR MOSFET devices with ideal contacts. The I_{OFF} consists of the thermionic (above barrier) and tunneling (under barrier) current components, as shown in Fig. 1c. The thermionic current is calculated using the ToB model that depends on the density of states (DOS) and transmission spectra obtained using the NEGF simulations [19]–[21], as implemented in our in-house code [9], [10], [22], [23]. Furthermore, UTB model [13] is employed to calculate the tunneling current through the bandgap of the S/D potential barrier. For the UTB model, tunneling attenuation is needed, which can be obtained from the complex bandstructure. While using real wave-vector k leads to dispersion of propagating electron waves, setting imaginary values of the wave-vector k and calculating the dispersion results in tunneling attenuation $\kappa(E)$ that describes evanescent electron waves. Transmission probability is calculated according to the Wentzel-Kramers-Brillouin (WKB) approximation

$$T_{WKB} = \sum_{n} \exp\left[-2\,l(E)\,\kappa(E)\right] \qquad (1)$$

where n represents the number of complex subbands included in the calculation, while $l(E)$ is an energy-dependent tunneling barrier length. For simplicity, the potential barrier between the source and drain (S/D) is approximated with a parabolic function. Tunneling current is calculated using the Landauer formula that depends on WKB transmission, barrier height and Fermi-window, i.e. difference between S/D Fermi functions.

In order to provide meaningful comparison between various MoS_2NR devices we set a common ToB I_{OFF} of 10 nA/μm as defined in the International Roadmap for Devices and Systems (IRDS) for future high-performance (HP) CMOS nodes [24]. The I_{OFF} is set by a proper gate work function, which modifies the flat-band voltage, and accordingly lowers the OFF-state ToB potential that is used in the UTB model. Gate equivalent oxide thickness (EOT) is set to 1 nm and S/D doping is set at 0.01 molar fraction of the MoS_2NR areal atom density. Device OFF-state performance is studied when the tunneling attenuation $\kappa(E)$ is extracted directly from the complex bandstructure, and when $\kappa(E)$ is approximated with a parabolic function as is originally done in the literature [13]. The parabolic $\kappa(E)$ is defined by the maximum attenuation, occurring usually near the mid-gap, and the bandgap value. Furthermore, nanoribbon width and length scaling effects on the tunneling component of I_{OFF} are studied because the thermionic current is ballistic and, hence, independent of nanoribbon length.

III. RESULTS AND DISCUSSION

Figure 2 reports the bandstructure consisting of the complex part for imaginary k as negative values, and the real part for real k as positive values, for $W = 0.81$ nm (Fig. 2a) and $W = 3.04$ nm (Fig. 2b). Scaling down the nanoribbon width decreases the number of subbands and, consequently, the number of complex subbands inside the bandgap also decreases. While scaling down the width generally decreases the bandgap, i.e. from 1.5 eV for $W = 3.04$ nm to 1.25 eV for the 0.81 nm-wide nanoribbon, the attenuation curves of the dominant subband do not change as much. We observe that the two attenuation characteristics exhibit qualitatively similar behavior with maximum attenuation of ~2 nm^{-1} being equal for both MoS_2NRs in Fig. 2.

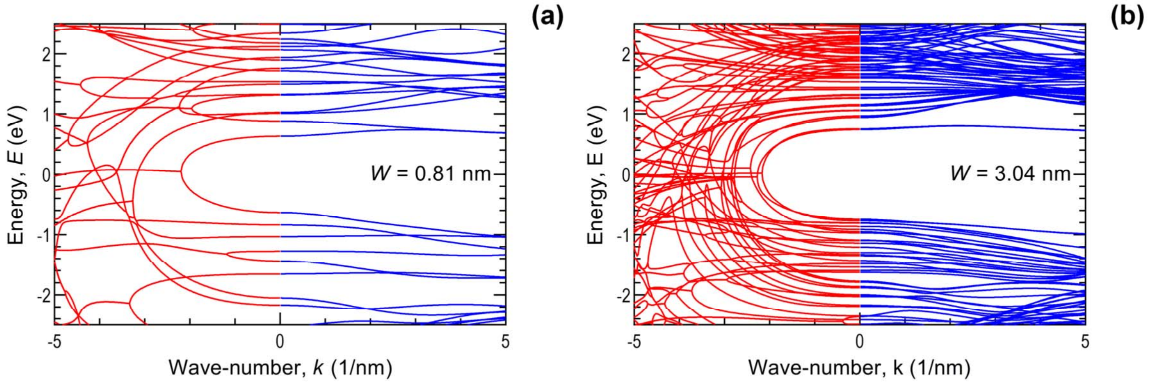

Fig. 2. Complex and real bandstructure of MoS$_2$NRs with the widths of (a) $W = 0.81$ nm, and (b) $W = 3.04$ nm. Real part is on the right-hand-side for positive k, and the complex part (attenuation) is on the left-hand-side for negative k.

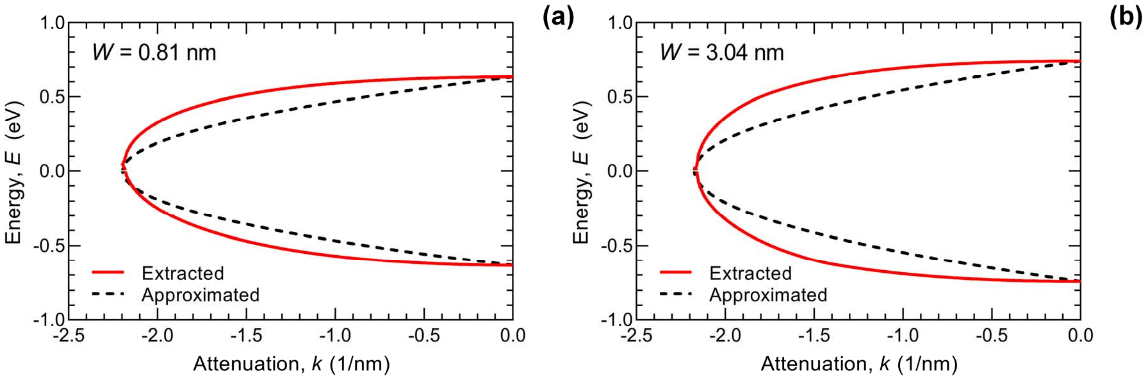

Fig. 3. Extracted and approximated attenuation characteristics of the dominant (with the lowest attenuation) complex subband for (a) 0.81 nm- and (b) 3.04 nm-wide MoS$_2$NRs.

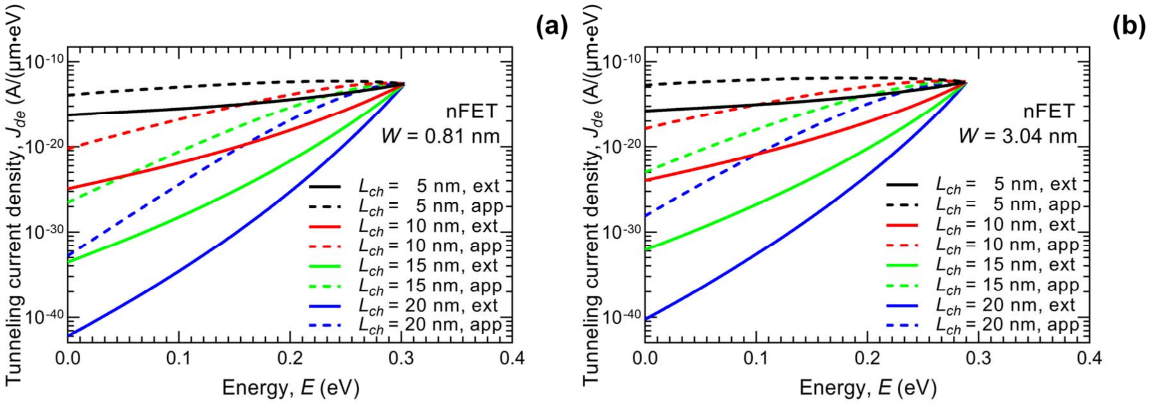

Fig. 4. Tunneling current energy density for MoS$_2$NR nFETs calculated with the exact extracted (ext) and approximated (app) attenuation for (a) $W = 0.81$ nm, and (b) $W = 3.04$ nm, and for four channel lengths equal to 5 nm, 10 nm, 15 nm and 20 nm.

The first subband belonging to evanescent waves, which connects the highest valence band with the lowest conduction band, can be extracted and then approximated with a parabola. Although using the approximation is much simpler to implement in the simulation environment, a large difference in attenuation is observed when comparing the extracted and approximated attenuation. The difference is reported in Fig. 3a for the 0.81 nm-wide nanoribbon, and an even larger mismatch is observed for $W = 3.04$ nm in Fig. 3b. Attenuation is the lowest near the conduction band minimum (CBM) and valence band maximum (VBM) which means that the tunneling OFF-state current is dominantly determined in the energy regions near the CBM for nFETs, and near the VBM for pFETs. Going towards mid-gap, the attenuation increases in both MoS$_2$NRs and reaches ~2.2 nm^{-1}, which turns off significant tunneling in this energy range.

In order to assess the differences in using the extracted and approximated attenuation curves, the tunneling current energy density (J_{de}), hereafter current density, is shown in Fig. 4 for various MoS$_2$NRs nFETs, with four different channel lengths in the range from ~5 nm to ~20 nm, and the widths of $W = 0.81$ nm (Fig. 4a) and $W = 3.04$ nm (Fig. 4b). The tunneling transport occurs between $E = 0$ eV (mid-gap) and $E \sim 0.3$ eV (CBM). The current density calculated with the approximated attenuation is up to 12 orders of magnitude higher than the current density calculated using the exact extracted attenuation, which demonstrates the inadequacy of the parabolic approximation for quantitative prediction of the tunneling component of I_{OFF}. In both attenuation models, J_{de} increases while scaling down MoS$_2$NR channel length from 20 nm to 5 nm due to decreasing tunneling length. When the extracted $\kappa(E)$ is used, the maximum J_{de} occurs at the top of the barrier for all channel lengths. On the other hand, J_{de} calculated using the parabolic $\kappa(E)$ exhibits a maximum at the top of the barrier only for channels longer than ~15 nm. As shown in Fig. 4, for shorter channels the J_{de} maximum shifts towards the mid-gap, which is clearly unphysical. Significant difference in J_{de} magnitude and the shift of the maximum show that the approximated parabolic $\kappa(E)$ model is not appropriate to assess the OFF-state performance and, therefore, in further calculations only the extracted $\kappa(E)$ is used.

The extracted attenuation exhibits differences between electron and hole attenuation characteristics, i.e. $\kappa(E)$ curves from the mid-gap towards either CBM or VBM, as shown in Fig. 5a. In turn, nFET and pFET devices with MoS$_2$NR channels are expected to have different tunneling characteristics. Scaling down MoS$_2$NR width increases the mismatch between the electron and hole attenuations, with hole $\kappa(E)$ being lower than the electron $\kappa(E)$. This difference points to a higher OFF-state current for pFET devices generally, and the difference is expected to increase as W decreases. Maximum attenuation equals ~2.2 nm^{-1} for all MoS$_2$NRs with the exception for $W = 1.11$ nm where the maximum $\kappa(E)$ is slightly higher at ~2.5 nm^{-1}, as reported in Fig. 5b.

The total OFF-state current per nanoribbon width is calculated for various MoS$_2$NR widths and channel lengths in the range from 20 nm to 5 nm and is shown in Fig. 6. The total I_{OFF} is a sum of the tunneling current, calculated by integrating the current density J_{de} over the Fermi window, and of the L-independent thermionic current, set to 10 nA/µm for all devices in ToB simulations. Scaling down channel length results in a significant increase of I_{OFF} in both nFETs (Fig. 6a) and pFETs (Fig. 6b), especially in 5 nm-long devices with the shortest S/D tunnel barrier. The total I_{OFF} is of the same magnitude for all n- and p- type MoS$_2$NR FETs with $L \geq 10$ nm, while a considerable difference is observed only for $L = 5$ nm. For nFETs with the 5 nm-long channel, maximum I_{OFF} of 16.5 nA/µm is observed for $W = 0.81$ nm and minimum

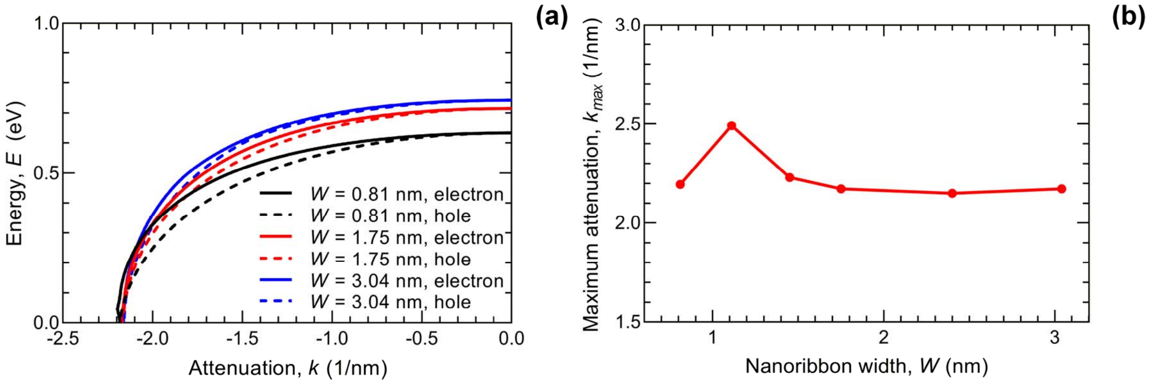

Fig. 5. (a) Extracted attenuation characteristics for electrons and holes for various widths of the MoS$_2$NR. The energy range spans from mid-gap at 0 eV to band minimum or maximum. (b) Dependence of the maximum attenuation of the dominant complex subband on the MoS$_2$NR width.

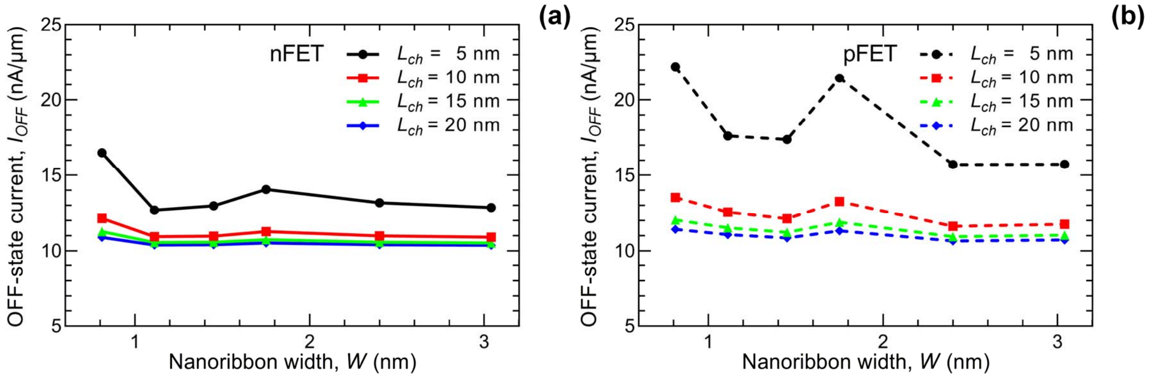

Fig. 6. Impact of MoS$_2$NR width scaling on total OFF-state current for (a) nFET and (b) pFET for various channel lengths ranging from 5 nm to 20 nm.

I_{OFF} of 12.7 nA/μm for the nFET with the 1.11 nm-wide MoS$_2$NR channel. On the other hand, pFET with the channel length of 5 nm shows the maximum I_{OFF} of 22 nA/μm for $W = 0.81$ nm and the minimum I_{OFF} of 15.7 nA/μm for $W = 3.04$ nm. These results show that a direct consequence of the lower hole attenuation compared to electron $\kappa(E)$ is the higher tunneling current in pFETs that ranges from 5.7 to 12 nA/μm in pFETs, in comparison to 2.7 to 6.5 nA/μm in nFETs. Finally, we note that the general increase and non-monotonic dependence of I_{OFF} on W reported in Fig. 6 is a consequence of non-monotonic features of $\kappa(E)$ (see Fig. 5b) and width-normalization of the drain current.

IV. CONCLUSIONS

Some features of NEGF calculations combined with the UTB and ToB models are used to calculate the tunneling and thermionic OFF-state currents in ultra-scaled MoS$_2$NR FETs with n- and p-type channels. Regarding the UTB model, we report a significant overestimation of tunneling leakage when a simple parabolic approximation of $\kappa(E)$ is used, rendering it useless for quantitative predictions about tunneling in ultra-scaled MoS$_2$ nanostructures. We report that scaling down channel length results in the expected growth of the tunneling current that is especially evident for sub-10 nm-long MoS$_2$NRs n- and pFETs. Due to weaker attenuation pFETs exhibit larger tunneling leakage, i.e. for $L = 5$ nm the total I_{OFF} is lower than 16.5 nA/μm for nFETs and under 22 nA/μm for pFETs. Generally, all MoS$_2$NRs show strong attenuation that ensures an appropriate suppression of tunneling in sub-3 nm-wide and sub-20 nm-long MoS$_2$NR FETs.

ACKNOWLEDGMENTS

This work was supported by the Croatian Science Foundation under the project CONAN2D (Grant No. UIP-2019-04-3493).

REFERENCES

[1] B. Radisavljevic, A. Radenovic, J. Brivio, V. Giacometti, and A. Kis, "Single-layer MoS2 transistors," *Nature Nanotechnology*, vol. 6, no. 3, pp. 147–150, 2011, doi: 10.1038/nnano.2010.279.

[2] W. Cao, J. Kang, D. Sarkar, W. Liu, and K. Banerjee, "Performance evaluation and design considerations of 2D semiconductor based FETs for sub-10 nm VLSI," in *2014 IEEE International Electron Devices Meeting*, Dec. 2014, p. 30.5.1-30.5.4. doi: 10.1109/IEDM.2014.7047143.

[3] A. Nourbakhsh *et al.*, "MoS2 Field-Effect Transistor with Sub-10 nm Channel Length," *Nano Lett.*, vol. 16, no. 12, pp. 7798–7806, Dec. 2016, doi: 10.1021/acs.nanolett.6b03999.

[4] Y. Lee, S. Fiore, and M. Luisier, "Ab initio mobility of single-layer MoS2 and WS2: comparison to experiments and impact on the device characteristics," in *2019 IEEE International Electron Devices Meeting (IEDM)*, Dec. 2019, p. 24.4.1-24.4.4. doi: 10.1109/IEDM19573.2019.8993477.

[5] C. Ataca, H. Şahin, E. Aktürk, and S. Ciraci, "Mechanical and Electronic Properties of MoS2 Nanoribbons and Their Defects," *J. Phys. Chem. C*, vol. 115, no. 10, pp. 3934–3941, Mar. 2011, doi: 10.1021/jp1115146.

[6] K. Dolui, C. D. Pemmaraju, and S. Sanvito, "Electric Field Effects on Armchair MoS2 Nanoribbons," *ACS Nano*, vol. 6, no. 6, pp. 4823–4834, Jun. 2012, doi: 10.1021/nn301505x.

[7] Q. Yue *et al.*, "Bandgap tuning in armchair MoS2 nanoribbon," *J. Phys.: Condens. Matter*, vol. 24, no. 33, p. 335501, Jul. 2012, doi: 10.1088/0953-8984/24/33/335501.

[8] L. Zhang *et al.*, "Modulation of Electronic Structure of Armchair MoS $_2$ Nanoribbon," *J. Phys. Chem. C*, vol. 119, no. 38, pp. 22164–22171, Sep. 2015, doi: 10.1021/acs.jpcc.5b04747.

[9] M. Matić;, T. Župančić, and M. Poljak, "Parallelized Ab Initio Quantum Transport Simulation of Nanoscale Bismuthene Devices," in *2022 45th Jubilee International Convention on Information, Communication and Electronic Technology (MIPRO)*, 2022, pp. 118–123. doi: 10.23919/MIPRO55190.2022.9803335.

[10] M. Matić and M. Poljak, "Ab initio quantum transport simulations of monolayer GeS nanoribbons," *Solid-State Electronics*, vol. 197, p. 108460, Nov. 2022, doi: 10.1016/j.sse.2022.108460.

[11] A. Rahman, J. Guo, S. Datta, and M. S. Lundstrom, "Theory of ballistic nanotransistors," *IEEE Trans. Electron Devices*, vol. 50, no. 9, pp. 1853–1864, Sep. 2003, doi: 10.1109/TED.2003.815366.

[12] M. Matic, M. Leljak, and M. Poljak, "Estimating OFF-state Leakage in Silicene Nanoribbon MOSFETs from Complex Bandstructure," in *2021 44th International Convention on Information, Communication and Electronic Technology (MIPRO)*, Opatija, Croatia: IEEE, Sep. 2021, pp. 85–89. doi: 10.23919/MIPRO52101.2021.9596876.

[13] A. Szabo and M. Luisier, "Under-the-Barrier Model: An Extension of the Top-of-the-Barrier Model to Efficiently and Accurately Simulate Ultrascaled Nanowire Transistors," *IEEE Trans. Electron Devices*, vol. 60, no. 7, pp. 2353–2360, Jul. 2013, doi: 10.1109/TED.2013.2263386.

[14] N. Marzari and D. Vanderbilt, "Maximally localized generalized Wannier functions for composite energy bands," *Phys. Rev. B*, vol. 56, no. 20, Art. no. 20, Nov. 1997, doi: 10.1103/PhysRevB.56.12847.

[15] P. Giannozzi *et al.*, "QUANTUM ESPRESSO: a modular and open-source software project for quantum simulations of materials," *J. Phys.: Condens. Matter*, vol. 21, no. 39, Art. no. 39, Sep. 2009, doi: 10.1088/0953-8984/21/39/395502.

[16] H. J. Monkhorst and J. D. Pack, "Special points for Brillouin-zone integrations," *Phys. Rev. B*, vol. 13, no. 12, Art. no. 12, Jun. 1976, doi: 10.1103/PhysRevB.13.5188.

[17] J. P. Perdew, K. Burke, and M. Ernzerhof, "Generalized Gradient Approximation Made Simple," *Phys. Rev. Lett.*, vol. 77, no. 18, Art. no. 18, Oct. 1996, doi: 10.1103/PhysRevLett.77.3865.

[18] G. Pizzi *et al.*, "Wannier90 as a community code: new features and applications," *J. Phys.: Condens. Matter*, vol. 32, no. 16, p. 165902, Apr. 2020, doi: 10.1088/1361-648X/ab51ff.

[19] S. Datta, *Electronic Transport in Mesoscopic Systems*. Cambridge University Press, 1997.

[20] M. Pourfath, *The Non-Equilibrium Green's Function Method for Nanoscale Device Simulation*. in Computational Microelectronics. Wien: Springer-Verlag, 2014. doi: 10.1007/978-3-7091-1800-9.

[21] Y. He, T. Kubis, M. Povolotskyi, J. Fonseca, and G. Klimeck, "Quantum transport in NEMO5: Algorithm improvements and high performance implementation," in *2014 International Conference on Simulation of Semiconductor Processes and Devices (SISPAD)*, Sep. 2014, pp. 361–364. doi: 10.1109/SISPAD.2014.6931638.

[22] M. Poljak, "Electron Mobility in Defective Nanoribbons of Monoelemental 2D Materials," *IEEE Electron Dev. Lett.*, vol. 41, no. 1, pp. 151–154, Jan. 2020, doi: 10.1109/LED.2019.2952661.

[23] M. Poljak, M. Matić, and A. Zeljko, "Minimum Contact Resistance in Monoelemental 2D Material Nanodevices With Edge-Contacts," *IEEE Electron Device Letters*, vol. 42, no. 8, pp. 1240–1243, Aug. 2021, doi: 10.1109/LED.2021.3087908.

[24] "'IEEE Intl. Roadmap for Devices and Systems (IRDS), 2019 Update.' https://irds.ieee.org/."

Biography

Mislav Matić was born in 1995 in Zagreb, Croatia, where he completed primary and secondary school. In 2018, he graduated from the BS degree program in Electrical Engineering and Information Technology at the Faculty of Electrical Engineering and Computing, University of Zagreb (UNIZG-FER). In June 2020, he graduated from the same institution with a MS in Electronics *cum laude* (4.92 GPA). Since October 2020, he has been working as a research assistant in the Department of Electronics, Microelectronics, Computer and Intelligent Systems (ZEMRIS) at UNIZG-FER on the CONAN2D project (Computational design of nanotransistors based on novel 2D materials, Grant. No. UIP-2019-04-3493, sponsored by the Croatian Science Foundation) under the supervision of Assoc. Prof. Mirko Poljak, PhD. During his PhD studies, he participated in the SiNANO 2022 summer school in Glasgow, UK, and the European School On Nanosciences and Nanotechnologies (ESONN) 2023 in Grenoble, France. In addition, he was a visiting researcher at IHP-Frankfurt, Germany, twice for two weeks in 2022 and 2023 as part of the bilateral Croatia-Germany project GRONGER led by Assoc. Prof. Mirko Poljak and Dr. Mindaugas Lukosius. His research efforts focus on the development of advanced atomistic simulation software to predict the performance of nanotransistors based on 2D materials. To date, he has authored or co-authored 12 journal papers and 14 conference papers.

Journal Papers

[J1] M. Matić and M. Poljak, “Intrinsic performance limits of extremely scaled field-effect transistors based on MX_2 (M = {Zr, Hf}, X = {S, Se}) nanoribbons,” *Journal of Applied Physics*, vol. 136, no. 8, p. 084307, Aug. 2024, doi: 10.1063/5.0224088.

[J2] M. Poljak, M. Matić, I. Prevarić, and K. Japec, “Ballistic performance and overshoot effects in gallenene nanoribbon field-effect transistors,” *Journal of Applied Physics*, vol. 135, no. 7, 2024. doi: 10.1063/5.0188216

[J3] M. Matić and M. Poljak, “Ballistic Performance of Quasi-One-Dimensional Hafnium Disulfide Field-Effect Transistors,” *Electronics*, vol. 13, no. 6, p. 1048, 2024. doi: 10.3390/electronics13061048

[J4] M. Matić and M. Poljak, “Modulation of ballistic injection velocity in phosphorene nanodevices by bias and confinement effects,” *Solid-State Electronics*, vol. 209, p. 108776, 2023. doi: 10.1016/j.sse.2023.108776

[J5] M. Matić and M. Poljak, “Electronic, transport and ballistic device properties of quasi-one-dimensional GeS,” *Journal of Computational Electronics*, vol. 22, no. 5, pp. 1350–1362, 2023. doi:10.1007/s10825-023-02054-4

[J6] M. Poljak and M. Matić, “Optimum Contact Configurations for Quasi-One-Dimensional Phosphorene Nanodevices,” *Nanomaterials*, vol. 13, no. 11, p. 1759, 2023. doi:10.3390/nano13111759

[J7] M. Matić and M. Poljak, “Ab initio quantum transport simulations of monolayer GeS nanoribbons,” *Solid-State Electronics*, vol. 197, p. 108460, 2022. doi:10.1016/j.sse.2022.108460

[J8] M. Poljak, M. Matić, and A. Zeljko, “Impact of Contact Configuration on Contact Resistance in Ultranarrow Graphene Nanoribbon Devices,” *IEEE Transactions on Electron Devices*, vol. 69, no. 9, pp. 5283–5288, 2022. doi: 10.1109/TED.2022.3188957

[J9] M. Poljak, M. Matić, T. Župančić, and A. Zeljko, “Lower Limits of Contact Resistance in Phosphorene Nanodevices with Edge Contacts. Nanomaterials 2022, 12, 656,” *Electronic Nanodevices*, p. 31, 2022. doi:10.3390/nano12040656

[J10] M. Poljak and M. Matić, “Bandstructure and Size-Scaling Effects in the Performance of Monolayer Black Phosphorus Nanodevices,” *Materials*, vol. 15, no. 1, p. 243, 2021. doi:10.3390/ma15010243

[J11] M. Poljak, M. Matić, and A. Zeljko, “Minimum contact resistance in monoelemental 2D material nanodevices with edge-contacts,” *IEEE Electron Device Letters*, vol. 42, no. 8, pp. 1240–1243, 2021. doi:10.1109/LED.2021.3087908

[J12] M. Poljak and M. Matić, “Metallization-induced quantum limits of contact resistance in graphene nanoribbons with one-dimensional contacts,” *Materials*, vol. 14, no. 13, p. 3670, 2021. doi:10.3390/ma14133670

Conference Papers

[C1] M. Matić and M. Poljak, “Validity of the Ballistic Top-of-the-Barrier Model for FETs Based on 2D Material Nanoribbons,” in *2024 47th MIPRO ICT and Electronics Convention (MIPRO)*, 2024, pp. 1596–1601. doi: 10.1109/MIPRO60963.2024.10569245

[C2] J. Jaram, M. Matić, and M. Poljak, “Impact of Vacancies on the Transport Properties of Monolayer Germanium-Sulfide Nanoribbons,” in *2024 47th MIPRO ICT and Electronics Convention (MIPRO)*, 2024, pp. 1608–1613. doi: 10.1109/MIPRO60963.2024.10569394

[C3] T. Vukadin, M. Matić, and M. Poljak, “Investigation of the One-Dimensional Semiconductor I_4Si_2 as a FET Channel Material,” in *2024 47th MIPRO ICT and Electronics Convention (MIPRO)*, 2024, pp. 1602–1607. doi: 10.1109/MIPRO60963.2024.10569371

[C4] K. Japec, M. Matić, R. Lukose, M. Lisker, M. Lukosius, and M. Poljak, “Determining Graphene and Substrate Quality from the Coupled Hall Mobility Measurements and Theoretical Modeling,” in *2023 46th MIPRO ICT and Electronics Convention (MIPRO)*, 2023, pp. 179–183. doi: 10.23919/MIPRO57284.2023.10159692

[C5] M. Matić and M. Poljak, “Transport Properties and Device Performance of Quasi-One-Dimensional MoS_2 FETs,” in *2023 46th MIPRO ICT and Electronics Convention (MIPRO)*, 2023, pp. 168–172. doi: 10.23919/MIPRO57284.2023.10159951

[C6] M. Poljak and M. Matić, “Bandgap Narrowing in Silicene Nanoribbons with Metal Edge Contacts,” in *2023 46th MIPRO ICT and Electronics Convention (MIPRO)*, 2023, pp. 173–178. doi: 10.23919/MIPRO57284.2023.10159933

[C7] I. Prevarić, M. Matić, and M. Poljak, “Tunneling Attenuation and Leakage Current in MoS_2 Nanoribbon MOSFETs,” in *2023 46th MIPRO ICT and Electronics Convention (MIPRO)*, 2023, pp. 163–167. doi: 10.23919/MIPRO57284.2023.10159745

[C8] M. Matić, T. Župančić, and M. Poljak, “Parallelized *Ab Initio* Quantum Transport Simulation of Nanoscale Bismuthene Devices,” in *2022 45th Jubilee International Convention on Information, Communication and Electronic Technology (MIPRO)*, 2022, pp. 118–123. doi: 10.23919/MIPRO55190.2022.9803335

[C9] M. Poljak, M. Matić, I. Prevarić, and K. Japec, “Bandstructure and Transport Properties of Semiconducting Gallenene Nanoribbons,” in *2022 45th Jubilee International Convention on Information, Communication and Electronic Technology (MIPRO)*, 2022, pp. 124–128. doi: 10.23919/MIPRO55190.2022.9803442

[C10] M. Poljak and M. Matić, “Extraction of contact resistance from Green’s function simulations of 2D material nanoribbon devices,” in *International Workshop on Computational Nanotechnology 2021*, 2021, pp. 123–124. ISBN: 978-89-89453-30-7

[C11] M. Poljak and M. Matić, “DFT-Based Tight-Binding Model for Atomistic Simulations of Phosphorene Nanoribbons,” in *2021 44th International Convention on Information, Communication and Electronic Technology (MIPRO)*, 2021, pp. 80–84. doi: 10.23919/MIPRO52101.2021.9596745

[C12] M. Matić, M. Leljak, and M. Poljak, “Estimating OFF-state Leakage in Silicene Nanoribbon MOSFETs from Complex Bandstructure,” in *2021 44th International Convention on Information, Communication and Electronic Technology (MIPRO)*, 2021, pp. 85–89. doi: 10.23919/MIPRO52101.2021.9596876

[C13] M. Poljak and M. Matić, ‘Bandstructure Effects in Phosphorene Nanoribbon MOSFETs from NEGF Simulations Using a New DFT-based Tight-binding Hamiltonian Model’, in *2021 International Conference on Simulation of Semiconductor Processes and Devices (SISPAD)*, 2021, pp. 180–183. doi: 10.1109/SISPAD54002.2021.9592544

[C14] M. Poljak and M. Matić, “Quantum Transport Simulations of Phosphorene Nanoribbon MOSFETs: Effects of Metal Contacts, Ballisticity and Series Resistance,” in *2020 International Conference on Simulation of Semiconductor Processes and Devices (SISPAD)*, 2020, pp. 371–374. doi: 10.23919/SISPAD49475.2020.9241601

Životopis

Mislav Matić rođen je 1995. godine u Zagrebu, Hrvatska, gdje je završio osnovnu i srednju školu. Godine 2018. završio je preddiplomski studij elektrotehnike i informacijske tehnologije na Fakultetu elektrotehnike i računarstva Sveučilišta u Zagrebu (UNIZG-FER). U lipnju 2020. diplomirao je *cum laude* na istoj instituciji u području elektronike (prosjek ocjena 4,92). Od listopada 2020. godine radi kao doktorand u Zavodu za elektroniku, mikroelektroniku, računalne i inteligentne sustave (ZEMRIS) na UNIZG-FER-u na projektu CONAN2D (Computational design of nanotransistors based on novel 2D materials, Grant. No. UIP-2019-04-3493, pokrovitelj Hrvatska zaklada za znanost) pod mentorstvom izv. prof. dr. sc. Mirka Poljaka. Tijekom doktorskog studija sudjelovao je na ljetnoj školi SiNANO 2022 u Glasgowu, Ujedinjeno Kraljevstvo, i European School on Nanosciences and Nanotechnologies (ESONN 2023) u Grenobleu, Francuska. Osim toga, bio je gostujući istraživač na IHP-Frankfurt, Njemačka, dva puta po dva tjedna u 2022. i 2023. godini u sklopu bilateralnog hrvatsko-njemačkog projekta GRONGER pod vodstvom izv. prof. dr. sc. Mirka Poljaka i dr. sc. Mindaugasa Lukosiusa. Njegovi istraživački interesi usmjereni su na razvoj naprednog softvera za atomističku simulaciju za predviđanje performansi nanotranzistora temeljenih na 2D materijalima. Autor je ili koautor na 12 radova u časopisima i 14 radova na konferencijama.